University of Liège - Faculty of Applied Sciences

Multi-Degree-of-Freedom Hybrid Fire Testing in a Non-Linear Environment

A Thesis Submitted in Partial Fulfilment of the Requirements for the Degree of Doctor of Philosophy

in APPLIED SCIENCES

by

Elke Mergny

February 2021

Supervisor

Prof. Dr. Ir. Jean-Marc Franssen

Research institute

Urban and Environmental Engineering
Faculty of Applied Sciences
University of Liege, Belgium

Examination committee

Prof. Dr. Ir. Laurent Duchêne (chairman)	University of Liege, Belgium Faculty of Applied Sciences	Department ArGEnCo Structural Engineering
Prof. Dr. Ir. Jean-Marc Franssen (supervisor)	University of Liege, Belgium Faculty of Applied Sciences	Department ArGEnCo Structural Engineering
Prof. Dr. Ir. Vincent Denoël (co-supervisor)	University of Liege, Belgium Faculty of Applied Sciences	Department ArGEnCo Structural Engineering
Dr. Ir. Guillaume Drion	University of Liege, Belgium Faculty of Applied Sciences	Department ArGEnCo Structural Engineering
Prof. Dr. Ir. Nicola Tondini	University of Trento, Italy	Department of Civil, Environmental and Mechanical Engineering
Dr. Ir. Fabienne Robert	CERIB, France	Fire Testing Center

Research funding

This work was supported by the Fonds de la Recherche Scientifique - FNRS under Grant n° 31297790.

Author's contact details

Elke Mergny
Urban and Environmental Engineering Research Unit, University of Liège
+1/419, B52 Quartier Polytech 1, Allée de la Découverte 9,
4000 Liège, Belgium
Email : e.mergny@gmail.com, elke.mergny@uliege.be

ACKNOWLEDGEMENT

This work was supported by the Fonds de la Recherche Scientifique - FNRS under Grant n° 31297790.

I would like to express my sincere gratitude to my supervisor, Prof. Jean-Marc Franssen, for his patient guidance during my PhD research work. I am impressed by his great passion for fire engineering and see him as a great example for me to follow.

Besides my advisor, I would like thank Prof. Guillaume Drion for sharing his knowledge of control theory. I am also thankful to Prof. Thomas Gernay, Prof. Vincent Denoël and Prof. Nicola Tondini for their expertise and precious advice.

I spent valuable time at the Fire Laboratory of the University of Liege. I am thankful to Eric Wellens, Fabien Dumont, Adil Ouardani and Nicolas Mestrée. They were always available for questions and devoted long hours of effort to set up the specimens and taught me many technical skills.

I also thank the members of the Laboratory for Materials and Structures that helped me during summer to prepare the specimen and plates, especially, Michel and Mario that taught me how to cut steel specimen and drill steel plates.

I am finally grateful to all the members of the Structural Engineering unit who warmly welcomed me and accompanied me in their own way during my time spent at the university. I thank especially Antonio Gamba, my lovely office colleague. I will miss our little gossips and I promise to never reveal our little secrets. Everything that happened in our *headquarters*, will remain in the *headquarters*.

Ich bin meiner geliebten Familie dankbar, die mich immer unterstützt hat (ily).

ABSTRACT

Hybrid Fire Testing (HFT) is a performance-based approach for structures in fire based on substructuring method. A complete structure is divided in two substructures, one being in a fire test laboratory (physical substructure [PS]), and one being numerically simulated (numerical substructure [NS]). By reducing the number of elements to be tested, this method overcome the huge costs of large-scale tests. Some hybrid fire tests have been successfully performed in the last decades, showing that this technique is promising. However, as HFT is still in its infancy, these hybrid tests were limited to one-degree-of-freedom (DOF) tests. In parallel with the tests, the stability of the HFT process has been studied and algorithms have been developed. These algorithms have been validated numerically but few have been used in experimental tests.

Purpose – This research aims first to propose a new framework based on linear control system theory and proportional integral controller to address identified stability issues and control the time properties in HFT. The final objective consists in performing multi-DOF tests based on this methodology.

Methodology – The research approaches HFT as a linear control problem. It first establishes the state-space representation to give the general stability conditions. Then, it shows how a proportional integral controller can be incorporated in the system to maintain stability. A virtual HFT is performed on a 2D steel frame for validation. Finally, fully automated HFT are conducted on half-scale steel specimen and using PI control procedure. Three tests are presented: a one DOF-test, a two-DOF test and a three-DOF test. The tested specimen are square steel hollow sections heated electrically. The NS of each tests are modelled on SAFIR and their behaviour is non-linear.

Findings – The research shows that control system theory provides an efficient framework for HFT. It rigorously formulates the stability conditions of the system and gives accurate stability zones for single DOF systems. It demonstrates that proportional integral control allows capturing the global behaviour of a structure, including if the numerical substructure behaves nonlinearly and is subjected to fire. In addition to numerical validation, multi-DOF tests are presented as previous research were limited to one-DOF tests.

Limitations – Even if the experimental tests were successfully performed, some criticisms can be formulated about the use of linear proportional integral control in HFT. First, a well-known drawback of control theory is that these methods are sensitive to errors between the model that is used to design the controller and the actual system. It is essential to at least know the mechanical properties at room temperature of the heated elements, which is not necessarily available. Then, because diagonal gain matrices are considered, the method neglects the fact that DOFs are coupled, which could involve a loss of accuracy and efficiency. Finally, as it is linear control, the gain matrices are designed with initial mechanical properties and are kept constant during the test as the stiffness of the PS will degrade during the test. This assumption did not cause stability problems or prevent maintaining force equilibrium. However, this is at the origin of oscillations in the system and there is no guarantee that it cannot be harmful for future tested specimen.

Contents

Introduction

Motivation

Displaying a satisfactory behaviour in case of fire is an essential requirement for any building constructions hosting a certain number of occupants such as dwellings, office buildings, hospitals, or hotels. In many cases, the fire situation is the one that drives the design of the building, more than any serviceability limit state or ultimate limit state situations considered at room temperature. A clear understanding of the behaviour of building structures subjected to fire is thus essential for the engineering community.

The *prescriptive design approach* provides rules to design structures in fire. These rules are mainly based on results of fire tests on single structural elements, such as beams, or columns, subjected to standard or natural fire. However, this design approach appears to be open to criticism because the predicted performance of a single structural element does not correspond to the performance of the same element in a structure. In the last decades, large-scale tests demonstrated in fact that the fire resistance of entire structures were better than the predicted one based on single elements analyses, among others, because of load redistributions (Fontana, Knobloch et Frangi 2013). Also, experimental investigations on columns with restrained axial elongation showed that the fire performance could be reduced in comparison with columns tested with unrestrained thermal elongation. (Korzen, Rodrigues et Correia 2009)

Performance based fire design are thus increasingly preferred from prescriptive design approach. These approaches aim to consider the behaviour of the entire structure when evaluating the performance of a structural element. To perform such analysis, there are currently two available options: Full-scale tests and numerical simulations.

Full-scale tests provide valuable insight into the behaviour of structures in fire. However, except in rare occasions, it cannot be envisaged to test complete building structures at full scale. This is because of budget constraints, but also because of the limited size of the equipment that is available to perform fire tests. Most furnaces allow testing a single element such as slabs, beams, walls or columns, for example. Nevertheless, as mentioned before, the main drawback of these tests is that, because of technical constraints and because of the lack of an established and robust theoretical framework, nearly all tests performed so far have systematically been performed with fixed boundary conditions.

Numerical modelling of structures has made tremendous progress in the recent decades and can be used as an alternative to large-scale tests (Franssen et Gernay 2017). In fact, large buildings are nowadays designed and built for which the fire situation has been considered entirely by numerical modelling. In some cases, the validity of the numerical approach has been demonstrated by confrontation with real incidents. Nevertheless, it does mean that experimental testing of the behaviour of structural elements to fire has become obsolete. Indeed, with few exceptions, a

numerical model can only reproduce failure modes that have been foreseen in the model and, for this, that have been observed experimentally. Spalling of concrete or local buckling in slender steel elements, for example, would not have been predicted by models built on experiments in which concrete did not spall or in which only stocky steel sections have been used. The construction industry, driven by economical as well as environmental constraints, is now in a process of rapid innovation; new structural solutions are proposed as well as new materials such as high-performance concretes, high strength steels, composite materials, bio sourced materials. Retrofit of the existing building also leads to the development of innovative technologies that had never been applied before.

To overcome the restrictions of numerical modelling and huge cost of full-scale testing, a novel testing technique has been developed. The main idea of the method can be summarized as follows: during the fire test, the boundary conditions at the ends of a tested specimen are continuously updated in such a way that they reflect the real conditions that would prevail if the specimen would be subjected to fire in a complete structure. Because the specimen is physically tested in a full-scale furnace while the behaviour of the rest of the structure and, hence, the reactions and displacements at the interface are computed during the test in parallel in a numerical model, see Fig. 1, this technology is called Hybrid Fire Testing or HFT.

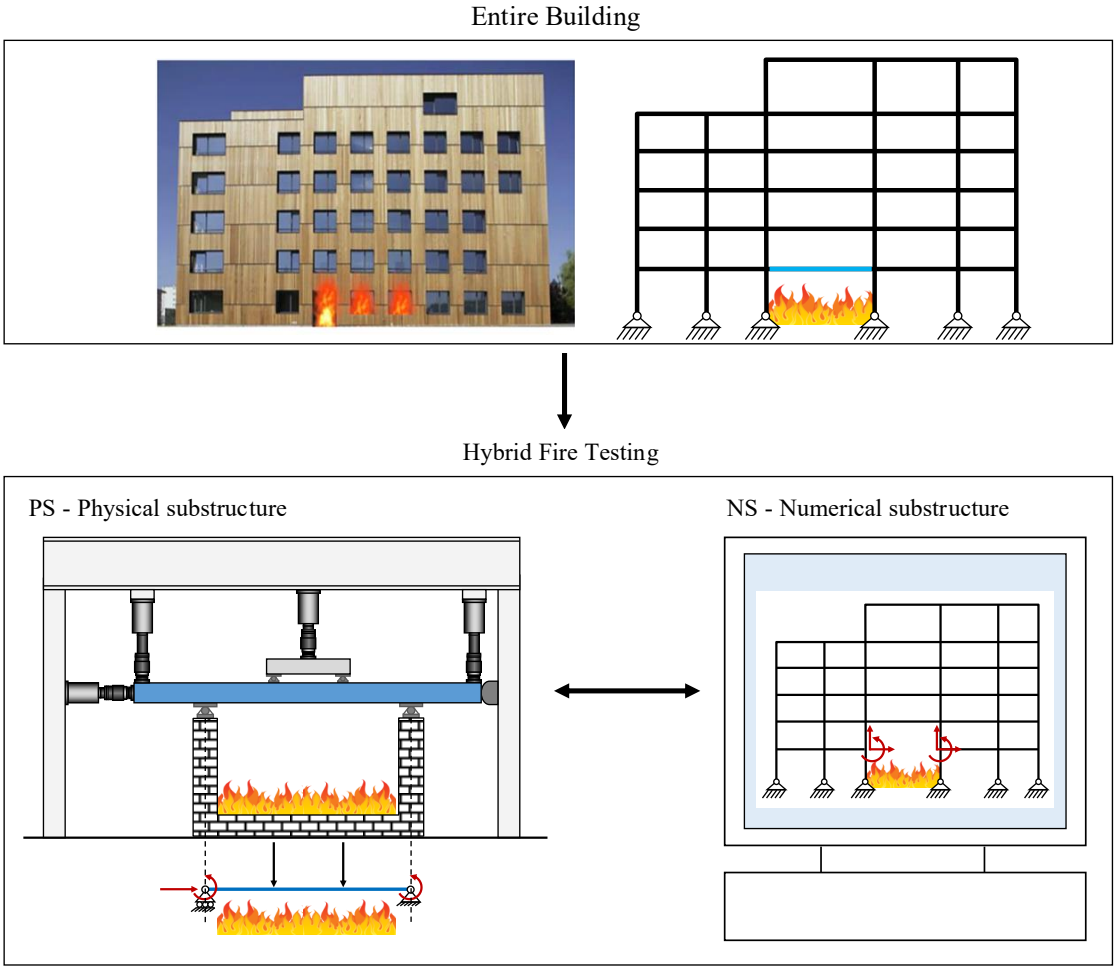

Fig. 1 – Hybrid Fire Testing

Hybrid testing is not new in structural engineering and have been applied for a long time in the field of seismic. However, despite the many contributions of this research in earthquake engineering, the adoption of hybrid testing in fire engineering is not straightforward because of phenomena specific to temperature increase. Anyway, some hybrid fire tests have been successfully performed in the last decades, showing that this technique is promising.

However, as HFT is still in its infancy, these hybrid tests were limited to one-degree-of-freedom (DOF) tests. In parallel with the tests, the stability of the process has been studied, and algorithms have been developed. These algorithms have all been validated numerically but few have been used in experimental tests. This lack of tests is mainly linked to the several issues research carried out on HFT must face. The main challenges are related to the numerous components that interact between each other during a test. They can be listed as follows:

- The physical substructure (PS) is the part of the structure which will be experimentally tested in the furnace because it is made of a new material or it is a new structural system difficult to be represented numerically.
- The numerical substructure (NS) to be analysed aside during the hybrid simulation. The NS can be modelled in a finite element (FE) model (especially recommended when parts of the NS are exposed to fire) or it can be predetermined in a matrix.
- The transfer system between the NS and PS, i. e., the actuators that apply the response of the NS (forces or displacements) to the PS.
- The data-acquisition system in the furnace, i. e., the instruments (displacements transducers and inclinometers, load cells, thermocouples) that register the mechanical and thermal response of the PS.

The interaction between NS and PS involves that equilibrium of forces and compatibility of displacement at the interface of these substructures must be continuously reached during the test. This is a major issue that can be divided into two important topics. First, it entails solving the theoretical problem of substructuring in the case of structures subjected to fire. This mathematical problem is not easy to deal with because it involves stiffness matrices which have very different DOFs from each other and properties that degrade because of heat. Secondly, it involves overcoming technical difficulties due to the actions of the other components of the HFT. Indeed, the transfer system can be behind delays and control errors that can lead to inaccuracies and instabilities if the developed method is not robust enough. The same goes for the acquisition system, whose measurement errors are also problematic. Moreover, to make all these components communicate with each other, software development is often necessary and constitutes a significant part of the research. For these reasons, hybrid fire tests are seldom, and most tests performed so far have been limited to one DOF.

Purpose

This research aims first to propose a new methodology for HFT based on linear control system theory. This methodology has been chosen because it provides a general framework that addresses stability issues, controls the time properties in HFT and allows to identify the effect of delay and experimental errors. Then, it intends to demonstrate that proportional integral control allows capturing the global behaviour of a structure, including if the numerical substructure behaves nonlinearly and is subjected to fire. This controller has the advantage of taking into account the history of the test in the corrections of displacements of the substructures, in addition to the previous mechanical response. The third objective consists in performing multi-DOF tests based on this methodology.

Outline

The presented dissertation is structured in three Chapters, starting with the introduction.

The first Chapter “State of the art” details the development of the hybrid test method in civil engineering. As hybrid testing consists in simulating the mechanical behaviour of a structure by splitting it into two subdomains, a numerical substructure NS and a physical specimen PS, a brief description of the domain decomposition methods is firstly presented. Then, one approaches the intensive research in hybrid testing that has been developed since the early 1970s in the field of earthquake engineering. This research paved the way for the development of HFT that is examined in the last part of this Chapter.

In Chapter 2, the mathematical concept that are used in this thesis are briefly described. Then, the state-space representation of HFT is established, and a general stability condition highlighted. It demonstrates the need of feedback control to stabilise the system. Afterwards, adopting a system representation for the process of HFT, a state-space representation is developed for the system using a control action that is optimum and stable in the case of a proportional and proportional integral controller. The optimization of the controllers deals with the rise time, absence of overshoot and oscillation. The developed theory is finally applied to a virtual hybrid test or VHFT (i.e., a test where both substructures are numerically modelled) on a multi-DOF system.

The last Chapter presents real-time fully automated HFT performed on half-scale steel specimen in the Fire Test Laboratory of Liege University and using proportional integral control procedure. Three tests were performed: a one DOF-test, a two-DOF test and a three-DOF test. The tested specimen are steel square hollow sections heated electrically. The NS of each tests are modelled on SAFIR® and their behaviour is non-linear.

Chapter I
State of the Art

This Chapter presents the domain decomposition methods and a review of the hybrid test method in earthquake and fire engineering.

I.1 Domain decomposition methods

A key aspect of hybrid testing is the substructuring technique. The critical elements of the structure are physically tested while the remainder of the structure whose response can be more easily predicted is numerically modelled. It is therefore a question of dividing a problem into several independent subdomains to solve it more easily. This method of resolution is at the base of a family of method called Domain Decomposition (DD) methods.

These DD methods can be classified into two categories. The first uses *overlapping domain decomposition* (see Fig. I-1 (a)) and mainly consists of the Schwarz alternating method and the additive Schwarz method (Schwarz 1890). These methods are not relevant to hybrid testing because the two subdomains NS and PS intersect on their interface. Thus, one will rather approach the second category of the DD methods that uses *non-overlapping domain decomposition* (see Fig. I-1 (b)) and includes two main methods: Balancing domain decomposition and finite element tearing and interconnecting method.

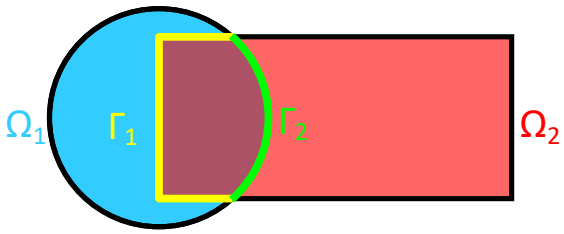

(a) Overlapping domain decomposition

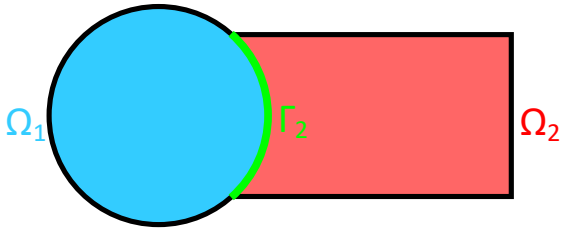

(b) Non-overlapping domain decomposition

Fig. I-1 Domain decomposition methods

I.1.1 Balancing domain decomposition

Balancing domain decomposition (BDD) method was introduced by (Mandel 1993) to improve the convergence of Neumann–Neumann algorithms with increasing subdomains. BDD method solves a Neumann problem on both sides of the interface between several subdomains. In each iteration, it combines the solution of local problems on non-overlapping subdomains with a coarse problem (version of the problem at a lower resolution) created from the subdomain nullspaces.

The use of this method in structural engineering was theoretically described by (Shioya, et al. 2003) for solving an interface problem that arises from a finite element discretization of a linear, elliptic, self-adjoint boundary value problem in domain Ω:

$$\mathbf{Ku} = \mathbf{f} \tag{I-1}$$

The components of the problem are shown in Fig. I-2. As Ω is the domain where the problem of equation (I-1) is defined, Ω_i are the non-overlapping subdomains of Ω (with $i = 1, \dots, k$), $\delta\Omega_i$ are the subdomains boundaries and Γ is the union of all subdomains' boundaries $\delta\Omega_i$. $\mathbf{u}_i$ is the vector of degrees of freedom (DOFs) corresponding to all elements in subdomain Ω_i (in this case, displacement vector), $\mathbf{K}$ is the stiffness matrix and $\mathbf{f}$ is the force vector.

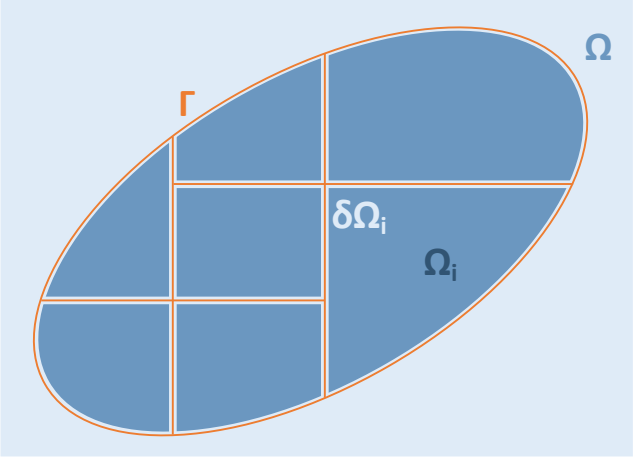

Fig. I-2 Balancing domain decomposition method

$\mathbf{u}_i$ can be divided into $\mathbf{u}_{B_i}$ (DOFs that correspond to the interface of the subdomains Ω_i) and $\mathbf{u}_{I_i}$ (remaining DOFs). The subdomain stiffness matrices are also split. The new system is:

$$\begin{bmatrix} \mathbf{K}_{II_i} & \mathbf{K}_{IB_i} \\ \mathbf{K}_{IB_i}^T & \mathbf{K}_{BB_i} \end{bmatrix} \begin{bmatrix} \mathbf{u}_{I_i} \\ \mathbf{u}_{B_i} \end{bmatrix} = \begin{bmatrix} \mathbf{f}_{I_i} \\ \mathbf{f}_{B_i} \end{bmatrix} \tag{I-2}$$

The unknowns in the interiors of the subdomain $\mathbf{u}_{I_i}$ are eliminated by reducing the problem to the Schur complement on the subdomains' interfaces. The system (I-1) is rewritten as follows:

$$\mathbf{S}\mathbf{u}_B = \mathbf{g} \tag{I-3}$$

$\mathbf{S}$ is the Schur complement and is the assembly of the local ones $\mathbf{S}_i$ (positive semidefinite):

$$\mathbf{S} = \sum_{i=1}^{k} \mathbf{N}_{B_i} \mathbf{S}_i \mathbf{N}_{B_i}^T$$
$$\mathbf{S}_i = \mathbf{K}_{BB_i} - \mathbf{K}_{IB_i}^T \mathbf{K}_{II_i}^{-1} \mathbf{K}_{IB_i} \tag{I-4}$$

$\mathbf{N}_{B_i}$ denotes the matrix with entries 0 or 1 mapping the local DOFs $\mathbf{u}_B$ into global DOFs.

To solve this problem, the preconditioned conjugate gradient method is chosen. This method requires to calculate at each time step, the solution of the following auxiliary problem:

$$\mathbf{Mz} = \mathbf{r} \tag{I-5}$$

With a symmetric positive definite matrix **M**, called a preconditioner. The algorithm of BDD returns $\mathbf{z} = \mathbf{M}^{-1}\mathbf{r}$, where:

$$\mathbf{M}^{-1} = \left[\mathbf{P} + (\mathbf{I} - \mathbf{P})\left(\sum_{i=1}^{k} \mathbf{N}_{B_i}\mathbf{D}_i\mathbf{S}_i^{+}\mathbf{D}_i^{T}\mathbf{N}_{B_i}^{T}\right)\mathbf{S}(\mathbf{I} - \mathbf{P})\right]\mathbf{S}^{-1} \tag{I-6}$$

The meaning of all matrices and the steps of the algorithm are given in Appendix A.

(Shioya, et al. 2003) showed the finite element system based on the DDM with preconditioner using BDD can be applied to structural analyses and effective performances have been obtained. However, another non-overlapping domain decomposition will be usually preferred in structural applications: the finite element tearing and interconnecting method.

I.1.2 Finite element tearing and interconnecting method

The finite element tearing and interconnecting method or FETI method was firstly published in (Farhat et Roux 1991). BDD and FETI are not mathematically equivalent. BDD combines the solution of local problems on non-overlapping subdomains with a coarse problem created from the subdomain null spaces. FETI method enforces the equality of the solution between the subdomains by Lagrange multipliers.

Let consider the finite element domain Ω divided into an arbitrary number n of non-overlapping subdomains Ω_i. The finite element mesh is also divided into a set of disconnected meshes. Within the subdomain Ω_i, n_i is the number of interior nodal unknowns and n_{I_i} is the number of interface nodal unknowns. n_I is the number of interface nodal unknowns in Ω. A representation of the problem is given in Fig. I-3.

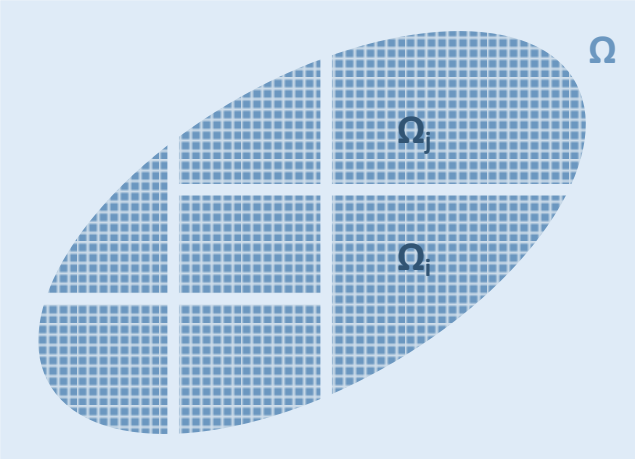

Fig. I-3 FETI method

If small displacements are considered, the general problem that must be solved on Ω is the following:

$$f(\mathbf{u}) = \frac{1}{2}\mathbf{u}^{\mathbf{T}}\mathbf{K}\mathbf{u} - \mathbf{u}^{\mathbf{T}}\mathbf{f} \tag{I-7}$$

K, **u** and **f** denotes the stiffness matrix, the displacement vector and the force vector.

Each subset Ω_i is characterized by a stiffness matrix $\mathbf{K}_i$, displacement vector $\mathbf{u}_i$, force vector $\mathbf{f}_i$ and a set Boolean symbolic matrix $\mathbf{B}_i^j$ that is set up to interconnect the meshes of Ω_i with those of its neighbours Ω_j. (Farhat et Roux 1991) demonstrated that the algebraic system that must be treated in the FETI method is the following:

$$\begin{aligned} \mathbf{K}_j\mathbf{u}_j &= \mathbf{f}_j + \sum_{k=1}^{k=a_j} \mathbf{B}_i^{j^T}\lambda && j = 1, n \\ \mathbf{B}_i^j\mathbf{u}_i &= \mathbf{B}_j^i\mathbf{u}_j && j = 1, n, \ \Omega_j \text{ connected to } \Omega_i \end{aligned} \tag{I-8}$$

Details about how the authors achieved this result as well as the expression of the Boolean matrix $\mathbf{B}_i^j$ are given in Appendix A.

DD methods are an important mathematical tool for approaching hybrid testing and some research will be based subsequently on them, especially the FETI method. Nevertheless, researchers have not necessarily used domain decomposition methods to develop hybrid tests in structural engineering. In addition, some methods have been sometimes even developed afterwards.

I.2 Hybrid testing in earthquake engineering

Hybrid testing is not new in structural engineering and have been applied for a long time in the field of seismic. Numerical models are not always available for modelling the dynamic response of structures to earthquakes, especially when the material becomes highly nonlinear (extreme deformations, cyclic degradation, low-cycle fatigue). It is in this case often difficult to model the dynamic response with satisfying accuracy. Quasi-static testing that provided codes and guidelines on element design can be used and are relatively easy to perform and economical. It is also useful for comparing the performance of different structural designs under a standardized load history. However, it does not consider the ductility demand of an earthquake ground motion on a structural specimen or the appropriate distribution of earthquake-induced forces. To fill this gap, dynamically testing is necessary. As the ground motion is reproduced with a rigid table, shaking table test method allows to simulate the earthquake response of structures. Nevertheless, it is not free from drawbacks. Large-scale testing is in fact expensive because it requires high-capacity actuation systems. The scaling of non-linear behaviour is also not recommended because it is subject to considerable uncertainty. Moreover, interactions between the table and the specimen can make difficult an accurate table control.

Thus, several couples physical-computational simulations of seismic response have been developed since the 1970's, including pseudo-dynamic testing (with and without substructuring), real-time test and effective force test method. The large amount of research makes that hybrid testing is now being applied as a reliable dynamic test method. Fig. I-4 shows a schematic diagram with the history of the method in earthquake engineering that will be approached in the following sections. The last Section I.2.6 will tackle the issue of accuracy and stability that have been investigated in this field.

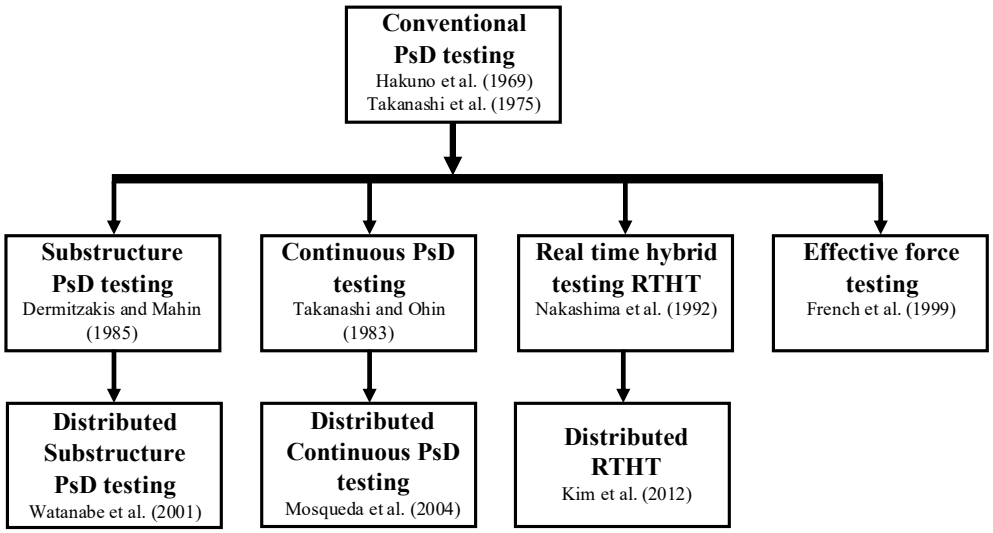

Fig. I-4 History of hybrid testing in earthquake engineering (adapted from (Carrion et Spencer 2007))

I.2.1 Pseudodynamic test

The earliest development of the Pseudodynamic test (PsD test) was published by (Hakuno, Shidawara et Hara 1969): a single DOF system was loaded by an actuator based on the result of the resolution of the equation of motion performed by an analog computer. With the introduction of the digital computer and the use of discrete systems, (Takanashi, Udagawa, et al. 1975) formally implemented the method in the mid 1970's. In this method, predicted displacements are imposed. Restoring forces are measured and used in the time integration scheme. The equation of motion is solved at the (i+1)th step:

$$\mathbf{M}\ddot{\mathbf{u}}_{i+1} + \mathbf{C}\dot{\mathbf{u}}_{i+1} + \mathbf{r}_{i+1} = \mathbf{f}_{i+1} \quad \text{(I-9)}$$

M and **C** are respectively the mass and the damping matrix, $\ddot{\mathbf{u}}_{i+1}$ is the nodal acceleration vector, $\dot{\mathbf{u}}_{i+1}$ is the nodal speed vector, $\mathbf{r}_{i+1}$ is the restoring force vector (measured) and $\mathbf{f}_{i+1}$ is the external force vector applied to the system. If the specimen behaves elastically, $\mathbf{r}_{i+1}$ is equal to $\mathbf{K}\mathbf{u}_{i+1}$. **K** is the stiffness matrix of the tested specimen/structure. Fig. I-5 (a) shows a two-storey building that is tested using this so-called *conventional PsD testing*. In this test, the structural mass, damping, and inertial forces are defined within a computational module that handles the equations of motion with two translational DOF. One assumes that each storey can be lumped to a single point of control. The predicted displacements are statically applied to the structure with actuators and the restoring forces are then measured with sensors.

In PsD testing, the loading rate is slow to not induce damping or inertia response because, these responses have already been considered in the computational module. The displacements are imposed on an expanded timescale that ranges from 100 to 1000 the actual earthquake duration. This expanded timescale allows the computation of the numerical integration step to be completed.

The first implementations of PsD applied the load with a ramp and hold procedure. However, load relaxation can occur in the holding phase and lead to inaccuracies. Consequently, (Takanashi et Ohi 1983) introduced the concept of *continuous PsD testing* and proposed to adjust continuously the actuator velocity. The actuator moves in the same direction until receiving the new signal. Afterwards, (Magonette 2001) proposed to follow the target displacement accurately within small time steps, preventing the need of a hold period. The force is measured at every sampling period Δt of the controller (typically 1 or 2 ms) and the equations of motion are integrated on the fly (without hold period) at the sampling rate.

To limit the experimental specimen to the most critical part of the structure, the idea of substructuring was brought in (Dermitzakis et Mahin 1985): the part of structure of special interest is tested and the rest of the structure is thus modelled numerically. Force equilibrium and compatibility of displacement must be assessed at the interface between the two substructures. Hence, in addition to the DOF with lumped masses, one must include the interface DOF in the equation of motion. In this so-called *conventional substructured PsD test*, one single dynamic analysis of the remaining structure is performed, as shown in Fig. I-5 (b). However, this kind of analysis may not be available. The *substructured PsD test* (Fig. I-5 (c)) separates the restoring force module and the time integration scheme. The equation of motion that is solved is thus the following:

$$\mathbf{M\ddot{u}_{i+1} + C\dot{u}_{i+1} + r_{NS_{i+1}} + r_{PS_{i+1}} = f_{i+1}} \quad \text{(I-10)}$$

$\mathbf{r}_{NS_{i+1}}$ and $\mathbf{r}_{PS_{i+1}}$ are respectively the numerical and experimental restoring forces.

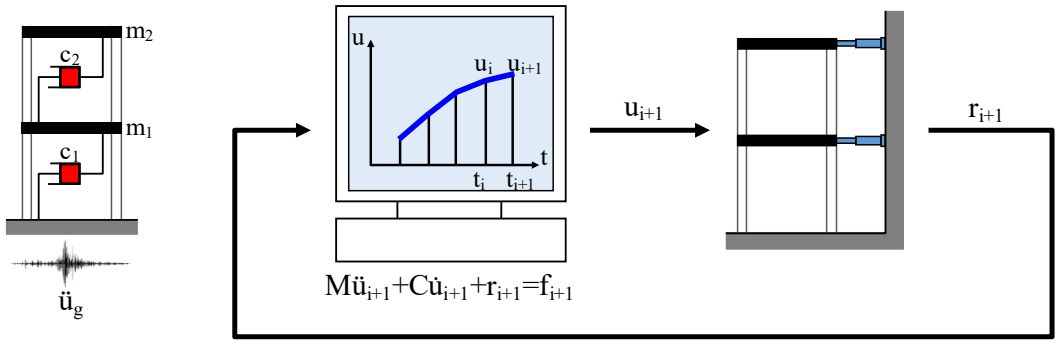

(a) Conventional PsD testing

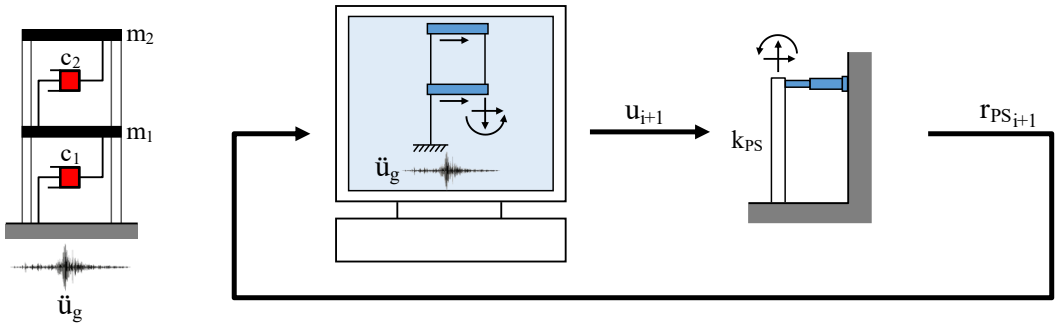

(b) Conventional substructured PsD test

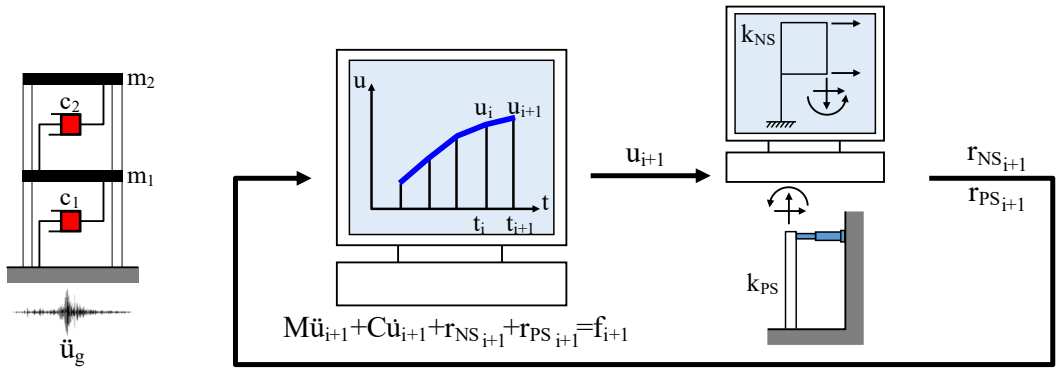

(c) Substructured PsD test

Fig. I-5 Pseudodynamic test PsD (adapted from (Carrion et Spencer 2007))

I.2.2 Real time hybrid test

The interest of PsD consists in providing realistic seismic simulation without the need for dynamically rated test equipment. As the rate of testing is slow, actuators without high hydraulic requirement can be used. Moreover, it allows complete monitoring, careful inspection of the state of the structure and ability to pause and resume the experiment. However, as the PsD test method is conducted on an expanded time scale, it cannot capture time dependent behaviour. Rate dependent material cannot be tested. (Nakashima, Kato et Takaoka, 1992) presented a real-time PsD (also called fast PsD) applied to a single DOF system with a dynamic actuator. The research required development of digital servomechanism to ensure accurate displacement and velocity control. Technical progress in the electronic fields allowed (Nakashima et Masaoka, 1999) to improve the technique proposed in 1992. They developed a method that allows uninterrupted command signals, in which the previous command displacements are used to extrapolate the next value.

In a substructured *RTHT test*, the equation of motion that is solved is the following:

$$\mathbf{M}_{NS}\ddot{\mathbf{u}}_{i+1} + \mathbf{C}_{NS}\dot{\mathbf{u}}_{i+1} + \mathbf{r}_{NS_{i+1}} + \mathbf{r}'_{PS_{i+1}} = \mathbf{f}_{i+1} \qquad \text{(I-11)}$$

$\mathbf{M}_{NS}$ and $\mathbf{C}_{NS}$ are respectively the mass matrix and the damping matrix of the NS. $\mathbf{r}_{NS_{i+1}}$ is the restoring force vector of the NS. $\mathbf{r}'_{PS_{i+1}}$ is the feedback force vector of the specimen and is different from $\mathbf{r}_{PS_{i+1}}$ because it includes inertia and damping. The procedure can be seen in Fig. I-6 (a).

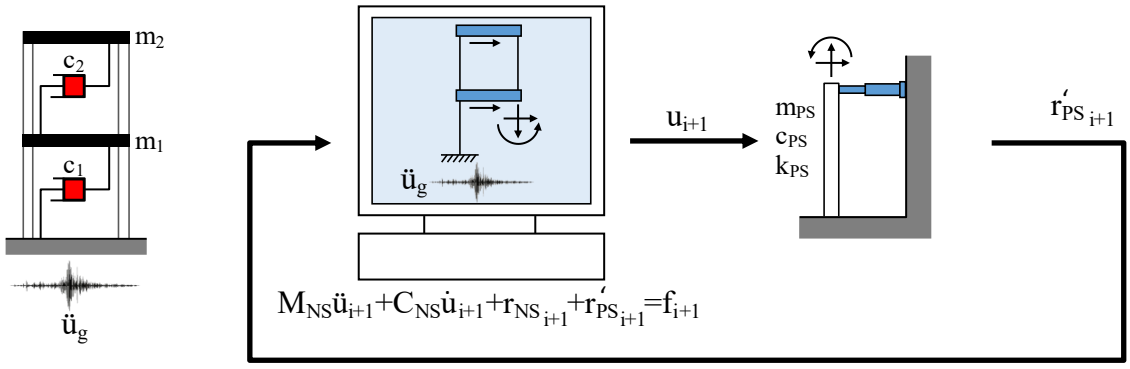

(a) RTHT (substructured)

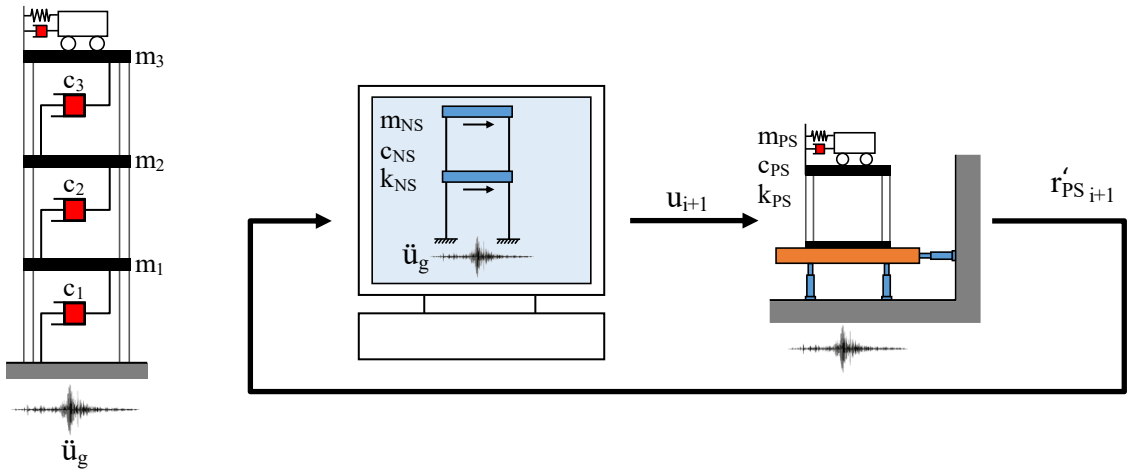

(b) RTHTST

Fig. I-6 Real hybrid time test RTHT (adapted from (Carrion et Spencer 2007))

Later, (Iemura, Igarashai et Takahashi 1999) and (Igarashi, Iemura et Suwa 2000) proposed the use of shaking table to perform RTHT to evaluate active and tuned mass damping devices. The test procedure is shown in Fig. I-6 (b). As the *real time hybrid shaking table test* or RTHTST records true dynamic behaviour, its application is appropriate for velocity dependent substructure and damping devices.

In RTHT as well as in RTHTST, researchers observed stability problem linked to phase lag between signal command and devices (actuators, shaking table) response. This point is approached in Section I.2.6.

I.2.3 Effective force testing EFT

Along with PsD and RTHT, another method has been developed and is commonly called *Effective force testing* (EFT). This method is based on a force control algorithm and is valid for systems that can be modelled as a series of lumped masses (e.g., frame structures where masses are assumed lumped at the floor level). The first test was reported by (Dimig, et al. 1999).

Fig. II-6 illustrates the testing procedure. The forces that are applied are known before the test based on the ground acceleration time history and are equal to the mass multiplied by the ground acceleration. Real-time computation is thus not necessary. However, the full structural mass needs to be modelled physically to achieve the correct dynamic response. Also, the advances in force control that enable the force application to nonlinear structures in real-time and resolve the natural velocity feedback issue of servohydraulic actuators is recent. For these reasons, its application is limited, and to date EFT has seldom been used.

As effective force testing (EFT) is a conceptually different from the previous methodologies and not relevant to HFT, this hybrid testing is not detailed in this Chapter.

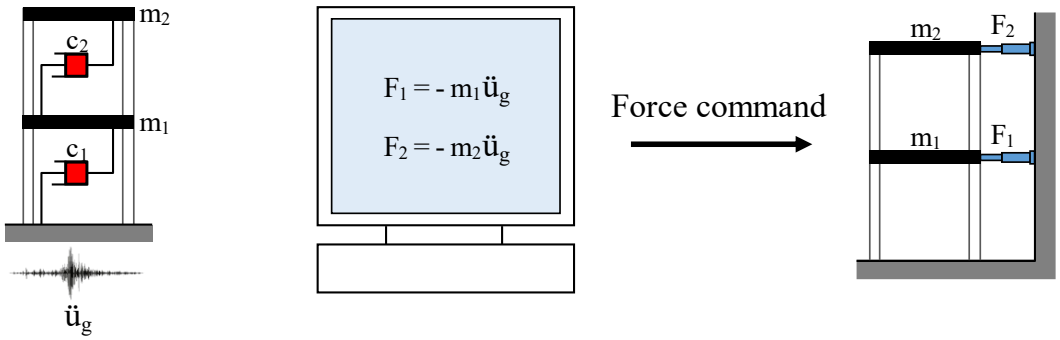

Fig. I-7 Effective force testing EFT (adapted from (Carrion et Spencer 2007))

I.2.4 Geographically distributed hybrid testing

When the development of hybrid tests was sufficiently advanced, the possibility of distributing the substructures in different places was quickly thought of. “Geographically distributed hybrid tests” are referred to tests whose different components (NS, PS, computation module) are split into two or more geographically separate laboratories. The communication between specimen and numerical model takes place via the internet. The interest consists in combining the capabilities of several sites to enable large-scale testing of bigger and more complex structures. The concept was first approached by (Campbell et Stojadinovic 1998) and (Watanabe, Sugiura, et al. 1998).

The first successful distributed hybrid tests were conducted by (Watanabe, Kitada, et al. 2001) between Kyoto University and Osaka City University. Tests were then performed within Taiwan (Yang, Wang, et al. 2007), the United States (Spencer et al. 2004) and United Kingdom (Saleem, et al. 2008). Collaboration were also conducted between Korea and Japan (Watanabe, Yun, et al.

2001), the United States and Japan (Park, et al. 2005), the United States and Taiwan (Wang, Tsai, et al. 2007) and the United States and New Zealand (Ma, et al. 2007). All these tests were conventional PsD tests. The first continuous PsD test was performed by (Mosqueda, Stojadinovic et Mahin 2004). The computer was five miles apart from the two remote specimens. Later, (Kim, Christenson et Phillips 2012) presented the first distributed RTHT between the University of Connecticut and UIUC.

In 1999, a major research project was initiated by the National Science Foundation (NSF): the George E. Brown, Jr. Network for Earthquake Engineering Simulation (NEES). This project allowed to enhance the testing facilities of 15 universities across the United States and build the necessary cyber infrastructure (NEESgrid) to link the different facilities. Other frameworks were thereafter developed as the ISEE (Wang, Wang, et al. 2003), NetSlab (Guo, Xiao et Hu 2006) and Openfresco (Schellenberg, et al. 2009).

The specific issues raised by the subject of geographically distributed hybrid testing are not related to the present research and are therefore not addressed in this Chapter.

I.2.5 Deep Learning

Even if hybrid tests are used with confidence in earthquake engineering, alternative methods such as machine learning models are still explored to perform hybrid testing. Recently, (Bas et Moustafa 2020) proposed to investigate the use of a deep learning algorithm in RTHT. The test combines linear brace model specimens (PS) along with nonlinear Machine Learning models that replace classical FE models (NS). The aim of this method is tackling the issue of complex analytical substructures that could involve delay in the process because of time computations.

The metamodels of the analytical substructure were developed with deep long short-term memory networks that were trained using the Python environment. The training dataset was obtained from pure analytical finite element simulations for the complete structure under earthquake excitation. The algorithm was tested on small-scale specimen and promising results have been published in (Bas et Moustafa 2020).

I.2.6 Accuracy and stability issues

Errors in PsD and RTHTs can be broadly separated into (McCrum et Williams 2016):

- Numerical errors associated to the integration scheme used in the computation module
- Errors associated to structural idealisation
- Experimental errors
- Delay

It has been demonstrated that these errors can be a source of inaccuracies and/or instabilities during the hybrid test. They are discussed in what follows.

Time integration technique

Many numerical integration techniques have been proposed to compute the displacement command in hybrid testing. As they are numerous and not relevant for this dissertation, only the most commonly integration scheme will be approached. One will briefly address the problems raised by the explicit numerical integration schemes, implicit numerical integration schemes and operator-splitting method.

Explicit numerical integration schemes have been used in the first implementations of hybrid testing. As the new response value for a step is calculated based on the previous step(s) value, these techniques are easy to implement and computationally efficient. However, the conditional stability of these methods limits the maximum time step to the natural frequency of the system. This

limitation is problematic for structures with higher modes of vibration. This issue can however be overcome by simplifying the structural models. The Central Difference Method (CDM) has been popular in PsD testing and RTHT. Unconditionally stable explicit methods were thereafter developed: Chang method for PsD testing (Chang 2007) and Chen-Riclès method for RTHT (Chen et Ricles 2008).

Implicit numerical integration schemes involve both the current response value and the later one. Even if these techniques are unconditionally stable, they were initially set aside. In fact, iterative corrections are necessary and can induce unloading in the system. Moreover, tangent stiffness is required and is difficult to evaluate during the hybrid test. The main contribution in that field consists of Hilber-Hughes-Taylor (HHT) numerical integration scheme (α-method) that was developed for PsD testing (Hilber, Hughes et Taylor 1977).

Operator-splitting methods or *OSM* are based on splitting of complex problems into a sequence of sub-problems that are associated with different numerical methods. The first implementation in PsD testing of this kind of technique was performed by (Nakashima, Kaminoso, et al. 1990) that used the procedure developed by (Hughes, Pister et Taylor 1979). The method was implicit in the linear part of the response and explicit in the nonlinear part. Afterwards, the use of OSM with α-damping was proposed by (Combescure et Pegon 1997) for PsD testing to combine fast computation of explicit method and numerical dissipation. Another notable contribution is the OS-SSP method developed by (Wang, Lee et Yo 2001) that proposed a state-space procedure (SSP) to rewrite the equation of motion as a first order differential equation.

Alternatives to these classical methods have also been proposed, as (Hung et El-Tawil 2009) that developed a full operator method (FOM) suitable for quasi-static testing and RTHT. Also, (Hung, Yen et Lu 2010) presented an unconditional stable predictor-corrector algorithm (Predictor alpha corrector or PAC method) for quasi static hybrid testing.

Structural idealisation

The structural idealisation affects notably the accuracy of PsD or RTH test. Special attention to experiment setup and specimen is thus required to accurately reproduce the structure that is studied. The complexity of the structure that can be tested is limited by laboratories constraints. The selection of the substructure is thus essential.

There are two main issues: the boundary conditions and the interface between PS and NS. For instance, it is difficult to reproduce complete fixity in a laboratory. Also, the number of actuators that can be used is limited on the interface: the necessary forces and/or displacements must be applied with very few actuators.

(Kwon et Kammula 2013) addressed this issue by developing a weighted systematic selection procedure to select the appropriate NS. (Yang, Tsai, et al. 2012) also developed a method to test multiple identical substructures by updating material parameter of the NS to match those of the specimen.

Experimental errors

As the experimental restoring forces are measured and fed back in the solution of the equations of motion, the experimental errors have a direct and cumulative effect on the computed displacement response. Moreover, they can propagate throughout and affect the results. Consequently, this hybrid test method is more sensitive to experimental errors than conventional test in which the displacements are known a priori (quasi-static and shake-table testing). In PsD testing, the issue has been extensively approached in (Shing et Mahin 1983) and a large part of these outcomes can be applied to RTHT.

Sources of experimental errors in hybrid testing are numerous and can include inaccurate displacement control of the hydraulic actuators, calibration errors, truncation error, noise (in the instrumentation and analog to digital converters), flexibility in the test setup and reaction frame, frictional force in the actuator connections, force relaxation, and strain-rate effects. These errors can be separated into random or systematic errors.

Random errors are unpredictable errors generated by measurement instrumentation such as random electrical noise in wires and electronic system. They cannot be compensated but can usually be reduced by increasing the number of observations. These errors are so irregular that no specific physical effect can be pointed out. However, in hybrid testing, their impact is negligible when compared to systematic errors.

Systematic errors that are consistent and repeatable error, are in fact more harmful, especially those that are caused by the actuators, because they introduced undesirable energy effects into the dynamic response of the system in (Shing et Mahin 1983). In fact, systematic overshooting numerically dissipates energy in the simulation (apparent high-system damping) and add energy to the system. This negative damping is a source of instability as shown in (Mahin, et al. 1989).

The effect of errors in hybrid testing has been minimized by using compensation scheme, improving displacement control, using I-modification (correcting the measured restoring force for the error between the target and measured displacements using the initial elastic stiffness), adding numerical damping (especially in the higher modes) to offset the effect of spurious negative damping and using lowpass filters to reduce high frequency noise in the measurements. However, very stiff structures are still an important issue. In fact, force error can be introduced even if the displacement is accurately controlled. (Carrion et Spencer 2007) developed a procedure to filter restoring force and measured displacement noise using a model-based approach and Kalman filter (Kalman 1960). The procedure was verified in a PsD test.

Delay

There is an unavoidable lag between sending a command to a servohydraulic actuator and reaching the desired position. This lag is called *delay* in hybrid testing. This delay is a significant issue in RTHT because it results in desynchronization between the measured restoring forces of the experimental substructure and the integration algorithm. Indeed, the actual force and the measured force do not correspond to each other.

The effect of actuator delay for real-time hybrid simulation has been investigated by numerous researchers. (Horiuchi, Inoue, et al. 1999) characterised this lag as being equivalent to negative damping in case of a linear elastic single DOF system. Instability happens when the negative damping is larger than structural damping. Fig. I-8 shows the effects of time delay on displacement history and load versus displacement hysteresis. Other stability analyses were performed thereafter with different ways:

- (Wallace, Sieber, et al. 2005) used a delay differential equation and introduced actuator delay in the feedback restoring force from the experimental substructure. They computed the critical values for system stability using two methods. The first one consisted of an analytical approach and the second one made use of a numerical software tool, DDE-BIFTOOL.
- (Mercan et Ricles, 2007) also used the delay differential equation but rather proposed the pseudodelay technique to perform an exact mapping of fixed delay terms and determined the stability boundary.
- (Chen et Ricles, 2008) introduced discrete control theory to include an explicit integration algorithm in the stability analysis and investigated the effect of actuator delay on real-time hybrid simulation.

All these studies showed that actuator delay is a major source of instability for the real-time simulation if not compensated properly. Several methods for compensating this delay has been thereafter examined.

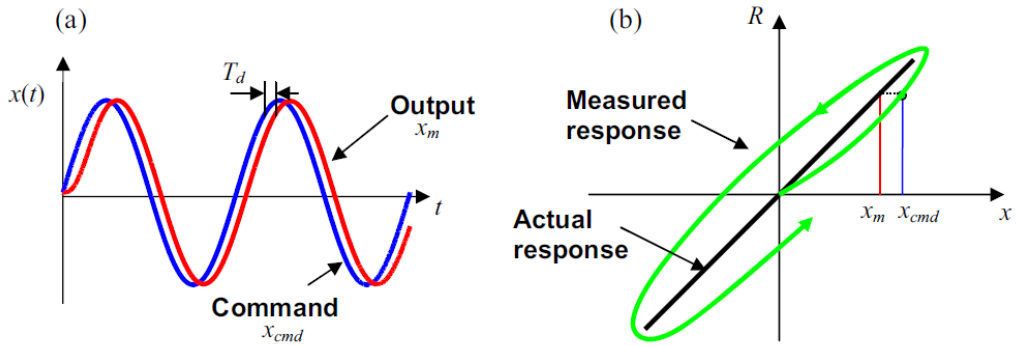

Fig. I-8 Effects of time delay on (a) displacement history; and (b) load versus displacement hysteresis (Carrion et Spencer 2007)

Constant delay compensation has been early used. These prediction schemes achieve accuracy through extrapolation and assume the delay and amplitude factor estimates are known and accurate. The first approach was proposed by (Horiuchi et Konno 1996) and consisted in using a polynomial extrapolation (Fig. I-9). A third order polynomial was recommended. In 2001, the same researchers proposed a second delay compensation based on an assumption of linear structural acceleration in (Horiuchi et Konno, 2001). Later, (Carrion et Spencer 2007) modified the method developed by (Horiuchi, Inoue, et al. 1999) to include structural properties and the external excitation force.

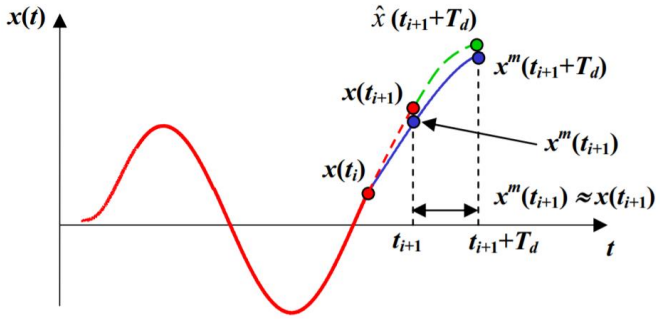

Fig. I-9 Delay compensation using response prediction (Carrion et Spencer 2007)

Other compensation methods were based on control theory and assumed that the servo-hydraulic system is a time delay system: a delay differential equation can be written and tools from control theory can be used. Among these publications, one can mention the following contributions:

- (Zhao, et al. 2003) that developed a phase lag compensator to make the phase adjustment to the compensation signal.
- (Wallace, Wagg et Neild 2005) that presented an algorithm to determine the critical delay with the delay differential equation and proposed an alternative polynomial extrapolation, considering a larger number of points than previous publications and using a least-squares approximation rather than an exact fit.
- (Jung et Shing 2006) that used PID control and feed-forward scheme.
- (Shao, Reinhorn et Sivaselvan 2006) that proposed to work with the Smith-type predictor to compensate for time delay in the displacement feedback.
- (Chen, 2007) that applied inverse compensation method to compensate for delay in a system that modelled the actuator as a first order discrete transfer function.

- (Christenson, et al. 2008) that used virtual stiffness and damping to ensure stability in case of delay.

Although it has been widely used, constant delay compensation has faced two major problems. On one hand, it is difficult to estimate accurately an actuator delay. This can lead to under- or over-compensation of delay, resulting in experimental error. On the other hand, the actuator delay might vary during the simulation due to the nonlinearities in the experimental substructure and the servohydraulic system. Adaptive delay compensation is thus required and has been developed in parallel to constant delay compensation.

The first publication about *adaptive delay compensation* was based on adaptive control theory. (Darby, Williams et Blakeborough 2002) pointed out the dependency of the actuator delay on the stiffness of the specimen and proposed a delay estimation method that used proportional feedback system to calculate delay error for each step. In the same field, (Neild, et al. 2005) implemented the adaptive minimal control synthesis (MCS) developed by (Wagg et Stoten 2001) in a proof-of-concept one DOF mass–spring–damper system. This controller is used in conjunction with the existing PID controller of the actuators to compensate the actuator phase lag. Numerous works about adaptive delay compensation were led related to this algorithm, of which the most advanced is the minimal controller synthesis algorithm with modified demand (MCSmd) developed by (Lim, et al. 2004). This controller is an adaptive controller that uses a reference model in the algorithm and a reference model compensator applied to desired displacement signal. The rate of adaptation is however defined by a user-defined (empirical) parameter.

As most approaches were limited to one-DOF systems, (Wallace, Wagg et Neild 2005) presented a more generic method that can be applied to multi-DOF systems and proposed to minimize the delay error in a servohydraulic system using techniques from synchronization theory. They developed a forward prediction algorithm that accurately coped with frequency dependent plant behaviour and operated with no prior knowledge of the plant characteristics.

Further works about adaptive delay compensation followed such as:

- (Chen et Ricles, 2010) that developed an error tracking based on adaptive inverse compensation approach.
- (Chen et Tsai 2013) that developed a combined adaptive second-order phase lead compensator (PLC) and an online restoring force compensator (RFC) for use in RTHT.
- (Wu, Wang et Bursi 2013) that presented a method using upper bound delay and optimisation of feedback.
- (Chae, Kazemibidokhti et Ricles 2013) that developed an adaptive time series (ATS) compensator.

In RTHTST, the use of delay compensation has also been met with mixed success in (Lee, Park et Min 2007) and (Wang, Gui et Zhu 2016).

This research topic is still currently studied and among the most recent approaches, some methods such as (Tao et Mercan 2019) or (Xu W., et al. 2019) are based on a frequency domain analysis to adjust parameters of a first-order transfer function, while others like (Palacio-Betancur et Gutierrez Soto 2019) proposed a conditional adaptive time series compensator. There are also approaches that consider polynomial extrapolations, such as (Wang, et al. 2019) or (Xu D., et al. 2019).

I.3 Hybrid fire testing

Regarding hybrid testing in earthquake engineering, developments in numerical integration methods, substructuring, experimental error reduction and delay compensation have led to a dynamic testing method that is reliable, accurate, efficient, and cost effective. This success largely motivated the development of hybrid tests in fire engineering from the 1990s. Thus, whereas the practice of hybrid testing was well implemented in earthquake engineering, early attempts of combining numerical simulation and experiments on structural members for the analysis of structure in fire were undertaken in several universities. The motivation of these research projects was to perform fire tests that can capture the behaviour of a heated structural element with realistic boundary conditions without the cost issue of large-scale test.

Although the experience accumulated with the hybrid tests in earthquake engineering is considerable, extension of the hybrid testing concept from earthquake engineering to fire engineering is not straightforward and leads to a new research domain that comes with a lot of challenges.

The first specific feature is that only tests performed in real time can be envisaged. In fact, except for simple metallic elements, the development of thermal gradients in the section of the elements makes time scaling impossible. Yet, different timescales are at stake: high temperature development is relatively slow (the characteristic duration of a fire test is in order of an hour) whereas the response of the specimen to a variation of boundary conditions is nearly instantaneous.

Then, in earthquake engineering, the focus is essentially on the relatively flexible DOF such as rotations and horizontal displacements. On the contrary, in the fire situation, axial elongation is one of the key effects of temperature increase and it cannot be ignored. This leads to interface matrices between the tested specimen and the rest of the structure that are quite ill conditioned as the DOF linked to axial elongation is much stiffer than the other DOF. It is thus a real challenge to develop robust numerical technique that can handle the stiff and the flexible DOF at the same time.

Finally, the NS can be exposed to fire as well, resulting in a more computationally expensive numerical simulation of its behaviour that can generate delays in real-time tests. This is the case especially if the temperature development was not imposed a priori but must be taken from the temperatures measured in the furnace during the test.

In conclusion, hybrid fire tests constitute a separate field. The history of which is detailed in the following sections.

I.3.1 lntelligenten Prüfmaschine (1989-1993)

In the mid-90s, (Hosser, Ameler, et al. 1993) developed at the Technical University of Brunswick an “Intelligent Test Apparatus” (“lntelligenten Prüfmaschine”, ITA). It consisted of a set up frame and system transfer that could perform isolated member tests on heated beams or columns. These elements were part of a numerically simulated planar steel framed structure. The ITA was designed to control 6 DOFs (3 translational DOFs, 3 rotational DOFs) at one end of the tested member. The second end was a static boundary condition (pinned, fully restrained, etc.). The procedure was described in (Kiel 1989). At each cycle, the displacement of the specimen was measured and sent to the simulated structure. Then, the force was calculated and sent to the transfer system (Fig. I-10).

Five tests were performed. Several technical difficulties were encountered and the ITA was improved. Nevertheless, the expected structural behaviour could not be reproduced satisfactorily. The results were recorded in a report (Hosser, Ameler, et al. 1995) but not published. The potential

of the new testing technique was recognized but it constituted a too daring project for the available lab control system and was not carried on.

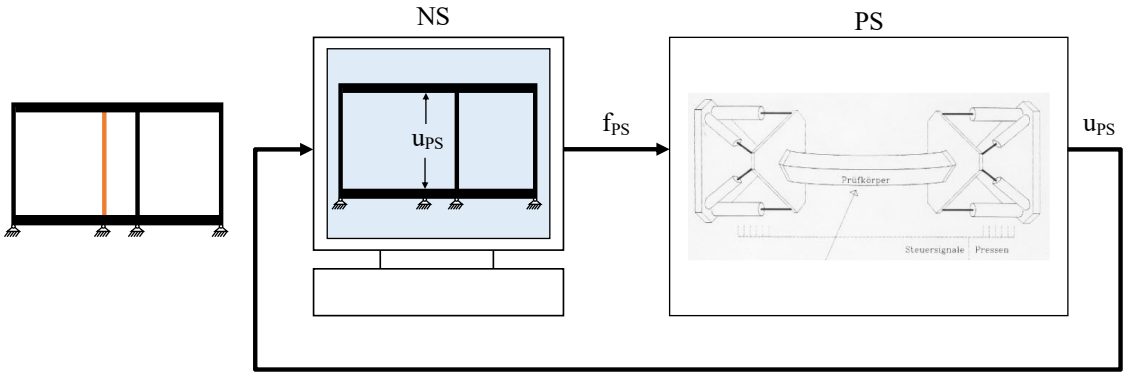

Fig. I-10 Intelligent Test Apparatus (adapted from (Kiel 1989))

I.3.2 HFT at BAM (1998-2013)

The first hybrid tests that have been published in fire engineering were performed by Korzen and associates at the BAM (Bundesanstalt für Materialforschung und -prüfung). The concept and experimental facility have been presented in (Korzen, Magonette et Buchet 1998). The BAM's furnace contains six electro-hydraulic control channels (two rotations for the top, two rotations for the bottom, one axial displacement for the bottom and one horizontal displacement for the top). During the hybrid tests, only the channel of the axial direction was controlled. The remaining channel were kept constant in displacement or rotation control. Several sections were tested in BAM:

- unprotected steel columns, HEM200 in (Korzen, Ziener, et al. 2002), HEA140 and HEB180 in (Korzen, Rodrigues et Correia 2009)
- partially encased steel columns HEA200 in (Korzen, Rodrigues et Correia 2009)
- reinforced concrete columns in (Korzen, Rodrigues et Laím 2013)

The procedure is the same in each publication, see Fig. I-11. During the hybrid test, forces are measured and sent to the simulated substructure that behaves elastically as a spring with stiffness K_{NS}. A new displacement is computed in such a way that the model force is equal to the measured force. The way the target displacement is calculated in the loop is not explicitly specified. However, the publication suggests that the measured force of the specimen f_{PS_i} is compared with the model force f_{NS_i} (computed as $K_{NS}u_i$) and that the displacement u_{i+1} is adjusted to obtain $f_{PS_{i+1}} = f_{NS_i}$. The results showed realistic trends in all publications.

In (Korzen, Neves, et al. 2006), the results of the hybrid tests performed on unprotected steel columns in (Korzen, Ziener, et al. 2002) were compared with a series of small axially compressed steel elements with restrained thermal elongation made at the Instituto Superior Tècnico (IST). At BAM, the restrained effect was numerically simulated whereas at IST the restrained effect was obtained by means of a real beam located outside the furnace. The values of the displacements and forces were different, but these differences could be explained by the varying specimen sizes and testing conditions used in the two testing facilities. Although the two tests were not equivalent (different scale, furnace and material), a similar trend was observed. The publication also showed that the tests performed at BAM were well correlated with numerical simulations that were afterwards performed.

A similar comparison was done in (Correia, Rodrigues et Korzen 2012) with partially encased steel columns subjected to ISO fire, in collaboration with the Faculty of Sciences and Technology of

University of Coimbra (FCTUC). Composite columns were tested in two different experimental systems for modelling the response of the surrounding structure. At the FCTUC, the surrounding structure was modelled experimentally by a steel restraining frame and at BAM, a hybrid test was performed. The specimens were partially encased HEA 200 steel sections (S355) in C25/30 concrete. They were also additionally reinforced with steel bars. The columns that were tested at FCTUC had the same cross-section but a lower length than those tested at BAM because of the different dimensions of the furnaces. It is also important to notice that the two testing facilities are different. On one hand, the furnace of University of Coimbra is electric, making that the high heating rates required in the first minutes of a standard fire test can generally not be achieved as in an oil gas burner. The researchers were aware of this challenge and tried to mitigate the problem by preheating the gas temperature to 100°C in Coimbra. On the other hand, the ends of the columns were outside of the furnace in Coimbra whereas the specimens were fully engulfed in fire at BAM. As in the comparison with IST (Korzen, Neves, et al. 2006), the results tests performed at FCTUC and BAM were difficult to compare and showed significant differences. A similar research project on circular reinforced concrete columns was carried out by (Korzen, Rodrigues et Laím 2013). The outcomes were identical.

The publications involving the hybrid tests performed at BAM showed that the surrounding structure of a heated column strongly influences the development of the axial forces in a tested element and thus put the emphasis on the need of performing hybrid tests in fire engineering. A complete facility was developed, and the comparison between physical tests and hybrid tests is of great interest for further research. However, no methodology issues such as experimental errors or delay were approached.

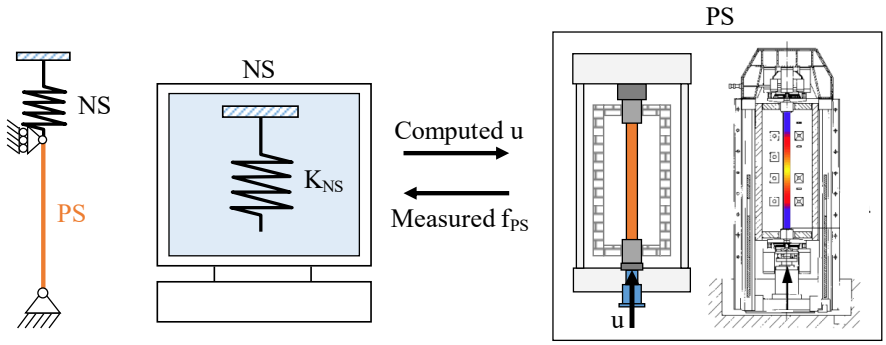

Fig. I-11 Procedure of the hybrid test performed at BAM (Korzen, Ziener, et al. 2002)

I.3.3 Robert et al. (2010)

In 2010, (Robert, Rimlinger et Collignon 2010) reported a hybrid fire test performed at the CERIB facility. The procedure is explicitly in force control. Contrary to the research carried out by the publications of BAM in Section I.3.2, the test was conducted with several DOFs.

The physical specimen was a reinforced concrete slab that was extracted from the central span of a building of five identical spans as shown in Fig. I-12. The slab was subject to ISO-384 fire and the remaining structure was cold.

After substructuring, the control of three DOFs was necessary to model the elastic response of the surrounding. The slab was restrained in the axial direction by the bracing wall and the rigidity of the cold surrounding floor and in rotation by the rigid connection between the elements. Horizontal actuators were used to apply forces in the axial direction. The slab was extended on each side of the furnace, allowing vertical jack to apply bending moment. Vertical actuators loaded the slab. The elastic response of the remaining structure was modelled by a 3x3 matrix $\mathbf{K}_{NS}$ that was calculated before the test using numerical simulation. At each time step, the displacement $\mathbf{u}_{PS}$ was read and

sent to the NS. Given the initial condition $\mathbf{f}_{in}$, the new target forces $\mathbf{f}_{PS}$ are computed using the following equation:

$$\mathbf{f}_{PS} = \mathbf{K}_{NS}\mathbf{u}_{PS} + \mathbf{f}_{in} \quad \text{(I-12)}$$

The procedure is illustrated in Fig. I-12. The test was stopped after three hours without reaching failure because of instabilities. The results presented in (Robert, Rimlinger et Collignon 2010) focussed on the value of the axial force applied by the actuators. No information about the bending moment was provided by the authors.

This hybrid test is of great interest because it was extremely ambitious in the number of controlled DOFs and pointed out stability problems. However, the lack of presented results, analytical developments, or comparison with numerical simulations of the complete structure makes difficult the evaluation and validation of the procedure.

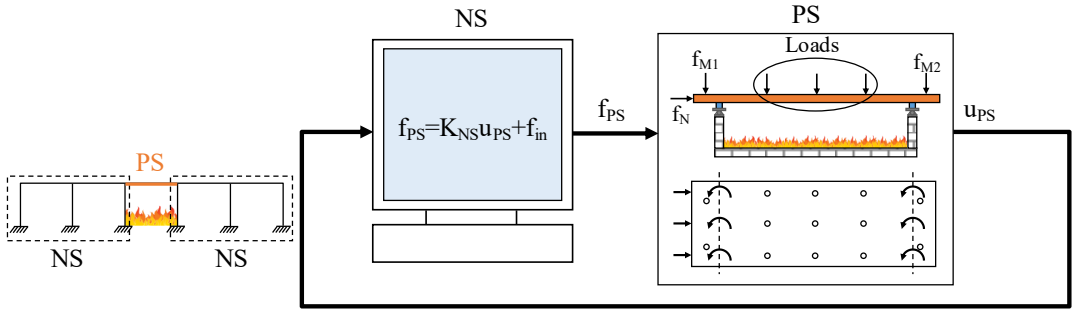

Fig. I-12 Procedure of the hybrid test performed in CERIB (Robert, Rimlinger et Collignon 2010)

I.3.4 Mostafaei (2013)

In 2013, (Mostafaei 2013a) and (Mostafaei 2013b) presented a hybrid tests that was performed at the National Research Council's testing facilities in Ottawa. This procedure is thus similar than the one used in (Robert, Rimlinger et Collignon 2010) with one DOF and is illustrated in Fig. I-13.

The physical specimen consisted of a 3.8-meter reinforced concrete column exposed to E119 standard curve. As shown in Fig. I-13, this column is part of a multi-storey building. The remaining structure was numerically modelled using the SAFIR® FE-software (Franssen et Gernay 2017).

Before the test, the initial normal force in the column was calculated using a numerical simulation and applied to the specimen with the actuators. The following procedure was then performed during the test. At the beginning of each time step, the axial displacement of the PS was measured, sent to the numerical model and imposed as a new boundary condition at the interface. The reaction was computed with SAFIR®. At the end of the time step, the force applied to the specimen was updated manually by the operator. The time step was equal to five minutes because of numerical analysis-run which lasted for two minutes.

The procedure was carried out successfully and the results were consistent to expected interaction of the column and the rest of the building. The author also included results of prescriptive fire resistance test performed on a column with identical specifications than the one used for the HFT. The comparison between the two tests showed that the fire resistance given by HFT is higher the one of the prescriptive approaches.

The displacement and force of the PS were not compared with the NS. Consequently, one cannot verify if both, compatibility of displacements and equilibrium of forces, were ensured at the interface. However, given that the time step between two updates of the force was long (five minutes) and the operator simply applied the current restoring force of the surrounding structure to the column, one can suppose that it led to a displacements mismatch and unbalanced forces at the

interface between NS and PS. The process probably accumulated significant errors, as observed afterwards by (Schulthess, Neuenschwander et Mosalam, et al. 2020).

Another issue consisted in the need of human operator during the test: the axial displacement was manually inserted and the input to the numerical model and the resulting load was also manually commanded to the physical column in the furnace.

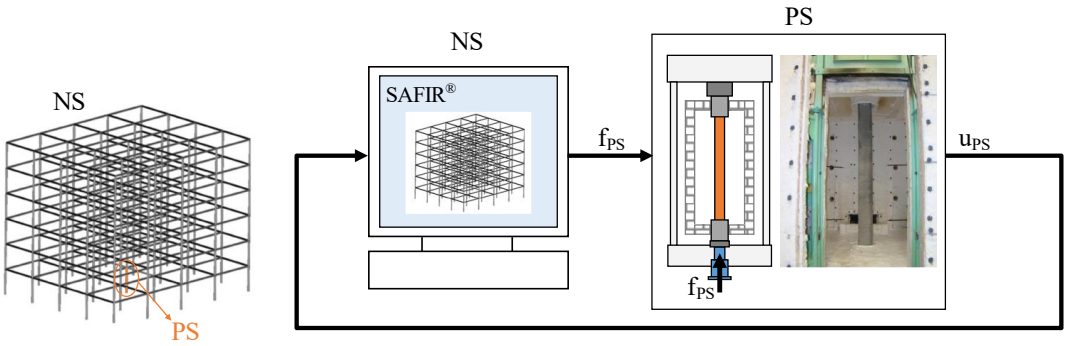

Fig. I-13 Procedure of the hybrid test performed in NRC's testing facilities (Mostafaei 2013a)

I.3.5 Whyte et al. (2016)

(Whyte, Mackie et Stojadinovic 2016) proposed thus in 2016 a fully automated hybrid simulation at the ETHZ (Eidgenössische Technische Hochschule Zürich). Unlike Section I.3.3 and I.3.4 that presented force control procedures, the hybrid test was performed with a displacement control procedure similar to PsD testing. In fact, this research was an attempt of extension of seismic hybrid testing to HFT. The OpenSees/OpenFresco architecture that is usually intended for advanced hybrid simulation in earthquake engineering was modified to handle temperature DOFs.

The structure that was studied is shown in Fig. I-14: it consisted of a cantilever supported by a bar. The cantilever was numerically modelled in OpenSees and the physical specimen was a S355 structural steel dogbone-shaped truss. The dimensions of the truss were 7.5 mm long, 10 mm wide and 3.6 mm thick. The PS was heated by a scaled ISO 834 curve (the peak temperature was 261°C) and a linearly load ramp P was applied to the specimen from 0 to 8 kN. OpenFresco (Schellenberg, et al. 2009), was the interface software between the numerical part, the actuators and the instrumentations.

The hybrid test was performed on an extended timescale: it resulted to a total duration of twelve minutes. Every time step, the axial reaction of the specimen was first measured. The equilibrium was restored by solving the equation of motion in OpenSees. The computed displacement and the new target temperature were sent respectively to the actuators and the furnace. Two proof-of-concept tests were conducted, using two different integration schemes. The first test was performed with an implicit scheme with ten iterations per step and the second with an explicit method.

The expected solution was reproduced. However, numerical oscillations were observed during the tests. The authors supposed that the thermal loading with a classic ramp-and-hold approach led in combination with the ongoing thermal expansion of the heated element led to displacement incompatibility in the dynamic integrator of OpenSees and instabilities. They suggested to rather use a static solution procedure in further research. One can also notice that the thermal loading with a ramp-and-hold approach is not convenient for fire tests. This approach was possible only because the specimen did not show time-dependent behaviour during the HFT (given that the temperature remained below 400°C and that the structural member remained in the elastic range).

It can be concluded from the research of (Whyte, Mackie et Stojadinovic 2016) that the adoption of the hybrid fire testing technique from earthquake engineering is not straightforward.

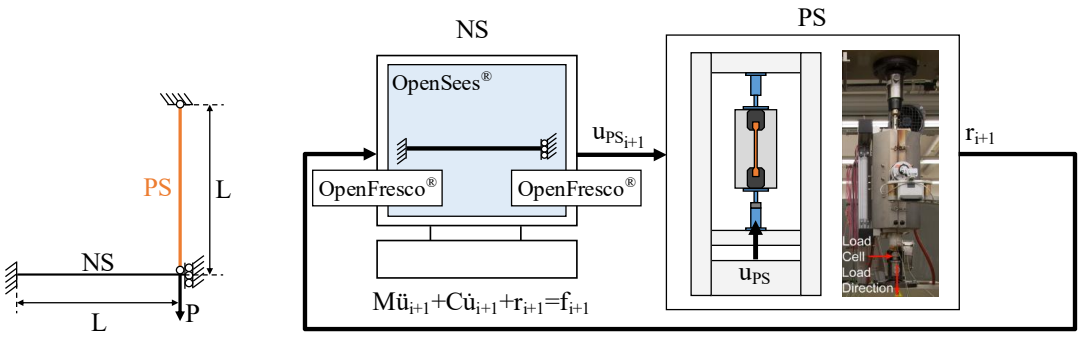

Fig. I-14 Procedure of the hybrid test performed in ETHZ (Whyte, Mackie et Stojadinovic 2016)

I.3.6 Tondini et al. (2016)

The main limitations of the research described in Sections I.3.2-5 is that the hybrid tests were led for demonstration purpose, applying existing methods or without clear theoretical framework supporting the control process. In fact, the problem of substructuring in the case of structures in fire were not studied. (Tondini, et al. 2016) focussed on this issue and proposed a static partition solver based on a major non-overlapping decomposition domain method: the FETI algorithm, developed by (Farhat et Roux 1991). Two subdomains are considered: the specimen tested in a furnace and the numerical model. The Lagrange multipliers vector corresponds to the force field that impose the continuity of the displacement field at the interface between the two substructures.

In the light of Section I.1.2 that approaches the method, let thus consider the finite element domain Ω divided into a set of two disconnected subdomains Ω_{PS} and Ω_{NS}. The following system must be solved:

$$\begin{aligned} \mathbf{r}(\mathbf{u}_{NS}) &= \mathbf{f}_{NS} + \mathbf{B}_{NS}^{T}\boldsymbol{\lambda} \\ \mathbf{r}(\mathbf{u}_{PS}) &= \mathbf{f}_{PS} + \mathbf{B}_{PS}^{T}\boldsymbol{\lambda} \\ \mathbf{B}_{NS}\mathbf{u}_{NS} + \mathbf{B}_{PS}\mathbf{u}_{PS} &= 0 \end{aligned} \tag{I-13}$$

$\mathbf{r}(\mathbf{u}_{NS})$ and $\mathbf{r}(\mathbf{u}_{PS})$ stand for the restoring forces, $\mathbf{f}_{NS}$ and $\mathbf{f}_{PS}$ for the external loads and $\mathbf{u}_{NS}$ and $\mathbf{u}_{PS}$ for the displacement fields. For a material that behaves elastically, $\mathbf{r}(\mathbf{u}_{\kappa})$ is equal to $\mathbf{K}_{\kappa}\mathbf{u}$, with $\mathbf{K}_{\kappa}$ being the stiffness matrix of the substructure Ω_{κ}. The Lagrange multiplier $\boldsymbol{\lambda}$ is the interface force fields to impose the continuity condition. $\mathbf{B}_{NS}$ and $\mathbf{B}_{PS}$ are Boolean matrices that localise the interface DOFs on each substructure. The system is solved with the Newton-Raphson's algorithm.

(Tondini, et al. 2016) presented first a basic algorithm for non-floating subdomains. For each time step i and each iteration k, the corrections were calculated as follows:

$$\begin{bmatrix} \Delta\mathbf{u}_{NS_i}^{k} \\ \Delta\mathbf{u}_{PS_i}^{k} \\ \Delta\boldsymbol{\lambda}_{i}^{k} \end{bmatrix} = -D\mathbf{A}^{-1}\mathbf{A}\left(\mathbf{u}_{NS_i}^{k}, \mathbf{u}_{PS_i}^{k}, \boldsymbol{\lambda}_{i}^{k}\right) \tag{I-14}$$

$\mathbf{A}$ is the residual matrix:

$$\mathbf{A} = \begin{bmatrix} \mathbf{r}\left(\mathbf{u}_{NS_i}^{k}\right) - \mathbf{f}_{NS} - \mathbf{B}_{NS}^{T}\boldsymbol{\lambda}_{i}^{k} \\ \mathbf{r}\left(\mathbf{u}_{PS_i}^{k}\right) - \mathbf{f}_{PS} - \mathbf{B}_{PS}^{T}\boldsymbol{\lambda}_{i}^{k} \\ \mathbf{B}_{NS}\mathbf{u}_{NS_i}^{k} + \mathbf{B}_{PS}\mathbf{u}_{PS_i}^{k} \end{bmatrix} \tag{I-15}$$

$D\mathbf{A}$ is the Jacobian of the residual matrix:

$$D\mathbf{A} = \begin{bmatrix} D\mathbf{r}\left(\mathbf{u}_{NS_i}^k\right) & 0 & \mathbf{B}_{NS} \\ 0 & D\mathbf{r}\left(\mathbf{u}_{PS_i}^k\right) & \mathbf{B}_{PS} \\ \mathbf{B}_{NS} & \mathbf{B}_{PS} & 0 \end{bmatrix} \tag{I-16}$$

$D\mathbf{r}\left(\mathbf{u}_{NS_i}^k\right)$ and $D\mathbf{r}\left(\mathbf{u}_{PS_i}^k\right)$ are the Jacobian of the restoring force. In the linear case, these matrices are the stiffness matrices of the substructures. One can mention that $D\mathbf{r}\left(\mathbf{u}_{PS_i}^k\right)$ is not known a priori and could change during the fire test. An estimation of the initial stiffness $\mathbf{K}_{PS}$ was used in the algorithm to stabilise the process.

The method was then extended to floating subdomains by dividing the displacement field into a deformation and a rigid body component. Rigid body $\boldsymbol{\alpha}_{PS}$ and $\boldsymbol{\alpha}_{NS}$ coordinates that are not applied to the specimen were added in the vectors. Modified residual matrix $\mathbf{A}$ and Jacobian $D\mathbf{A}$ were used. It still requires estimating the stiffness of the PS. The Newton-Raphson's algorithm of equation (I-14) was thus rewritten as follows:

$$\begin{bmatrix} \Delta\mathbf{u}_{NS_i}^{k+1} \\ \Delta\mathbf{u}_{PS_i}^{k+1} \\ \Delta\boldsymbol{\lambda}_i^k \\ \Delta\boldsymbol{\alpha}_{NS_i}^{k+1} \\ \Delta\boldsymbol{\alpha}_{PS_i}^{k+1} \end{bmatrix} = -D\mathbf{A}^{-1}\mathbf{A}\left(\mathbf{u}_{NS_i}^k, \mathbf{u}_{PS_i}^k, \boldsymbol{\lambda}_i^k, \boldsymbol{\alpha}_{NS_i}^k, \boldsymbol{\alpha}_{PS_i}^k\right) + \begin{bmatrix} \mathbf{u}_{NS_i}^k \\ \mathbf{u}_{PS_i}^k \\ \boldsymbol{\lambda}_i^k \\ \boldsymbol{\alpha}_{NS_i}^k \\ \boldsymbol{\alpha}_{PS_i}^k \end{bmatrix} \tag{I-17}$$

The algorithm was not tested experimentally but validated numerically. As shown in Fig. I-15, the PS and NS were both modelled numerically. The PS was an IPE300 steel beam extracted from a multi-storey building and was heated linearly. Experimental errors and delay were introduced.

At the beginning of the time step, the displacement and normal force were measured. Then, $\mathbf{A}$ and $D\mathbf{A}$ were computed. Finally, Newton-Raphson's algorithm (I-17) calculated the correction of the displacements, Lagrange multipliers and rigid body coordinates. The vectors were updated at the end of the time step after k iterations:

$$\begin{bmatrix} \mathbf{u}_{NS_{i+1}}^{k+1} \\ \mathbf{u}_{PS_{i+1}}^{k+1} \\ \boldsymbol{\lambda}_{i+1}^k \\ \boldsymbol{\alpha}_{NS_{i+1}}^{k+1} \\ \boldsymbol{\alpha}_{PS_{i+1}}^{k+1} \end{bmatrix} = \begin{bmatrix} \Delta\mathbf{u}_{NS_i}^{k+1} \\ \Delta\mathbf{u}_{PS_i}^{k+1} \\ \Delta\boldsymbol{\lambda}_i^k \\ \Delta\boldsymbol{\alpha}_{NS_i}^{k+1} \\ \Delta\boldsymbol{\alpha}_{PS_i}^{k+1} \end{bmatrix} + \begin{bmatrix} \mathbf{u}_{NS_i}^{k+1} \\ \mathbf{u}_{PS_i}^{k+1} \\ \boldsymbol{\lambda}_i^k \\ \boldsymbol{\alpha}_{NS_i}^{k+1} \\ \boldsymbol{\alpha}_{PS_i}^{k+1} \end{bmatrix} \tag{I-18}$$

The method succeeded to reproduce the results of the simulation of the complete building. Moreover, the proposed numerical scheme seemed to be less sensitive to noise, delay and errors, entailing a good robustness.

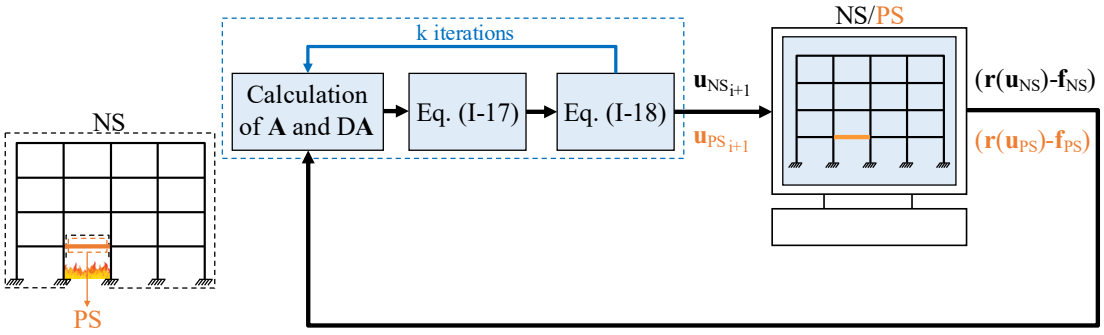

Fig. I-15 Procedure of the static partition solver (Tondini, et al. 2016)

I.3.7 Sauca et al. (2016-2018)

(Sauca, Gernay, et al. 2018) also focussed on the problem of substructuring in HFT and presented a detailed theoretical analysis of a single DOF system made of two springs, as shown Fig. I-16 (a). The PS was heated, and the NS remained cold. The substructures were characterised by interface stiffness K_{PS} and K_{NS}.

First, a force control procedure (see Fig. I-16 (b)) was applied as it was used in (Robert, Rimlinger et Collignon 2010) and (Mostafaei 2013a). (Sauca, Gernay, et al. 2018) demonstrated that for n time steps, the force f_{PS} applied to the specimen at any time step t_n can be expressed as follows:

$$f_{PS}(t_n) = K_{NS}\alpha L_{PS}\sum_{i=0}^{n-1}\left\{(-R)^i[\theta(t_{n-i}) - \theta(t_0)\,]\right\} \quad n = 1,2,\ldots \tag{I-19}$$

R is the ratio K_{NS}/K_{PS}, θ is the temperature, α the thermal expansion coefficient and L_{PS} the initial length of the specimen. Then, the same developments were made for a displacement control procedure (see Fig. I-16 (c)). The displacement u_{PS} applied to the PS can be written as:

$$u_{PS}(t_n) = -\frac{1}{R}\alpha L_{PS}\sum_{i=0}^{n-1}\left\{\left(-\frac{1}{R}\right)^i[\theta(t_{n-i}) - \theta(t_0)]\right\} \quad n = 1,2,\ldots \tag{I-20}$$

For t_∞, one can notice that the stability of the two previous methods depends on the stiffness ratio between the two substructures. According to equation (I-19), if the stiffness of the specimen is less stiff than the surrounding structure ($R > 1$), $f_{PS}(t_\infty)$ reaches for infinity when the test is performed in force control. Conversely, the method is unstable when implemented in displacement control in the case of a PS stiffer than the NS ($R < 1$). The authors also explained that the test performed by (Mostafaei 2013a) was stable because the stiffness of the tested column was higher than the stiffness of the NS.

Given this limitation, (Sauca, Gernay, et al. 2018) proposed to implement a methodology that can be described as follows. The displacement u is first imposed at the interface in both substructures. Then, the reactions f_{PS} and f_{NS} are measured. The forces are not equilibrated as the PS is heated. The displacement is finally corrected to restore equilibrium with the hereunder equation:

$$\Delta u = -\frac{f_{PS} + f_{NS}}{K^*_{PS} + K_{NS}} \tag{I-21}$$

f_{PS} and f_{NS} are the force of PS and NS. f_{PS} is measured and f_{NS} is equal to $K_{NS}u$. As the stiffness of the specimen K_{PS} is not known before the test, an estimation of the stiffness K^*_{PS} at ambient temperature is used. (Sauca, Gernay, et al. 2018) expanded the equations for n time steps. The computed displacement can be calculated:

$$u(t_n) = \frac{K_{PS}}{K^*_{PS} + K_{NS}}\alpha L_{PS}[\theta(t_n) - \theta(t_0)] \quad n = 1,2,\ldots \tag{I-22}$$

Equation (I-22) shows that this method is stable, independently on the stiffness ratio R. The algorithm is schematised in Fig. I-16 (d).

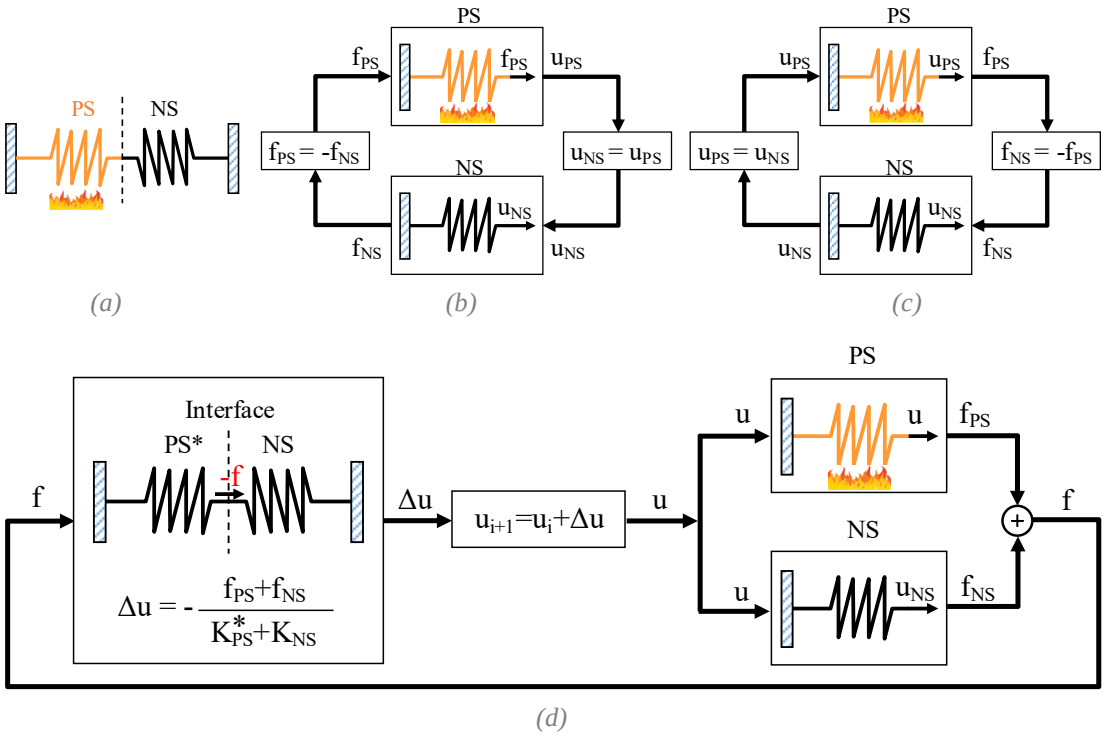

Fig. I-16 Procedures presented in (Sauca, Gernay, et al. 2018) for a single DOF system

For multi-DOF system, (Sauca, Gernay, et al. 2018) suggested calculating the corrected displacement vector as follows:

$$\mathbf{\Delta u} = -(\mathbf{K}_{PS}^{*} + \mathbf{K}_{NS})^{-1}(\mathbf{f}_{PS} + \mathbf{f}_{NS}) \qquad \text{(I-23)}$$

Numerical validation was performed in the case of a reinforced concrete moment resisting frame. The PS was a concrete beam heated by ISO-834 fire and was modelled in SAFIR®. The remaining structure was replaced by a predetermined matrix $\mathbf{K}_{NS}$. Each column of $\mathbf{K}_{NS}$ was obtained by applying a unit displacement (the others were imposed to be zero) at the interface and calculating the resulting internal forces. An automatic procedure was developed in SAFIR® to perform "virtual" HFT tests: the HFT subroutine computed the interface displacements to be imposed at the interface of the substructures at every time step. The procedure is shown in Fig. I-17.

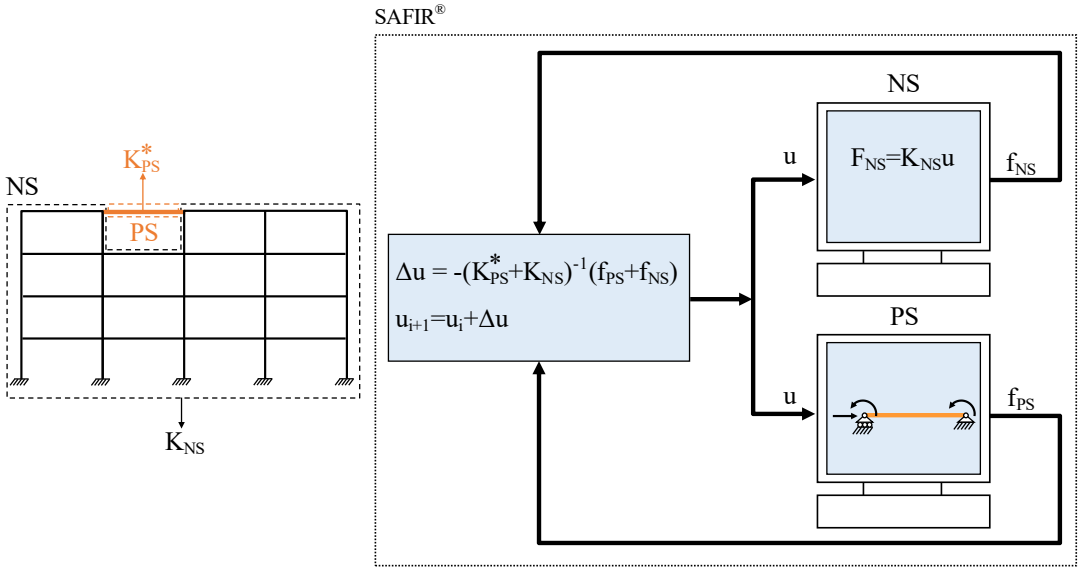

Fig. I-17 Procedure presented in (Sauca, Gernay, et al. 2018) for a multi-DOF system

The results of this analysis showed first that the solution measured at the interface of the PS coincides with the solution of the NS, meaning that equilibrium of forces and compatibility of displacements were ensured at the interface during the virtual test. Then, the results were compared to the simulation of the complete structure in SAFIR®. The method reproduced well the solution in the beginning of the test but diverges somehow from the correct solution after 30 min (example of these results are shown in Section II.4.7). The authors explained the differences by the fact that the NS is considered as elastic in the virtual HFT, whereas the simulation of the complete structure in SAFIR® considered a geometrically and materially nonlinear behaviour.

Parametric studies were also performed to evaluate the sensitivity of the method to the estimation of the stiffness of the PS, $\mathbf{K}_{PS}^{*}$. It was concluded that an underestimation of the stiffness could lead to instabilities. Such problem was not observed with overestimation. The author recommended to multiply the estimation $\mathbf{K}_{PS}^{*}$ with 1,5 for safety.

The method presented in (Sauca, Gernay, et al. 2018) has the advantage of being easy to apply and showed promising results. However, it suffers from a number of limitations that was highlighted in further research such as (Schulthess, Neuenschwander et Mosalam, et al. 2020) that showed that the method accumulates error during the test. The procedure handles thermal expansion and linear NS but the as soon as temperature-dependent degradation of the stiffness and strength of the building are considered, it fails to reproduce the behaviour of the complete building if the time increment is too large. This issue will be discussed in Section II.4.8 of the thesis.

I.3.8 Schulthess et al. (2015-2020)

(Schulthess, Neuenschwander et Mosalam, et al. 2020) published in 2020 a complete analysis of a thermo-mechanical "benchmark" problem. This publication is the result of a research project that includes numerous publications as (Schulthess, Neuenschwander, et al. 2015), (Schulthess, Neuenschwander, et al. 2016) and (Schulthess 2019).

The aim of the research consisted in comparing the results of a pure physical test, with the ones of a hybrid simulation. The structure consisted of a simply supported beam that remained at ambient temperature, connected at mid-span to a truss element exposed to thermal loads. The truss element was heated linearly at a rate of 15°C/min. The complete structure was tested experimentally in ETH: the truss element was mounted into the testing machine inside the electric furnace and the beam was replaced by a spring with appropriate stiffness. In the hybrid test, the truss was the tested specimen and the beam modelled in ABAQUS®.

The testing procedure is presented in Fig. I-18. Every 8 s, the temperature was increased of 2°C and maintained constant during this time step. The actuators were in force control procedure until the desired temperature was reached. The displacement compatibility was then restored, and the iterations started afterwards. The measured reaction and displacement were sent to ABAQUS®. The displacement was applied to the NS (beam element) and used with the measured force as an input of a user's subroutine that described the behaviour of the physical truss. The right-hand side vector of the force equilibrium equation was calculated. If the equilibrium was not reached, the solver was executed to find the displacement correction. The stiffness at ambient temperature was used in the solver. The temperature was updated after convergence. The results of the tests were presented, and minor differences were observed, mainly due to the stiffness that was slightly different from a sample truss to another.

The research is a valuable contribution as it brought a validation of the testing technique through a comparison to purely physical fire tests, in a temperature range relevant to structural fire engineering. It is also a first step towards the development of a generic HFT technique. However, limitations can be pointed out. The hybrid test was performed on a small-scale specimen in a well-

controlled environment (universal testing machine). Usually, fire tests are performed on full-scale specimen with actuators that have limited precision. Maintaining the temperature constant for a period of time is also not possible in tests conducted in oil gas burners.

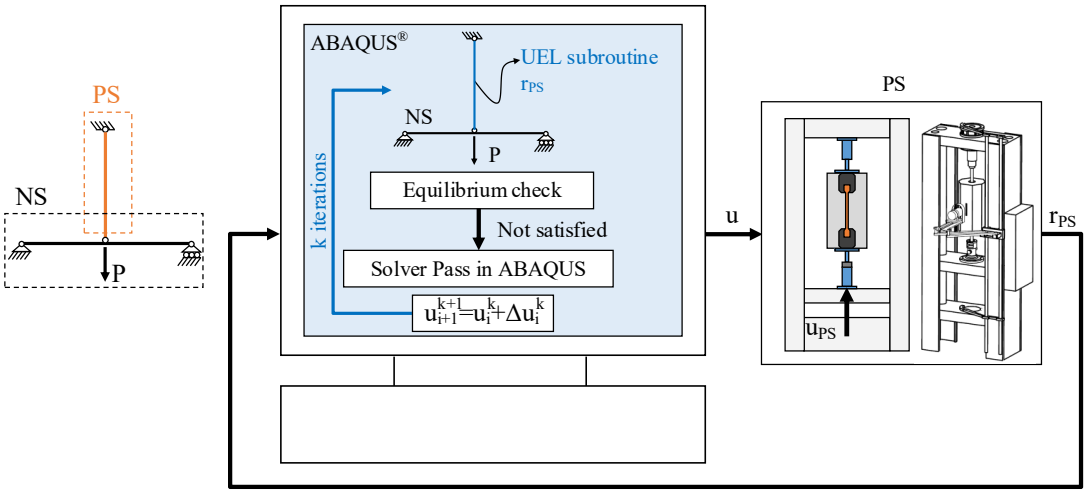

Fig. I-18 Simplified diagram of the procedure of the hybrid test performed in ETHZ (Schulthess, Neuenschwander et Mosalam, et al. 2020)

I.3.9 Wang et al. (2018)

(Wang, et al. 2018) performed a fully automated hybrid test at the KICT testing facilities. Compared to the hybrid test presentation in Section I.3.8, the great novelty is that the PS is full scale and tested in a standardized furnace and with usual hydraulic actuators.

The tested specimen was a steel column extracted from a 4-storey building. The remaining structure was modelled in ABAQUS with the tested column that was substituted with a substructure element developed in-house to allow data exchange between the numerical model and the physical specimen. Several tests are presented in this publication but the more relevant for HFT is the one denoted “Test D”.

The procedure is shown in Fig. I-19. Every time step, the force vector of the numerical and physical substructure, respectively, $\mathbf{R}_{PS}$ and $\mathbf{R}_{NS}$, as well as the structural temperature profile $\boldsymbol{\theta}_{PS}$ were measured and sent to the framework developed by the authors. A nonlinear structural analysis was performed to solve the following equilibrium equation:

$$\mathbf{r}(u,T) = \mathbf{f}_{ext} \tag{I-24}$$

$\mathbf{r}(u,T)$ is the restoring force vector and is equal to $\mathbf{r}_{PS} + \mathbf{r}_{NS}$. $\mathbf{f}_{ext}$ is the applied external force vector which was the gravity load in this test. The displacement increment was computed as follows:

$$\Delta\mathbf{u} = -\mathbf{K}^{-1}(\mathbf{r}_{PS} + \mathbf{r}_{NS} - \mathbf{f}_{ext}) \tag{I-25}$$

$\mathbf{K}$ is a stiffness matrix representing the linear relationship between the displacement $\mathbf{u}$ and the force $\mathbf{f}$ as it can be seen in Fig. I-19. Based on $\boldsymbol{\theta}_{PS}$, a heat transfer analysis was also performed, and the result of this analysis was then applied as the thermal boundary condition to the NS and the non-linear structural analysis. The displacement increment $\Delta\mathbf{u}$ was imposed to the specimen and the NS. Finally, the restoring forces were re-evaluated. The value of $\mathbf{K}$ depends on the temperature and path-dependent properties of the material. However, given that it is difficult to evaluate the stiffness of the specimen during the test, the initial stiffness of the structure was thus used to solve the equation (I-25).

The time step was set to 10 s. No iteration was carried out within each time step as it was done by (Tondini, et al. 2016) and (Schulthess, Neuenschwander et Mosalam, et al. 2020) because as temperature in the furnace changed continuously, it made challenging to achieve a converged solution through iterations in each time step. The displacement was not maintained constant during this time step. Extrapolation and interpolation were used for continuously generating displacement commands during the simulation as it was developed in PsD tests in earthquake engineering (Nakashima et Masaoka 1999). Also, the elastic deformation of the loading frame was compensated to measure and control the elongation of the column.

The expected response was reproduced in an acceptable way, although differences between numerical predictions and experimental results were pointed out and attributed to limitations of the experimental set-up. This test allowed to tackle technical issues in HFT such as communication software to link NS and actuators in the furnace.

(Menari, et al. 2020) performed afterwards a single DOF hybrid simulation of a small-scale braced frame subjected to fire with the same communication frame used in (Wang, et al. 2018) and showed the applicability in case of hybrid simulation for fire following an earthquake event.

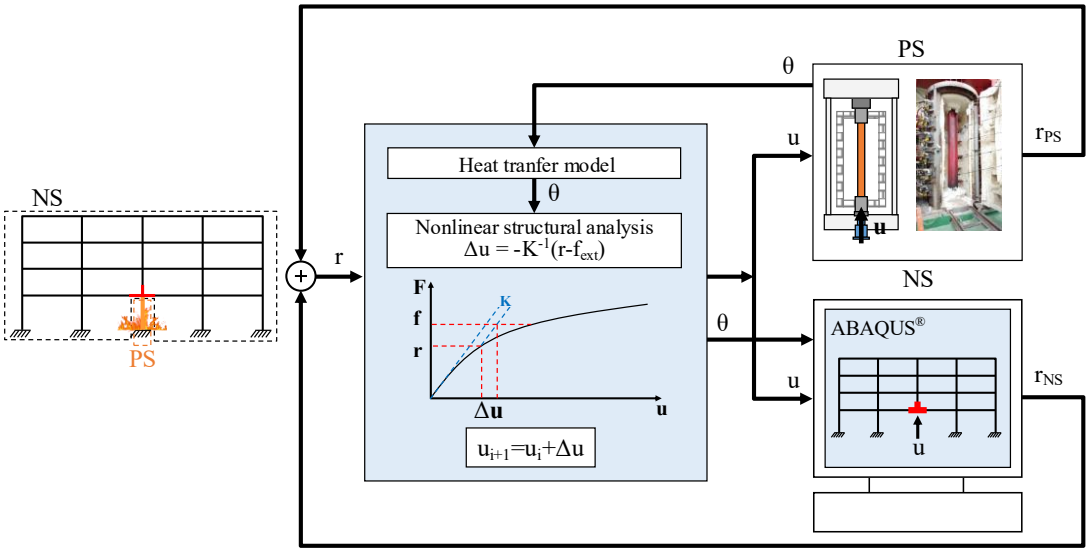

Fig. I-19 Procedure of the hybrid test performed in KICT testing facilities (Wang, et al. 2018)

I.3.10 Qureshi, Khorasani et Gernay (2019)

The methods described in (Tondini, et al. 2016), (Sauca, Gernay, et al. 2018), (Schulthess, Neuenschwander et Mosalam, et al. 2020) and (Wang, et al. 2018) used the stiffness of the PS at room temperature to correct the displacement at the interface. However, this could lead to inaccurate results at high temperature when the material properties of the specimen are degraded. Moreover, these publications are only focused on displacement control procedure as force control procedure seems to be unstable according (Sauca, Gernay, et al. 2018). This can be a limitation for tests that involves very stiff DOF as in columns. In fact, an accurate control of the actuators is necessary to avoid large error in the force as well as a continuous movement of the jack as large thermal forces can develop if the displacement is restrained. Also, as shown in (Wang, et al. 2018), the stiffness of the frame must be compensated if the elongation of the specimen is not available.

(Qureshi, Khorasani et Gernay 2019) proposed to use the force-displacement response history of test specimen to update the stiffness of the PS during the test to make force control procedure achievable for HFT and improve displacement control procedure. The authors recommended to use the secant stiffness, according to formulation proposed in (Nakata, Spencer et Elnashai 2006).

For a displacement procedure the degrading secant stiffness $\mathbf{K}^*_{PS_t}$ at time t is estimated as follows:

$$\mathbf{K}^*_{PS_t} = \left\| \mathbf{K}^*_{PS_{t-1}} + \frac{\left(\mathbf{f}_{NS_t} - \mathbf{f}_{NS_{t-1}}\right) - \mathbf{K}^*_{PS_{t-1}}\left(\mathbf{u}_{NS_t} - \mathbf{u}_{NS_{t-1}}\right)}{\mathbf{u}_{NS_t} - \mathbf{u}_{NS_{t-1}}} \right\| \quad \text{(I-26)}$$

$\mathbf{f}_{NS_t}$ is the mechanical force vector at time t and $\mathbf{u}_{NS_t}$ is the displacement vector. Both are measured at the interface.

For a force control procedure, $\mathbf{K}^*_{PS_t}$ is calculated with the following equation:

$$\mathbf{K}^*_{PS_t} = \left\| \mathbf{K}^*_{PS_{t-1}} + \frac{\left(\mathbf{f}_{NS_{t-1}} - \mathbf{f}_{NS_{t-2}}\right) - \mathbf{K}^*_{PS_{t-1}}\left(\mathbf{u}_{NS_{t-1}} - \mathbf{u}_{NS_{t-2}}\right)}{\mathbf{u}_{NS_{t-1}} - \mathbf{u}_{NS_{t-2}}} \right\| \quad \text{(I-27)}$$

The authors performed numerical validations of the method for a single DOF system for force- and displacement control procedure. The procedures are shown in Fig. I-20. The implemented methodology reproduced the excepted behaviour for these two simple cases but no procedure for multi-DOF tests were proposed.

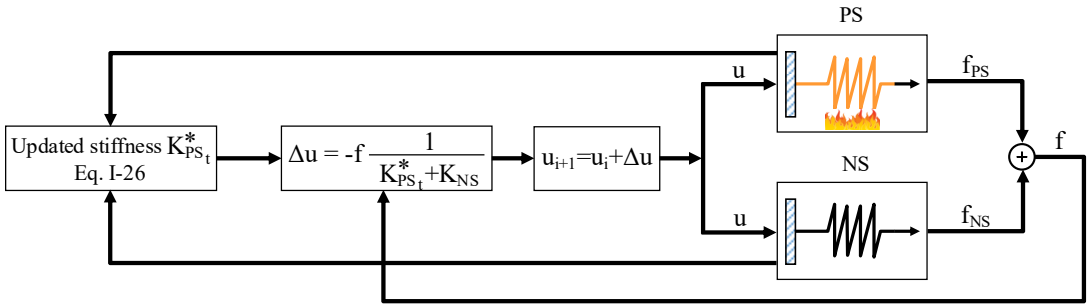

(a) Displacement control procedure

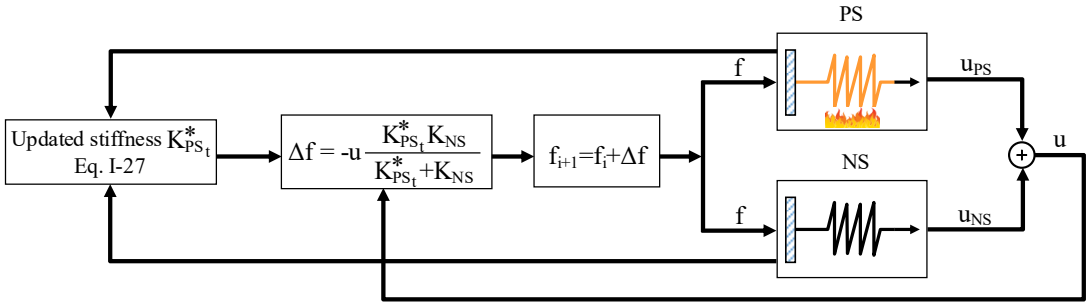

(b) Force control procedure

Fig. I-20 Procedures proposed in (Qureshi, Khorasani et Gernay 2019)

I.3.11 Renard, et al. (2020)

(Renard, et al. 2020) proposed a hybrid procedure, allowing the control of the actuator system without explicit knowledge of estimated parameters from the tested structural element. This procedure is based on sliding mode control that is a nonlinear control technique. It aimed to drive the system states onto a particular surface $\sigma_i = 0\ \forall i$ in the state space, named sliding surface. Once the sliding surface is reached, sliding mode control keeps the states on the close neighbourhood of the sliding surface. The surface that is chosen is as follows:

$$\boldsymbol{\sigma}_i = c\mathbf{f}_i + \dot{\mathbf{f}}_i \quad \text{(I-28)}$$

Where $c > 0$ and $f_i = f_{PS_i} + f_{NS_i}$. f_{PS_i} and f_{NS_i} are the force vectors of PS and NS and f_i is thus the unbalanced force vector. The derivative $\dot{f}_i$ is determined as $f_i - f_{i-1}$.

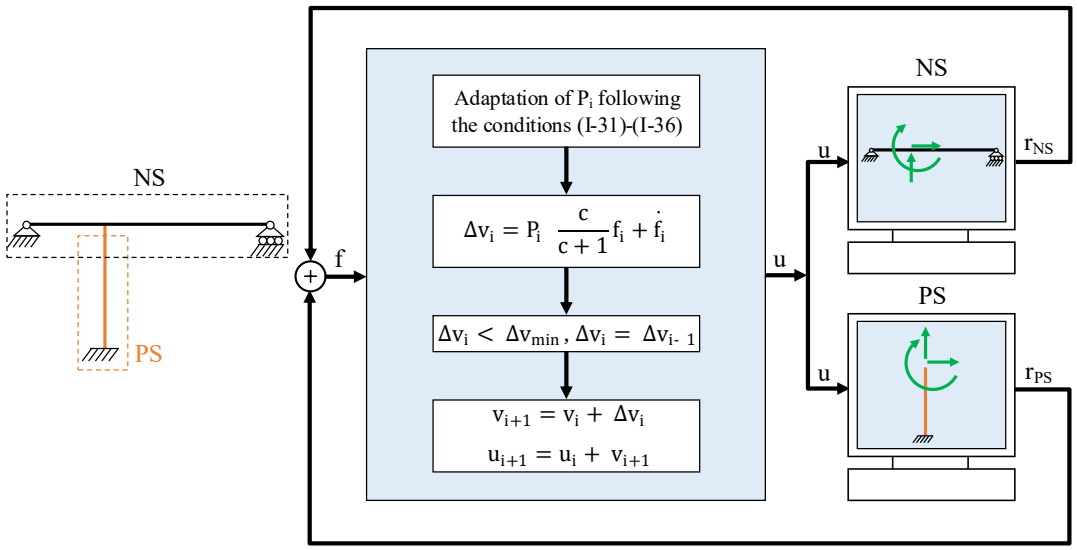

Fig. I-21 Procedure proposed in (Renard, et al. 2020) (adapted from the publication)

Each time step, the displacement **u** and speed **v** (normalized to the time step) are corrected:

$$\begin{aligned} \mathbf{v}_{i+1} &= \mathbf{v}_i + \Delta\mathbf{v}_i \\ \mathbf{u}_{i+1} &= \mathbf{u}_i + \mathbf{v}_{i+1} \end{aligned} \tag{I-29}$$

The control law that is chosen by the researchers to determine Δv_i and reach this sliding surface is the following:

$$\Delta\mathbf{v}_i = \mathbf{P}_i \left(\frac{c}{c+1} \mathbf{f}_i + \dot{\mathbf{f}}_i \right) \tag{I-30}$$

$\Delta\mathbf{v}_i = \mathbf{v}_{i+1} - \mathbf{v}_i$ is the speed increment of the hydraulic cylinder. $\mathbf{P}_i$ is a diagonal matrix and unknown. The researchers suggest taking arbitrary small initial values that will be adapted from the observation of the system behaviour. The following conditions that must be checked every time step i and iteration k were listed:

$$\text{sign}\left(\frac{c}{c+1} \mathbf{f}_i^k + \dot{\mathbf{f}}_i^k \right) \neq \text{sign}\left(\boldsymbol{\sigma}_i^k \right) \tag{I-31}$$

$$\left(\frac{\mathbf{f}_i^k}{\mathbf{f}_{min}^k} \right)^2 + \left(\frac{\dot{\mathbf{f}}_i^k}{\mathbf{f}_{min}^k} \right)^2 < 1 \tag{I-32}$$

$$\Delta\mathbf{v}_i^k < \Delta\mathbf{v}_{min}^k \tag{I-33}$$

$$\text{sign}\left(\boldsymbol{\sigma}_i^k \right) \neq \text{sign}\left(\boldsymbol{\sigma}_{i-1}^k \right) \tag{I-34}$$

$$\left| \text{atan2}\left(\mathbf{f}_i^k, \dot{\mathbf{f}}_i^k \right) - \text{atan2}\left(\mathbf{f}_{i-1}^k, \dot{\mathbf{f}}_{i-1}^k \right) \right| > \frac{\pi}{T_{max}} \quad \text{with } T_{max} \geq 2 \tag{I-35}$$

$$\text{sign}\left(\Delta\mathbf{v}_{i-1}^k \right) \neq \text{sign}\left(\left(1 - \frac{\Delta t}{\Delta delay} \right) \boldsymbol{\sigma}_{i-1}^k + \left(\frac{\Delta t}{\Delta delay} \right) \boldsymbol{\sigma}_{i-2}^k \right) \tag{I-36}$$

f_{min}^k and Δv_{min}^k are respectively the smallest singulative force increment and the smallest singulative speed increment. The delay $\Delta delay$ is considered lower than the time step Δt.

$\mathbf{P}_i$ is not adapted, if an excessive control effort could pull the system trajectory away from the sliding surface (I-31), the system is considered converged (I-32) or the output of the control algorithm is considered too small (I-33). The diagonal terms p_j of $\mathbf{P}_i$ are decreased as p_j/a, if the sliding surface

is crossed (I-34) or the trajectory is compatible with oscillations of a period smaller than a given limit $\frac{\pi}{T_{max}}$ (I-35). The diagonal terms are increased as $a \times p_j$, if the condition (I-31) is false.

The adaptation parameter a is chosen arbitrary and can be read into a "learning gain". Numerical validation was performed on the structure that can be seen in Fig. I-21 as well as preliminary experimental tests on a non-heated small-scale beam. Promising results were obtained. More ambitious experimental tests have been carried out, but the results have not yet been published.

I.3.12 Abbiati, et al. (2020)

Following the same line of (Tondini, et al. 2016), (Abbiati, et al. 2020) proposed an algorithm based on dynamic relaxation, partitioned time integration and Lagrange multipliers to couple PS and NS. The basic idea of Dynamic Relaxation algorithm is to mimic a static response:

$$\mathbf{r}(\mathbf{u}) = \mathbf{f}(t) \tag{I-37}$$

by computing the transient response of an equivalent dynamic system, with the following equation of motion:

$$\mathbf{M}\ddot{\mathbf{u}} + \mathbf{C}\dot{\mathbf{u}} + \mathbf{r}(\mathbf{u}) = \mathbf{f}(t) \tag{I-38}$$

r is the internal restoring force vector, **u** is the displacement vector, **f** is the varying external loading. **M** and **C** are fictitious mass and damping matrices, and their diagonal entries are as follows:

$$M_{ii} = \frac{(1.1\Delta t_{CD})^2}{4}\sum|K_{ij}| \ , \qquad C_{ii} = 2\omega_0 M_{ii} \tag{I-39}$$

These expressions are chosen to maximize the convergence rate of the algorithm. K_{ij} is a generic element of the initial tangent stiffness matrix, ω_0 is the lowest undamped frequency of the dynamic equation (I-38) and Δt_{CD} is the time step of the equivalent transient analysis solved using the Central Difference algorithm. Fig. I-22 provides the architecture of the implementation of the method.

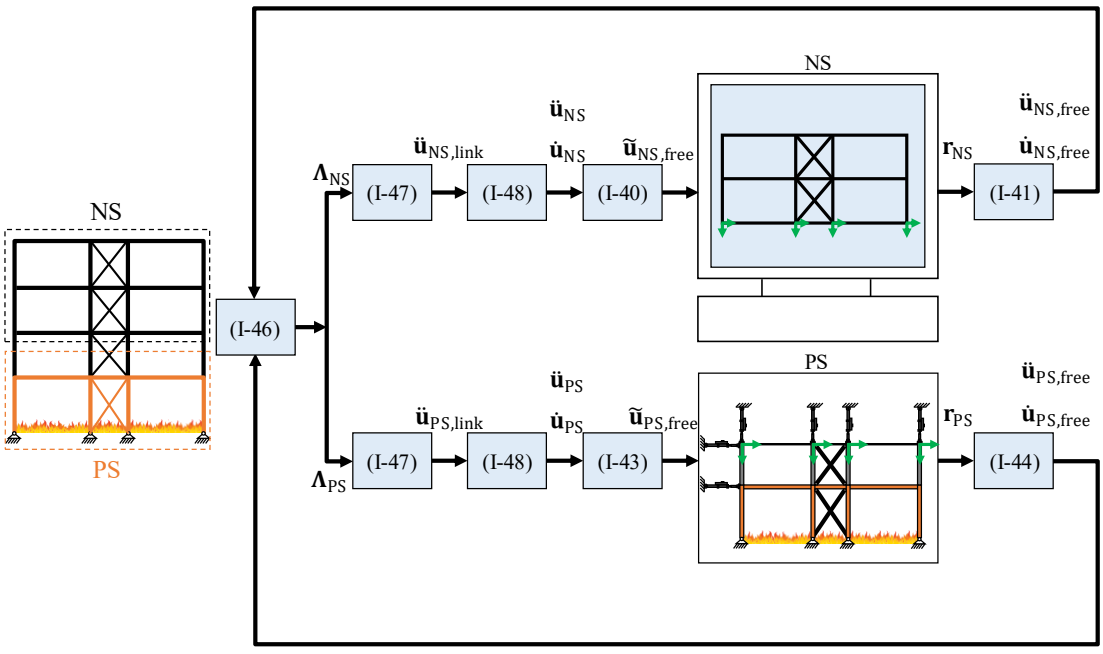

Fig. I-22 Architecture of the implementation of hybrid fire simulation based on dynamic relaxation and partitioned time integration (Adapted from (Abbiati, et al. 2020))

The first step consists in solving the PS and NS equations of motion independently in parallel (also called "free" problem). Then, a set of Lagrange multipliers that restore interface velocity compatibility between substructures is calculated. The "link" problem is solved by computing the interface velocities. Finally, the "coupled" ("free"+"link") quantities are computed.

The algorithm is called LLM-DR (Localized Lagrange Multiplier-Dynamic Relaxation) algorithm and follows the hereunder steps from t_i to t_{i+1} ($\Delta t = t_i - t_{i+1}$):

1. The NS free problem is solved. The displacement predictor, $\tilde{\mathbf{u}}_{\mathrm{NS,free}_{i+1}}$ and the velocity predictor $\tilde{\dot{\mathbf{u}}}_{\mathrm{NS,free}_{i+1}}$ are computed with equation (I-40) and sent to the FE software that computes the corresponding restoring force $\mathbf{r}_{\mathrm{NS}_{i+1}}$:

$$\begin{aligned} \tilde{\mathbf{u}}_{\mathrm{NS,free}_{i+1}} &= \mathbf{u}_{\mathrm{NS}_{i+1}} + \dot{\mathbf{u}}_{\mathrm{NS}_i}\Delta t + \left(\frac{1}{2} - \beta\right)\Delta t^2 \ddot{\mathbf{u}}_{\mathrm{NS}_i} \\ \tilde{\dot{\mathbf{u}}}_{\mathrm{NS,free}_{i+1}} &= \dot{\mathbf{u}}_{\mathrm{NS}_i} + (1-\gamma)\Delta t \ddot{\mathbf{u}}_{\mathrm{NS}_i} \end{aligned} \tag{I-40}$$

   Then, the free acceleration, velocity and displacement are corrected:

$$\begin{aligned} \ddot{\mathbf{u}}_{\mathrm{NS,free}_i} &= \mathbf{D}_{\mathrm{NS}}^{-1}\left(\mathbf{f}_{\mathrm{NS}_{i+1}} - \mathbf{C}_{\mathrm{NS}}\tilde{\dot{\mathbf{u}}}_{\mathrm{NS,free}_{i+1}} - \mathbf{r}_{\mathrm{NS}_{i+1}}\left(\tilde{\mathbf{u}}_{\mathrm{NS,free}_{i+1}}\right)\right) \\ \mathbf{u}_{\mathrm{NS,free}_{i+1}} &= \tilde{\mathbf{u}}_{\mathrm{NS,free}_{i+1}} + \ddot{\mathbf{u}}_{\mathrm{NS,free}_{i+1}}\beta\Delta t^2 \\ \dot{\mathbf{u}}_{\mathrm{NS,free}_{i+1}} &= \tilde{\dot{\mathbf{u}}}_{\mathrm{NS,free}_{i+1}} + \ddot{\mathbf{u}}_{\mathrm{NS,free}_{i+1}}\gamma\Delta t \end{aligned} \tag{I-41}$$

   The matrix $\mathbf{D}_{\mathrm{NS}}$ is written as follows:

$$\mathbf{D}_{\mathrm{NS}} = \mathbf{M}_{\mathrm{NS}} + \mathbf{C}_{\mathrm{NS}}\gamma\Delta t + \mathbf{K}_{\mathrm{NS}}\beta\Delta t^2 \tag{I-42}$$

   With $\mathbf{K}_{\mathrm{NS}}$, the initial tangent stiffness matrix at the beginning of the simulation. $\mathbf{M}_{\mathrm{NS}}$ and $\mathbf{C}_{\mathrm{NS}}$ are the fictitious mass and damping matrices of the NS.

2. In parallel, the PS free problem is solved.
   The free displacements and velocity predictor, $\tilde{\mathbf{u}}_{\mathrm{PS,free}_{i+1}}$ and $\tilde{\dot{\mathbf{u}}}_{\mathrm{PS,free}_{i+1}}$ are computed with the hereunder equations:

$$\begin{aligned} \tilde{\mathbf{u}}_{\mathrm{PS,free}_{i+1}} &= \mathbf{u}_{\mathrm{PS}_{i+1}} + \dot{\mathbf{u}}_{\mathrm{PS}_i}\Delta t + \left(\frac{1}{2} - \beta\right)\Delta t^2 \ddot{\mathbf{u}}_{\mathrm{PS}_i} \\ \tilde{\dot{\mathbf{u}}}_{\mathrm{PS,free}_{i+1}} &= \dot{\mathbf{u}}_{\mathrm{PS}_i} + (1-\gamma)\Delta t \ddot{\mathbf{u}}_{\mathrm{PS}_i} \end{aligned} \tag{I-43}$$

   $\tilde{\mathbf{u}}_{\mathrm{PS,free}_{i+1}}$ is imposed to the PS by means of servo-controlled actuators and the corresponding restoring force $\mathbf{r}_{\mathrm{PS}_{i+1}}$ vector is measured. Then, the free acceleration, velocity and displacement of the PS are corrected:

$$\begin{aligned} \ddot{\mathbf{u}}_{\mathrm{PS,free}_i} &= \mathbf{D}_{\mathrm{PS}}^{-1}\left(\mathbf{f}_{\mathrm{PS}_{i+1}} - \mathbf{C}_{\mathrm{PS}}\tilde{\dot{\mathbf{u}}}_{\mathrm{NS,free}_{i+1}} - \mathbf{r}_{\mathrm{PS}_{i+1}}\left(\tilde{\mathbf{u}}_{\mathrm{PS,free}_{i+1}}\right)\right) \\ \mathbf{u}_{\mathrm{PS,free}_{i+1}} &= \tilde{\mathbf{u}}_{\mathrm{PS,free}_{i+1}} + \ddot{\mathbf{u}}_{\mathrm{PS,free}_{i+1}}\beta\Delta t^2 \\ \dot{\mathbf{u}}_{\mathrm{PS,free}_{i+1}} &= \tilde{\dot{\mathbf{u}}}_{\mathrm{PS,free}_{i+1}} + \ddot{\mathbf{u}}_{\mathrm{PS,free}_{i+1}}\gamma\Delta t \end{aligned} \tag{I-44}$$

   The matrix $\mathbf{D}_{\mathrm{PS}}$ is similar to equation (I-42) :

$$\mathbf{D}_{\mathrm{PS}} = \mathbf{M}_{\mathrm{PS}} + \mathbf{C}_{\mathrm{PS}}\gamma\Delta t + \mathbf{K}_{\mathrm{PS}}\beta\Delta t^2 \tag{I-45}$$

   $\mathbf{K}_{\mathrm{PS}}$ is the initial tangent stiffness matrix which is measured from the PS with small displacement perturbations once before the experiment. $\mathbf{M}_{\mathrm{PS}}$ and $\mathbf{C}_{\mathrm{PS}}$ are the fictitious mass and damping matrices of the PS.

3. The interface Lagrange multiplier vector are computed:

$$\begin{bmatrix} \mathbf{\Lambda}_{\mathrm{NS_i}} \\ \mathbf{\Lambda}_{\mathrm{PS_i}} \\ \dot{\mathbf{u}}_{\mathrm{g_i}} \end{bmatrix} = -\mathbf{G}^{-1} \begin{bmatrix} \mathbf{L}_{\mathrm{NS}} \dot{\mathbf{u}}_{\mathrm{NS,free_i}} \\ \mathbf{L}_{\mathrm{PS}} \dot{\mathbf{u}}_{\mathrm{PS,free_i}} \\ 0 \end{bmatrix} \tag{I-46}$$

G is the Steklov-Poincare's operator, computed only once based on the initial tangent stiffness of both PS and NS and inverted before the simulation starts. $\mathbf{L}_{\mathrm{NS}}$ and $\mathbf{L}_{\mathrm{PS}}$ are Boolean matrices used to collocate these interface forces on both substructures' DOFs. $\dot{\mathbf{u}}_{\mathrm{g_i}}$ is the velocity of the reference body g. The link accelerations are calculated:

$$\begin{aligned} \ddot{\mathbf{u}}_{\mathrm{NS,link_{i+1}}} &= \mathbf{D}_{\mathrm{NS}}^{-1} \mathbf{L}_{\mathrm{NS}}^{\mathrm{T}} \mathbf{\Lambda}_{\mathrm{NS_i}} \\ \ddot{\mathbf{u}}_{\mathrm{PS,link_{i+1}}} &= \mathbf{D}_{\mathrm{PS}}^{-1} \mathbf{L}_{\mathrm{PS}}^{\mathrm{T}} \mathbf{\Lambda}_{\mathrm{PS_i}} \end{aligned} \tag{I-47}$$

4. The coupled velocities and accelerations of PS and NS are finally computed:

$$\begin{aligned} \ddot{\mathbf{u}}_{\mathrm{NS_{i+1}}} &= \ddot{\mathbf{u}}_{\mathrm{NS,free_{i+1}}} + \ddot{\mathbf{u}}_{\mathrm{NS,link_{i+1}}} \\ \ddot{\mathbf{u}}_{\mathrm{PS_{i+1}}} &= \ddot{\mathbf{u}}_{\mathrm{PS,free_{i+1}}} + \ddot{\mathbf{u}}_{\mathrm{PS,link_{i+1}}} \\ \dot{\mathbf{u}}_{\mathrm{NS_{i+1}}} &= \dot{\mathbf{u}}_{\mathrm{NS,free_{i+1}}} + \dot{\mathbf{u}}_{\mathrm{NS,link_{i+1}}} \\ \dot{\mathbf{u}}_{\mathrm{PS_{i+1}}} &= \dot{\mathbf{u}}_{\mathrm{PS,free_{i+1}}} + \dot{\mathbf{u}}_{\mathrm{PS,link_{i+1}}} \end{aligned} \tag{I-48}$$

The compatibility of velocities at the interfaces, instead of displacements, guarantees a stable coupled simulation as long as each time integration scheme is stable when uncoupled. The algorithm was validated in a virtual environment through the structure shown in Fig. I-22. Experimental tests are planned but have not yet been carried out.

I.3.13 Qureshi, Khorasani et Sivaselvan (2020)

Recently, (Qureshi, Khorasani et Sivaselvan 2020) proposed a methodology which is conceptually completely different from what has been investigated so far: a control strategy for real-time hybrid fire simulation that decouples the PS response from the control design.

The method consists in adding a new control input to the transfer system to tune the internal dynamics of the actuator and have the transfer system mimic the behaviour of the NS, independently of the PS. Fig. I-23 gives the conceptual representation of the control strategy. The aim of this method is to design a transfer function $\mathrm{H_{uf}}$ that tunes the actuators to obtain $\mathrm{u_{NS}} = \mathrm{u_{ACT}}$. $\mathrm{u_{NS}}$ and $\mathrm{u_{ACT}}$ are respectively the displacement of the NS and the actuator. $\mathrm{H_{uf}}$ can be written as follows:

$$\mathrm{u} = \mathrm{H_{uf}} \mathrm{f} \tag{I-49}$$

u is the displacement and f is the force. It can be demonstrated that this function $\mathrm{H_{uf}}$ is composed of other transfer functions:

- $\mathrm{H_{NS}}$ is the tranfer function of NS such that:

$$\mathrm{u_{NS}} = \mathrm{H_{NS}} \mathrm{f} \tag{I-50}$$

- $\mathrm{H_{\Delta f}^{ACT}}$ and $\mathrm{H_{\Delta u}^{ACT}}$, are the transfer functions of the actuator taking the force f and the displacement u as input such that:

$$\mathrm{u_{ACT}} = \mathrm{H_{\Delta f}^{ACT}} \mathrm{f} + \mathrm{H_{\Delta u}^{ACT}} \mathrm{u} \tag{I-51}$$

Another expression of the transfer function $\mathrm{H_{uf}}$ can finally be obtained by rearranging the previous equations:

$$\mathrm{H_{uf}} = \mathrm{H_{\Delta u}^{ACT}} \left(\mathrm{H_{\Delta f}^{NS}} - \mathrm{H_{\Delta f}^{ACT}} \right) \tag{I-52}$$

To design H_{uf}, one must know the internal dynamics of the actuator (such as oil column frequency and damping, etc.). The accuracy of the method also depends on the reactivity of the actuator that has to perform the process in real-time. The authors considered in their work a high-speed servo-controlled actuator teamed with a three-stage electro-hydraulic servovalve.

The method is still in its infancy but shows promising results in simple tests.

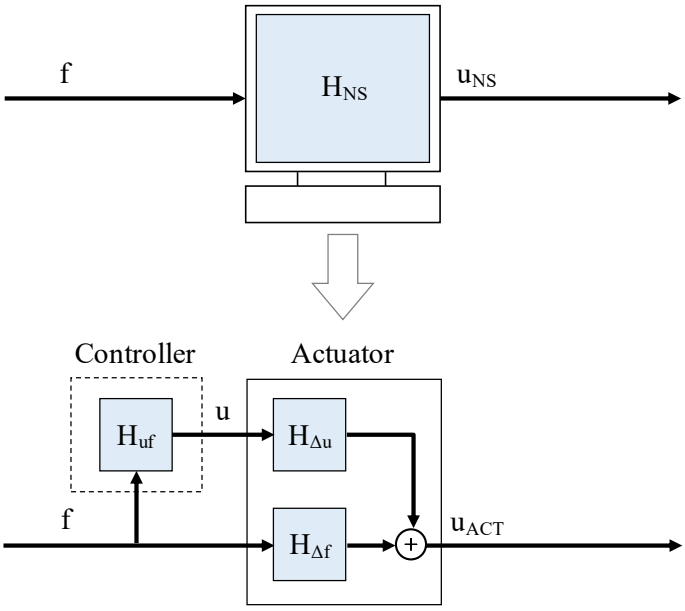

Fig. I-23 Conceptual representation and block diagram of the strategy presented in (Qureshi, Khorasani et Sivaselvan 2020) (adapted from the publication)

I.4 Summary and outlook

Hybrid tests allow testing a structural element with realistic boundary conditions without full-scale tests. In earthquake engineering, this method has been widely explored and can now be used with confidence. Given the advantages of hybrid tests and the positive results in the seismic field, it is not surprising that they have been also developed in fire engineering. For the reasons mentioned in Section 0 and as seen in (Whyte, Mackie et Stojadinovic 2016), the extension of the outcomes of hybrid testing performed in earthquake engineering to fire engineering is not achievable. Hybrid fire testing or HFT is therefore a separate field of research which has its own development and specific challenges.

The research began with the development of simple processes, as in (Mostafaei 2013a) and (Korzen, Magonette et Buchet 1998). Each time step, the displacement of the PS was measured and applied to the NS. The interface force was computed, and the force applied by the actuator was updated to reach equilibrium. This early method was found to be effective in case of one-DOF tests but could not be extended for tests with several DOFs (Robert, Rimlinger et Collignon 2010) because of stability problems. In fact, further research about stability showed that the process is conditionally stable and that the field of application of these simple loops would always be limited to one-DOF tests with the condition that the stiffness of the tested element (PS) is greater than the stiffness of the NS.

Afterwards, methods based on displacement control procedures took centre stage and has been published by different research groups (Sections I.3.6–I.3.12). They can be classified as follows:

- Algorithms based on decomposition domain methods, Lagrange multipliers and Newton–Raphson method: (Tondini, et al. 2016), (Abbiati, et al. 2020).
- Algorithms that correct the interface displacements based on the response of PS and NS that is measured or computed in the previous step: (Sauca, Gernay, et al. 2018), (Schulthess, Neuenschwander et Mosalam, et al. 2020), (Wang, et al. 2018), (Qureshi, Khorasani et Gernay 2019), (Renard, et al. 2020).
- Tuning of the actuators to mimic the response of the NS: (Qureshi, Khorasani et Sivaselvan 2020).

The last category is the subject of recent work and the results of which have not yet been published. However, it should be noted that it is very demanding from a technological point of view, unlike the first two categories of methods which can be used with a standard control system and sensors. The third category is therefore set aside.

From a methodological point of view, the procedures developed in the two first categories met some challenges. First, stability must be ensured during the entire test despite stiff and flexible DOF. Then, the method must allow equilibrium of the forces and compatibility of displacements at the interface of the two substructures. Finally, it must be robust to delay and experimental errors. The developed algorithms have been validated numerically, and a few tested experimentally. In fact, experimental validation is often lacking and when tests are performed, it is usually limited to one-DOF tests.

The first category regroups complex methods that explicitly tackle the mathematical problem of substructuring in fire engineering. They require the development of numerous calculation modules and the knowledge of the properties of the PS, in particular the stiffness matrix.

The methods of the second category analyse the forces and displacements of the substructures computed or measured in the previous time step and based on these data, correct the displacement of the PS (and NS). This correction is determined by solving equilibrium equation in a separate calculation module. The equation can be linear as in (Sauca, Gernay, et al. 2018) and (Qureshi, Khorasani et Gernay 2019) and (Renard, et al. 2020) or nonlinear as in (Wang, et al. 2018) and (Schulthess, Neuenschwander et Mosalam, et al. 2020). These methods also often need the properties of the tested specimen or at least an estimate of them, although some have been able to do without them as (Renard, et al. 2020). The algorithms are generally less expensive in terms of calculation than the first category and so far, obtain results comparable to those of more complex methods. Therefore, one will therefore prefer the latter category in this thesis.

The methods of this second group are quite different from each other. Nevertheless, they meet at one point: the displacement of the PS $i + 1$ (and possibly of the NS) is corrected based on the response of the substructures (displacement, force, velocity) measured or computed in the previous step i. However, given that the materials are time dependent at high temperature, the use of parameters which consider the history of the test to update the displacement in addition to the instantaneous response could improve accuracy as the corrections is determined in view of past corrections.

The following Chapters present a new displacement control procedure based on control theory that addresses the challenges mentioned above and especially consider the history of the test. Numerical simulations are carried out as well as multi-DOF tests.

Chapter II
Hybrid Fire Testing as a Control Problem

This Chapter approaches the mathematical concepts of modern control theory (Section II.2) and shows how HFT can be formulated and treated as a control problem, including numerical examples (Section II.3-6).

II.1 Introduction

Control theory includes a family of methods that deals with dynamical systems. The objective of these methods is to design a control action in an optimum manner without delay or overshoot and ensuring control stability. Developed since the 19th century, it aimed to solve complex high-order differential equations. Control theories that are commonly used today are c*lassical control theory*, *modern control theory* and *robust control theory* (Ogata 2009). Classical control theory uses the Laplace transform to change an Ordinary Differential Equation (ODE) in the time domain into a regular algebraic polynomial in the frequency domain. This method is now well established, simple to apply and requires few computations. However, its field of application is limited to linear time invariant systems and is more convenient for SISO system (Single Input Single Output). Modern control theory is based on time-domain analysis of differential equation system. Instead of changing domains to avoid the complexities of time-domain ODE mathematics, it converts the differential equations into a system of lower-order time domain equations called state equations, which can then be manipulated using techniques from linear algebra. The main limitation is that these methods are sensitive to errors between the model that is used to design the controller and the actual system. Consequently, robust control theory was developed to explicitly deal with uncertainty. Robust control methods incorporate both the frequency response approach and the time-domain approach, require complex techniques and are still the subject of much research.

What follows aims to approach HFT from the point of view of modern control theory. Despite its limitations, modern control theory proved its worth in many fields such as electronics, climate modelling and neural network. The use of the time-domain state space representation allows to deal with complex MIMO system (Multiple Input Multiple Output) without many computations. Hybrid fire testing (HFT) is a process like any other that can take advantage of these well-established methods.

II.2 A brief overview of modern control theory

II.2.1 Open loop system/Closed loop system

A discrete-time system is a set that introduces a relationship between input variables and output variables, in which these variables have a finite number of values. There are two types of systems:

- **Open loop system**, also referred to as non-feedback system, in which the output has no influence or effect on the control action of the input signal (Fig. II-1 (a)).
- **Closed loop system**, also known as a feedback control system which uses the concept of an open loop system as its forward path but has one or more feedback loops (hence its name) or paths between its output and its input (Fig. II-1 (b)). A closed loop system can be described with an equivalent open loop system.

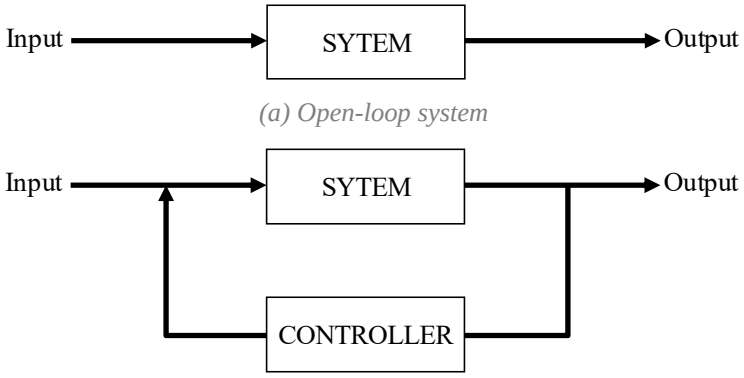

(a) Open-loop system

(b) Closed-loop system

Fig. II-1 Block diagrams of discrete time systems

II.2.2 Controller

A controller aimed to regulate the behaviour of other systems using control loops. Each time step, the process variable or system output being controlled is measured with a sensor and compared to the value of the desired value, also called setpoint or reference. If a deviation from the reference is measured, the error signal results in the control action of the controller. This deviation is generally called *error* in literature. The controlled input is computed by the controller following a control equation or *control law* that determines the desired excitation based on the error signal.

Control systems of this kind are also called *feedback control systems* or *closed loop control system* because the output is fed back to the input, forming a closed loop. The measured output can also be affected by external disturbances and noise. Basic block diagram of a feedback control system is shown in Fig. II-2.

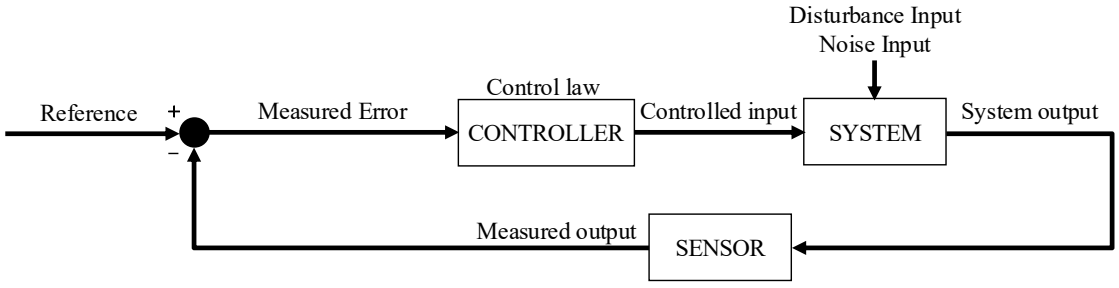

Fig. II-2 Block diagram of a negative feedback control system

The properties of a well-designed controller are the following:

- Stability: the output remains bounded (there are no unbounded oscillations).
- Accuracy: the output converges to the desired reference value
- Speed: the output settles to the desired value quickly
- Overshoot minimized

These properties can be adjusted with the parameters of step response that are described in Section II.2.4. The most important of these is stability. Once stability is achieved, accuracy, speed, and minimization of overshoot are desirable properties to be optimized. One common type of control system used the *PID controller*. The control input is obtained from the control error by adding three terms:

- Proportional P: directly proportional to the control error ($\mathbf{k}_P$)
- Integral I: directly proportional to the integral of the control error with respect to time ($\mathbf{k}_I$)
- Derivative D: directly proportional to the derivative of the control error with respect to time ($\mathbf{k}_D$)

A PID controller follow the hereunder *control law*:

$$\mathbf{Input} = \mathbf{k}_P\mathbf{error} + \mathbf{k}_I \int \mathbf{error} + \mathbf{k}_D \frac{\mathrm{d}}{\mathrm{dt}}\mathrm{error} \tag{II-1}$$

$\mathbf{k}_P$, $\mathbf{k}_I$ and $\mathbf{k}_D$ are called *gains of the system.* They are scalar for SISO systems and matrices for MIMO systems. For linear control, the gains are kept constant during the process.

The design of controllers in modern control theory is based on state-space approach.

II.2.3 State-space approach

A state-space representation is a mathematical model of a physical system. In discrete time, the state difference system is given by equation (II-2):

$$\begin{aligned} \mathbf{x}_{i+1} &= \mathbf{A}\mathbf{x}_i + \mathbf{B}\mathbf{w}_i \\ \mathbf{y}_i &= \mathbf{C}\mathbf{x}_i + \mathbf{D}\mathbf{w}_i \end{aligned} \tag{II-2}$$

$\mathbf{x}_i$ is the state variable at discrete time step i. It is the smallest subset of system variables that defines the entire state of the system at any given time. The size of $\mathbf{x}_i$ is the dimension of the system. $\mathbf{w}_i$ is called the input vector and $\mathbf{y}_i$ the output vector. **A** is the dynamics matrix, **B** is the input matrix, **C** is the output matrix and **D** is the feedthrough matrix. A state-space representation is potentially complex and high-dimensional. It is not unique and closely related to the model.

A linear discrete-time system described by the state equation $\mathbf{x}_{i+1} = \mathbf{A}\mathbf{x}_i + \mathbf{B}\mathbf{w}_i$ is asymptotically stable if and only if all eigenvalues of the dynamics matrix **A** have module smaller than one. The eigenvalues of **A** are also called *poles* of the system and are the roots of the characteristic equation $|z\mathbf{I} - \mathbf{A}|$ (**I** is the identity matrix).

In other words, the system is stable if the poles are inside the unit circle in complex plane. The location of these poles determines the characteristics of the system response.

II.2.4 Step response

The step response is the time behaviour of the output of a system when its inputs change from zero to one in a very short time. It can be described by the following parameters (Fig. II-3):

- Rise time T_r: time for the waveform to go from 0.1 to 0.9 of its final value.
- Settling time T_s: time required for the oscillations to stay within some specified small percentage (=error band) of the final value. The most common values used are 1%, 2% and 5%.
- Overshoot M_P: maximum deviation of system output from its final value.

T is the sample time.

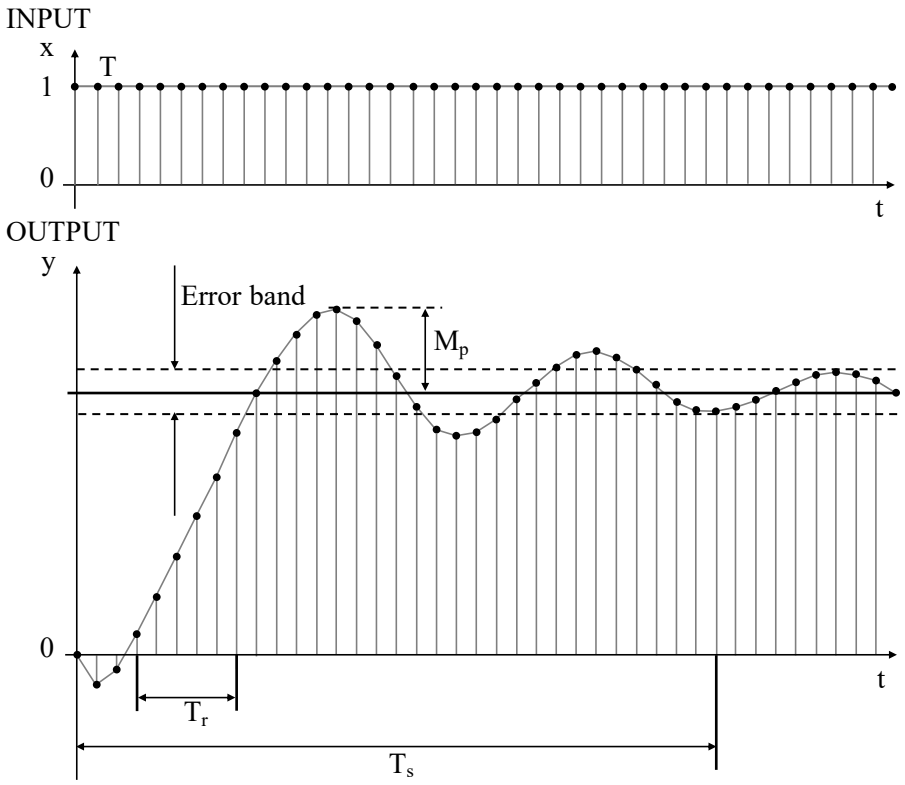

Fig. II-3 Step Response and its time properties

II.2.5 Pole placement design

The pole placement design is the procedure through which the matrix **A** is defined to obtain the desired system behaviour. It consists in fixing the value of the poles of the system. The location of the eigenvalues/poles in the complex plane determines the behaviour of the closed loop dynamics. The step response parameters can be obtained as follows (Åström et Murray 2008):

$$T_r \approx \frac{T \times \exp\left(-\frac{\arccos(\zeta)}{\tan(\arccos(\zeta))}\right)}{\omega_n} \quad \text{(II-3)}$$

$$M_p = \exp\left(-\frac{\pi\zeta}{\sqrt{1-\zeta^2}}\right) \quad \text{(II-4)}$$

$$T_s \approx \frac{4}{\zeta\omega_n} \quad \text{(II-5)}$$

T is the "sample time" and is equal to the time interval between two updates of the controlled value. ζ is the damping ratio and ω_n is the natural frequency. They are properties of the system that is chosen by the user given the needs of the control problem. The natural frequency and damping ratio are defined in Table II-1 and depends on the location of the poles in complex plane. Concerning the value of ζ and ω_n, one can make the following comments:

- The system is stable if $\omega_n > 0$ and $\zeta > 0$.
- If $0 < \zeta < 1$, the poles are complex or real negative. Otherwise, the poles are real and positive.
- If $\zeta = 1$, $M_p = 0$. That means the oscillation part of the response just disappears when the damping ratio becomes unity.

As the value of ζ and ω_n depends on the poles or eigenvalues of the system, it takes part in the process of "Pole Placement Design". This process is well established for first (one DOF) and second order (two DOFs) systems, see e.g., (Åström et Murray 2008). For systems of higher order, the response is governed by the dominant eigenvalues, i.e., the ones that have the highest modules.

Fig. II-4 shows the poles locations given ζ and ω_n in the complex plane. There are two types of lines. The highlighted red lines are the constant natural frequency lines, and the blue lines are the constant damping ratio lines. The plane is symmetrical around the real axis.

Table II-1

Pole location	$z \in \mathbb{C}$	
Natural Frequency	$\omega_n = \left\lvert \frac{\ln z}{T} \right\rvert$	(II-6)
Damping ratio	$\zeta = -\cos(\measuredangle \ln z)$	(II-7)

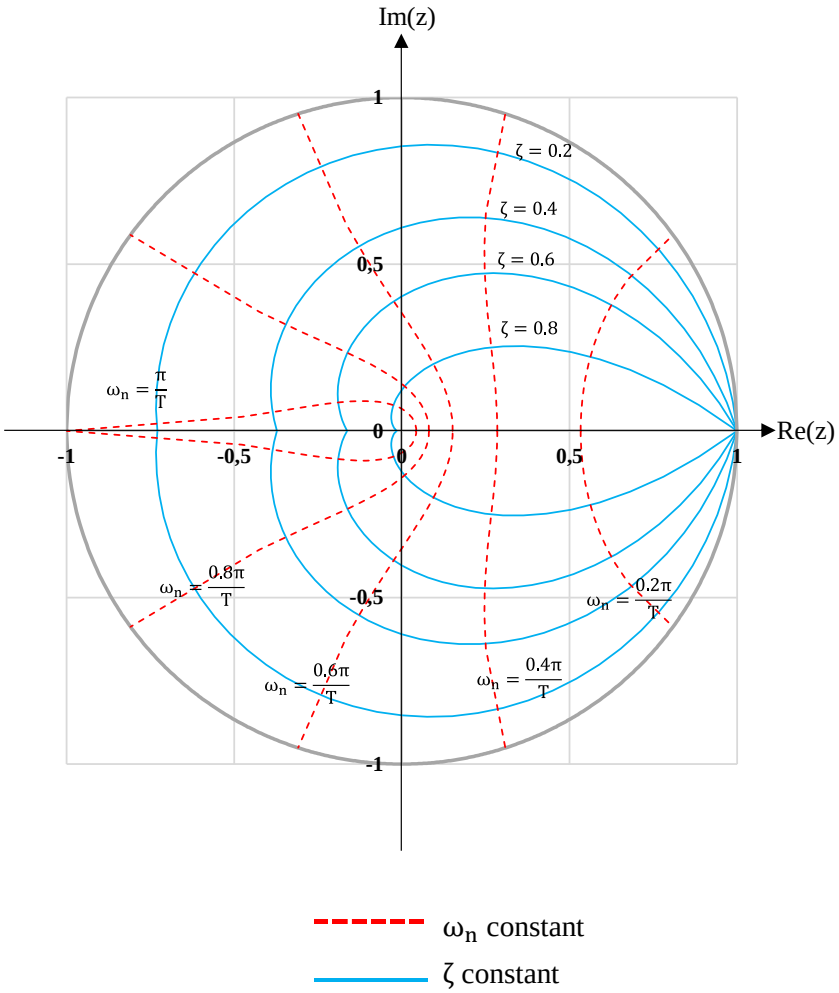

Fig. II-4 Complex plane with damping ratio and natural frequency

First-order system

In a first-order system, the characteristic equation $|z\mathbf{I} - \mathbf{A}|$ is a 1st degree polynomial. There is only one pole on the real axis. Table II-2 and Fig. II-5 give the response of the system given the location of the pole in the complex plane. The pole is written as follows:

$$p = \exp(\omega_n T) \tag{II-8}$$

Usually, real positive poles are chosen to avoid oscillations. If the pole of the first-order system is real and positive, overshoot and settling time does not make sense anymore. The pole is located by setting the rise time with equation (II-3):

$$p = \exp\left(-\exp(1)\frac{T}{T_r}\right) \approx \exp\left(-2{,}72\frac{T}{T_r}\right) \tag{II-9}$$

Table II-2

	Pole location	System response
3-6	Pole inside the unit circle.	The system is stable.
2, 7	Pole on the unit circle.	The system is marginally stable[1].
1, 8	Pole outside the unit circle.	The system is unstable.
6, 5	Real pole at 0 < z < 1.	The system has an exponential (decaying in time) response.
3	Real pole at -1 < z < 0.	The system has response decaying in time with oscillations with alternate signs.

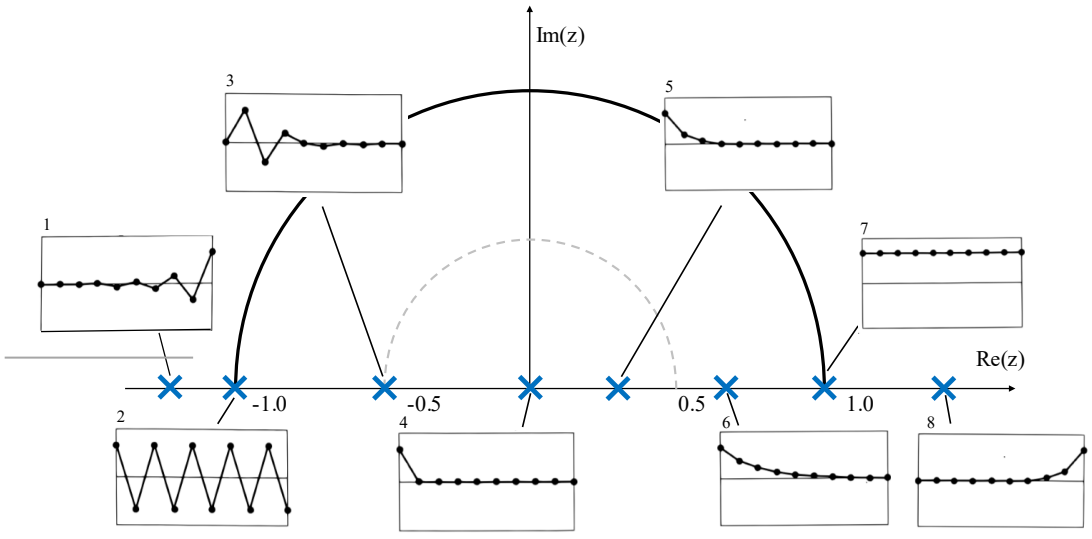

Fig. II-5 First-order system: effect of pole location

[1] The system is oscillatory and undamped. The magnitude of the homogeneous system response neither decays nor grows.

Second-Order system

The characteristic equation $|z\mathbf{I} - \mathbf{A}|$ is a 2nd degree polynomial. The poles can either be real (and may or may not have the same location) or complex conjugate. Table II-3 and Fig. II-6 give the response of the system given the location of the poles in the complex plane. Usually, poles are chosen as positive real numbers less than one or complex conjugate poles with real positive part. The poles can be easily determined through (II-10).

$$p_1 = \exp\left(\omega_n \zeta T - \omega_n T\sqrt{\zeta^2 - 1}\right)$$
$$p_2 = \exp\left(\omega_n \zeta T + \omega_n T\sqrt{\zeta^2 - 1}\right) \quad \text{(II-10)}$$

Table II-3

	Pole location	System response
3-6, 10-12	Poles are inside the unit circle.	The system is stable.
2, 8	Poles on the unit circle.	The system is marginally stable.
1, 9	Poles are outside the unit circle.	The system is unstable.
6, 7	Real poles at 0 < z < 1.	The system has an exponential response.
3, 4	Real poles at -1 < z < 0.	The system has response decaying in time with oscillations with alternate signs.
10-12	Poles with larger argument.	The system response has higher frequency of oscillations.

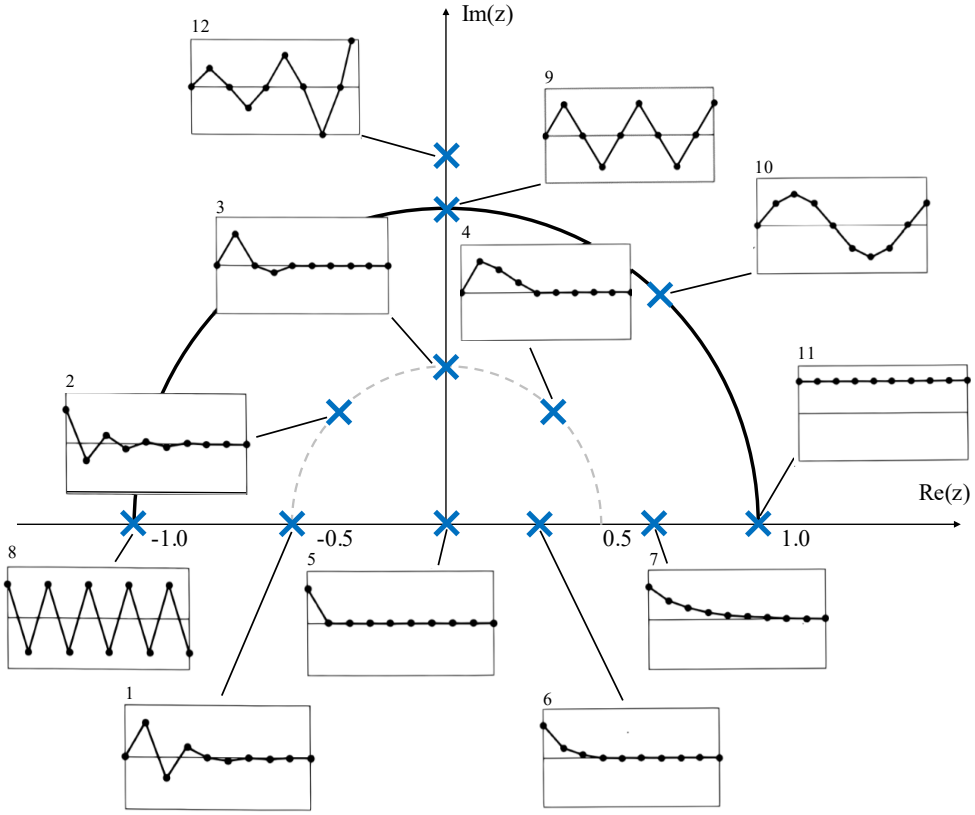

Fig. II-6 Second-order system: effect of poles location

High-Order Systems

First-order systems and second-order systems play an important role for characterizing high-order systems. Indeed, even for more complicated systems, the response is often characterized by the dominant eigenvalues, that have highest module. If a system is stable, the dominant eigenvalue or the dominant pair of eigenvalues tends to be the most important element of the response. Consequently, for the pole placement design, one defines a dominant pair of eigenvalues or one real eigenvalue and uses time parameters of the second or first order system.

For instance, in case of a third-order system, one can have the following pole locations (if only real positive poles or poles with a positive real part are considered):

- Fig. II-7 (a) shows three real poles. The parameters of the first order system are used for the pole that has the highest value.
- Fig. II-7 (b) shows two complex conjugate poles and one real pole. In this case, the complex poles can be defined as dominant eigenvalues and time parameters of the second order system are used. Indeed, the module of the complex poles is much higher than the one of the real pole.
- Fig. II-7 (c) shows two complex conjugate poles and one real pole. The three eigenvalues must be considered in the design because the module of the three poles is not negligible.

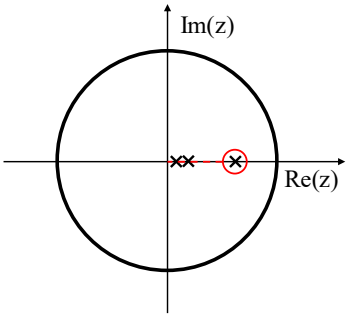

(a) One dominant eigenvalue

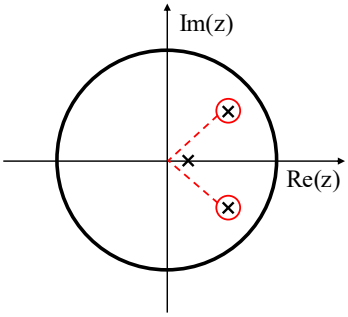

(b) Pair of dominant eigenvalues

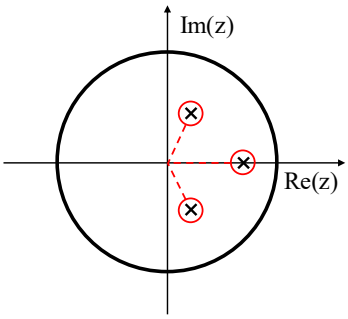

(c) No dominant eigenvalues

Fig. II-7 Poles of a three-order system

II.3 General state equation of HFT

HFT is a closed-loop system composed of two subsystems, a physical specimen and a numerical substructure, respectively called “PS” and “NS”. The input/output of these subsystems are forces or displacements. The aim of the following developments is to establish the state-space representation of the HFT system. This mathematical model used in modern control theory was approached in Section II.2.3.

As HFT is a closed loop system, it can be described with an equivalent open loop. It is assumed here that the PS and the NS have the same number d of controlled degrees of freedom (DOFs). If this is not the case, additional transformations must be considered, which complicates the notation but does not change the outcomes. This specific point is discussed is Section II.5.5 of this Chapter. Forces, displacements, and stiffness matrices are considered at the interface of the two substructures. In a force control procedure (FCP), the input of PS and NS are respectively forces and displacements as shown in Fig. II-8 (a). One can notice that this system is close to the procedure described in (Mostafaei 2013a). In a displacement control procedure (DCP), the situation is reversed (Fig. II-8 (b)).

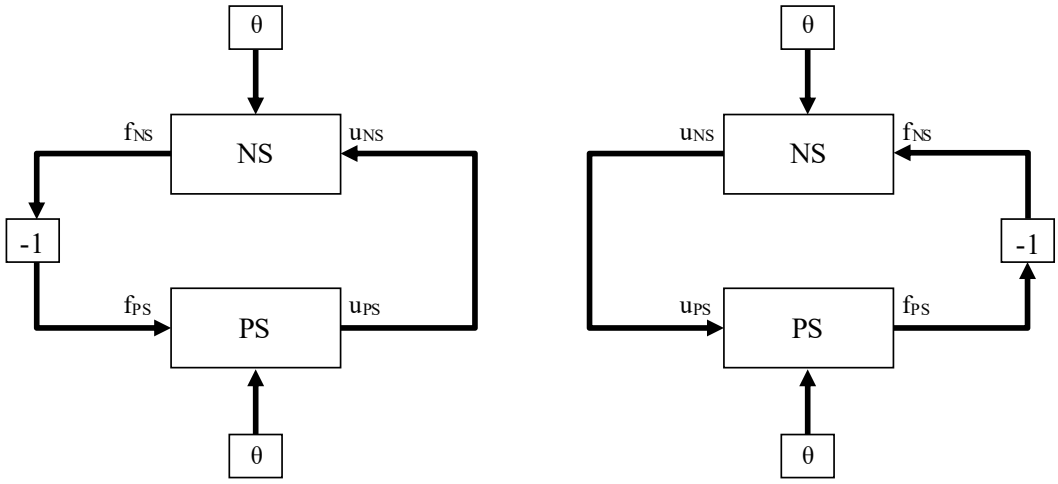

(a) Force control procedure *(b) Displacement control procedure*

Fig. II-8 Block diagram of the simple loop

Because the temperature and the loads are applied slowly in building structures subjected to fire, the interface between PS and NS can be described by the following static equations:

$$\mathbf{K}_{\mathrm{PS_i}}\mathbf{u}_{\mathrm{PS_i}} + \mathbf{f}^{\mathrm{TH}}_{\mathrm{PS_i}} = \mathbf{f}_{\mathrm{PS_i}} \tag{II-11}$$

$$\mathbf{K}_{\mathrm{NS_i}}\mathbf{u}_{\mathrm{NS_i}} + \mathbf{f}^{\mathrm{TH}}_{\mathrm{NS_i}} = \mathbf{f}_{\mathrm{NS_i}} \tag{II-12}$$

The vectors $\mathbf{u}_{\mathrm{PS_i}} \in \mathbb{R}^{d\times 1}$ and $\mathbf{u}_{\mathrm{NS_i}} \in \mathbb{R}^{d\times 1}$ refer to the displacement of the PS and the NS at discrete time i. $\mathbf{K}_{\mathrm{PS_i}} \in \mathbb{R}^{d\times d}$ and $\mathbf{K}_{\mathrm{NS_i}} \in \mathbb{R}^{d\times d}$ stand for the stiffness. These stiffness matrices are defined at the interface of the two substructures. $\mathbf{f}_{\mathrm{PS_i}}$ and $\mathbf{f}_{\mathrm{NS_i}}$ are the vectors of the mechanical loads. $\mathbf{f}^{\mathrm{TH}}_{\mathrm{PS_i}} \in \mathbb{R}^{d\times 1}$ and $\mathbf{f}^{\mathrm{TH}}_{\mathrm{NS_i}} \in \mathbb{R}^{d\times 1}$ are the thermal forces of the substructures. The vector $\mathbf{f}^{\mathrm{TH}}$ can be written as $\mathbf{K}^{\theta}_{\mathrm{i}}\boldsymbol{\theta}_{\mathrm{i}}$, with $\mathbf{K}^{\theta}_{\mathrm{i}} \in \mathbb{R}^{d\times d}$ that provides the internal forces due to thermal deformations and $\boldsymbol{\theta}_{\mathrm{i}}$ that is the temperature field.

This assumption is valid during most of the test, before the failure of the PS. When the specimen collapses, static equations are not appropriate.

II.3.1 Force control procedure FCP

The loop is closed using the equilibrium of forces and the compatibility of displacement:

$$\mathbf{f}_{\mathrm{PS_{i+1}}} = -\mathbf{f}_{\mathrm{NS_i}} \tag{II-13}$$

$$\mathbf{u}_{\mathrm{PS_i}} = \mathbf{u}_{\mathrm{NS_i}} \tag{II-14}$$

The state-space approach described in Section II.2.3 is used. $\mathbf{f}_{\mathrm{PS}}$ is chosen as the state variable of the system. Starting with equation (II-13), $\mathbf{f}_{\mathrm{NS_i}}$ is replaced with the equation (II-12) and then $\mathbf{u}_{\mathrm{NS_i}}$ with equation (II-14). After substituting $\mathbf{u}_{\mathrm{PS_i}}$ with equation (II-11), the state-space representation of the system is obtained:

$$\begin{gathered}\mathbf{f}_{\mathrm{PS_{i+1}}} = -\mathbf{K}_{\mathrm{NS_i}}\mathbf{K}_{\mathrm{PS_i}}^{-1}\mathbf{f}_{\mathrm{PS_i}} - \left(\mathbf{f}_{\mathrm{NS_i}}^{\mathrm{TH}} - \mathbf{K}_{\mathrm{NS_i}}\mathbf{K}_{\mathrm{PS_i}}^{-1}\mathbf{f}_{\mathrm{PS_i}}^{\mathrm{TH}}\right) \\ \mathbf{y}_{\mathrm{i}} = \mathbf{f}_{\mathrm{PS_i}}\end{gathered} \tag{II-15}$$

Referring to equation (II-2), $-\mathbf{K}_{\mathrm{NS_i}}\mathbf{K}_{\mathrm{PS_i}}^{-1} \in \mathbb{R}^{\mathrm{d\times d}}$ is the dynamics matrix (matrix **A**) of the system.

As mentioned in Section II.2.3, stability requires the module of the eigenvalues of this dynamics matrix be lower than 1.

In a single DOF system, the matrix simplifies into $-\mathrm{K}_{\mathrm{NS_i}}/\mathrm{K}_{\mathrm{PS_i}}$, i.e., the ratio between the stiffness of the PS and NS and the condition of stability is the following:

$$\frac{\mathrm{K}_{\mathrm{NS_i}}}{\mathrm{K}_{\mathrm{PS_i}}} < 1 \tag{II-16}$$

This condition aligns with the findings of (Sauca, Gernay, et al. 2018) given in Section I.3.7.

II.3.2 Displacement control procedure DCP

In case of a DCP, the loop is also closed by the equilibrium of forces and compatibility of displacement:

$$\mathbf{f}_{\mathrm{NS_i}} = -\mathbf{f}_{\mathrm{PS_i}} \tag{II-17}$$

$$\mathbf{u}_{\mathrm{PS_{i+1}}} = \mathbf{u}_{\mathrm{NS_i}} \tag{II-18}$$

The displacement $\mathbf{u}_{\mathrm{PS}}$ is chosen as the state variable of the system. In equation (II-18), $\mathbf{u}_{\mathrm{NS_i}}$ is substituted with equation (II-12). Then, $\mathbf{f}_{\mathrm{NS_i}}$ is replaced with $-\mathbf{f}_{\mathrm{PS_i}}$ because of force equilibrium. $\mathbf{f}_{\mathrm{PS_i}}$ is finally substituted with equation (II-11). The state-space representation of the system can be written as follow:

$$\begin{gathered}\mathbf{u}_{\mathrm{PS_{i+1}}} = -\mathbf{K}_{\mathrm{NS_i}}^{-1}\mathbf{K}_{\mathrm{PS_i}}\mathbf{u}_{\mathrm{PS_i}} - \mathbf{K}_{\mathrm{NS_i}}^{-1}\left(\mathbf{f}_{\mathrm{NS_i}}^{\mathrm{TH}} + \mathbf{f}_{\mathrm{PS_i}}^{\mathrm{TH}}\right) \\ \mathbf{y}_{\mathrm{i}} = \mathbf{u}_{\mathrm{PS_i}}\end{gathered} \tag{II-19}$$

In this case, the dynamics matrix of equation (II-2), matrix **A**, is $-\mathbf{K}_{\mathrm{NS_i}}^{-1}\mathbf{K}_{\mathrm{PS_i}} \in \mathbb{R}^{\mathrm{d\times d}}$.

The loop of HFT is stable if the eigenvalues lie in the unit circle in the complex plane. For a single DOF system, the condition of stability is the same as the one developed in (Sauca, Gernay, et al. 2018) for a DCP and comes down to:

$$\frac{\mathrm{K}_{\mathrm{PS_i}}}{\mathrm{K}_{\mathrm{NS_i}}} < 1 \tag{II-20}$$

II.3.3 Discussion

A HFT can be controlled in displacement (DCP) or in force (FCP). Using the formalism of control theory, the state-space representation has been established for both cases. This allows deriving an equation for the condition of stability of the system that depends on the dynamics matrix. The state space representation aligns with the stability conditions given in (Sauca, Gernay, et al. 2018) for a single DOF system and allows to extend these findings to multi-DOF systems.

Because the eigenvalues of the system exclusively depend on the stiffness matrices of the PS and NS for both procedures, this state representation contains two major issues. On one hand, it involves that no HFT could be performed (because it would be not stable) on structural configurations for which the stiffness of the PS and NS yield a dynamics matrix that has at least one eigenvalue out of the unit circle in complex plane. This condition is indeed not always filled in a single DOF system and hardly ever reached for multi-DOF tests, as these tests can involve flexible and stiff DOFs. The second issue is that no characteristics of the system (such as rise time for instance) can be improved, as the step response directly depends on the location of the poles as mentioned in Section II.2.5.

These limitations can be overcome by using a controller to stabilise the system and correct the deviation between controlled values and desired values. This issue is treated in the following sections.

II.3.4 Controller for HFT

To stabilise the loop, a controller is added. By comparison with Fig. II-2, the three main components of a controller are the *measured error* (input of the controller), the *controlled input* (output of the controller) and the *control law*. These components are summarized in Fig. II-9.

The *measured error* is the difference between a feedback signal and a reference signal provided by an external source. In the case of the HFT, there is no external reference. In fact, the two subsystems must not reach specific values of displacements or forces. However, at the interface, the forces must be equilibrated and the displacements compatible. Thus, the error introduced in the controller is the difference between two feedback signals provided by the subsystems NS and PS. In the NS, this signal is computed and in PS, it is measured by a sensor.

The PS and the NS are two controlled systems and receive directly or indirectly a *controlled input.* As in Section II.3.1, the procedure is called *force control procedure* if the controlled input is the interface force of the PS. If the controlled input is the interface displacement of the PS, the system is referred as a *displacement control procedure.*

The controlled input is computed by the controller following a control equation or *control law* that is chosen by the user. This equation updates the input based on the error signal. In the following sections two control laws will be approach: the proportional control in Section II.4 and the proportional integral control in Section II.5. *Linear controller*s are considered, meaning the parameters of the control law are not updated.

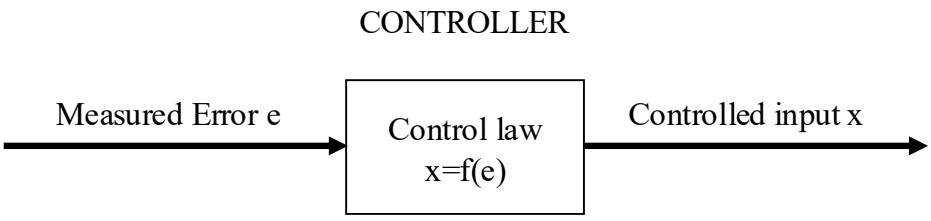

Fig. II-9 Components of the controller

Given the measured error and the controlled input that are chosen, the two systems PS and NS can be in series (Fig. II-10 (a)) or in parallel (Fig. II-10 (b)). In the following sections four cases will be approached:

- Force control procedure with PS and NS in series
- Force control procedure with PS and NS in parallel
- Displacement control procedure with PS and NS in series
- Displacement control procedure with PS and NS in parallel

Table II-4 gives the measured error and the controlled input for each case.

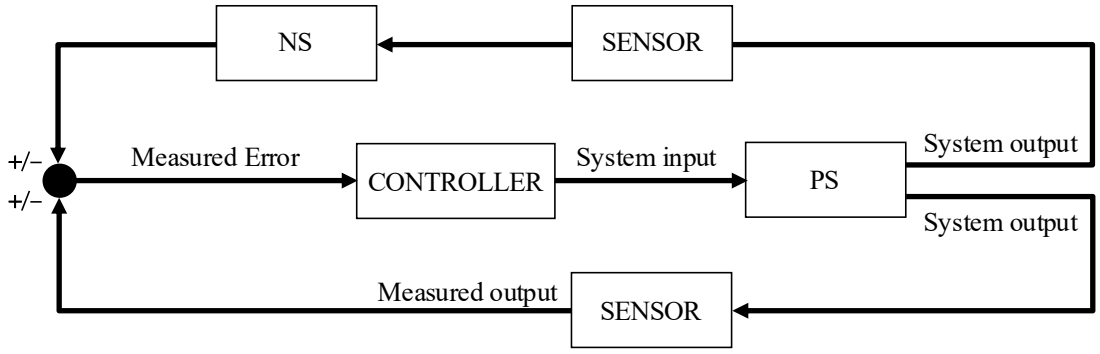

(a) Subsystems in series

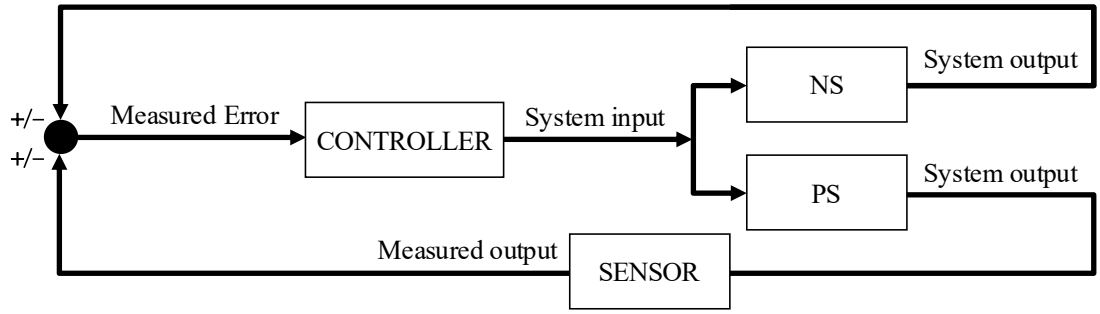

(b) Subsystems in parallel

Fig. II-10 Block diagram of HFT with controller

Table II-4

		Measured error	Controlled input
Force control procedure	PS and NS in series	$-(\mathbf{f}_{\mathrm{NS_i}} + \mathbf{f}_{\mathrm{PS_i}})$	$\mathbf{f}_{\mathrm{PS_{i+1}}}$
	PS and NS in parallel	$\mathbf{u}_{\mathrm{NS_i}} - \mathbf{u}_{\mathrm{PS_i}}$	$\mathbf{f}_{\mathrm{PS_{i+1}}}$
Displacement control procedure	PS and NS in series	$\mathbf{u}_{\mathrm{NS_i}} - \mathbf{u}_{\mathrm{PS_i}}$	$\mathbf{u}_{\mathrm{PS_{i+1}}}$
	PS and NS in parallel	$-(\mathbf{f}_{\mathrm{NS_i}} + \mathbf{f}_{\mathrm{PS_i}})$	$\mathbf{u}_{\mathrm{PS_{i+1}}}$

II.4 Linear proportional controller

This section discusses the case of a proportional controller. A proportional controller applies a response to the system that is proportional to the measured error. The controlled input vector $\mathbf{x}_i$ is updated based on the instantaneous error vector $\mathbf{e}_i^{inst}$ following the hereunder control law:

$$\mathbf{x}_{i+1} = \mathbf{x}_i + \mathbf{L}_P \mathbf{e}_i^{inst} \tag{II-21}$$

$\mathbf{L}_p$ is the gain matrix of the system that is designed to place the pole of the system in the complex plane (see *pole placement design* in Section II.2.5). As the proportional controller is linear, the gain matrix $\mathbf{L}_p$ is designed with initial parameters if the system and kept constant during the entire test.

The introduction of a proportional controller can be done both in FCP and DCP and the PS and NS can be placed in series or in parallel.

II.4.1 Force control procedure - Subsystems in series

As explained in Chapter I in Section I.3.10, DCP could be questionable for some cases. First, it can be a limitation for very stiff DOFs because an accurate control of the actuators is necessary to avoid large errors in the force. Then, DCP needs a continuous movement of the jack as large thermal forces can develop if the displacement is restrained. Finally, the stiffness of the frame must be often compensated to measure the values of the displacements of the PS (see (Wang, et al. 2018)). The case of the FCP should thus be studied as a priority.

For a FCP with subsystems in series (see Fig. II-11), the force at time step i+1 at the interface of the PS is modified with the following control law:

$$\mathbf{f}_{PS_{i+1}} = \mathbf{f}_{PS_i} - \mathbf{L}_P\left(\mathbf{f}_{NS_i} + \mathbf{f}_{PS_i}\right) \tag{II-22}$$

$\mathbf{L}_P \in \mathbb{R}^{d\times d}$ is the gain matrix of the proportional controller. One considers that $\mathbf{f}_{PS_i}$ is the state variable of the system. The feedback vectors are $\mathbf{f}_{PS_i}$ and $\mathbf{f}_{NS_i}$. $\mathbf{f}_{PS_i}$ is the mechanical load vector at time step i of the PS. $\mathbf{f}_{NS_i}$ is the force vector of NS after the application of the displacement $\mathbf{u}_{NS_i}$, equal to $\mathbf{u}_{PS_i}$. Following the same process as in Section II.3.1, $\mathbf{f}_{NS_i}$ is replaced with equation (II-12) in equation (II-22). Compatibility of displacement makes that $\mathbf{u}_{NS_i}$ can then be replaced with $\mathbf{u}_{PS_i}$. Finally, $\mathbf{u}_{PS_i}$ is substituted with equation (II-11). The state-space representation of the control system is obtained:

$$\begin{gathered}\mathbf{f}_{PS_{i+1}} = \left[\mathbf{I} - \mathbf{L}_P\mathbf{K}_{NS_i}\mathbf{K}_{PS_i}^{-1} - \mathbf{L}_P\right]\mathbf{f}_{PS_i} + \mathbf{L}_P\mathbf{f}_{NS_i}^{TH} - \mathbf{L}_P\mathbf{K}_{NS_i}\mathbf{K}_{PS_i}^{-1}\mathbf{f}_{PS_i}^{TH} \\ \mathbf{y}_i = \mathbf{f}_{PS_i}\end{gathered} \tag{II-23}$$

The gain matrix $\mathbf{L}_P$ must be designed to ensure stability of the system during the entire test for any matrix $\mathbf{K}_{PS_i}$ and $\mathbf{K}_{NS_i}$. In fact, these matrices vary during the test, especially $\mathbf{K}_{PS_i}$ as the PS is heated. Moreover, as the specimen collapses, it involves that the $\mathbf{K}_{PS_i}$ will be singular, meaning that the inverse does not exist anymore, and the eigenvalues tends to infinity ($-\infty$). So there will always be stability issues at the end of the test. A linear controller is thus not appropriate in this case. This procedure is consequently put aside.

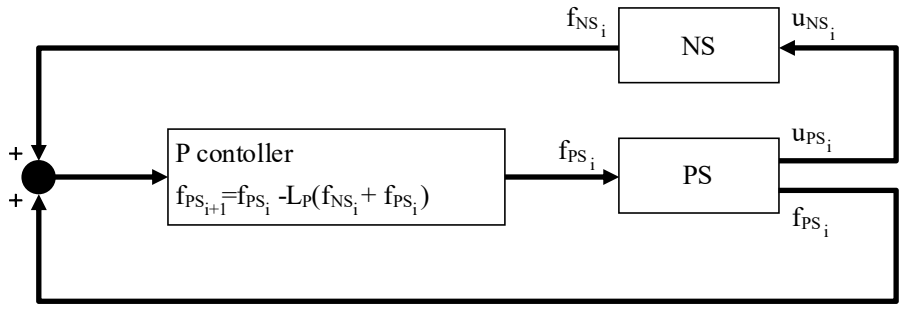

Fig. II-11 Block diagram of the force control procedure - Subsystems in series

II.4.2 Force control procedure - Subsystems in parallel

For a FCP with subsystems in parallel (see Fig. II-12), the control equation is as follows:

$$\mathbf{f}_{\mathrm{PS_{i+1}}} = \mathbf{f}_{\mathrm{PS_i}} + \mathbf{L}_{\mathrm{P}}\left(\mathbf{u}_{\mathrm{NS_i}} - \mathbf{u}_{\mathrm{PS_i}}\right) \tag{II-24}$$

The feedback vectors are the displacement $\mathbf{u}_{\mathrm{NS_i}}$ and $\mathbf{u}_{\mathrm{PS_i}}$ obtained when the force vectors of the subsystem PS and NS are equal to $\mathbf{f}_{\mathrm{PS_i}}$ and $-\mathbf{f}_{\mathrm{PS_i}}$, respectively. The vectors $\mathbf{u}_{\mathrm{NS_i}}$ and $\mathbf{u}_{\mathrm{PS_i}}$ can be substituted using equations (II-11) and (II-12). Using force equilibrium, the state representation can be written as:

$$\begin{gathered}\mathbf{f}_{\mathrm{PS_{i+1}}} = \left[\mathbf{I} - \mathbf{L}_{\mathrm{P}}\mathbf{K}_{\mathrm{NS_i}}^{-1} - \mathbf{L}_{\mathrm{P}}\mathbf{K}_{\mathrm{PS_i}}^{-1}\right]\mathbf{f}_{\mathrm{PS_i}} + \mathbf{L}_{\mathrm{P}}\left(\mathbf{K}_{\mathrm{PS_i}}^{-1}\mathbf{f}_{\mathrm{PS_i}}^{\mathrm{TH}} - \mathbf{K}_{\mathrm{NS_i}}^{-1}\mathbf{f}_{\mathrm{NS_i}}^{\mathrm{TH}}\right) \\ \mathbf{y}_{\mathrm{i}} = \mathbf{f}_{\mathrm{PS_i}}\end{gathered} \tag{II-25}$$

The same observation resulting from the use of $\mathbf{K}_{\mathrm{PS_i}}^{-1}$ can be done: no linear controller that ensures stability can be designed based on this state-space representation. Moreover, one can notice that the matrix $\mathbf{K}_{\mathrm{NS_i}}$ cannot be singular, which limits the application to non-floating structure.

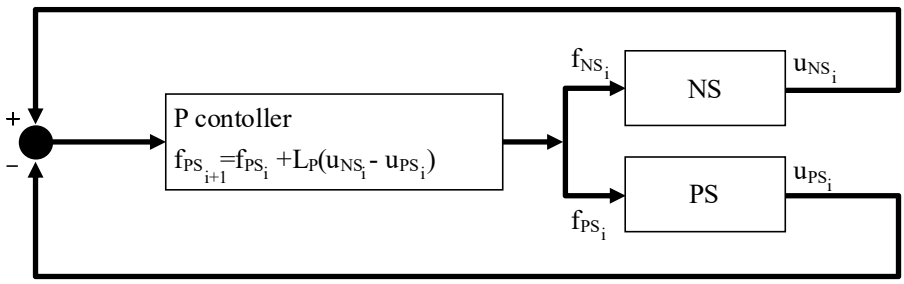

Fig. II-12 Block diagram of the force control procedure - Subsystems in parallel

As linear control is not convenient for FCP, this case will not be discussed further and DCP will be preferred.

II.4.3 Displacement control procedure - Subsystems in series

For a DCP with subsystems in series (see Fig. I-14), the new displacement at time step i+1 at the interface of the PS can be written as follows:

$$\mathbf{u}_{\mathrm{PS_{i+1}}} = \mathbf{u}_{\mathrm{PS_i}} + \mathbf{L}_{\mathrm{p}}\left(\mathbf{u}_{\mathrm{NS_i}} - \mathbf{u}_{\mathrm{PS_i}}\right) \tag{II-26}$$

$\mathbf{L}_{\mathrm{p}} \in \mathbb{R}^{\mathrm{d}\times\mathrm{d}}$ is the gain matrix of the proportional controller. $\mathbf{u}_{\mathrm{PS}}$ is chosen as state variable of the system. Following the same process as in Section II.3.2, $\mathbf{u}_{\mathrm{NS_i}}$ is replaced with equation (II-12) in equation (II-26). Force equilibrium makes that $\mathbf{f}_{\mathrm{NS_i}}$ is substituted with $-\mathbf{f}_{\mathrm{PS_i}}$. Finally, $\mathbf{f}_{\mathrm{PS_i}}$ is replaced with equation (II-11). The new state-space representation is obtained:

$$\mathbf{u}_{\mathrm{PS_{i+1}}} = \left[\mathbf{I} - \mathbf{L}_\mathrm{P}\mathbf{K}_{\mathrm{NS_i}}^{-1}\mathbf{K}_{\mathrm{PS_i}} - \mathbf{L}_\mathrm{P}\right]\mathbf{u}_{\mathrm{PS_i}} - \mathbf{L}_\mathrm{P}\mathbf{K}_{\mathrm{NS_i}}^{-1}\left(\mathbf{f}_{\mathrm{NS_i}}^{\mathrm{TH}} + \mathbf{f}_{\mathrm{PS_i}}^{\mathrm{TH}}\right)$$
$$\mathbf{y}_\mathrm{i} = \mathbf{u}_{\mathrm{PS_i}} \qquad \text{(II-27)}$$

The dynamics matrix $\left[\mathbf{I} - \mathbf{L}_\mathrm{P}\mathbf{K}_{\mathrm{NS_i}}^{-1}\mathbf{K}_{\mathrm{PS_i}} - \mathbf{L}_\mathrm{P}\right]$ depends on $\mathbf{L}_\mathrm{P}$ in addition to the stiffness matrix. The terms of $\mathbf{L}_\mathrm{p}$ can be chosen purposely to satisfy stability and obtain appropriate time properties using equations (II-3)-(II-5). However, one can notice that the matrix $\mathbf{K}_{\mathrm{NS_i}}$ cannot be singular, which limits the application to non-floating NS. For this reason, this procedure will not be discussed further. However, it has been the subject of publications as (Mergny, et al. 2019) and has demonstrated convincing performances for non-floating structures.

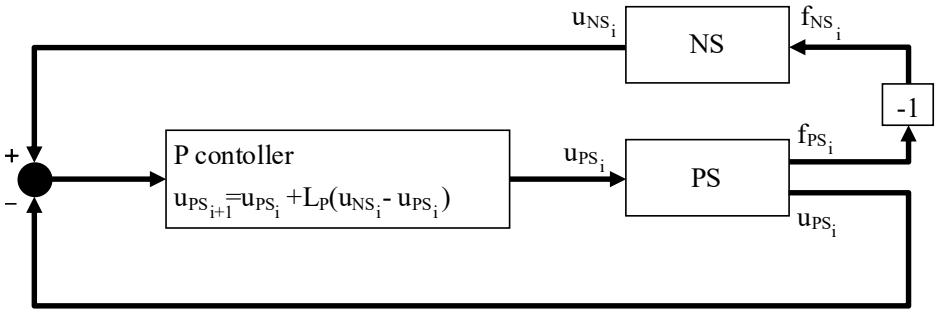

Fig. II-13 Block diagram of the displacement control procedure - Subsystems in series

II.4.4 Displacement control procedure - Subsystems in parallel

For a DCP (Fig. II-14) with subsystems in parallel, the new displacement vector at time step i+1 at the interface of NS and PS is applied to both subsystems and is determined given the difference between the interface force vectors.

$$\mathbf{u}_{\mathrm{PS_{i+1}}} = \mathbf{u}_{\mathrm{PS_i}} - \mathbf{L}_\mathrm{p}\left(\mathbf{f}_{\mathrm{NS_i}} + \mathbf{f}_{\mathrm{PS_i}}\right) \qquad \text{(II-28)}$$

Using similar substitutions as in the previous Sections, the state-space representation of the control system can be written as follows:

$$\mathbf{u}_{\mathrm{PS_{i+1}}} = \left[\mathbf{I} - \mathbf{L}_\mathrm{P}(\mathbf{K}_{\mathrm{PS_i}} + \mathbf{K}_{\mathrm{NS_i}})\right]\mathbf{u}_{\mathrm{PS_i}} - \mathbf{L}_\mathrm{P}\mathbf{K}_{\mathrm{NS_i}}^{-1}\left(\mathbf{f}_{\mathrm{NS_i}}^{\mathrm{TH}} + \mathbf{f}_{\mathrm{PS_i}}^{\mathrm{TH}}\right)$$
$$\mathbf{y}_\mathrm{i} = \mathbf{u}_{\mathrm{PS_i}} \qquad \text{(II-29)}$$

The dynamics matrix is $\left[\mathbf{I} - \mathbf{L}_\mathrm{P}(\mathbf{K}_{\mathrm{PS_i}} + \mathbf{K}_{\mathrm{NS_i}})\right]$. $\mathbf{L}_\mathrm{P}$ must be designed to ensure stability at every time step i. One can notice that this state equation is not limited to non-floating domain.

One will consider that $\mathbf{L}_\mathrm{P}$ is diagonal and designed for real positive eigenvalues. This assumption reduces the number of parameters to determine as explain further. However, it neglects the fact that DOFs are coupled which could involve a loss of accuracy and efficiency.

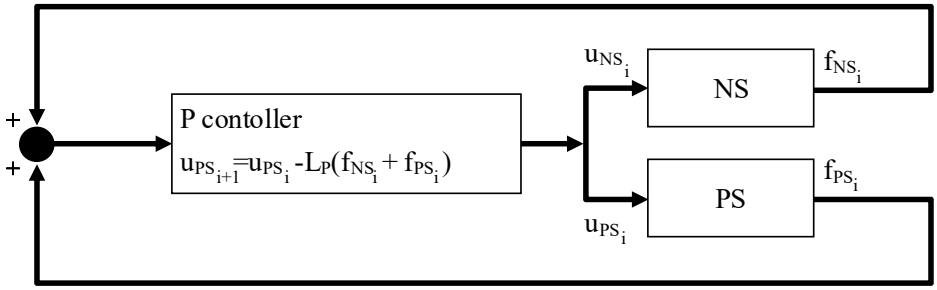

Fig. II-14 Block diagram of the displacement control procedure - Subsystems in parallel

II.4.5 Single DOF system

In this Section, the conditions of stability are explicitly given for a single DOF system. The two substructures are described as two springs with stiffness K_{PS} and K_{NS} at the interface, as shown in Fig. II-15.

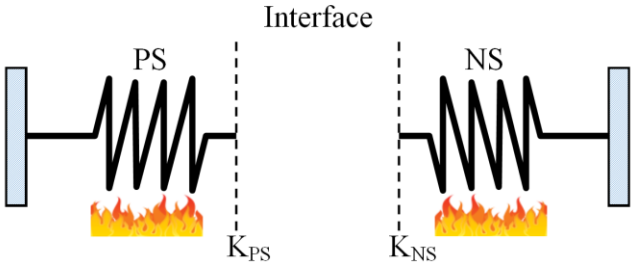

Fig. II-15 Single DOF system

The resulting state equation is now the following:

$$u_{PS_{i+1}} = \left[1 - L_P(K_{PS_i} + K_{NS_i})\right]u_{PS_i} - L_P K_{NS_i}^{-1}\left(f_{NS_i}^{TH} + f_{PS_i}^{TH}\right) \quad \text{(II-30)}$$

The system is stable if the eigenvalue of the state matrix lies into the unit circle in the complex plan. The conditions of stability can be expressed using the characteristic polynomial $|\mathbf{I}z - \mathbf{A}|$ of the state matrix **A**, that is in this case a first-degree polynomial:

$$z + L_P\left(K_{PS_i} + K_{NS_i}\right) - 1 \quad \text{(II-31)}$$

The root of this polynomial is the eigenvalue of the system and is the following real number:

$$\lambda = 1 - L_P(K_{PS_i} + K_{NS_i}) \quad \text{(II-32)}$$

As the eigenvalue must lie in the interval $[-1,1]$, the conditions of stability are the following:

$$\begin{aligned} L_P\left(K_{PS_i} + K_{NS_i}\right) &\leq 1 \\ L_P\left(K_{PS_i} + K_{NS_i}\right) &\geq 0 \end{aligned} \quad \text{(II-33)}$$

If L_P is designed so that these two conditions are met at the start of the test with $K_{PS_i} = K_{PS_0}$ and $K_{NS_i} = K_{NS_0}$, one can see that the system will be stable during the whole test. In fact, as K_{NS_i} and K_{PS_i} decrease during the test because of fire, the inequalities remain true.

In this case, the system has one real eigenvalue and is thus a first order system. The only parameter of the step response that can be designed is the rise time T_r. Following Section II.2.5, the equation (II-3) can be rewritten:

$$T_r = \frac{T\exp(-1)}{|\ln(\lambda^*)|} \approx 2.72\frac{T}{|\ln(\lambda^*)|} \quad \text{(II-34)}$$

T is the sample time. It corresponds to the time step for updating the boundary conditions. This parameter is chosen by the user, considering the constraints such as CPU time to run the model of the NS, response time of the actuators, etc. T_r is directly proportional to this time step, but also depends on the pole/eigenvalue λ^*.

λ^* is the design eigenvalue and is also chosen by the user. As mentioned in Section II.2.5, it is preferable that this eigenvalue is a positive real less than one to avoid oscillations. Consequently $\lambda^* \in [0,1]$. For λ^* varying between 0 and 1, T_r decreases if λ^* decreases. If λ^* tends to 0, T_r is null, meaning that the reactivity of the system is instantaneous. If λ^* tends to 1, T_r tends to infinity, meaning that the system never reaches the target value. In practice, this means that the matrix **A** of

the state-space representation of the HFT system must be chosen wisely, because its eigenvalues directly influence the time needed by the system to reach the target value when the boundary conditions are updated (through T_r). The design eigenvalue λ^* has the following expression:

$$\lambda^* = \exp\left(-2.72\frac{T}{T_r}\right) \tag{II-35}$$

Using equation (II-32), the gain L_P can be determined based on the eigenvalue λ^* (chosen by the user given T_r and T) and the initial stiffness of NS and PS. The interface stiffness $\mathbf{K}_{NS_0}$ can be computed while $\mathbf{K}_{PS_0}$ can only be estimated, with the estimated value being noted $\mathbf{K}_{PS_0}^{EST}$. The gain value is determined as follows from equation (II-32):

$$L_P = \frac{1-\lambda^*}{K_{PS_i} + K_{NS_i}} = \frac{1-\lambda^*}{K_{PS_0}^{EST} + K_{NS_0}} \tag{II-36}$$

The fact that L_P is not designed with the real stiffness involves that λ^* chosen by the user is different from λ, the actual eigenvalue of the system. Moreover, the value of the stiffness will change because of fire. Using equation (II-32) and (II-36), the evolution of the value of λ during the test can be written:

$$\lambda = 1 - \frac{(1-\lambda^*)(K_{PS_i} + K_{NS_i})}{K_{PS_0}^{EST} + K_{NS_0}} \tag{II-37}$$

To simplify this equation, one can consider that during fire:

- K_{PS_i} decreases as αK_{PS_0} with real $\alpha \in [0;1]$ ($\alpha = 1$ at the beginning of the test and $\alpha = 0$ at the end). The decreasing of K_{NS_i} is negligible and $K_{NS_i} = K_{NS_0}$
- The estimation diverges from this real stiffness as $K_{PS_0}^{EST} = \nu K_{PS_0}$, with $\nu \in \mathbb{R}^+$.

Considering $r = K_{PS_0}/K_{NS_0}$, equation (II-37) can thus be rewritten:

$$\lambda = 1 - (1-\lambda^*)\left(\frac{\alpha r + 1}{\nu r + 1}\right) \tag{II-38}$$

To ensure stability, the value of this function must be included between 0 and 1 during the whole duration of the test for every value of $\alpha \in [0;1]$. It is thus necessary to analyse the function $\lambda(\alpha)$ and evaluate the derivative:

$$\frac{d\lambda}{d\alpha} = -\frac{(1-\lambda^*)r}{\nu r + 1} \tag{II-39}$$

Given that $r \in \mathbb{R}^+$, $\nu \in \mathbb{R}_0^+$ and $\lambda^* \in [0;1]$, the derivative (II-39) is always negative. For a given ν and r, the function λ is a linear function in α and its slope is negative. It means that if the condition $-1 \leq \lambda \leq 1$ is verified at $\alpha = 0$ and $\alpha = 1$, this condition will be satisfied for any value of $\alpha \in [0;1]$. One calculates the two extremities:

Beginning of HFT
$$\lambda_{\alpha=1} = 1 - \frac{(1-\lambda^*)(r+1)}{\nu r + 1} \tag{II-40}$$

End of HFT
$$\lambda_{\alpha=0} = 1 - \frac{1-\lambda^*}{\nu r + 1} \tag{II-41}$$

Consequently, the stability of the single DOF test is ensured if these two inequalities are satisfied:

$$-1 \leq 1 - \frac{(1-\lambda^*)(r+1)}{\nu r + 1} \leq 1 \tag{II-42}$$

$$-1 \leq 1 - \frac{1-\lambda^*}{\nu r + 1} \leq 1 \tag{II-43}$$

As λ^* is chosen by the user and r depends on the stiffness of the substructures, these two inequalities must be verified for any value of ν. Three cases are considered:

- Exact estimation of the stiffness K_{PS_i}, $\nu = 1$
- Overestimation $\nu > 1$
- Underestimation $\nu < 1$

If the stiffness is well estimated ($\nu = 1$), the extremities $\lambda_{\alpha=1}$ and $\lambda_{\alpha=0}$ are as follows:

Beginning of HFT $$\lambda_{\alpha=1,\nu=1} = \lambda^* \tag{II-44}$$

End of HFT $$\lambda_{\alpha=0,\nu=1} = 1 - \frac{1-\lambda^*}{r+1} \tag{II-45}$$

As $\lambda^* \in [0;1]$ and $r \in \mathbb{R}^+$, $\lambda_{\alpha=1,\nu=1}$ and $\lambda_{\alpha=0,\nu=1}$ belongs to the interval $[-1;1]$.The HFT is thus stable for the entire test if $\nu = 1$.

For the other cases ($\nu > 1$ and $\nu < 1$), the derivative of λ of the variable ν is interesting to calculate and is given by:

$$\frac{d\lambda}{d\nu} = \frac{(1-\lambda^*)(\alpha r + 1)r}{(\nu r + 1)^2} \tag{II-46}$$

Given that $r \in \mathbb{R}^+$ and $\alpha, \lambda^* \in [0;1]$, the derivative is positive. It is thus sufficient to verify the conditions for the ends of the interval.

Overestimation $\nu > 1$

In case of *overestimation*, as $\nu \in [1, +\infty[$, it means that the inequalities (II-42) and (II-43) are verified if $\lambda_{\alpha=1,\nu=1}$, $\lambda_{\alpha=1,\nu\to+\infty}$, $\lambda_{\alpha=0,\nu=1}$ and $\lambda_{\alpha=0,\nu\to+\infty}$belongs to the interval $[-1;1]$. It is true for $\lambda_{\alpha=1,\nu=1}$ and $\lambda_{\alpha=0,\nu=1}$ because of equation (II-44) and (II-45). $\lambda_{\alpha=1,\nu\to+\infty}$ and $\lambda_{\alpha=0,\nu\to+\infty}$are given hereunder:

Beginning of HFT $$\lambda_{\alpha=1,\nu\to+\infty} = \lim_{\nu\to+\infty} \lambda_{\alpha=1} = 1 \tag{II-47}$$

End of HFT $$\lambda_{\alpha=0,\nu\to+\infty} = \lim_{\nu\to+\infty} \lambda_{\alpha=0} = 1 \tag{II-48}$$

Given (II-47) and (II-48), the system is stable for any value of $\nu > 1$, $\alpha \in [0;1]$ and $r \in \mathbb{R}^+$. However, the actual eigenvalue λ is higher than the designed value λ^*, meaning that the rise time during the test is higher than expected.

Underestimation $\nu > 1$

In case of *underestimation*, one can proceed to the same analysis. As ν lies into $[0;1]$, the inequalities (II-42) and (II-43) are verified if $\lambda_{\alpha=1,\nu=1}$, $\lambda_{\alpha=1,\nu=0}$, $\lambda_{\alpha=0,\nu=1}$ and $\lambda_{\alpha=0,\nu=0}$ belongs to the interval $[-1;1]$. $\lambda_{\alpha=1,\nu=1}$ and $\lambda_{\alpha=0,\nu=1}$ are verified with (II-44) and (II-45). Thus, $\lambda_{\alpha=1,\nu=0}$ and $\lambda_{\alpha=0,\nu=0}$ are calculated:

Beginning of HFT $$\lambda_{\alpha=1,\nu=0} = 1 - (1-\lambda^*)(r+1) \tag{II-49}$$

End of HFT $$\lambda_{\alpha=0,\nu=0} = \lambda^* \tag{II-50}$$

One can see in case of underestimation, that the stability is not ensured for any value of $\alpha \in [0;1]$ because of $\lambda_{\alpha=1,\nu=0}$ that could be lower than -1. Underestimation of the stiffness can thus be an issue at the beginning of the test when $\alpha = 1$.

The smallest underestimation ν_{min} that is acceptable can be obtained by studying the inequality $\lambda_{\alpha=1,\nu=0} \geq -1$. The following stability condition is given by equation (II-51):

$$\nu \geq \frac{(1-\lambda^*)(r+1)-2}{2r} \tag{II-51}$$

if this smallest underestimation $\nu_{min} = \frac{(1-\lambda^*)(r+1)-2}{2r}$ is negative, the system is stable in case of underestimation. For instance, if $r = 1$, the condition is $\nu \geq -\lambda^*$, which is always verified as $\lambda^* \in [0;1]$. Thus, there exist ranges of values of r for which an estimation of the stiffness of the PS does not involve instabilities.

These ranges of r can be obtained by solving the equation $\frac{(1-\lambda^*)(r+1)-2}{2r} \leq 0$:

$$r \geq \frac{2}{(1-\lambda^*)} - 1 \tag{II-52}$$

The stability is not the only criterion. In fact, if the eigenvalue increases during the test, the step response of the system is modified. The following observations can be made:

- Equation (II-40) shows that λ increases for α decreasing from 1 to 0. It involves that the rise time T_r increases during the test (see equation (II-34)), meaning that the controller takes more time to reach the reference.
- Equation (II-46) shows that $\lambda > \lambda^*$ if the stiffness is overestimated, meaning that the controller is less reactive. Equation (II-36) shows that L_P decreases with ν increasing.
- Equation (II-46) shows that $\lambda < \lambda^*$ if the stiffness is underestimated and possibly negative. The controller is more reactive and can have oscillations if λ is negative (see Section II.2.5, first-order system). The value of L_P is also higher according to (II-36).

Fig. II-16 and Table II-5 shows a summary of the different cases.

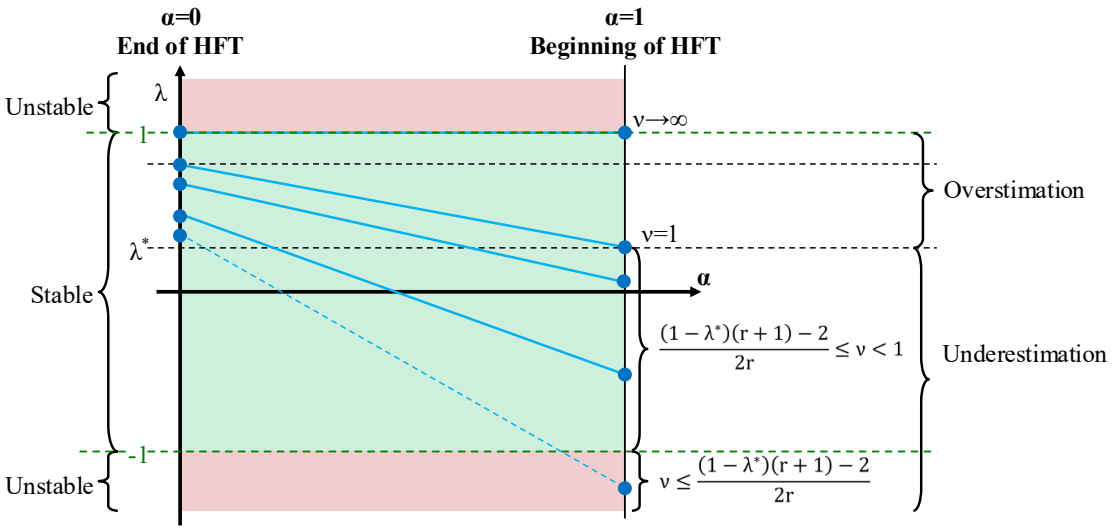

Fig. II-16 Eigenvalues of the single DOF system

Table II-5

$\nu = 1$	Stable $\forall\alpha \in [0;1]$, $r \in \mathbb{R}^+$	$\alpha = 1 : \lambda = \lambda^*$ $\alpha < 1 : \lambda > \lambda^*$	Controller less reactive
$\nu > 1$	Stable $\forall\alpha \in [0;1]$, $r \in \mathbb{R}^+$	$\lambda > \lambda^*$	Controller less reactive
$\nu < 1$ and $r \geq \frac{2}{(1-\lambda^*)} - 1$ $\nu < 1$ and $r < \frac{2}{(1-\lambda^*)} - 1$	Stable $\forall\alpha \in [0;1]$ Stable if $\nu \geq \frac{(1-\lambda^*)(r+1)-2}{2r}$	$\lambda < \lambda^*$	Controller more reactive + oscillations if λ is negative

One-DOF example

In this Section, a numerical example is used to illustrate the proportional controller in the case of a one-DOF system. The elastic system presented in Fig. II-17 is analysed in a virtual environment, meaning that PS and NS are modelled analytically. This example is similar to the single DOF system published in (Sauca, Gernay, et al. 2018).

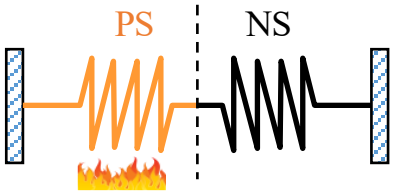

Fig. II-17 Single DOF example

The following input data are considered:

- Coefficient of thermal expansion of the material of the PS is equal to $12 \times 10^{-6}/°C$
- Sectional area of the PS and NS: $A_{PS} = A_{NS} = 20\,000\ mm^2$
- Length of the PS equal to 1.50 m and a length of the NS equal to 3.00 m
- Heating rate of the PS: $0.5°/s$
- Young modulus of the PS and NS at ambient temperature: $E_{PS} = E_{NS} = 210\,000\ N/mm^2$
- The Young modulus E_{PS} of the PS decreases with temperature as αE_{PS}. The factor α is equal to the reduction factor k_E for the slope of the linear elastic range given in Table 3 CEN. EN 1993-1-2:2005 (see Fig. II-18).
- The displacement of the PS and NS are updated every 10s, meaning that the sample time T is equal to 10s.
- The computation time is negligeable and between two updates, the position of the actuator is interpolated. The movement of the actuator is thus continuous.

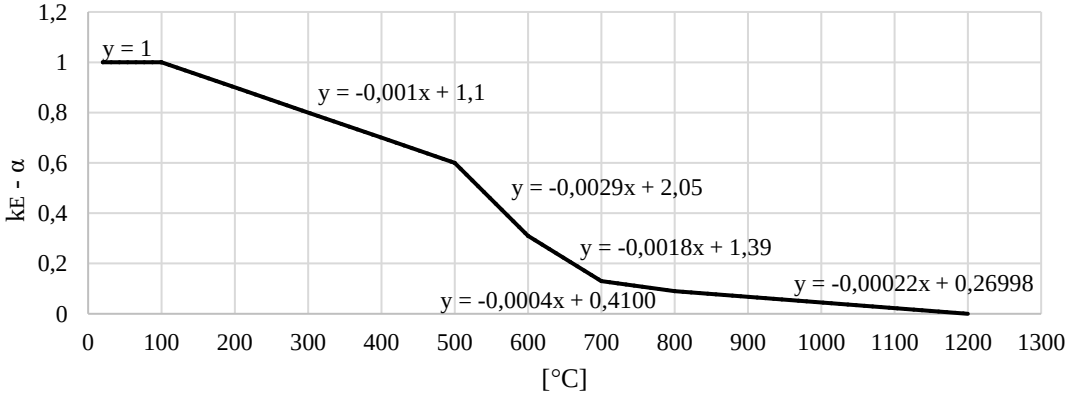

Fig. II-18 Reduction factor for the slope of the linear elastic range

As mentioned before, the design of the proportional controller is based on the desired rise time T_r. The design eigenvalue λ^* is determined with equation (II-35). If T_r increases, the eigenvalue λ^* increases. For an instantaneous correction, λ^* must be equal to 0. Fig. II-19 (a) and (b) gives the normal force and axial displacement of the PS for several design eigenvalues λ^* and rise time T_r:

$$\begin{aligned} T_r = 12s \rightarrow \lambda^* = 0.1 \ \rightarrow L_p &= \frac{1-0.1}{(2.8+1.4)\times 10^9} = 2.1429\times 10^{-10}\ \mathrm{m/N} \\ T_r = 30s \rightarrow \lambda^* = 0.4 \ \rightarrow L_p &= \frac{1-0.4}{(2.8+1.4)\times 10^9} = 1.4286\times 10^{-10}\ \mathrm{m/N} \\ T_r = 120s \rightarrow \lambda^* = 0.8 \ \rightarrow L_p &= \frac{1-0.8}{(2.8+1.4)\times 10^9} = 4.7619\times 10^{-11}\ \mathrm{m/N} \end{aligned} \quad \text{(II-53)}$$

The results of each case are compared with the correct solution, called "u" and "F" (black line).

Fig. II-16 shows that the real eigenvalue λ of the system increases with decreasing α. Fig. II-19 (c) illustrates that increasing for the three cases. Fig. II-19 (d) displays the instantaneous error $e_i^{inst} = -(f_{NS_i} + f_{PS_i})$. As the controller with $\lambda^* = 0.8$ is the least reactive the error is also the highest. Moreover, the rise time T_r increases when temperature increases as shown in Fig. II-19 (e).

Fig. II-20 shows the effect of the *overestimation* of K_{PS_0} on the design of the proportional controller, considering $\lambda^* = 0.1$. The three following cases are displayed on the graphs:

$$\begin{aligned} \nu = 1.0 \ \rightarrow \ L_p &= \frac{1-0.1}{(2.8\times 1.0+1.4)\times 10^9} = 2.1429\times 10^{-10}\ \mathrm{m/N} \\ \nu = 2.0 \ \rightarrow \ L_p &= \frac{1-0.1}{(2.8\times 2.0+1.4)\times 10^9} = 1.2857\times 10^{-10}\ \mathrm{m/N} \\ \nu = 10 \ \rightarrow \ L_p &= \frac{1-0.1}{(2.8\times 10+1.4)\times 10^9} = 3.0612\times 10^{-11}\ \mathrm{m/N} \end{aligned} \quad \text{(II-54)}$$

The overestimation of K_{PS_0} makes that the gain value L_P decreases. Consequently, the control action that corrects the displacements of PS and NS is less efficient. In fact, as shown in Fig. II-20 (c), the actual eigenvalue of the cases $\nu = 2.0$ and $\nu = 10$ are respectively equal to 0.4 and 0.85, instead of 0.1. The real rise time and the instantaneous error displayed in Fig. II-20 (d) and (e) are thus higher. Consequently, the curves of these cases follow less well the correct solution "F" and "u" in Fig. II-20 (a)-(b).

The effect of the *underestimation* is shown in Fig. II-21. The theory above demonstrated that the system could be unstable if the parameter ν was lower than a critical value ν_{min}. In this one-DOF example, ν_{min} can be calculated as follows:

$$\nu_{min} = \frac{(1-0.1)(2+1)-2}{2\times 2} = 0.175 \quad \text{(II-55)}$$

Fig. II-21 (a) and (b) shows the force and the displacement for the three following cases:

$$\begin{aligned} \nu = 1.0 \ \rightarrow \ L_p &= \frac{1-0.1}{(2.8\times 1.0+1.4)\times 10^9} = 2.1429\times 10^{-10}\ \mathrm{m/N} \\ \nu = 0.5 \ \rightarrow \ L_p &= \frac{1-0.1}{(2.8\times 0.5+1.4)\times 10^9} = 3.2143\times 10^{-10}\ \mathrm{m/N} \\ \nu = 0.1 \ \rightarrow \ L_p &= \frac{1-0.1}{(2.8\times 0.1+1.4)\times 10^9} = 5.3571\times 10^{-10}\ \mathrm{m/N} \end{aligned} \quad \text{(II-56)}$$

The gain value L_P increases with decreasing ν. The controller is thus more reactive. Fig. II-21 (d) shows that the error of the case $\nu = 0.5$ is in fact lower than the case $\nu = 1.0$. However, because of the initial negative eigenvalue, the rise time is higher at 20°C (see Fig. II-21 (e)) and decreases until the eigenvalue is positive around $t = 15$ min. The overshoot is not equal to 0 and is displayed in Fig. II-21 (f). The consequences on the results are nonetheless marginal. If $\nu = 0.1$, the underestimation is lower than the critical value. As can be seen in Fig. II-21, the system is unstable.

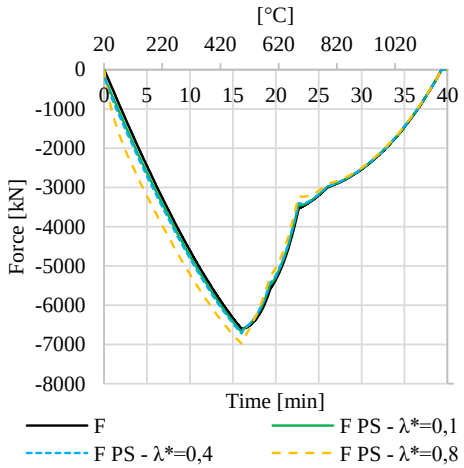

(a) Normal Force

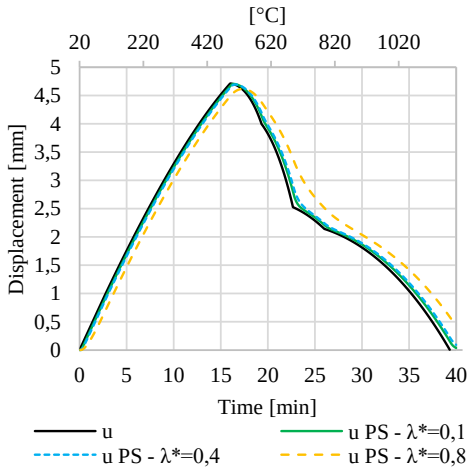

(b) Displacement

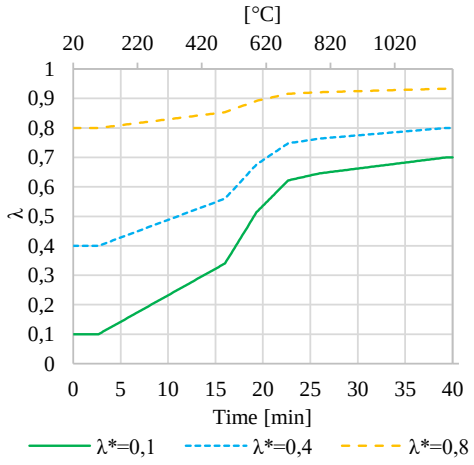

(c) Eigenvalue

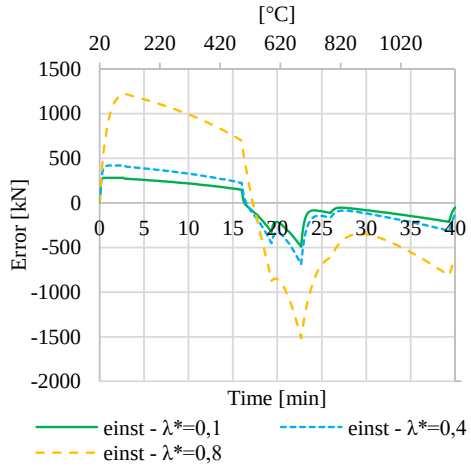

(d) Instantaneous error

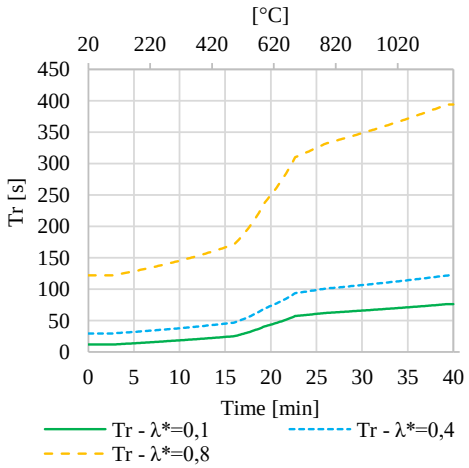

(e) Rise time

Fig. II-19 One-DOF example: λ^*=0.1, λ^*=0.4, λ^*=0.8

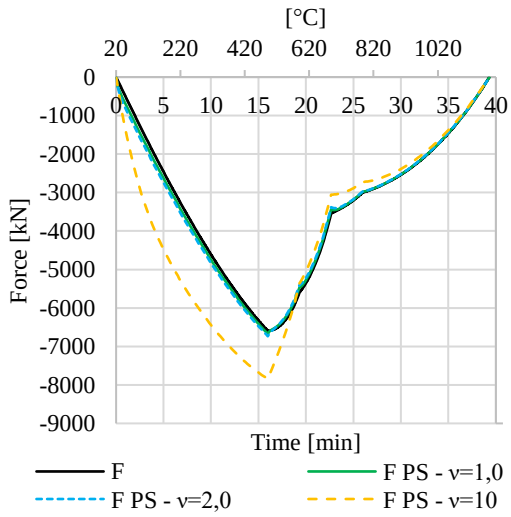

(a) Normal Force

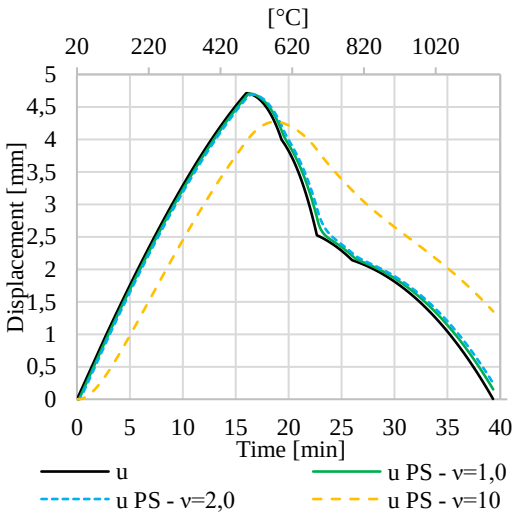

(b) Displacement

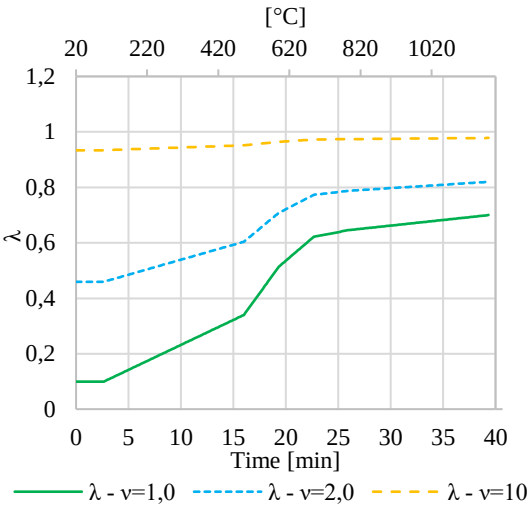

(c) Eigenvalue

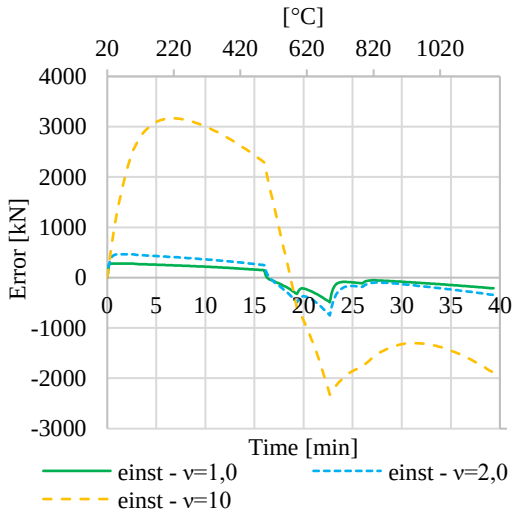

(d) Instantaneous error

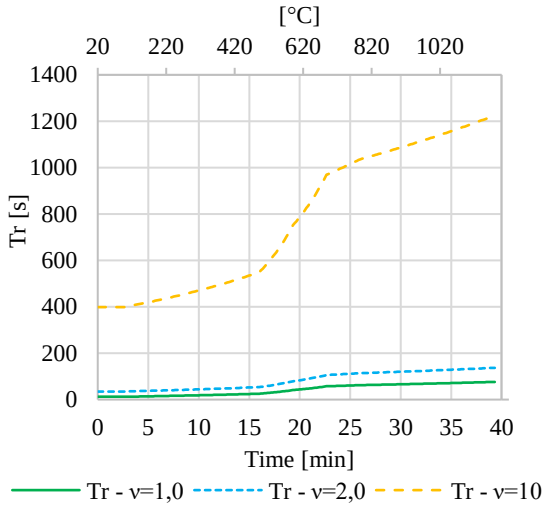

(e) Rise time

Fig. II-20 One-DOF example: ν=1.0, ν=2.0, ν=10

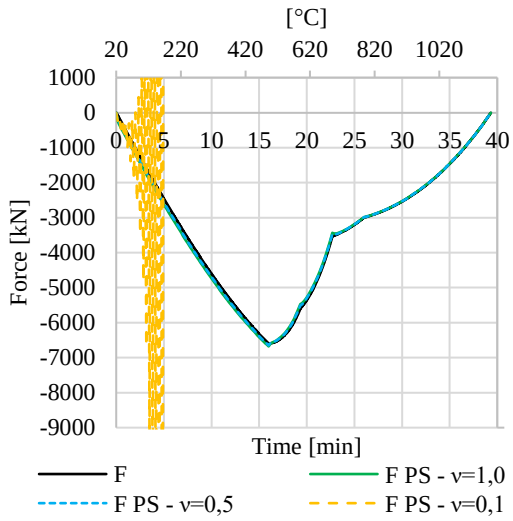

(a) Normal Force

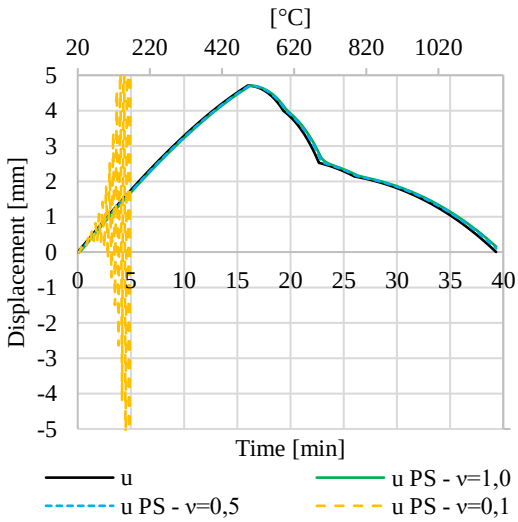

(b) Displacement

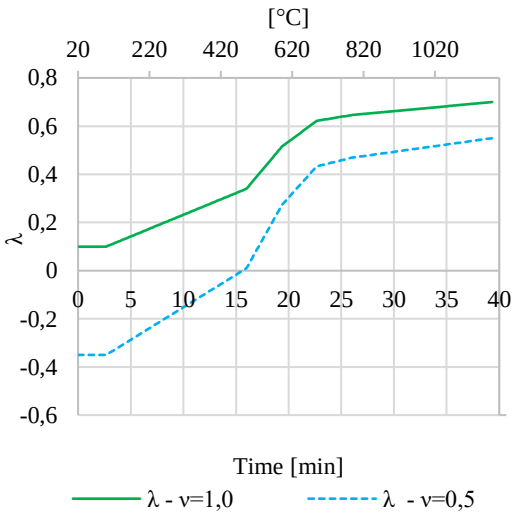

(c) Eigenvalue

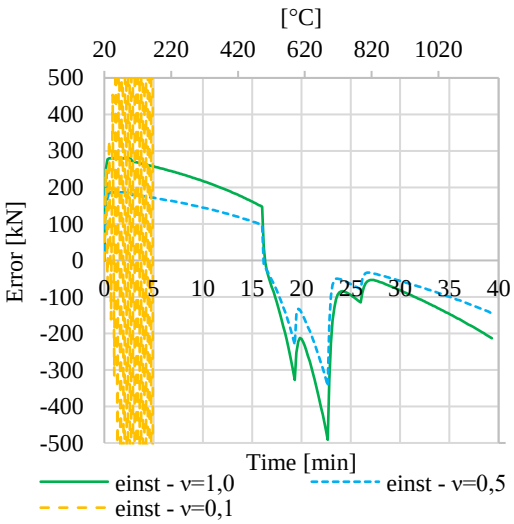

(d) Instantaneous error

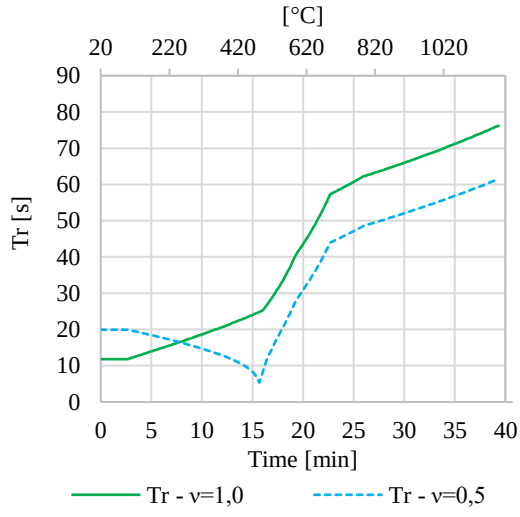

(e) Rise time

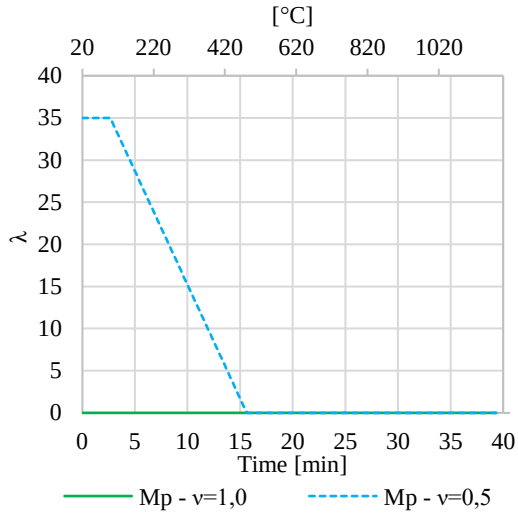

(f) Overshoot

Fig. II-21 One-DOF example: ν=1.0, ν=0.5, ν=0.1

II.4.6 Multi-DOF system

As for single DOF system, the gain matrix $\mathbf{L_P}$ must be designed to keep eigenvalues of the dynamics matrix **A** into the unit circle during the test. Given equation (II-29), $\mathbf{L_P}$ is acting as flexibility matrix (i.e., inverse of stiffness matrix). In fact, the new displacement increment is calculated by multiplying $\mathbf{L_P}$ to an unbalanced force vector $-\left(\mathbf{f}_{\mathrm{NS_i}} + \mathbf{f}_{\mathrm{PS_i}}\right)$.

As explained in Section II.2.5, to get around the problem of high-order system that contains many eigenvalues, the controller is designed in order to obtain dominant eigenvalues. High-order system are thus approximated to a first order (one dominant eigenvalue) or second order system (a pair of dominant eigenvalues) that can be linked to the parameter of the step response. In this research, high-order systems are approximated to a second order system with double eigenvalues (the others are set to 0).

To determine the d eigenvalues $\lambda_1, \lambda_2, \ldots \lambda_d$ of the state matrix $\mathbf{A} \in \mathbb{R}^{d\times d}$, the general equation that must be solved is the following:

$$|\mathbf{I}z - \mathbf{A}| = (z - \lambda_1)(z - \lambda_2) \ldots (z - \lambda_d) \tag{II-57}$$

The two polynomials are equal if their coefficients are equal. As the coefficient of the highest degree term is equal to 1, the system has d equations to solve. As $\mathbf{L_P}$ is diagonal, there are d unknowns, which makes the hypothesis of uncoupled DOFs convenient. The gain matrix is calculated using initial stiffness matrices and kept constant during the whole duration of the test.

During the test, the eigenvalues of the state matrix depend also on the evolution over time of $\left(\mathbf{K}_{\mathrm{PS_i}} + \mathbf{K}_{\mathrm{NS_i}}\right)$. Although the evolution of the stiffness of both substructures is not known a priori, it can be qualitatively described. Assuming that, in each matrix, all the elements are affected by the same factor. As for the single DOF system, $\mathbf{K}_{\mathrm{PS_i}}$ is simplified to $\alpha\mathbf{K}_{\mathrm{PS_0}}$ with real $\alpha \in [0; 1]$ and $\mathbf{K}_{\mathrm{NS_i}}$ is reduced to $\beta\mathbf{K}_{\mathrm{NS_0}}$ with real $\beta \in [0; 1]$. The simplified state space-representation is as follows:

$$\begin{gathered}\mathbf{u}_{\mathrm{PS_{i+1}}} = \left[\mathbf{I} - \mathbf{L_P}(\alpha\mathbf{K}_{\mathrm{PS_0}} + \beta\mathbf{K}_{\mathrm{NS_0}})\right]\mathbf{u}_{\mathrm{PS_i}} - \mathbf{L_p}\beta\mathbf{K}_{\mathrm{NS_0}}^{-1}\left(\mathbf{f}_{\mathrm{NS_i}}^{\mathrm{TH}} + \mathbf{f}_{\mathrm{PS_i}}^{\mathrm{TH}}\right) \\ \mathbf{y_i} = \mathbf{u}_{\mathrm{PS_i}}\end{gathered} \tag{II-58}$$

As for the single DOF system, one considers that the evolution of $\mathbf{K}_{\mathrm{NS}}$ is negligible and that $\beta = 1$. The state matrix $\mathbf{A_P}$ obtained with the proportional controller depends on α during the test and is written as:

$$\mathbf{A_P}(\alpha) = \left[\mathbf{I} - \mathbf{L_P}(\alpha\mathbf{K}_{\mathrm{PS_0}} + \mathbf{K}_{\mathrm{NS_0}})\right] \tag{II-59}$$

In the case of multi-DOF system, it is not possible to write stability conditions as for the single DOF system. However, one can observe some tendencies.

Two mathematical concepts will be necessary. The first concept is the definition of diagonally dominant matrices. A square matrix is said to be row/column diagonally dominant if for every row/column of the matrix, the magnitude of the diagonal entry in a row/column is larger than or equal to the sum of the magnitudes of all the other (non-diagonal) entries in that row/column. The matrix M is:

row diagonally dominant if: $$|m_{ii}| \geq \sum_{j\neq 1} |m_{ij}| \ \forall i \tag{II-60}$$

column diagonally dominant if: $$|m_{ii}| \geq \sum_{i\neq 1} |m_{ij}| \ \forall j \tag{II-61}$$

where m_{ij} denotes the entry in the i^{th} row and j^{th} column. The second concept is the "Gershgorin circles", that identify a region in the complex plane that contains all the eigenvalues of a complex square matrix. Let $M \in \mathbb{C}^{n\times n}$, m_{ij} be the entry in the i^{th} row and j^{th} column of M and D_i be the closest disk in the complex plane, centered at m_{ii} with radius equal to the row sum $r_i = \sum_{j\neq 1}|m_{ij}|$:

$$D_i = \{z \in \mathbb{C}: |z - m_{ii}| \leq r_i\} \equiv D(m_{ii}, r = r_i) \quad \text{(II-62)}$$

According to the Gershgorin circle theorem, all the eigenvalues of M lie in the union of the disks D_i for $i = 1, \dots, n$.

Concerning system (II-58), the following hypothesis are considered :

(1) $\mathbf{K}_{NS_0}$ and $\mathbf{K}_{PS_0}$ are symmetric and diagonally dominant matrices (row and column) with positive diagonal elements.

(2) $\alpha\mathbf{K}_{PS_0} + \mathbf{K}_{NS_0}$ is also a diagonally dominant matrix (row and column) with positive diagonal element.

(3) $\mathbf{L}_P$ acts as a flexibility matrix. Its terms are lower than the inverse of the diagonal term of $\alpha\mathbf{K}_{PS_0} + \mathbf{K}_{NS_0}$ and positive.

(4) $\mathbf{L}_P$ is computed with an exact estimation of $\mathbf{K}_{PS_0}$.

As $\mathbf{L}_P$ is diagonal and considering hypothesis (2) and (3), the matrix $\mathbf{L}_P(\alpha\mathbf{K}_{PS_0} + \mathbf{K}_{NS_0})$ is minimum a row diagonally dominant matrix[2] with terms that are lower than one. As $\mathbf{I}$ is the identity matrix, the dynamics matrix $\mathbf{A}_P(\alpha) = \mathbf{I} - \mathbf{L}_P(\alpha\mathbf{K}_{PS_0} + \mathbf{K}_{NS_0})$ has the following properties:

- The diagonal element is positive and lower than one.
- It is a minimum row diagonally dominant matrix[3].

In this case, the centre of the Gershgorin circles of the matrix $\mathbf{A}_P$ are on the positive real axis with value lower than one. Also, the radius of these circles are lower than the diagonal term of $\mathbf{A}_P$. Fig. II-22 shows an example of Gershgorin circles for the matrix $\mathbf{A}_P$, at the initial phase and considering that $\mathbf{K}_{PS_0}$ is well estimated.

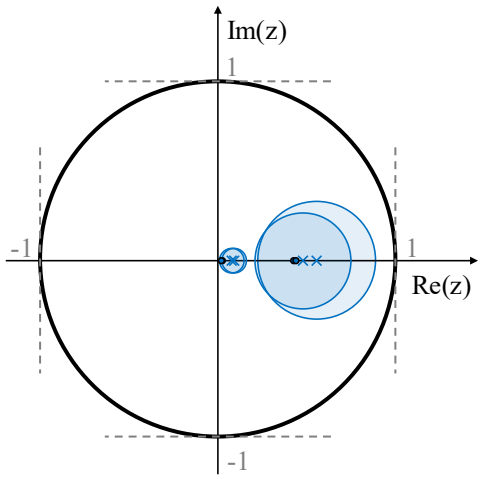

Fig. II-22 Gershgorin circles of the dynamics matrix at the initial phase

As for the single DOF system, the effect of the parameters α and ν on the location of the eigenvalues of $\mathbf{A}_P$ are analysed. During fire, α decreases from 1 to 0. As $\mathbf{A}_P$ varies from $\mathbf{I} - \mathbf{L}_P(\mathbf{K}_{PS_0} + \mathbf{K}_{NS_0})$ to $\mathbf{I} - \mathbf{L}_P\mathbf{K}_{NS_0}$, one can suppose that the value of the diagonal elements of $\mathbf{A}_P$ increases and the

[2] Demonstration in (Evmorfbpoulos s.d.), Lemma 1

[3] Demonstration in (Evmorfbpoulos s.d.), Lemma 2

value of the non-diagonal elements decreases. The centre of the Gershgorin circles moves to the right on real axis and the radius of these circles decreases.

This does not give a guarantee of stability, but it shows that the area where the eigenvalues can locate (union of Gershgorin circles) reduces favourably during the test as the radius of these circles decreases. The evolution is illustrated in Fig. II-23.

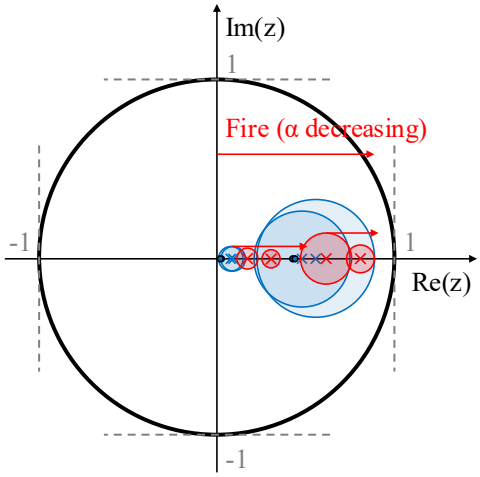

Fig. II-23 Gershgorin circles if α decreases from 1 to 0

The effect of ν can also be studied in the light of Gershgorin circles. As the single DOF system shows that an overestimation of the stiffness $\mathbf{K}_{PS_0}$ induces lower values of gain, one can suppose that the overestimation is translated by lower diagonal element in $\mathbf{L}_P$. As each diagonal element of $\mathbf{L}_P$ multiply each line of $\left(\alpha\mathbf{K}_{PS_0} + \mathbf{K}_{NS_0}\right)$, it involves that, the radius of the Gershgorin circles decreases and the centres moves to the right. If $\mathbf{L}_P$ is equal to zero, $\mathbf{A}_P$ is equal to the identity matrix. All eigenvalues are thus equal to one and the radius of the circles is equal to zero. One can see in Fig. II-24 that the region in the complex plane that contains all the eigenvalues has a favourable evolution if ν increases.

In case of underestimation of the stiffness, one can suppose that the diagonal element of $\mathbf{L}_P$ will increase. Consequently, the centre of the Gershgorin moves to the left and the radius of these circles increases. The region that includes the eigenvalues is thus larger and can move outside the unit circle, as shown in Fig. II-24. As for single DOF system, the underestimation of the stiffness of the PS can lead to a design of the controller that does not ensure stability.

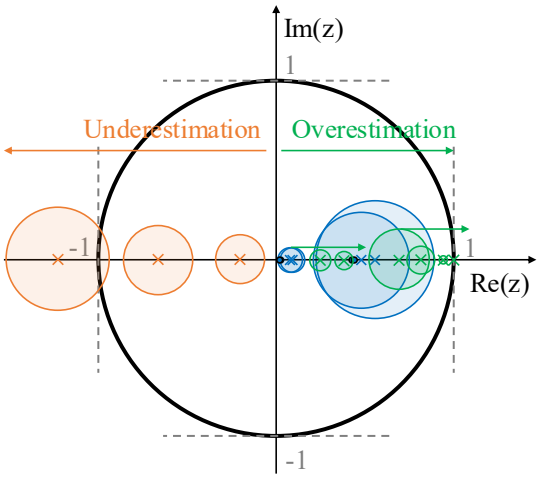

Fig. II-24 Effect of overestimation and underestimation in Gershgorin circles

II.4.7 Comments about methodology developed in (Sauca, Gernay, et al. 2018)

The methodology developed in (Sauca, Gernay, et al. 2018) is also a DCP and can be expressed as follows:

$$\mathbf{u}_{\mathrm{PS}_{i+1}} = \mathbf{u}_{\mathrm{PS}_i} - \left(\mathbf{K}_{\mathrm{PS}_0}^{\mathrm{EST}} + \mathbf{K}_{\mathrm{NS}_i}\right)^{-1}\left(\mathbf{f}_{\mathrm{PS}_i} + \mathbf{f}_{\mathrm{NS}_i}\right) \tag{II-63}$$

If $\mathbf{f}_{\mathrm{PS}_i}$ and $\mathbf{f}_{\mathrm{NS}_i}$ are substituted with equations (II-11) and (II-12), and using the compatibility of displacement, (II-63) yields the following state equation:

$$\begin{aligned}\mathbf{u}_{\mathrm{PS}_{i+1}} = &\left[\mathbf{I} - \left(\mathbf{K}_{\mathrm{PS}_0}^{\mathrm{EST}} + \mathbf{K}_{\mathrm{NS}_i}\right)^{-1}\left(\mathbf{K}_{\mathrm{PS}_i} + \mathbf{K}_{\mathrm{NS}_i}\right)\right]\mathbf{u}_{\mathrm{PS}_i} \\ &- \left(\mathbf{K}_{\mathrm{PS}_0}^{\mathrm{EST}} + \mathbf{K}_{\mathrm{NS}_i}\right)^{-1}\mathbf{K}_{\mathrm{NS}_i}^{-1}\left(\mathbf{f}_{\mathrm{NS}_i}^{\mathrm{TH}} + \mathbf{f}_{\mathrm{PS}_i}^{\mathrm{TH}}\right)\end{aligned} \tag{II-64}$$

It shows that the methodology is in fact using a proportional controller algorithm where the gain matrix $\mathbf{L_P}$ is a full matrix equal to:

$$\mathbf{L}_{\mathrm{P}} = \left(\mathbf{K}_{\mathrm{PS}_0}^{\mathrm{EST}} + \mathbf{K}_{\mathrm{NS}_i}\right)^{-1} \tag{II-65}$$

It can be observed that if $\mathbf{K}_{\mathrm{PS}_0}^{\mathrm{EST}} = \mathbf{K}_{\mathrm{PS}_0}$, the dynamics matrix at the initial phase is equal to the null matrix. The designed eigenvalue λ^* is thus equal to zero, that corresponds to a reactive system. For the single DOF system, equations of the previous sections are still valid but must be written with λ^* equal to 0:

$$\mathrm{L_P} = \frac{1-0}{\mathrm{K}_{\mathrm{PS}_i} + \mathrm{K}_{\mathrm{NS}_i}} = \frac{1}{\mathrm{K}_{\mathrm{PS}_0}^{\mathrm{EST}} + \mathrm{K}_{\mathrm{NS}_0}} \tag{II-66}$$

The thesis (Sauca 2017, p 116-132) studied the accuracy of the results as well as the possibility of instability in a single DOF system equivalent to the one shown in Fig. II-15. The PS was heated at a rate of 0.5°/s and the stiffness of the PS was degraded during the test due to the fire exposure (the parameter α was a function of temperature). The stiffness of the NS was constant. In Section 5.4.2 of the dissertation (Sauca 2017), a parametric study was performed to evaluate the impact of the estimated stiffness of the PS, $\mathrm{K}_{\mathrm{PS}_0}^{\mathrm{EST}}$, used in the calculation. $\mathrm{K}_{\mathrm{PS}_0}^{\mathrm{EST}}$ was also equal to $\nu\mathrm{K}_{\mathrm{PS}_0}$. Five values of ν were tested, $[0.01; 0.1; 1.5; 10; 50]$, for two stiffness ratios $\mathrm{R} = \mathrm{K}_{\mathrm{NS}_0}/\mathrm{K}_{\mathrm{PS}_0}$, respectively 2 and 0.5. One can notice that $\mathrm{R} = 1/\mathrm{r}$.The displacement were updated every second. In the case of $\mathrm{R} = 2$ ($\mathrm{r} = 0.5$), the process was stable for the five values of ν. This can be easily explained through the hereunder equation that gives the critical value of $\nu_{\min}$:

$$\nu_{\min} = \frac{(1-0)(0.5+1)-2}{2\times 0.5} \Leftrightarrow \nu_{\min} = -0.5 \tag{II-67}$$

The critical value $\nu_{\min}$ is negative, which means that the system is stable for $\nu \in \mathbb{R}^+$. An example of those results is given in Fig. II-25 for $\mathrm{R} = 2$ and $\nu = 0.1$. Compatibility of displacements and equilibrium of the forces of PS (red curve) and NS (green markers) are satisfied and the correct solution is reproduced (black line). The grey curves are not relevant and are the margin of error.

If $\mathrm{R} = 0.5$ ($\mathrm{r} = 2$), the process was not stable for $\nu = 0.1$ and $\nu = 0.01$. The same verification can be done:

$$\nu_{\min} = \frac{(1-0)(2+1)-2}{2\times 2} = 0.25 \Leftrightarrow \nu_{\min} = 0.25 \tag{II-68}$$

As ν must be higher than 0.25, the HFT cannot be stable for $\nu = 0.1$ and $\nu = 0.01$. The result for $R = 2$ and $\nu = 0.1$ is shown in Fig. II-26.

The overestimation was not problematic as planned by the above theory.

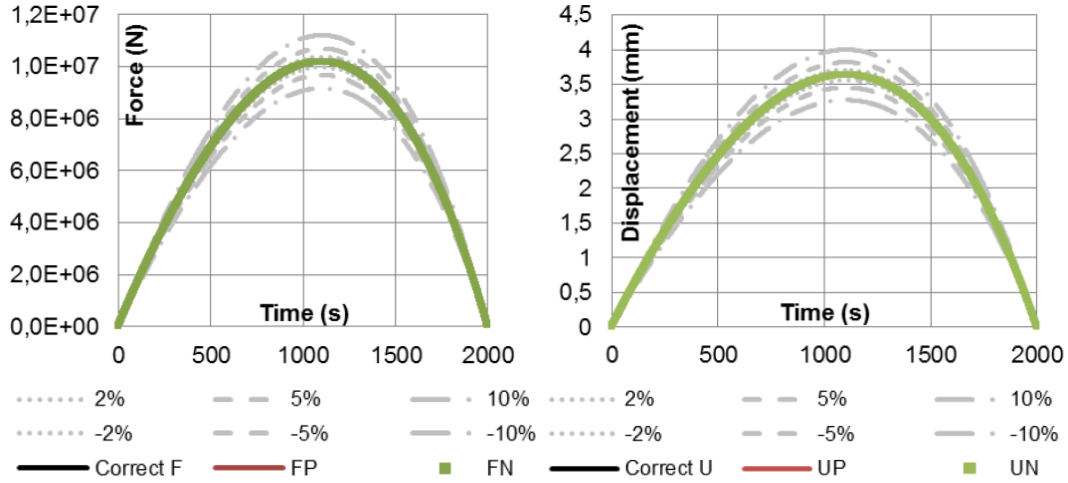

Fig. II-25 Force and displacement when R=2 and $\nu = 0.1$ (Sauca 2017, p 127)

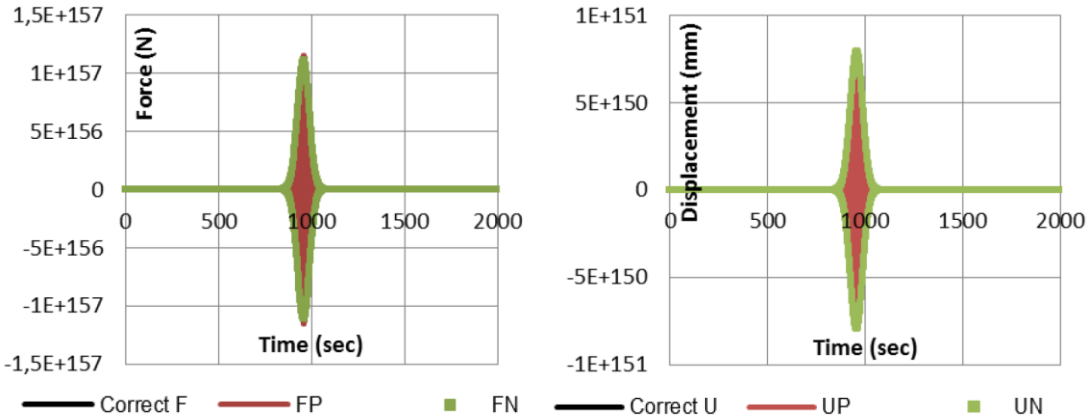

Fig. II-26 Force and displacement when $R = 0.5$ and $\nu = 0.1$ (Sauca 2017, p 126)

(Sauca 2017, p 166-170) also presented a case of study that consisted of a concrete multi-storey building. The PS was a concrete beam simulated in SAFIR® extracted from the last floor of the frame and the NS was a predetermined matrix that replaced the behaviour of the remaining structure. The procedure is described in Section I.3.7 and the complete structure is illustrated in Fig. II-27. PS and NS are shown in Fig. II-28. More details about the design of this frame and the substructures can be found in Section 6.2.1 of the thesis (Sauca 2017). The initial stiffness matrices of PS and NS were as follows (in m, rad, N):

$$\mathbf{K}_{\mathrm{PS}_0} = 10^6 \begin{bmatrix} 479 & 0 & 0 \\ 0 & 25.60 & 12.80 \\ 0 & 12.80 & 25.60 \end{bmatrix} \qquad \mathbf{K}_{\mathrm{NS}_0} = 10^6 \begin{bmatrix} 10.50 & -11.70 & 8.26 \\ -11.70 & 64.80 & -8.72 \\ 8.26 & -8.72 & 63.60 \end{bmatrix} \qquad \text{(II-69)}$$

A parametric study was performed in (Sauca 2017) to evaluate the effect of the estimation $\mathbf{K}_{\mathrm{PS}_0}^{\mathrm{EST}}$ in the procedure. The studied cases were the following:

- Case 1: $\mathbf{K}_{\mathrm{PS}_0}^{\mathrm{EST}} = 5\mathbf{K}_{\mathrm{PS}_0}$
- Case 2: $\mathbf{K}_{\mathrm{PS}_0}^{\mathrm{EST}} = 10\mathbf{K}_{\mathrm{PS}_0}$
- Case 3: $\mathbf{K}_{\mathrm{PS}_0}^{\mathrm{EST}} = 50\mathbf{K}_{\mathrm{PS}_0}$
- Case 4: $\mathbf{K}_{\mathrm{PS}_0}^{\mathrm{EST}} = 0.5\mathbf{K}_{\mathrm{PS}_0}$

Every time step (1 s) a new displacement vector $\mathbf{u}_{PS_{i+1}}$ was calculated and applied as new boundary conditions to the virtual beam. Table II-6 sums up the observations for each case. The graphs with the results (axial displacement, rotations, normal force, bending moments) can found in Section 6.4.2 of the thesis (Sauca 2017). Fig. II-29 only shows the axial force which illustrates representatively the effect of the estimation.

The observations of Table II-6 can be explained under the light of control theory. For the multi-DOF system, as $\mathbf{L}_p$ is a full matrix, the previous developments using the Gershgorin circles are not valid. However, one can use the simplified matrix:

$$\mathbf{A}_P(\alpha) = \left[\mathbf{I} - \mathbf{L}_P(\alpha\mathbf{K}_{PS_0} + \mathbf{K}_{NS_0})\right] = \mathbf{I} - \left(\mathbf{K}_{PS_0}^{EST} + \mathbf{K}_{NS_0}\right)^{-1}(\alpha\mathbf{K}_{PS_0} + \mathbf{K}_{NS_0}) \qquad \text{(II-70)}$$

Fig. II-30 shows the poles location for each case at the beginning of the test ($\alpha = 1$). One can notice that all poles are inside the unit circle in complex plane, which is expected because the four cases were stable. The loss of equilibrium is case 2 and 3 is explained by the fact that the computed poles have three poles with large values. Consequently, as the rise time increases with the value of the poles, the controler is less reactive as planned by the theory. The oscillations of case 4 are due to the negative poles. The controller is also highly reactive and can ensure the equilibrium of the forces.

During the test, as α decreases from 1 to 0, the eigenvalues of $\mathbf{A}_P(\alpha)$ can also be calculated explicitely. Fig. II-31 shows the location of the poles for each case for some values of α. The poles do not go outside the unit circle, which indicates that the system is stable as observed in (Sauca 2017, p 166-170).

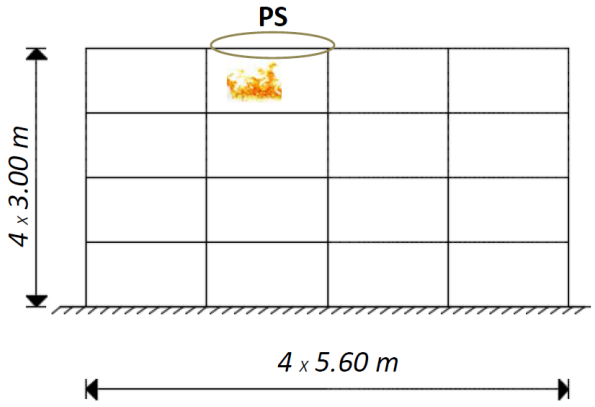

Fig. II-27 Case of study (Sauca 2017, p 145): Complete structure

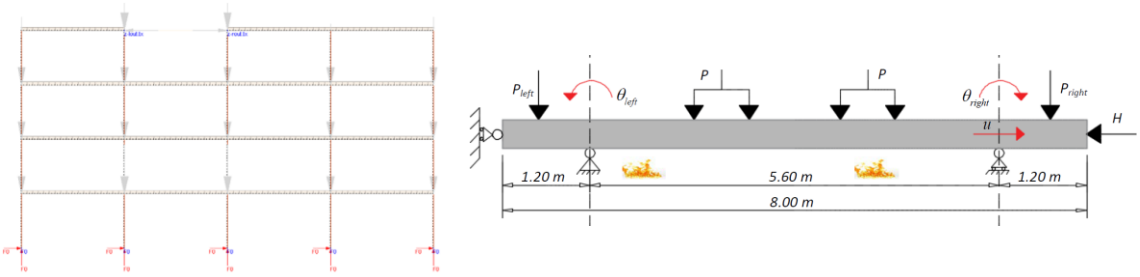

(a) NS (Sauca 2017, p 143) *(b) PS (Sauca 2017, p 145)*

Fig. II-28 Case of study (Sauca 2017): Substructures

Table II-6

Case 1	The system is stable. The equilibrium of forces is satisfied
Case 2	The system is stable. There is a noticeable gap between the forces.
Case 3	The system is stable. Important loss of equilibrium in the axial force.
Case 4	The system is stable. The equilibrium of forces is satisfied. However, oscillations were observed at the beginning of the test.

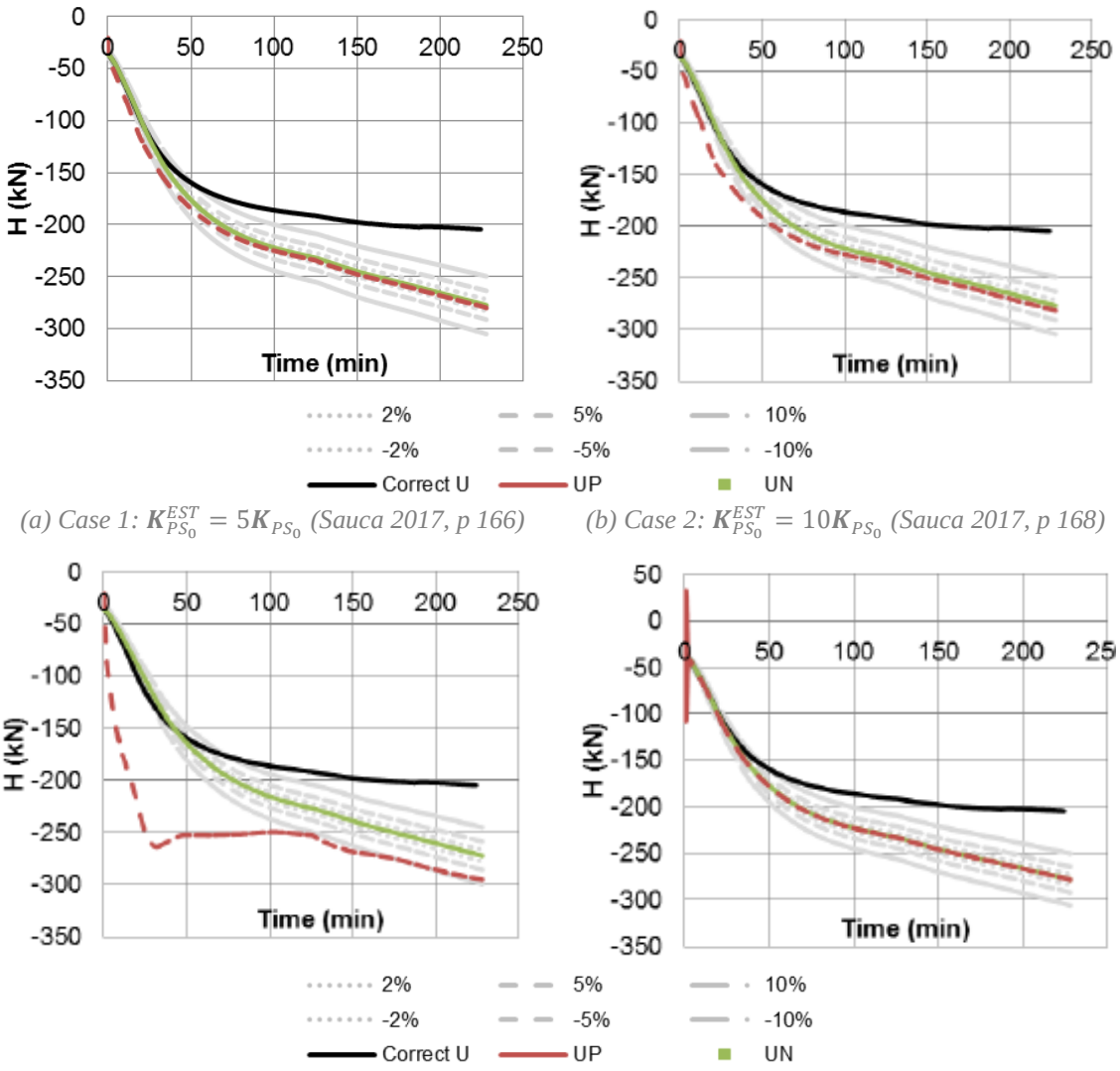

(a) Case 1: $\boldsymbol{K}_{PS_0}^{EST} = 5\boldsymbol{K}_{PS_0}$ (Sauca 2017, p 166) *(b) Case 2: $\boldsymbol{K}_{PS_0}^{EST} = 10\boldsymbol{K}_{PS_0}$ (Sauca 2017, p 168)*

(c) Case 3: $\boldsymbol{K}_{PS_0}^{EST} = 50\boldsymbol{K}_{PS_0}$ (Sauca 2017, p 169) *(d) Case 4: $\boldsymbol{K}_{PS_0}^{EST} = 0.5\boldsymbol{K}_{PS_0}$ (Sauca 2017, p 170)*

Fig. II-29 Normal force of the PS (Sauca 2017, p 168-170) in cases 1-4

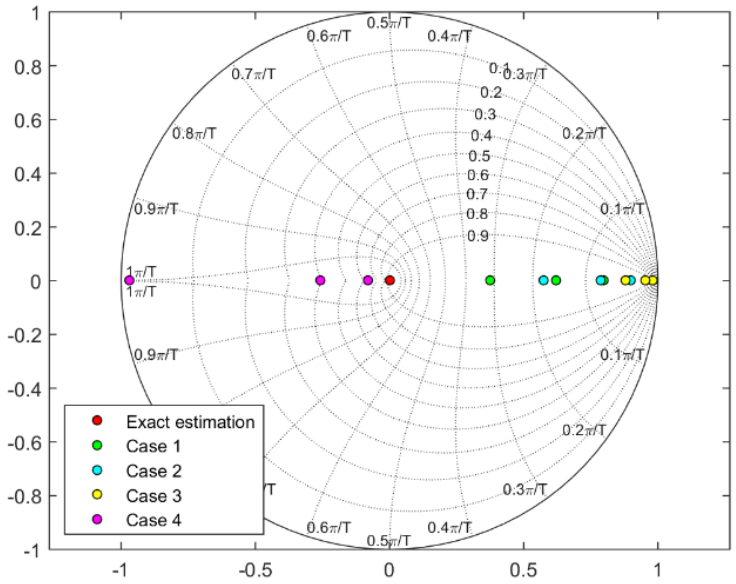

Case 1:	Case 3:
0.7975	0.9797
0.5793	0.9440
0.4286	0.9019

Case 2:	Case 4:
0.8986	-0.9691
0.7560	-0.2079
0.6279	-0.1035

Fig. II-30 Poles location for cases 1-4 at the beginning of the virtual test of (Sauca 2017)

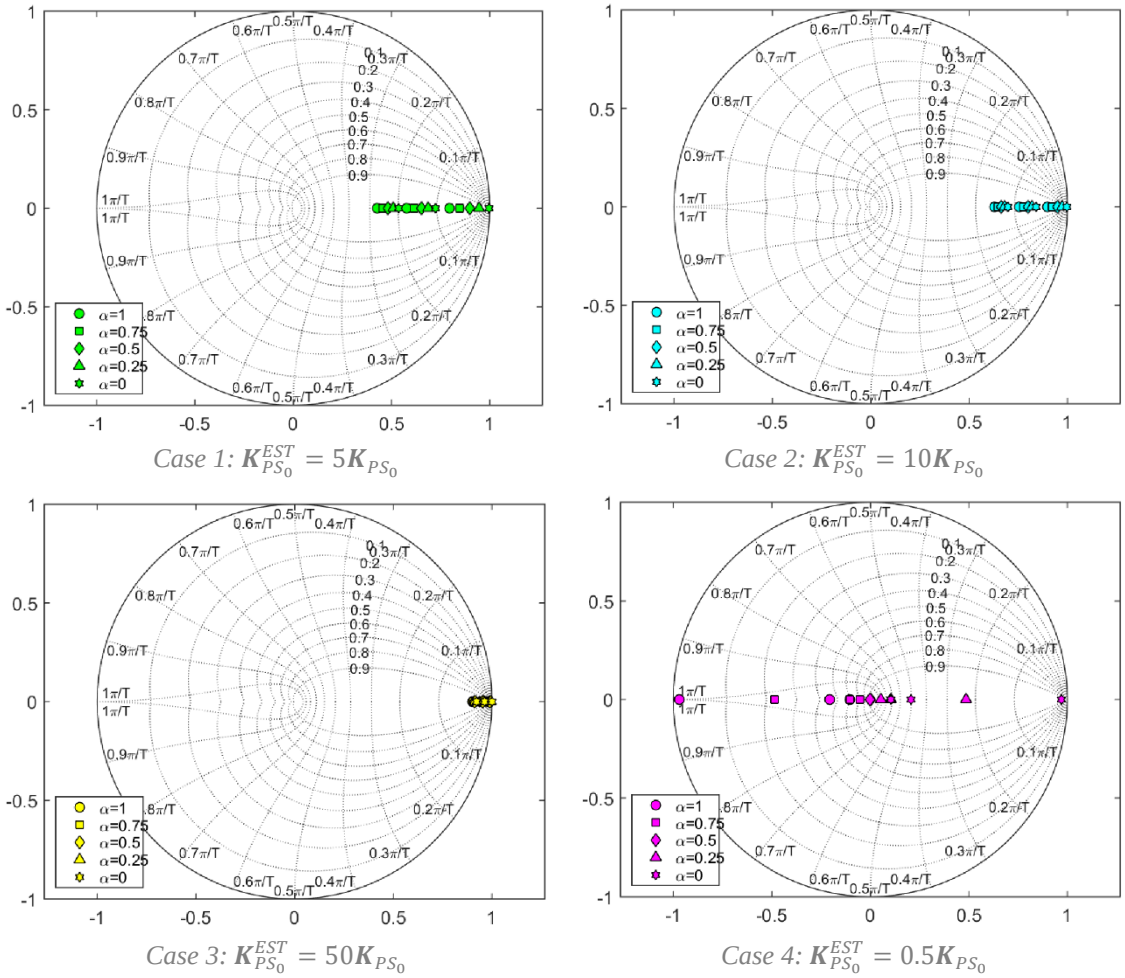

Case 1: $\boldsymbol{K}_{PS_0}^{EST} = 5\boldsymbol{K}_{PS_0}$ *Case 2:* $\boldsymbol{K}_{PS_0}^{EST} = 10\boldsymbol{K}_{PS_0}$

Case 3: $\boldsymbol{K}_{PS_0}^{EST} = 50\boldsymbol{K}_{PS_0}$ *Case 4:* $\boldsymbol{K}_{PS_0}^{EST} = 0.5\boldsymbol{K}_{PS_0}$

Fig. II-31 Poles location for cases 1-4 during the virtual test of (Sauca 2017)

II.4.8 Discussion

Proportional control is the simplest of the PID controller form and is easy to design. However, as the controller is limited to one gain matrix, it results in two major drawbacks.

First, the controller presents a tendency for offset. Offset is a continuous difference between a set point and the input of the loop. A linear proportional controller cannot correct this error and is in fact not adapted for handling prolonged changes, nor sudden variation. In HFT, both substructures are affected by a fire that is a continuous disturbance and even if the changes are relatively slow, failure can be sudden.

The second drawback is that for a same value of error between interface forces, the correction of the displacement is the same even if the properties of the system have changed because the gain matrix is designed given the initial parameters and is kept constant during the whole duration of the test. However, the system that is controlled is non-linear and thus the initial gain will not be appropriate during the whole duration of the test.

This method issue is pointed out through the methodology of (Sauca, Gernay, et al. 2018) in (Schulthess, Neuenschwander et Mosalam, et al. 2020) in the case of single DOF system. PS is an elastic perfect plastic constitutive model with temperature-dependent Young's modulus and 0.2% yield strength degradation, and NS is elastic. If one DOF is controlled, (Sauca, Gernay, et al. 2018) and the proportional controller developed in Section II.4.5 are equivalent. The trend of the results is illustrated in Fig. II-32 (a) and (b). u_{ABQ} and F_{ABQ} are respectively the displacement and force obtained by the numerical simulation of the single DOF system in ABAQUS®. Four numerical simulations were performed for four different time increments and the hereunder graphs show the inaccuracies of the solution given by the algorithm of (Sauca, Gernay, et al. 2018) when the stiffness is degraded. This issue is mitigated if the time step is equal to 1s, which is practically difficult to reach, especially if the NS is a large nonlinear structure. The same result can be obtained with the one-DOF example presented in Section II.4.5. Considering $\lambda^* = 0.1$, Fig. II-33 (a) and (b) shows the force and the displacement for several update times T: 10s, 30s and 60s. The observations are similar to Fig. II-32: the curves with the highest time step do not fit the correct solution. In fact, the rise time shown in Fig. II-33 (c) increase with the update time according to equation (II-3). Consequently, the reactivity of the controller decreases and the instantaneous error increases (Fig. II-33 (d)). (Schulthess, Neuenschwander et Mosalam, et al. 2020) used an algorithm similar to (Sauca, Gernay, et al. 2018) in their published one-DOF test but improved the results by performing several iterations during a time step, with a temperature that was maintained constant (see Section I.3.8). This is however not possible for standard fire test.

To overcome this limitation, non-linear control can be used. However, the mathematics of non-linear control theory remain a work in progress, with the current theoretical frameworks being more difficult, less general and targeting only narrow categories of systems.

A second solution is the use of adaptive control, especially, based on discrete-time process identification of the stiffness of both substructures. It aims to update the gain matrix during the test by estimating the physical property of the PS. This compensation scheme was proposed in (Qureshi, Khorasani et Gernay 2019) that calculates the instantaneous secant stiffness of the PS by applying the Broyden update (Section I.3.10). This method was validated numerically for a one DOF system and is still in progress. Nevertheless, the update of the stiffness of the PS is potentially hazardous because the behaviour of the tested element is unknown.

To address the shortcomings of proportional control more thoroughly, an alternative type of controller can be used, namely a proportional integral controller. The latter is proposed here below in the framework of HFT.

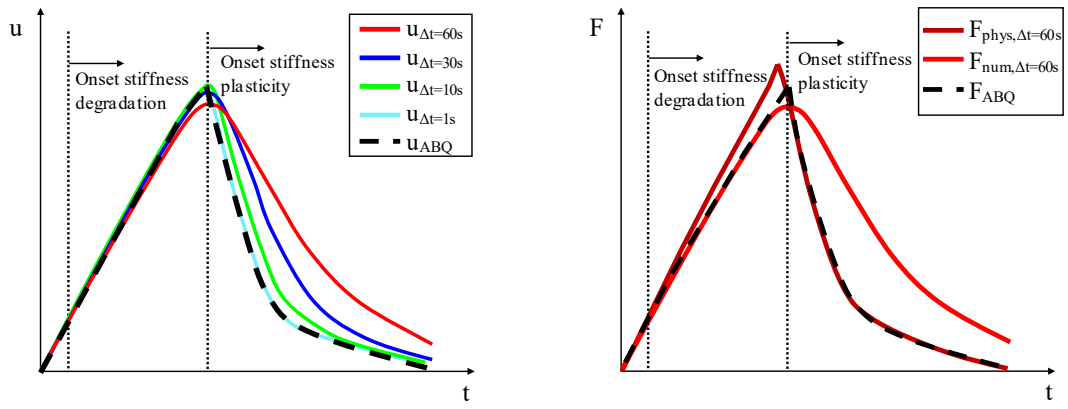

(a) Simulated displacements for four different time increment and correct solution u_{ABQ}

(b) Simulated interface forces obtained using a time increment and the correct solution F_{ABQ}

Fig. II-32 Adapted from (Schulthess, Neuenschwander et Mosalam, et al. 2020)

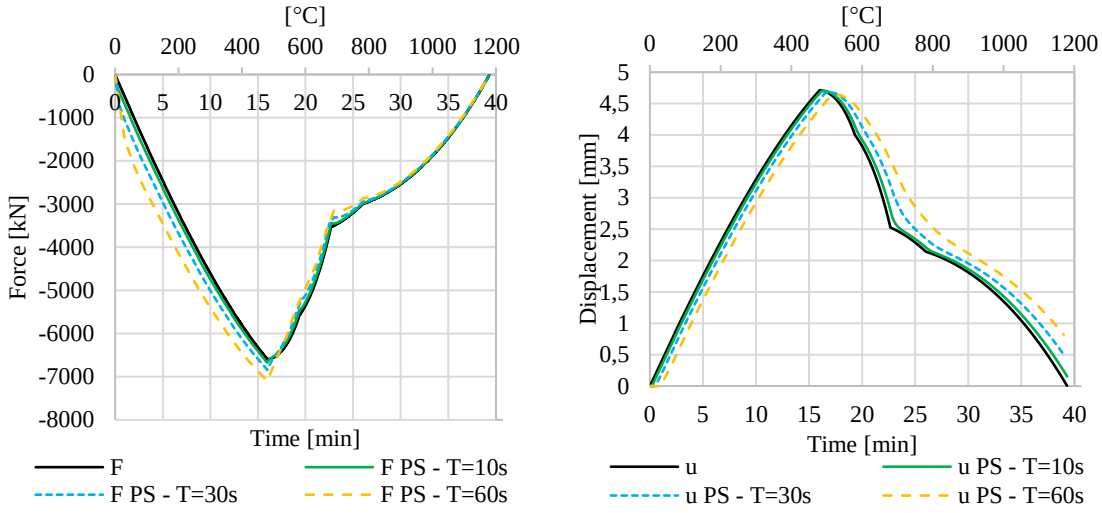

(a) Normal Force

(b) Displacement

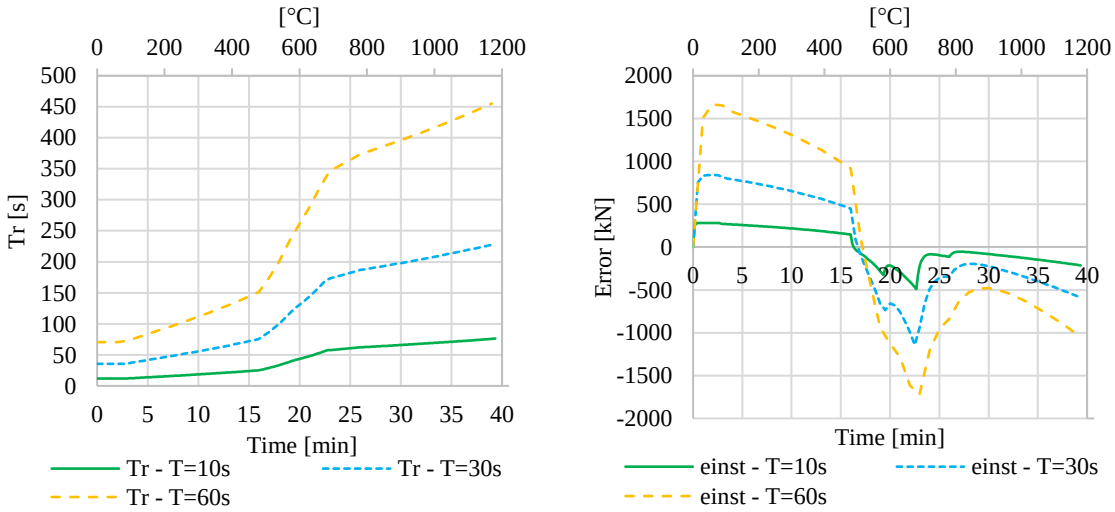

(c) Rise time

(d) Instantaneous error

Fig. II-33 One-DOF example: 10s, 30s, 60s

II.5 Linear proportional integral controller

This Section discusses the case of a proportional integral controller. This controller is made of two components:

- A proportional action that calculates the difference between the process variable signal and the set point signal, which is called as an error.
- An integral action that calculates the integral of error signal over time (history of the error).

As the proportional action measures *how far* the process variable (in this case the displacement) is deviating from the set point, the integral action decides *how fast* to move the output. The control law is:

$$\begin{aligned} \mathbf{x}_{i+1} &= \mathbf{x}_i + \mathbf{L}_P \mathbf{e}_i^{inst} + \mathbf{L}_J \mathbf{j}_i \\ \mathbf{j}_{i+1} &= \mathbf{j}_i + \mathbf{e}_i^{inst} \end{aligned} \tag{II-71}$$

$\mathbf{e}_i^{inst} \in \mathbb{R}^{d\times 1}$ is the instantaneous error and $\mathbf{j}_i \in \mathbb{R}^{d\times 1}$ is the sum of $\mathbf{e}_i^{inst}$ over time. $\mathbf{L}_P \in \mathbb{R}^{d\times d}$ and $\mathbf{L}_J \in \mathbb{R}^{d\times d}$ are the gain matrices of the proportional integral controller. The advantage of this controller is it is fast acting and immediate. Moreover, if the characteristics of the system change, the integral term allows larger corrections.

The proportional integral control is introduced as follows in the HFT. The displacement $\mathbf{u}_{PS}$ is corrected at every time step by means of a term proportional to the instantaneous error and an integral term that considers the history of this error. As in Section II.4.4, the displacement $\mathbf{u}_{PS}$ is corrected using an instantaneous error $\mathbf{e}_i^{inst}$ equal to $-\left(\mathbf{f}_{NS_i} + \mathbf{f}_{PS_i}\right)$. The basic equation is as:

$$\begin{aligned} \mathbf{u}_{PS_{i+1}} &= \mathbf{u}_{PS_i} - \mathbf{L}_P\left(\mathbf{f}_{NS_i} + \mathbf{f}_{PS_i}\right) + \mathbf{L}_J \mathbf{j}_i \\ \mathbf{j}_{i+1} &= \mathbf{j}_i - \left(\mathbf{f}_{NS_i} + \mathbf{f}_{PS_i}\right) \end{aligned} \tag{II-72}$$

Equations (II-72) can be transformed by substituting $\mathbf{f}_{PS_i}$ and $\mathbf{f}_{NS_i}$ with equations (II-11) and (II-12). With $\mathbf{u}_{NS_i} = \mathbf{u}_{PS_i}$, a new state equation can be established as follows:

$$\begin{aligned} \begin{bmatrix} \mathbf{u}_{PS_{i+1}} \\ \mathbf{j}_{i+1} \end{bmatrix} &= \begin{bmatrix} \mathbf{I} - \mathbf{L}_P(\mathbf{K}_{PS_i} + \mathbf{K}_{NS_i}) & \mathbf{L}_J \\ -(\mathbf{K}_{PS_i} + \mathbf{K}_{NS_i}) & \mathbf{I} \end{bmatrix} \begin{bmatrix} \mathbf{u}_{PS_i} \\ \mathbf{j}_i \end{bmatrix} + \begin{bmatrix} -\mathbf{L}_P\left(\mathbf{f}_{NS_i}^{TH} + \mathbf{f}_{PS_i}^{TH}\right) \\ -\left(\mathbf{f}_{NS_i}^{TH} + \mathbf{f}_{PS_i}^{TH}\right) \end{bmatrix} \\ \mathbf{y}_i &= \mathbf{u}_{PS_i} \end{aligned} \tag{II-73}$$

$\mathbf{I} \in \mathbb{R}^{d\times d}$ is the identity matrix. The state variables of the system are the controlled displacements of the PS $\mathbf{u}_{PS}$ and the integral term $\mathbf{j}$. $\mathbf{L}_P$ and $\mathbf{L}_J$ are designed based on the eigenvalues or poles of the system. These eigenvalues are chosen following the desired value of the parameters of the step response of the system: rise time, settling time and overshoot. As equation (II-29), this state is not limited to non-floating domain. Fig. II-34 illustrates the procedure.

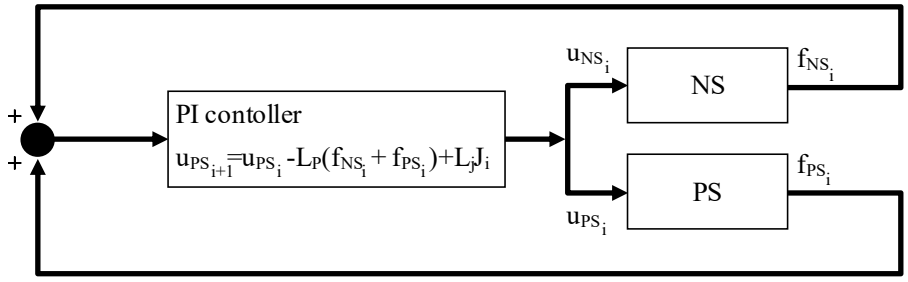

Fig. II-34 Block diagram of the displacement control procedure - Subsystems in parallel

II.5.1 Single DOF system

In this Section, the conditions of stability are explicitly developed for a single DOF system. The two substructures are described as two springs with stiffness K_{PS} and K_{NS} as shown in Fig. II-35.

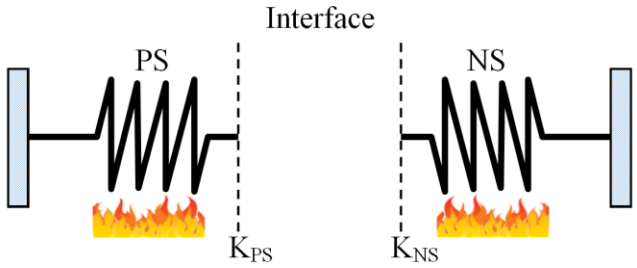

Fig. II-35 Single DOF system

The system is stable if the eigenvalues of their state matrix lie into the unit circle in the complex plan. The gains L_P and L_j must be designed to fulfil this condition. Thus, the eigenvalues of the state matrix depend on the evolution over time of $(K_{PS_i} + K_{NS_i})$. As in Section II.4.4, one considers that during the test, K_{PS_i} decreases as αK_{PS_0} with real $\alpha \in [0; 1]$ and K_{NS_i} can be reduced to βK_{NS_0} with real $\beta \in [0; 1]$. Equation (II-74) is rewritten:

$$\begin{bmatrix} u_{PS_{i+1}} \\ J_{i+1} \end{bmatrix} = \begin{bmatrix} I - L_P(\alpha K_{PS_0} + \beta K_{NS_0}) & L_J \\ -(\alpha K_{PS_0} + \beta K_{NS_0}) & I \end{bmatrix} \begin{bmatrix} u_{PS_i} \\ J_i \end{bmatrix} + \begin{bmatrix} -L_P\left(F_{NS_i}^{TH} + F_{PS_i}^{TH}\right) \\ -\left(F_{NS_i}^{TH} + F_{PS_i}^{TH}\right) \end{bmatrix} \quad \text{(II-74)}$$

The conditions of stability can be expressed using the characteristic polynomial $|\mathbf{I}z - \mathbf{A}|$ of the state matrix **A** because the roots of this second-degree polynomial are the eigenvalues of this matrix. For the single DOF system (II-74), the polynomial $|\mathbf{I}z - \mathbf{A}|$ and its roots are as follows:

$$z^2 + z\left(L_P\left(\alpha K_{PS_0} + \beta K_{NS_0}\right) - 2\right) - \left(L_P - L_J\right)\left(\alpha K_{PS_0} + \beta K_{NS_0}\right) + 1 \quad \text{(II-75)}$$

$$z = -\frac{L_P}{2}\left(\alpha K_{PS_0} + \beta K_{NS_0}\right) + 1 \pm \frac{1}{2}\sqrt{L_P^2\left(\alpha K_{PS_0} + \beta K_{NS_0}\right)^2 - 4L_J\left(\alpha K_{PS_0} + \beta K_{NS_0}\right)} \quad \text{(II-76)}$$

The module of these roots must be lower than 1. There are three cases: a real double root, two complex conjugate roots and two real distinct roots. Equations (II-77), (II-78) and (II-79) shows the condition of stability for each case:

Real double root	$0 \le L_P(\alpha K_{PS_0} + \beta K_{NS_0}) \le 4$	(II-77)
Two complex conjugate roots	$L_P^2\left(\alpha K_{PS_0} + \beta K_{NS_0}\right) - \left(L_P + L_J\right) \le 0$	(II-78)
Two real distinct roots	$L_J\left(\alpha K_{PS_0} + \beta K_{NS_0}\right) \ge 0$ $\left(2L_P + L_J\right)\left(\alpha K_{PS_0} + \beta K_{NS_0}\right) \le 4$	(II-79)

The equations (II-77)-(II-79) highlight that the stability conditions are fulfilled for α and β varying from 0 to 1, if L_P and L_J are designed as the inequalities are verified, at the beginning of test.

The proportional integral controller is usually designed with eigenvalues that are real (no overshoot) and positive (no oscillation). As the characteristic polynomial is a second-degree polynomial, one considers a second order system. The Section II.2.5 showed that these systems are designed with a double eigenvalue. Thus, one assumes that L_P and L_J are designed to fix two real roots, λ_1^* and λ_2^*, that are equal to a positive real number λ^* (chosen by the user given the desired rise time as shown in equation (II-35)). The following equations give the relationships between the gain values L_P and L_J, the designed eigenvalue λ^* and the initial stiffness of NS and PS:

$$L_P = 2\frac{1-\lambda^*}{K_{PS_0}^{EST} + K_{NS_0}} \tag{II-80}$$

$$L_J = \frac{(1-\lambda^*)^2}{K_{PS_0}^{EST} + K_{NS_0}} \tag{II-81}$$

One can notice that L_P and L_J are not designed with the real stiffness K_{PS_0}, but with an estimated value $K_{PS_0}^{EST}$. As for the proportional controller, it involves that the location of the eigenvalues during the test is not necessary the one defined by the user. The eigenvalues, λ_1 and λ_2, that are reached during the test are determined with equation (II-76) with exact stiffness K_{PS_0} and considering that L_P and L_J are calculated using equations (II-80) and (II-81) with estimated stiffness $K_{PS_0}^{EST}$. Considering $\beta = 1$, $K_{PS_0}^{EST} = \nu K_{PS_0}$ and a non-floating NS (in order to use the ratio of $r = K_{PS_0}/K_{NS_0}$), the resulting eigenvalues are shown hereunder:

$$\lambda_1 = 1 - (1-\lambda^*)\left(\frac{\alpha r+1}{\nu r+1}\right) + (1-\lambda^*)\sqrt{\left(\frac{\alpha r+1}{\nu r+1}\right)^2 - \left(\frac{\alpha r+1}{\nu r+1}\right)} \tag{II-82}$$

$$\lambda_2 = 1 - (1-\lambda^*)\left(\frac{\alpha r+1}{\nu r+1}\right) - (1-\lambda^*)\sqrt{\left(\frac{\alpha r+1}{\nu r+1}\right)^2 - \left(\frac{\alpha r+1}{\nu r+1}\right)} \tag{II-83}$$

The analysis of the sign of the expression under the square root gives that $\left(\frac{\alpha r+1}{\nu r+1}\right)^2 - \left(\frac{\alpha r+1}{\nu r+1}\right)$ is negative for $\alpha \in [-\frac{1}{r}, \nu]$. As α is a positive real number, λ_1 and λ_2 are complex conjugate if $\alpha \in [0, \nu]$ because:

$$\left(\frac{\alpha r+1}{\nu r+1}\right)^2 - \left(\frac{\alpha r+1}{\nu r+1}\right) < 0 \quad \text{if } \alpha \in [0, \nu] \tag{II-84}$$

One will approach separately the case of the overestimation and the underestimation.

Overestimation $\nu > 1$

As $\nu > 1$ and $\alpha \in [0; 1]$, λ_1 and λ_2 are complex conjugate according to equation (II-84). The real part is thus equal to:

$$\mathrm{Re}(\lambda_1) = \mathrm{Re}(\lambda_2) = 1 - (1-\lambda^*)\left(\frac{\alpha r+1}{\nu r+1}\right) \tag{II-85}$$

One can observe that $\mathrm{Re}(\lambda_1)$ and $\mathrm{Re}(\lambda_2)$ are equal to the function (II-38) related to the proportional controller. The previous conclusion of Section II.4 is thus valid here: in case of overestimation, $\mathrm{Re}(\lambda)$ is included in the interval $[0; 1]$ for any value of α.

The imaginary part of the two roots can be written as follows:

$$\mathrm{Im}(\lambda_1) = -\mathrm{Im}(\lambda_2) = (1-\lambda^*)\sqrt{\left(\frac{\alpha r+1}{\nu r+1}\right)^2 - \left(\frac{\alpha r+1}{\nu r+1}\right)} \tag{II-86}$$

As $\lambda^* \in [0; 1]$ and $\nu > \alpha$, $(1-\lambda^*)$ and $\sqrt{\left(\frac{\alpha r+1}{\nu r+1}\right)^2 - \left(\frac{\alpha r+1}{\nu r+1}\right)}$ are lower than one for any value of $\alpha \in [0; 1]$. Consequently, if the real part and the imaginary part of the eigenvalues are lower that one, it means that their module ($|\lambda_1| = |\lambda_2|$) is also lower that one (Triangle inequality) for any value of $\alpha \in [0; 1]$. The system is thus stable for any $\nu > 1$. However, the eigenvalues are complex during the whole duration of the test, meaning that overshoot and the settling time are not null. The damping ratio

is also as $0 < \zeta < 1$. Fig. II-36 shows how the parameters of the step response vary on the real and imaginary axis.

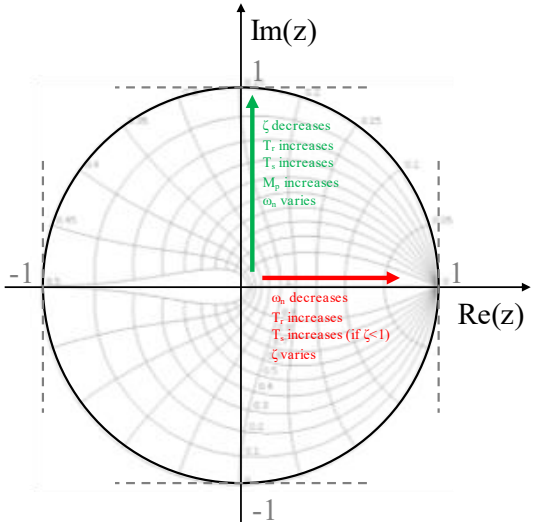

Fig. II-36 Variation of the step response parameter on the real and imaginary axis

The above figure can be summed up as follows:

- If the imaginary part of the poles increases, the damping ratio decreases and consequently, given equation (II-4) and (II-5), M_p and T_s increases.
- If the real part of the poles increases, ω_n decreases, involving that T_r and T_s increases.

Thus, even if the system remains stable, it is interesting to study how will evolve the real part and the imaginary part during the test. Given that $\mathrm{Re}(\lambda_1)$ and $\mathrm{Re}(\lambda_2)$ have the same expression as equation (II-38), it has been already demonstrated that the function increases linearly during the fire.

The imaginary part is a more complicated function. As in Section II.4.4, the study of the derivative is instructive. The derivative of the imaginary part with respect to α can be written as follows:

$$\frac{d\mathrm{Im}(\lambda_1)}{d\alpha} = -\frac{d\mathrm{Im}(\lambda_2)}{d\alpha} = \frac{1}{2}\frac{(1-\lambda^*)r}{(\nu r+1)^2}\frac{2\alpha r-\nu r+1}{\sqrt{\left(\frac{\alpha r+1}{\nu r+1}\right)^2-\left(\frac{\alpha r+1}{\nu r+1}\right)}} \tag{II-87}$$

One can see that the imaginary part of the poles has a maximum for $\alpha_{max} = \frac{\nu r-1}{2r}$. This maximum corresponds to the following complex number:

$$\lambda_{1,max} = \frac{1+\lambda^*}{2} + \frac{1-\lambda^*}{2}\mathrm{i} \qquad \lambda_{2,max} = \frac{1+\lambda^*}{2} - \frac{1-\lambda^*}{2}\mathrm{i} \tag{II-88}$$

The real part and the imaginary part of the complex numbers $\lambda_{1,max}$ and $\lambda_{2,max}$ can be used to rewrite $\mathrm{Im}(\lambda_1)$ and $\mathrm{Im}(\lambda_2)$ as two half circles:

$$\begin{aligned}\mathrm{Im}(\lambda_1) &= \sqrt{\left(\frac{1-\lambda^*}{2}\right)^2-\left(\left(1-(1-\lambda^*)\left(\frac{\alpha r+1}{\nu r+1}\right)\right)-\left(\frac{1+\lambda^*}{2}\right)\right)^2} \\ &= \sqrt{\left(\frac{1-\lambda^*}{2}\right)^2-\left(\mathrm{Re}(\lambda_1)-\left(\frac{1+\lambda^*}{2}\right)\right)^2}\end{aligned} \tag{II-89}$$

$$\begin{aligned}\mathrm{Im}(\lambda_2) &= -\sqrt{\left(\frac{1-\lambda^*}{2}\right)^2 - \left(\left(1-(1-\lambda^*)\left(\frac{\alpha r+1}{\nu r+1}\right)\right) - \left(\frac{1+\lambda^*}{2}\right)\right)^2} \\ &= -\sqrt{\left(\frac{1-\lambda^*}{2}\right)^2 - \left(\mathrm{Re}(\lambda_2) - \left(\frac{1+\lambda^*}{2}\right)\right)^2}\end{aligned} \tag{II-90}$$

It means that in case of overestimation, the eigenvalues λ_1 and λ_2 belong to a circle $\mathbf{C}$ of radius equal to $\frac{1-\lambda^*}{2}$ and centred on the real axis on abscissa $\frac{1+\lambda^*}{2}$:

$$\forall\, \nu \geq 1 \quad \lambda_1, \lambda_2 \in \mathbf{C} \equiv \left(\mathrm{Im}(z)\right)^2 + \left(\mathrm{Re}(z) - \left(\frac{1+\lambda^*}{2}\right)\right)^2 = \left(\frac{1-\lambda^*}{2}\right)^2 \tag{II-91}$$

The circle $\mathbf{C}$ does not depend on α and ν and is only a function of λ^*. If λ^* increases, the radius $\frac{1-\lambda^*}{2}$ decreases and the centre to $\frac{1-\lambda^*}{2}$ increases. If $\lambda^* \in [0;1]$, the circle $\mathbf{C}$ is inside the unit circle. Fig. II-37 shows $\mathbf{C}$ for some values of λ^*.

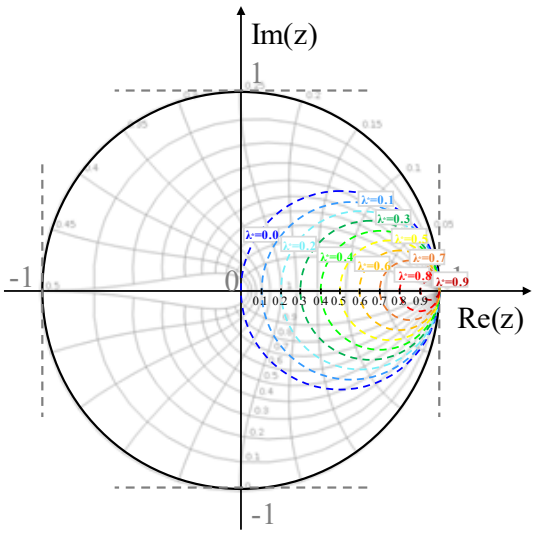

Fig. II-37 Circle C (II-91) for some values of $\lambda^* \in [0;1]$

The parameters α and ν do not appear in the centre and radius of $\mathbf{C}$. Nevertheless, these two parameters will determine the position and the scattering of the poles on the circle. The maximum $\alpha_{max} = \frac{\nu r-1}{2r}$ is helpful:

- If $\alpha_{max} < 0$, the poles are located on the first half of the circle $\mathbf{C}$. It involves that $\nu < 1/r$, which is possible only for $r < 1$ (Fig. II-38 (a), blue markers).
- If $\alpha_{max} > 1$, the eigenvalues are scattered on the second half of the circle $\mathbf{C}$. It involves that the overestimation is as $\nu > 2 + 1/r$. In this case, the estimated stiffness $K_{PS_0}^{EST}$ is more than two times the real one K_{PS_0} (Fig. II-38 (a)-(b), green markers).
- If $0 < \alpha_{max} < 1$, the eigenvalues are distributed on the first and second half of the circle. It involves that $1/r < \nu < 2 + 1/r$ (Fig. II-38 (a)-(b), orange markers).

The different cases are shown in Fig. II-38 (a) and (b). One can notice that the eigenvalues are more scattered if $r > 1$.

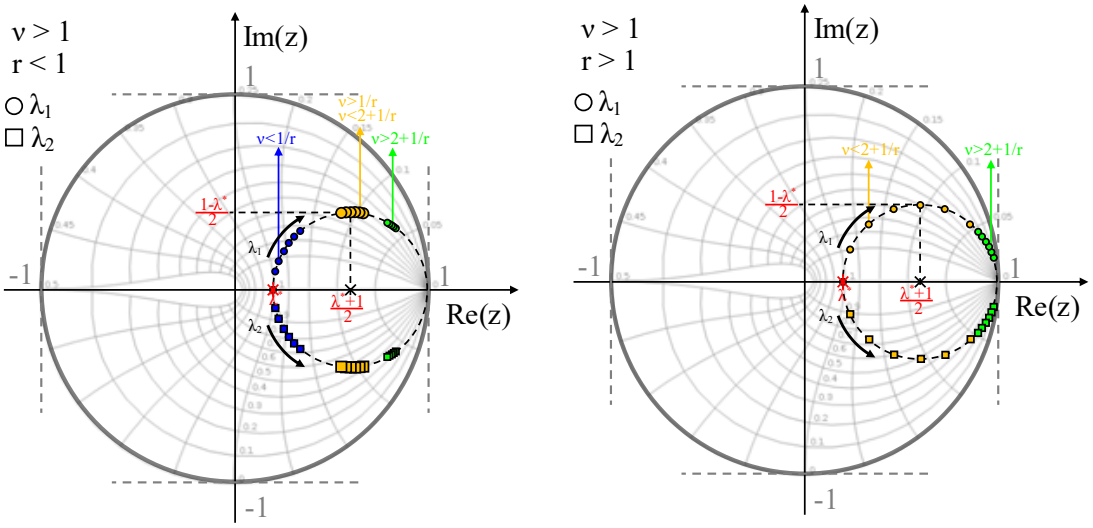

(a) r<1 *(b) r>1*

Fig. II-38 Poles location if the stiffness is overestimated

Underestimation $\nu < 1$

There are two cases to differentiate:

- $\alpha > \nu$: at the beginning of the test because $\alpha = 1$ and afterwards if the stiffness of the PS does not degrade too much.
- $\alpha < \nu$: during the test when the stiffness of the PS is degraded.

The second case is similar to the overestimation and has been already treated. In the first case, the two eigenvalues λ_1 and λ_2 are real according to equation (II-84) because $\alpha > \nu$. Their location with respect to the eigenvalue chosen by the user can be determine by solving the inequations $\lambda_1 > \lambda^*$ and $\lambda_2 > \lambda^*$:

$$1 - (1-\lambda^*)\left(\frac{\alpha r+1}{\nu r+1}\right) + (1-\lambda^*)\sqrt{\left(\frac{\alpha r+1}{\nu r+1}\right)^2 - \left(\frac{\alpha r+1}{\nu r+1}\right)} > \lambda^* \qquad \text{(II-92)}$$

$$1 - (1-\lambda^*)\left(\frac{\alpha r+1}{\nu r+1}\right) - (1-\lambda^*)\sqrt{\left(\frac{\alpha r+1}{\nu r+1}\right)^2 - \left(\frac{\alpha r+1}{\nu r+1}\right)} > \lambda^* \qquad \text{(II-93)}$$

The development of equation (II-92) and (II-93) show that $\lambda_1 > \lambda^*$ is always true and $\lambda_2 > \lambda^*$ is always false for $\alpha \in [0;1]$ and $\alpha > \nu$. The derivative of the eigenvalues is equal to:

$$\frac{d\lambda_1}{d\alpha} = -\frac{(1-\lambda^*)r}{\nu r+1} - \frac{(1-\lambda^*)r}{\nu r+1}\frac{\left(1-2\left(\frac{\alpha r+1}{\nu r+1}\right)\right)}{2\sqrt{\left(\frac{\alpha r+1}{\nu r+1}\right)^2 - \left(\frac{\alpha r+1}{\nu r+1}\right)}} \qquad \text{(II-94)}$$

$$\frac{d\lambda_2}{d\alpha} = -\frac{(1-\lambda^*)r}{\nu r+1} + \frac{(1-\lambda^*)r}{\nu r+1}\frac{\left(1-2\left(\frac{\alpha r+1}{\nu r+1}\right)\right)}{2\sqrt{\left(\frac{\alpha r+1}{\nu r+1}\right)^2 - \left(\frac{\alpha r+1}{\nu r+1}\right)}} \qquad \text{(II-95)}$$

If $\alpha > \nu$, one can demonstrate that, the derivative of λ_1 is positive and the derivative of λ_2 is negative. It means that:

- λ_1 is to the right of λ^* when $\alpha = 1$ and decreases for decreasing α (if $\alpha > \nu$)

- λ_2 is to the left of λ^* when $\alpha = 1$ (possibly negative) and increases for decreasing α (if $\alpha > \nu$)

The system is stable if:

$$-1 \leq 1-(1-\lambda^*)\left(\frac{\alpha r+1}{\nu r+1}\right)+(1-\lambda^*)\sqrt{\left(\frac{\alpha r+1}{\nu r+1}\right)^2-\left(\frac{\alpha r+1}{\nu r+1}\right)} \leq 1 \quad \text{(II-96)}$$

$$-1 \leq 1-(1-\lambda^*)\left(\frac{\alpha r+1}{\nu r+1}\right)-(1-\lambda^*)\sqrt{\left(\frac{\alpha r+1}{\nu r+1}\right)^2-\left(\frac{\alpha r+1}{\nu r+1}\right)} \leq 1 \quad \text{(II-97)}$$

The two inequalities can be translated into the four hereunder conditions:

$$-\frac{\alpha r+1}{\nu r+1} \leq 0 \quad \text{(II-98)}$$

$$\frac{\alpha r+1}{\nu r+1} \geq \frac{4}{\lambda^{*2}+2\lambda^*-3} \quad \text{(II-99)}$$

$$-\frac{\alpha r+1}{\nu r+1} - \leq 0 \quad \text{(II-100)}$$

$$\frac{\alpha r+1}{\nu r+1} \leq \frac{-4}{\lambda^{*2}+2\lambda^*-3} \quad \text{(II-101)}$$

The equations (II-98), (II-99) and (II-100) are always verified for all $\alpha > \nu$, $\nu < 1$ and $\lambda^* \in [0;1]$. The last condition is true only if ν is as follows:

$$\nu \geq -\alpha\frac{\lambda^{*2}+2\lambda^*-3}{4}-\frac{\lambda^{*2}+2\lambda^*-3}{4r}-\frac{1}{r} \Leftrightarrow \nu \geq B \quad \text{(II-102)}$$

Otherwise, it means that λ_2 is lower than -1. The most restrictive case is when $\alpha = 1$. The critical value is thus as:

$$\nu_{min} = -\frac{\lambda^{*2}+2\lambda^*-3}{4}-\frac{\lambda^{*2}+2\lambda^*-3}{4r}-\frac{1}{r} \quad \text{(II-103)}$$

The system is thus already unstable when the structure is not heated because λ_2 is lower than -1. One can also notice that the equation (II-102) is less restrictive if the ratio r decreases. The location of the eigenvalues of the different cases are summed up in Fig. II-39.

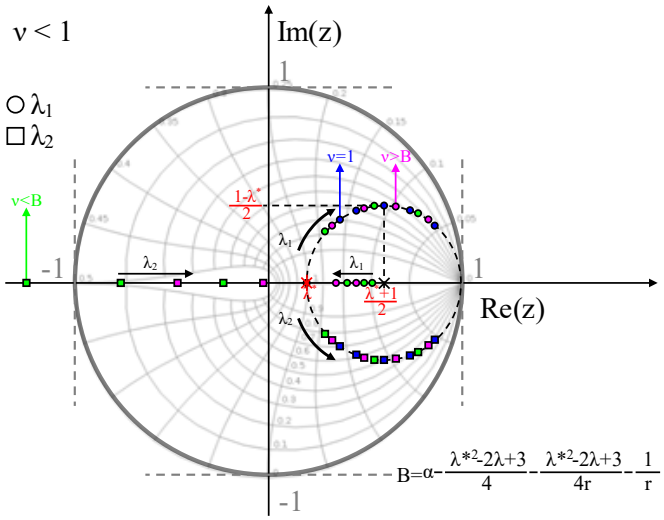

Fig. II-39 Pole locations if the stiffness is underestimated

Some values of λ_1 and λ_2 when $\alpha = 1$ are shown in Fig. II-40 (a)-(d) for estimation $\nu \in [0;1]$ and several ratio $r = [0.001,0.01,0.1,1,10,100,1000]$. One can made the following observations:

- The real eigenvalues move away from the original design value λ^* and as demonstrated, λ_2 is responsible for instabilities.
- if the ratio r is low ($r = 0.001, 0.01, 0.1$), the system is stable for any $\nu \in [0;1]$ because the smallest acceptable estimation ν given by equation (II-102) is negative.
- if λ^* increases, the range of acceptable underestimation increases, which is consistent with equation (II-102).

All cases of the single DOF test are summarized in Table II-7.

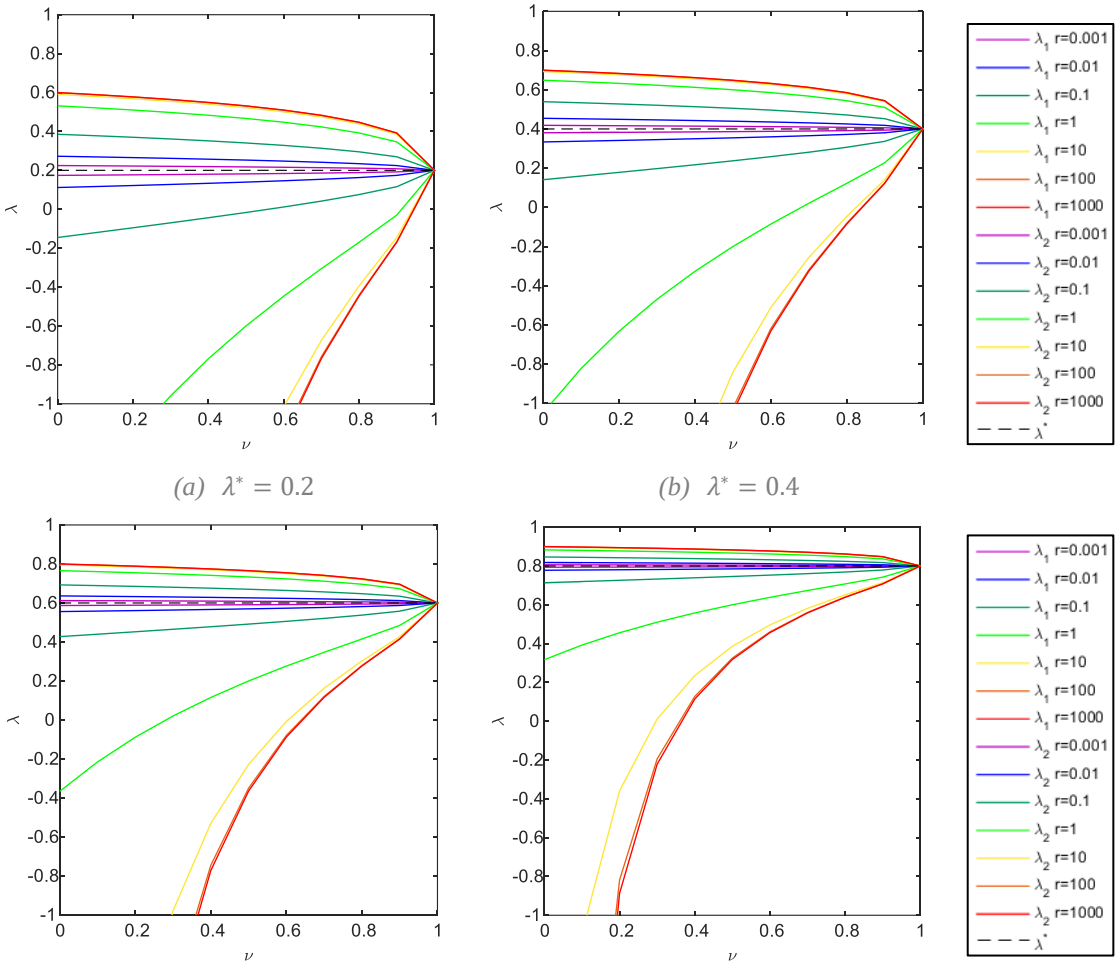

(a) $\lambda^* = 0.2$ *(b)* $\lambda^* = 0.4$

(c) $\lambda^* = 0.6$ *(d)* $\lambda^* = 0.8$

Fig. II-40 Values of λ_1 and λ_2 for $\alpha = 1$ and $r = [0.001,0.01,0.1,1,10,100,1000]$

Table II-7

$\nu > 1$	Stable $\forall\alpha \in [0;1]$, $r \in \mathbb{R}^+$	λ_1 and λ_2 are complex conjugate and belong to circle C.	Controller less reactive with overshoot
$\nu < 1$ $\nu \geq B$	Stable $\forall\alpha \in [0;1]$ $\forall\alpha \in [0;1]$, $r \in \mathbb{R}^+$	$\alpha > \nu$: λ_1 and λ_2 are real, $\lambda_1 > \lambda^*$ and $\lambda_2 < \lambda^*$ $\alpha < \nu$: λ_1 and λ_2 are complex conjugate and belong to circle C.	Controller more reactive + oscillations if λ_2 is negative $\alpha < \nu$: overshoot
$\nu < 1$ $\nu \leq B$	Unstable		

One-DOF example

In this Section, a numerical example is used to illustrate the proportional integral controller in the case of a one-DOF system. The elastic system presented in Fig. II-41 is analysed in a virtual environment, meaning that PS and the NS are modelled numerically.

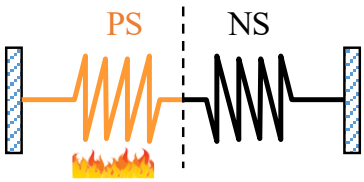

Fig. II-41 – Single DOF example

The same data that are considered are the same as Section II.4.5:

- Coefficient of thermal expansion of the material of the PS is equal to 12×10^{-6}
- Sectional area of the PS and NS: $A_{PS} = A_{NS} = 20\,000\ mm^2$
- Length of the PS equal to 1.50 m and a length of the NS equal to 3.00 m
- Heating rate of the PS: $0.5°/s$
- Young modulus of the PS and NS at ambient temperature: $E_{PS} = E_{NS} = 210\,000\ N/mm^2$
- The Young modulus E_{PS} of the PS decreases with temperature according to Table 3 in CEN. EN 1993-1-2:2005 (see Fig. II-18).
- The displacement of the PS and NS are updated every 10s, meaning that the sample time T is equal to 10s.
- The computation time is negligeable and between two updates, the position of the actuator is interpolated. The movement of the actuator is thus continuous.

Fig. II-43 and Fig. II-44 compare the performance of a proportional controller and an integral proportional controller. Both controllers are designed with an eigenvalue/a pair of eigenvalues λ^* equal to 0.1. The gain values are computed with equations (II-36), (II-80) and (II-81):

Proportional controller
$$\rightarrow L_P = \frac{1 - 0.1}{(2.8 + 1.4) \times 10^9} = 2.1429 \times 10^{-10}\ m/N \qquad \text{(II-104)}$$

Proportional integral controller
$$\rightarrow L_P = \frac{2 \times (1 - 0.1)}{(2.8 + 1.4) \times 10^9} = 4.2857 \times 10^{-10}\ m/N$$
$$\rightarrow L_J = \frac{(1 - 0.1)^2}{(2.8 + 1.4) \times 10^9} = 1.9286 \times 10^{-10}\ m/N \qquad \text{(II-105)}$$

In Fig. II-44 (a) and (b), the forces and the displacement of the PS obtained by the two processes fit the correct solution (black line, “u” and “F”). However, Fig. II-44 (c) shows that the instantaneous error is much lower in the case of the proportional integral controller. The equilibrium of the forces is thus better ensured. Peaks of errors in the green curve correspond to abrupt changes in the slope of the curve “u” and “F”. However, the equilibrium is quickly restored by the proportional integral controller. Fig. II-43 shows the displacement-force relationship obtained by the two controllers. The curve of the proportional controller displays more differences than the curve of the proportional integral controller.

These efficient corrections are allowed thanks to the integral term displayed in Fig. II-44 (d) that adjust *how fast* the corrections must be made. Consequently, this term is high at the beginning of the test when the heating starts and then decreases as the slope of the force and displacement decrease with time. It increases when the slope changes sign around t=17 min (~530°C) and when its value varies suddenly as around t=19min (600°C) and t=22min (700°C).

Fig. II-42 (a) shows the location of the poles of the integral proportional controller in the complex plane for some temperatures. As demonstrated before, the poles are on the perimeter of a circle C of radius equal to $\frac{1-\lambda^*}{2} = 0.45$ and centred on the real axis on abscissa $\frac{1+\lambda^*}{2} = 0.55$.

Fig. II-45 (a) and (b) shows how the rise time and the overshoot are affected with degrading stiffness, in the integral proportional controller. Their values are computed for the following temperatures:

Table II-8

$\theta = 20°C - 100°C$	$\rightarrow \alpha = 1.00$	$\theta = 600°C$	$\rightarrow \alpha = 0.31$
$\theta = 200°C$	$\rightarrow \alpha = 0.90$	$\theta = 800°C$	$\rightarrow \alpha = 0.09$
$\theta = 400°C$	$\rightarrow \alpha = 0.70$	$\theta = 1200°C$	$\rightarrow \alpha = 0.00$

The rise time T_r increases mostly because the natural frequency ω_n of the system increases. Indeed, according to Fig. II-4, ω_n depends mainly on the real part of the pole and increases with the latter. M_p varies with the damping ratio ζ as shown in equation (II-7) and globally increases with degrading stiffness K_{PS_i} as expected by the theory.

The effect of overestimation is shown in Fig. II-46. The cases $\nu = 1.0$, $\nu = 2.0$ and $\nu = 10$ are considered and the gain values L_p and L_J are computed as follows:

$$\nu = 1.0 \quad \begin{cases} \rightarrow L_P = \dfrac{2 \times (1 - 0.1)}{(2.8 + 1.4) \times 10^9} = 4.2857 \times 10^{-10}\ \text{m/N} \\ \rightarrow L_J = \dfrac{(1 - 0.1)^2}{(2.8 + 1.4) \times 10^9} = 1.9286 \times 10^{-10}\ \text{m/N} \end{cases} \tag{II-106}$$

$$\nu = 2.0 \quad \begin{cases} \rightarrow L_P = \dfrac{2 \times (1 - 0.1)}{(2.8 \times 2.0 + 1.4) \times 10^9} = 2.5714 \times 10^{-10}\ \text{m/N} \\ \rightarrow L_J = \dfrac{(1 - 0.1)^2}{(2.8 \times 2.0 + 1.4) \times 10^9} = 1.1571 \times 10^{-10}\ \text{m/N} \end{cases} \tag{II-107}$$

$$\nu = 10 \quad \begin{cases} \rightarrow L_P = \dfrac{2 \times (1 - 0.1)}{(2.8 \times 10 + 1.4) \times 10^9} = 1.1571 \times 10^{-10}\ \text{m/N} \\ \rightarrow L_J = \dfrac{(1 - 0.1)^2}{(2.8 \times 10 + 1.4) \times 10^9} = 2.7551 \times 10^{-11}\ \text{m/N} \end{cases} \tag{II-108}$$

The poles are displayed in Fig. II-42 (b) and (c) and corresponds to the rules given in Fig. II-38 (b). If one compares with the case of the proportional controller studied in the previous section, the curves of forces and displacement better follow the correct solution in Fig. II-46 (a) and (b) than in Fig. II-20 (a) and (b), even if the overestimation is high ($\nu = 10$).

The controller is however less reactive if the stiffness of the PS is overestimated. Indeed, one can observe in equations (II-106)-(II-108) that the gain value of the controller decreases with the parameter ν increasing. Consequently, the error between the interface forces increases as can be seen in Fig. II-46 (c) but is much lower than the instantaneous error of the proportional controller shown in Fig. II-20 (d), as the integral term allow greater corrections. However, one can notice some overshoots in Fig. II-46 (a) and (b) around $t = 22$ min because of the sudden change of slope due to the variation of the Young modulus with temperature, which is difficult to follow by a less reactive controller. Also, as described before, the rise time and the overshoot increase with

overestimation and degrading stiffness K_{PS_i}. The evolution of these step response parameters with time and temperature are shown in Fig. II-46 (d) and (e) for each case.

The effect of underestimation is shown in Fig. II-47 (d)-(e). Three cases are considered, and the corresponding gain values are computed:

$$\nu = 1.0 \quad \begin{cases} \rightarrow L_P = \dfrac{2 \times (1 - 0.1)}{(2.8 + 1.4) \times 10^9} = 4.2857 \times 10^{-10}\ \mathrm{m/N} \\ \rightarrow L_J = \dfrac{(1 - 0.1)^2}{(2.8 + 1.4) \times 10^9} = 1.9286 \times 10^{-10} \end{cases} \tag{II-109}$$

$$\nu = 0.8 \quad \begin{cases} \rightarrow L_P = \dfrac{2 \times (1 - 0.1)}{(2.8 \times 0.5 + 1.4) \times 10^9} = 6.4286 \times 10^{-10}\ \mathrm{m/N} \\ \rightarrow L_J = \dfrac{(1 - 0.1)^2}{(2.8 \times 0.5 + 1.4) \times 10^9} = 2.8929 \times 10^{-10}\ \mathrm{m/N} \end{cases} \tag{II-110}$$

$$\nu = 0.1 \quad \begin{cases} \rightarrow L_P = \dfrac{2 \times (1 - 0.1)}{(2.8 \times 0.1 + 1.4) \times 10^9} = 1.0714 \times 10^{-9}\ \mathrm{m/N} \\ \rightarrow L_J = \dfrac{(1 - 0.1)^2}{(2.8 \times 0.1 + 1.4) \times 10^9} = 4.8214 \times 10^{-10}\ \mathrm{m/N} \end{cases} \tag{II-111}$$

The gain value of the proportional controller increases if ν decreases, which indicated that the controller is more reactive. The theory previously demonstrated that the system is stable if the parameter ν is higher than the critical value ν_{min}. The critical value is equal to:

$$\nu_{min} = \left(-\frac{1}{4} - \frac{1}{4r}\right)\left(\lambda^{*2} + 2\lambda^* - 3\right) - \frac{1}{r} = \left(-\frac{1}{4} - \frac{1}{8}\right)\left(0.1^2 + 0.2 - 3\right) - \frac{1}{2} = 0.55 \tag{II-112}$$

The location of the poles when $\nu = 0.8$ are shown in Fig. II-42 (d). As $\nu > \nu_{min}$, the poles are inside the unit circle. Their location is similar to what can be seen in Fig. II-39. If $\alpha > \nu$, λ_1 is a positive real number higher than 0.1 and λ_2 is a negative real number. When the temperature is higher than 300°C, $\alpha < 0.8$. Consequently, the eigenvalues are complex conjugate and on the perimeter of a circle centred on the real axis on abscissa $\frac{1+\lambda^*}{2} = 0.55$, with radius equal to $\frac{1-\lambda^*}{2} = 0.45$.

Fig. II-47 (a)-(b) does not show any noticeable difference between $\nu = 1.0$ and $\nu = 0.8$ in the force and the displacement. In Fig. II-47 (c)-(d), one can notice that the error and the integral term is slightly lower in case of underestimation.

The rise time and the overshoot are displayed in Fig. II-47 (e) and (f) for the temperature given in Table II-8. Fig. II-47 (f) shows that the overshoot of the case $\nu = 0.8$ is much higher than the case $\nu = 1.0$ temperatures below 200°C. This is due to the negative pole λ_2 that is the dominant eigenvalue at the beginning of the test:

$$\zeta = -\cos(\measuredangle \ln(-0.417)) = 0.2682 \rightarrow M_p = \exp\left(-\frac{\pi\zeta}{\sqrt{1-\zeta^2}}\right) = 41.70\ \% \tag{II-113}$$

If $\nu = 0.5$, the system is unstable because one poles has a module greater than one as shown in Fig. II-42 (e).

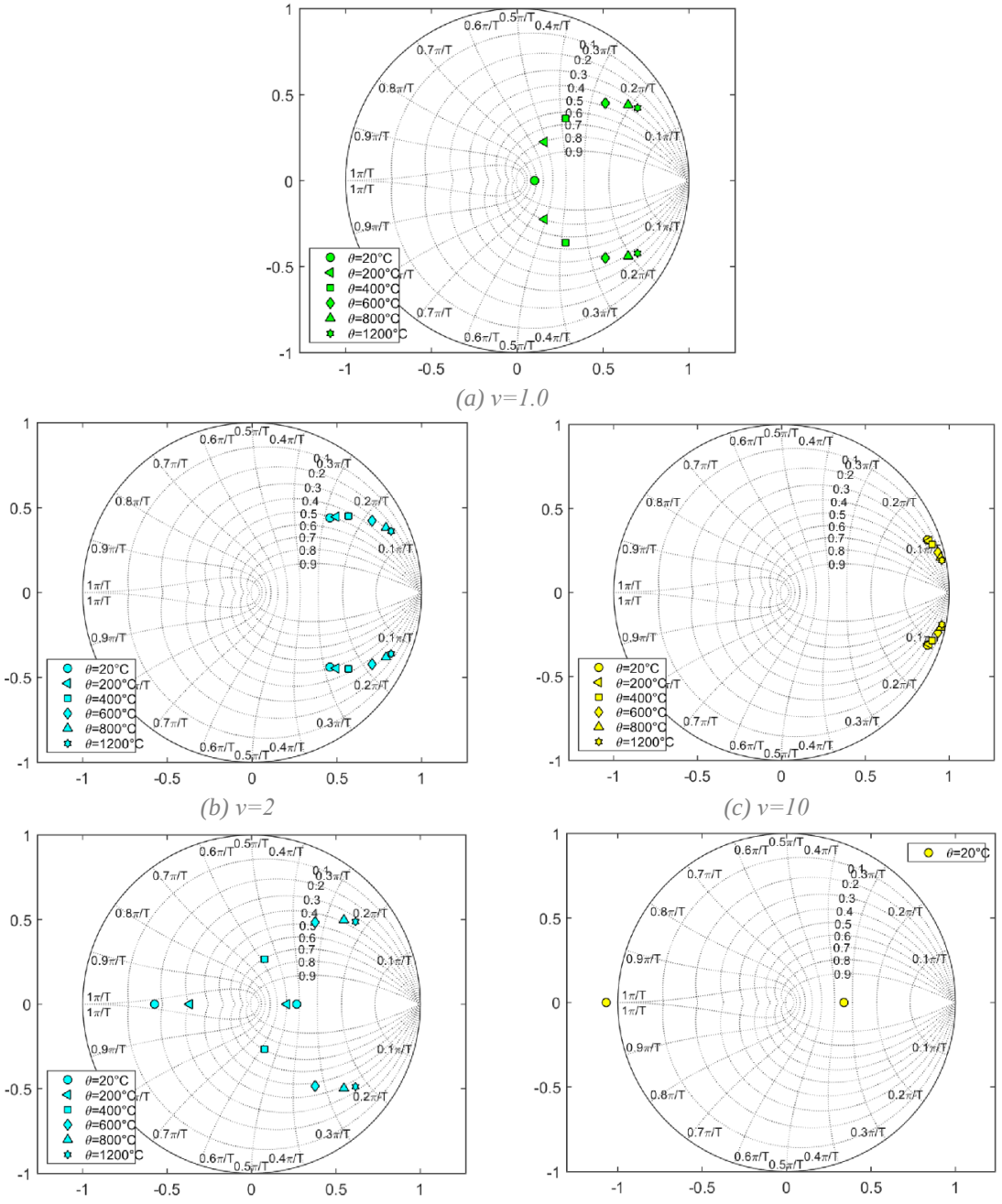

(a) v=1.0

(b) v=2

(c) v=10

(d) v=0.8

(e) v=0.5

Fig. II-42 One-DOF example: Location of the poles for several estimation of K_{PS_0}

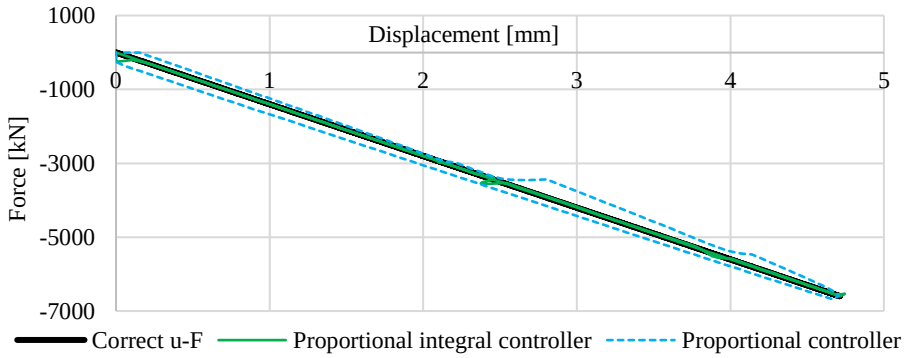

Fig. II-43 One-DOF example: force-displacement relationship

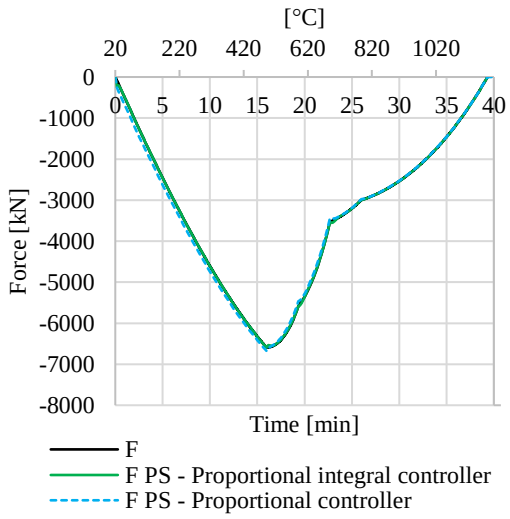

(a) Normal Force

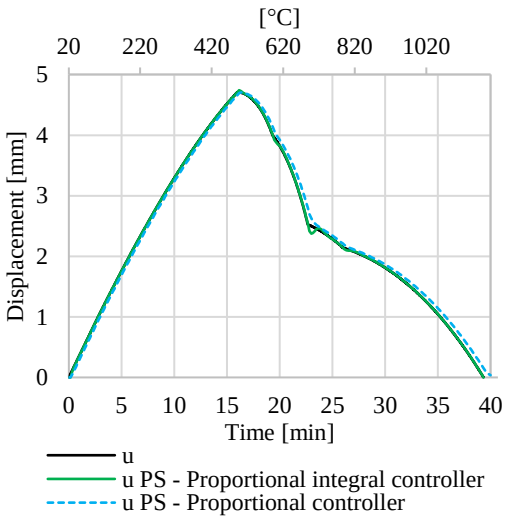

(b) Displacement

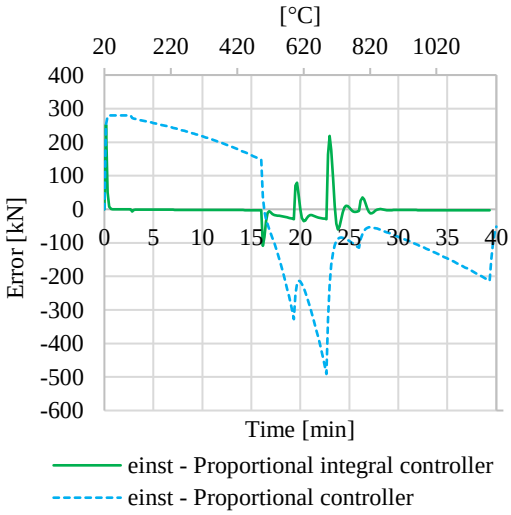

(c) Instantaneous error

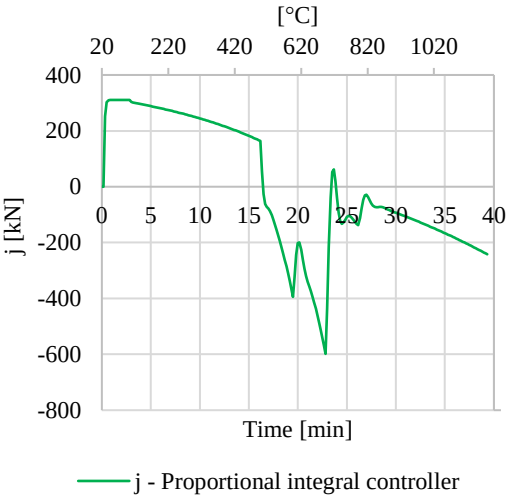

(d) Integral term of the proportional integral controller

Fig. II-44 One-DOF example: proportional controller and proportional integral controller

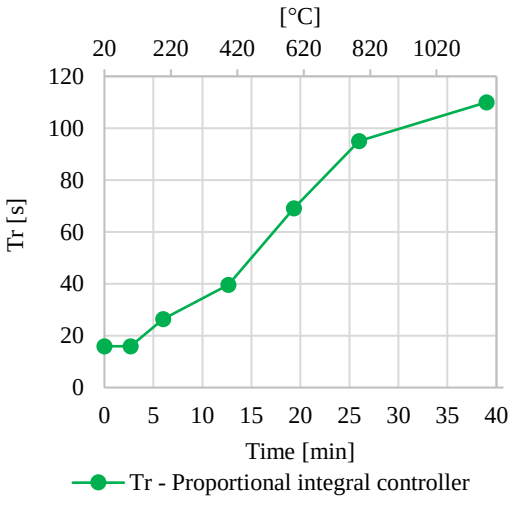

(a) Rise time

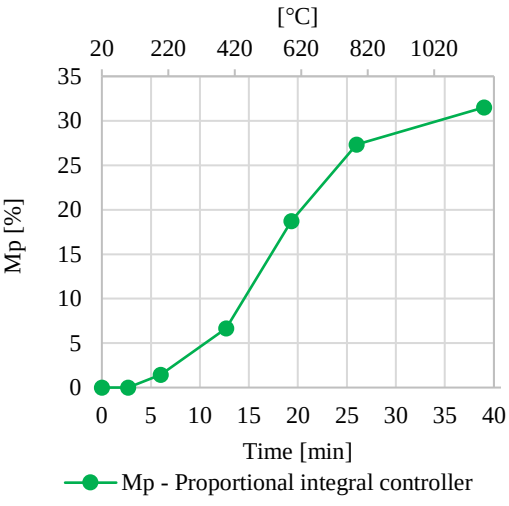

(b) Overshoot

Fig. II-45 One-DOF example: Rise time and overshoot of the proportional integral controller

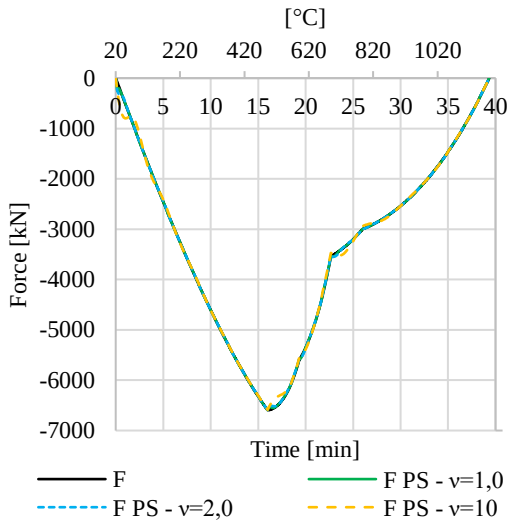

(a) Normal Force

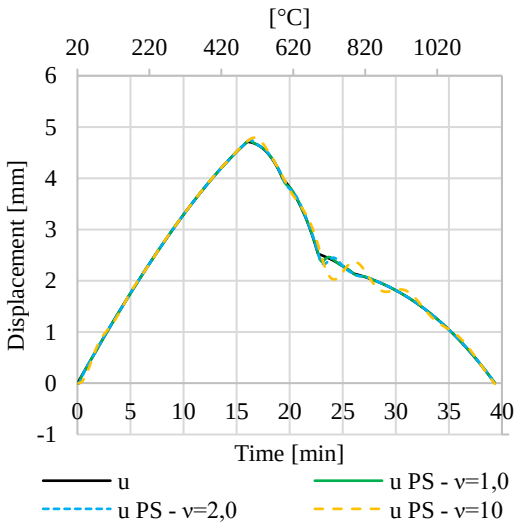

(b) Displacement

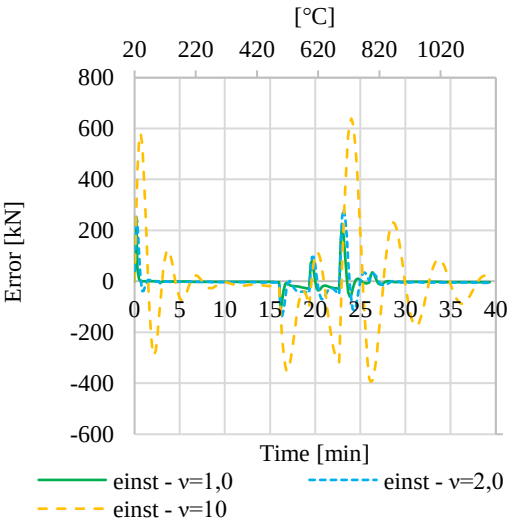

(c) Instantaneous error

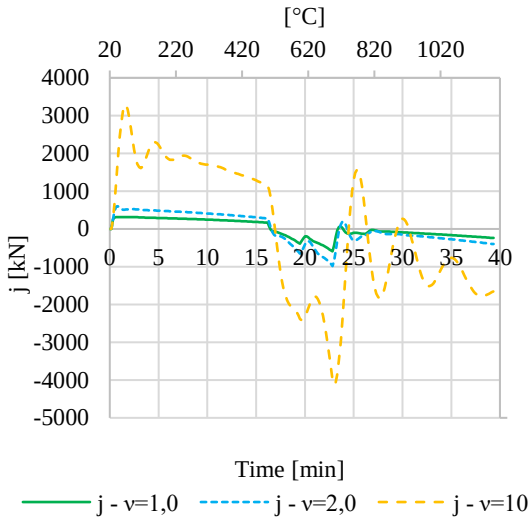

(d) Integral term

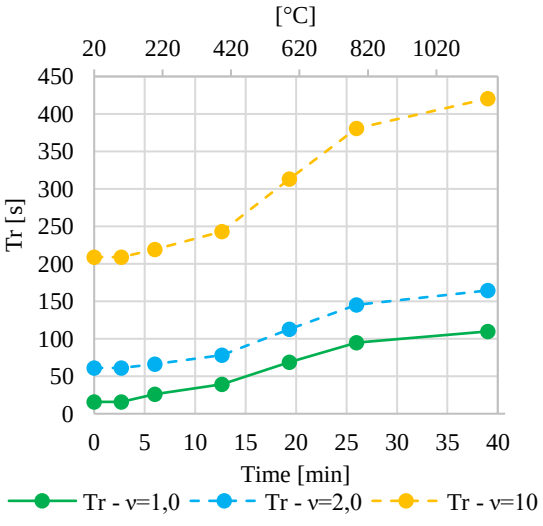

(e) Rise time

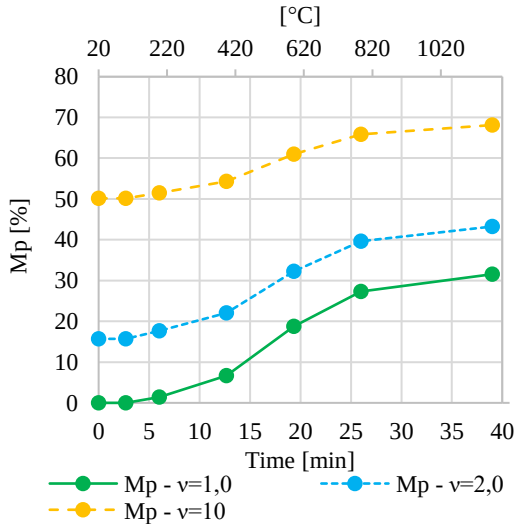

(f) Overshoot

Fig. II-46 One-DOF example: v=1.0, v=2.0, v=10

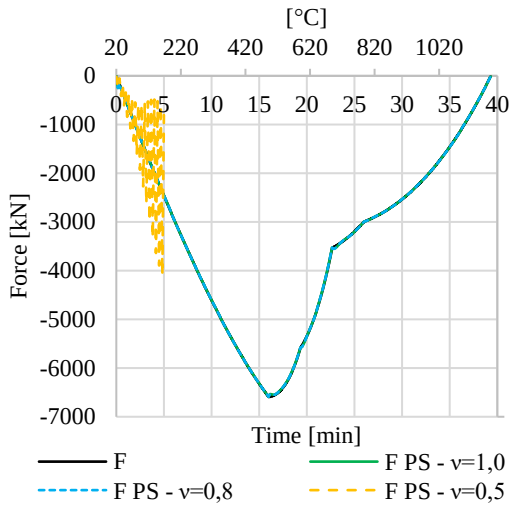

(a) Normal Force

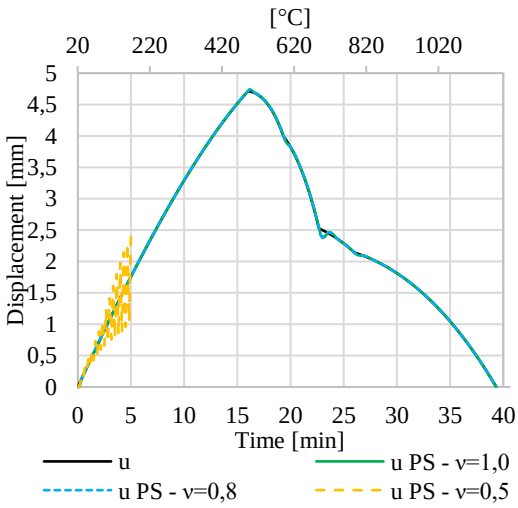

(b) Displacement

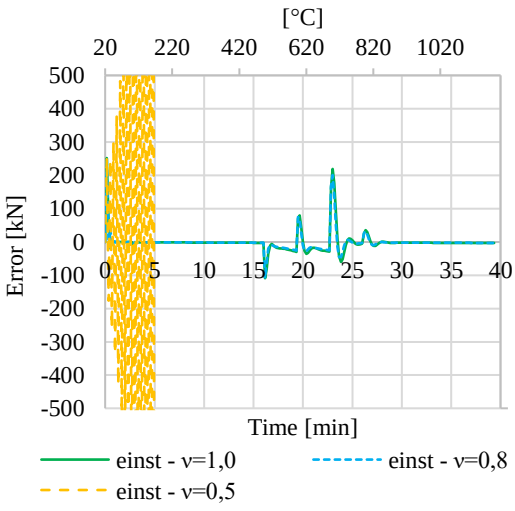

(c) Instantaneous error

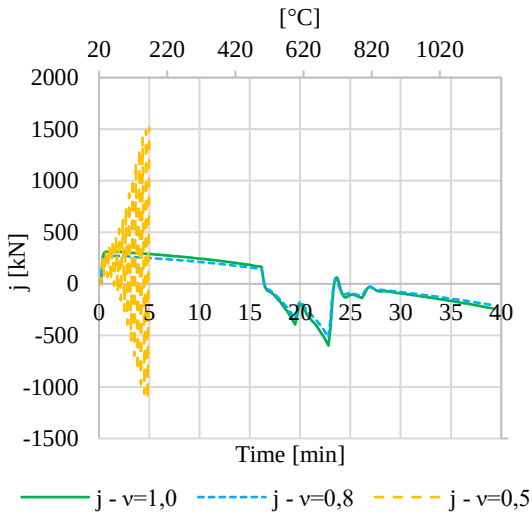

(d) Integral term

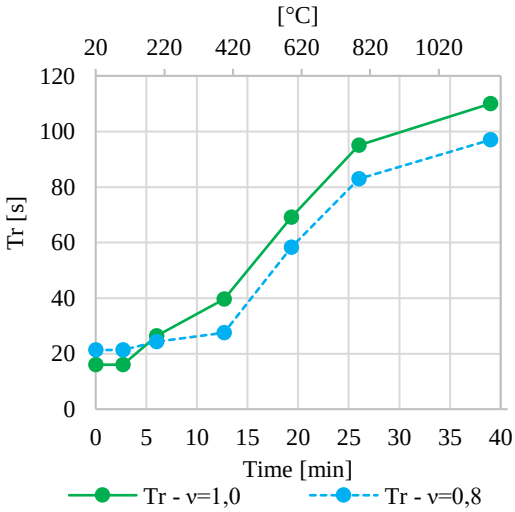

(e) Rise time

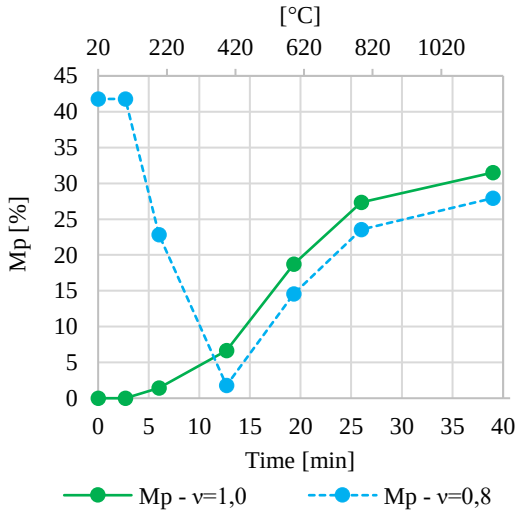

(f) Overshoot

Fig. II-47 One-DOF example: ν=1.0, ν=0.8, ν=0.6

II.5.2 Multi-DOF system

As for the proportional controller, the state equation can be simplified as follows:

$$\begin{bmatrix} \mathbf{u}_{\mathrm{PS}_{i+1}} \\ \mathbf{J}_{i+1} \end{bmatrix} = \begin{bmatrix} \mathbf{I} - \mathbf{L}_{\mathrm{P}}(\alpha\mathbf{K}_{\mathrm{PS}_0} + \beta\mathbf{K}_{\mathrm{NS}_0}) & \mathbf{L}_{\mathrm{J}} \\ -(\alpha\mathbf{K}_{\mathrm{PS}_0} + \beta\mathbf{K}_{\mathrm{NS}_0}) & \mathbf{I} \end{bmatrix} \begin{bmatrix} \mathbf{u}_{\mathrm{PS}_i} \\ \mathbf{J}_i \end{bmatrix} + \begin{bmatrix} -\mathbf{L}_{\mathrm{P}}\left(\mathbf{F}_{\mathrm{NS}_i}^{\mathrm{TH}} + \mathbf{F}_{\mathrm{PS}_i}^{\mathrm{TH}}\right) \\ -\left(\mathbf{F}_{\mathrm{NS}_i}^{\mathrm{TH}} + \mathbf{F}_{\mathrm{PS}_i}^{\mathrm{TH}}\right) \end{bmatrix} \tag{II-114}$$

To determine the eigenvalues $\lambda_1, \lambda_2, \ldots \lambda_n$ of the dynamics matrix $\mathbf{A}$, the general equation that must be solved is the following:

$$|\mathbf{I}z - \mathbf{A}| = (z - \lambda_1)(z - \lambda_2) \ldots (z - \lambda_{2d}) \tag{II-115}$$

The two polynomials are equal if their coefficients are equal. As the coefficient of the highest degree term is equal to 1, the system has 2d equations to solve. The determination of $\mathbf{L}_{\mathrm{P}}$ and $\mathbf{L}_{\mathrm{J}}$ is not easy if these matrices are full because the characteristic polynomial $|\mathbf{I}z - \mathbf{A}|$ of the dynamics matrix $\mathbf{A}$ would contain too many unknowns. The use of diagonal matrices allows to have 2d unknowns. Full gain matrices can also be used. Additional equations are however necessary to determine them. For instance, a simple case consists in determining $\mathbf{L}_{\mathrm{P}}$ and $\mathbf{L}_{\mathrm{J}}$ as $\mathbf{A}$ has null eigenvalues. By solving $\mathbf{A}^2 = 0$ (nilpotent matrix has null eigenvalues) with $\alpha = 1$, $\beta = 1$ and $\mathbf{K}_{\mathrm{PS}_0} = \mathbf{K}_{\mathrm{PS}_0}^{\mathrm{EST}}$, one can obtain the following gain matrices:

$$\begin{aligned} \mathbf{L}_{\mathrm{P}} &= 2\left(\mathbf{K}_{\mathrm{PS}_0}^{\mathrm{EST}} + \mathbf{K}_{\mathrm{NS}_0}\right)^{-1} \\ \mathbf{L}_{\mathrm{J}} &= \left(\mathbf{K}_{\mathrm{PS}_0}^{\mathrm{EST}} + \mathbf{K}_{\mathrm{NS}_0}\right)^{-1} \end{aligned} \tag{II-116}$$

The controllers designed with null eigenvalues are highly reactive and must be used only for systems that are subjected to fast changes. Otherwise, it can lead to oscillations that can be harmful for the system.

As for the single DOF system, one can consider that the evolution of $\mathbf{K}_{\mathrm{NS}_i}$ is negligible in comparison to $\mathbf{K}_{\mathrm{PS}_i}$ and that $\beta = 1$. The dynamics matrix $\mathbf{A}_{\mathrm{PI}}$ is the following block matrix:

$$\mathbf{A}_{\mathrm{PI}}(\alpha) = \begin{bmatrix} \mathbf{I} - \mathbf{L}_{\mathrm{P}}(\alpha\mathbf{K}_{\mathrm{PS}_0} + \mathbf{K}_{\mathrm{NS}_0}) & \mathbf{L}_{\mathrm{J}} \\ -(\alpha\mathbf{K}_{\mathrm{PS}_0} + \mathbf{K}_{\mathrm{NS}_0}) & \mathbf{I} \end{bmatrix} \tag{II-117}$$

The matrix is composed of four blocks. The first one is the same matrix $\mathbf{I} - \mathbf{L}_{\mathrm{P}}(\alpha\mathbf{K}_{\mathrm{PS}_0} + \mathbf{K}_{\mathrm{NS}_0})$ as the proportional controller. The block $\mathbf{L}_{\mathrm{J}}$ is the second gain matrix and act as a flexibility matrix as $\mathbf{L}_{\mathrm{P}}$. Its entries are thus extremely low compared to the three other blocks. On the contrary, the block $-(\alpha\mathbf{K}_{\mathrm{PS}_0} + \mathbf{K}_{\mathrm{NS}_0})$ contains high elements as it is a sum of two stiffness matrices. The unit matrix $\mathbf{I}$ has an order of magnitude comparable to $\mathbf{I} - \mathbf{L}_{\mathrm{P}}(\alpha\mathbf{K}_{\mathrm{PS}_0} + \mathbf{K}_{\mathrm{NS}_0})$.

Unlike the proportional controller, the Gershgorin circles of the matrix are not helpful to determine the spectrum of this matrix. The two first blocks $\mathbf{I} - \mathbf{L}_{\mathrm{P}}(\alpha\mathbf{K}_{\mathrm{PS}_0} + \mathbf{K}_{\mathrm{NS}_0})$ and $\mathbf{L}_{\mathrm{J}}$ give Gershgorin circles similar to ones of the proportional controller as $\mathbf{L}_{\mathrm{J}}$ has low entries. For this first line, the observations made in Section II.4.4 are still valid. However, the second line of the matrix $\mathbf{A}_{\mathrm{PI}}$ involves that the Gershgorin circles are centred in 1 on the real axis with a large radius equal to the sum of the element of $\alpha\mathbf{K}_{\mathrm{PS}_0} + \mathbf{K}_{\mathrm{NS}_0}$. These large circles include more than the unit circle and do not depend on the gain matrices. Consequently, no information about tendencies can be extracted using the Gershgorin circles of $\mathbf{A}_{\mathrm{PI}}$. Moreover, this block matrix is hard to diagonalize.

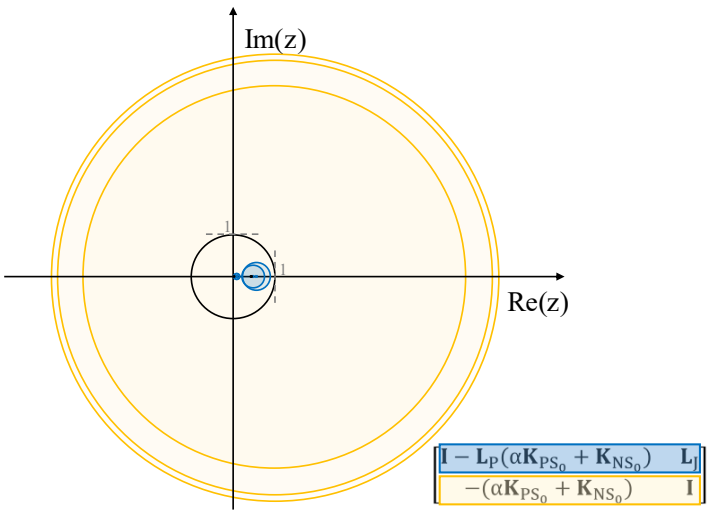

Fig. II-48 Gershgorin circles of the dynamics matrix (proportional integral controller)

Even if one cannot elaborate accurate stability conditions as for a single DOF system, one can however suppose that similar tendencies will be observed. Underestimation of the initial parameters results in oscillating and potentially unstable systems because of high values of gains. Overestimation does not involve instabilities but results in low values of gains and low reactive system. Two methods can be used to verify the stability in this case :

- First the simplified equation can be used. This method consists in computing explicitly the eigenvalue of the state matrix $\mathbf{A}_{PI}$for α (and possibly β values) :

$$\mathbf{A}_{PI}(\alpha,\beta) = \begin{bmatrix} \mathbf{I} - \mathbf{L}_P(\alpha\mathbf{K}_{PS_0} + \beta\mathbf{K}_{NS_0}) & \mathbf{L}_J \\ -(\alpha\mathbf{K}_{PS_0} + \beta\mathbf{K}_{NS_0}) & \mathbf{I} \end{bmatrix} \quad \text{(II-118)}$$

- Another method consists in simulating the hybrid test virtually. It consists in replacing the physical substructure by a numerical simulation that approximate the behaviour of the specimen. A specific tool was developed to perform and consists in performing a hybrid test with two substructures modelled in SAFIR (see Fig. II-49)

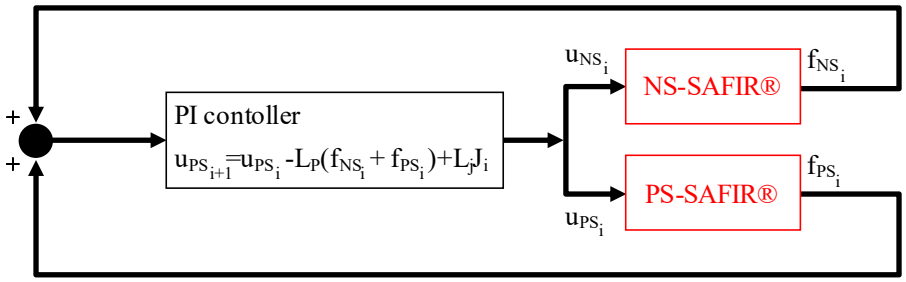

Fig. II-49 Virtual Hybrid Fire Testing

The two techniques will be used in Section II.6 and Chapter III.

II.5.3 Delay

Hybrid testing is a closed loop procedure that contains several components: computer, servo controller, hydraulic actuators, test specimen, data acquisition. Delays are unavoidable. They can be sorted into three categories: communication delay τ_C, computing time delay τ_N, and actuator dynamics delay τ_P. Fig. II-50 shows where the delays occur in the HFT. The sum of these delays results in a lag τ that can be reduced (by simplifying the numerical model, for instance) but not eliminated.

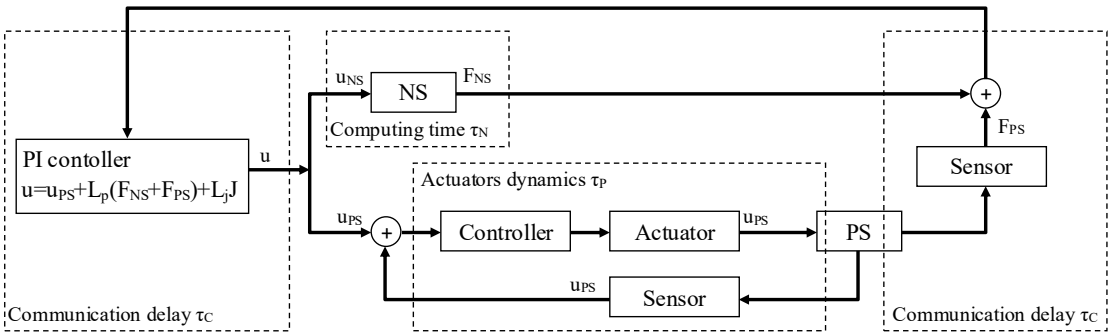

Fig. II-50 Delays in HFT

In seismic hybrid testing, (Horiuchi et Konno 1996) characterised this lag as being equivalent to negative damping in case of a linear elastic single DOF system. Instability happens when the negative damping is larger than structural damping. In HFT, this negative damping is not observed because the specimen is static or quasi-static before the failure. The fact of using systems in parallel makes it possible to reduce the delay and to avoid desynchronization in the displacements and the force as it has been observed in earthquake engineering.

From the point of view of control theory, as it does not appear in the dynamics matrix of the state-space representation, the delay is not an issue for stability. However, it is related to the sampling period T which is presented in Section II.2.5. If the delay increases, the time step between two updates increases and therefore T increases. According to equations (II-3)-(II-5), the performance on discrete systems is dependent on T: if T increases, the rise time and the settling time increases. Consequently, the system will take more time to correct the error as shown in Fig. II-51. Before designing the controller, this sampling period must be known.

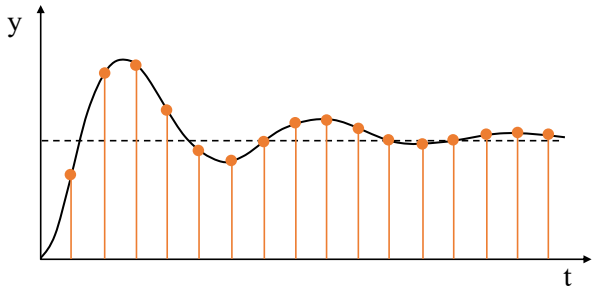

(a) Step response with sampling period T

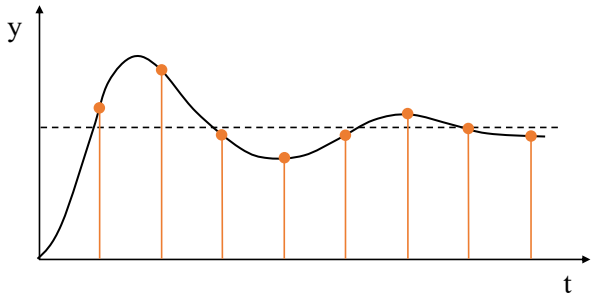

(b) Step response with sampling period 2T

Fig. II-51 Step response for several sampling time T

Fig. II-52 shows the effect of delay on the one-DOF system illustrated in Fig. II-41 with a double eigenvalue equal to 0.1 and three sample time T: 10s, 30s and 60s. If one compares the results of this proportional integral controller with the proportional controller shown in Fig. II-33, one can notice that the proportional integral controller is less sensitive to delay and deviates slightly from

the solution. Nevertheless, one can observe some oscillations around 700°C because of the sudden change of slope that cannot be followed because the correction is too slow.

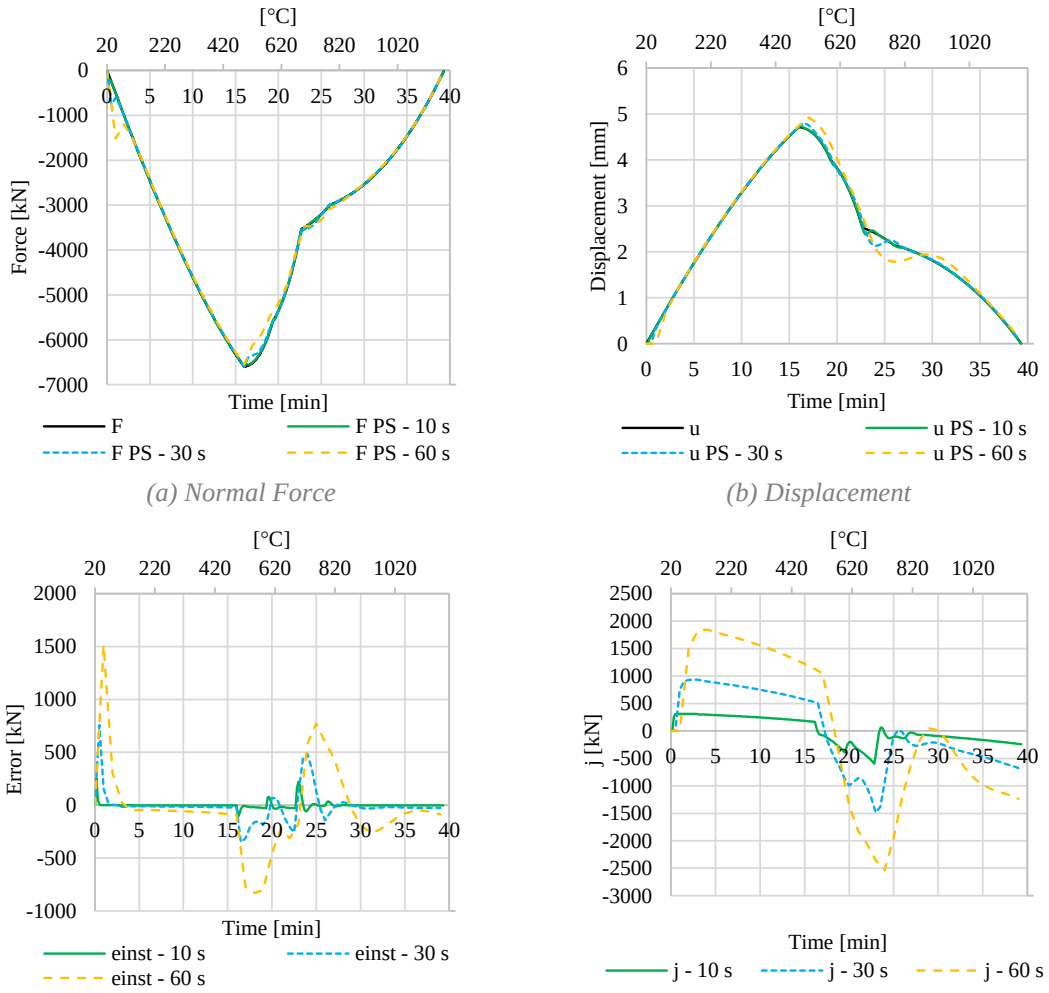

(a) Normal Force *(b) Displacement*

(c) Instantaneous error *(d) Integral term*

Fig. II-52One-DOF example: 10s, 30s, 60s

II.5.4 Experimental error

In hybrid testing performed in earthquake engineering, experimental errors are a crucial issue because they can result in failure in the test procedure. They were approached in numerous publications such as (Shing et Mahin 1983) and (Mosqueda, Stojadinovic et Mahin 2005) to determine their physical effects.

During a HFT, displacements are determined by numerical computation and applied with hydraulic actuators that are monitored by displacements transducers. Forces developed by the specimen are measured with load cells. Experimental errors are thus unavoidable. The actual controlled displacement $\hat{\mathbf{u}}_{PS_i}$ and the measured reaction $\hat{\mathbf{f}}_{PS_i}$ can be expressed as:

$$\begin{aligned} \hat{\mathbf{u}}_{PS_i} &= \bar{\mathbf{u}}_{PS_i} + \mathbf{e}_{u,i} \\ \hat{\mathbf{f}}_{PS_i} &= \bar{\mathbf{f}}_{PS_i} + \mathbf{e}_{f,i} \end{aligned} \tag{II-119}$$

$\mathbf{e}_{u,i}$ and $\mathbf{e}_{f,i}$ are respectively the experimental errors committed on the displacement $\bar{\mathbf{u}}_{PS_i}$ that was computed, and the reaction $\bar{\mathbf{f}}_{PS_i}$. According to (Shing et Mahin 1983), they can be divided into measurement error $\mathbf{e}^m$ and control error $\mathbf{e}^c$:

$$\begin{aligned}\mathbf{e}_{u,i} &= \mathbf{e}_{u,i}^{c} + \mathbf{e}_{u,i}^{m} \\ \mathbf{e}_{f,i} &= \mathbf{e}_{f,i}^{c} + \mathbf{e}_{f,i}^{m} = \mathbf{K}_{PS_i}\mathbf{e}_{u,i}^{c} + \mathbf{e}_{f,i}^{m}\end{aligned} \tag{II-120}$$

Using equation (II-120) and given that $\bar{\mathbf{f}}_{PS_i}=\mathbf{K}_{PS_i}\bar{\mathbf{u}}_{PS_i} + \mathbf{f}_{PS_i}^{TH}$, one can rewrite equation (II-119) as:

$$\begin{aligned}\hat{\mathbf{u}}_{PS_i} &= \bar{\mathbf{u}}_{PS_i} + \mathbf{e}_{u,i}^{c} + \mathbf{e}_{u,i}^{m} \\ \hat{\mathbf{f}}_{PS_i} &= \mathbf{K}_{PS_i}\left(\bar{\mathbf{u}}_{PS_i} + \mathbf{e}_{u,i}^{c}\right) + \mathbf{e}_{F,i}^{m} + \mathbf{f}_{PS_i}^{TH}\end{aligned} \tag{II-121}$$

As the corrections are based on the errors between the interface forces, the experimental errors on the forces and displacements will inevitably alter the solution obtained by the HFT which uses a proportional integral control. The instantaneous error and integral term can be rewritten as follows:

$$\begin{aligned}\widehat{\mathbf{e}_i}^{inst} &= -\left(\hat{\mathbf{f}}_{NS_i} + \hat{\mathbf{f}}_{PS_i}\right) \\ &= -\left(\left(\mathbf{K}_{NS_i}\left(\bar{\mathbf{u}}_{PS_i} + \mathbf{e}_{u,i}^{m}\right) + \mathbf{f}_{NS_i}^{TH}\right) + \left(\mathbf{K}_{PS_i}\left(\bar{\mathbf{u}}_{PS_i} + \mathbf{e}_{u,i}^{c}\right) + \mathbf{f}_{PS_i}^{TH} + \mathbf{e}_{F,i}^{m}\right)\right) \\ &= \bar{\mathbf{e}}_i^{inst} - \left(\mathbf{K}_{NS_i}\mathbf{e}_{u,i}^{m} + \mathbf{K}_{PS_i}\mathbf{e}_{u,i}^{c} + \mathbf{e}_{F,i}^{m}\right) \\ \hat{\mathbf{j}}_{i+1} &= \hat{\mathbf{j}}_i + \widehat{\mathbf{e}_i}^{inst}\end{aligned} \tag{II-122}$$

The equations show that experimental errors alter the proportional term and can accumulate in the integral term. As the measurement or control errors are bounded, they do not pose any stability problems. Nevertheless, they can be responsible for overcorrections and therefore a loss of performance of the controller. Consequently, the order of magnitude of the experimental error should not be greater than the performed corrections.

The effect of experimental errors is illustrated in the hereunder graph (Fig. II-53) in the case of the elastic system described in Section II.5.1. The double eigenvalue λ^* is equal to 0.1 and the displacement of PS and NS are updated every 10s ($T = 10s$). Experimental errors in displacements and forces of the PS evaluated with the rules given in the "Guide to the expression of uncertainty in measurement" (BIPM 2008), following the case presented in the Section 4.3.5 : one considers that the value of the input quantity lies within an interval $[a^-, a^+]$ is equal to 0.5. The standard recommends to assume an equivalent normal distribution of possible values of displacements or forces with standard deviation σ equal to 1.48s, "s" being the notation of the half-width of the interval, $\frac{a^+ - a^-}{2}$.

The following intervals are assumed for the forces and displacements:

- $\pm 0.1\%$ of the maximum force reached by the system (6500 kN)
- ± 0.005 mm for the displacement transducers.

The force and the displacement fit the correct solutions with or without experimental errors. Fig. II-53 (c) and (d) shows that the instantaneous error and the integral term are affected by small overcorrections.

If the previous intervals are multiplied by 10, one obtains the following bounds:

- $\pm 1\%$ of the maximum force reached by the system (6500 kN)
- ± 0.05 mm for the displacement transducers.

This case is particularly unfavourable but allows to show more clearly the effects of experimental errors in Fig. II-54, especially the small spikes that can appear in the force of the PS and the NS. Nevertheless, despite this very unfavourable case, the solution is well reproduced by the controller.

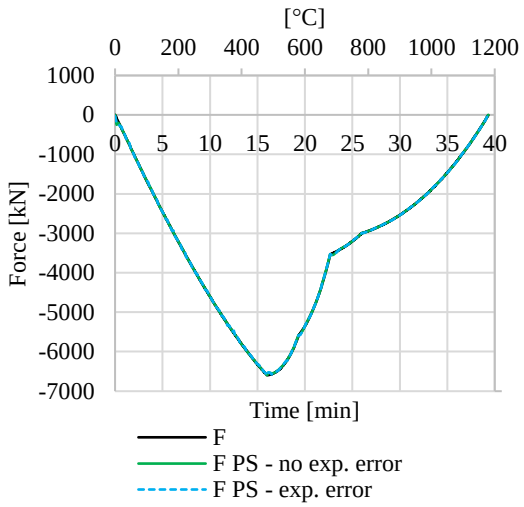

(a) Normal Force

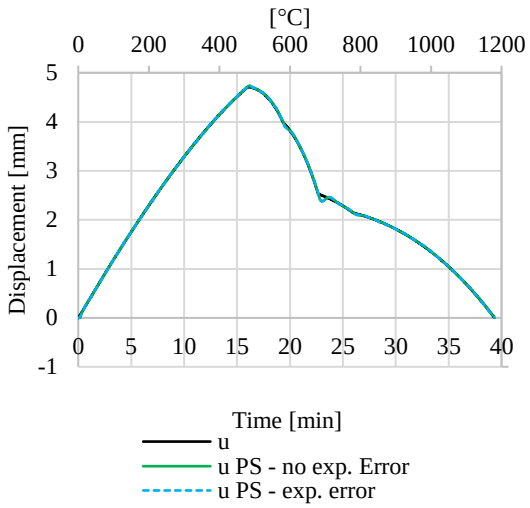

(b) Displacement

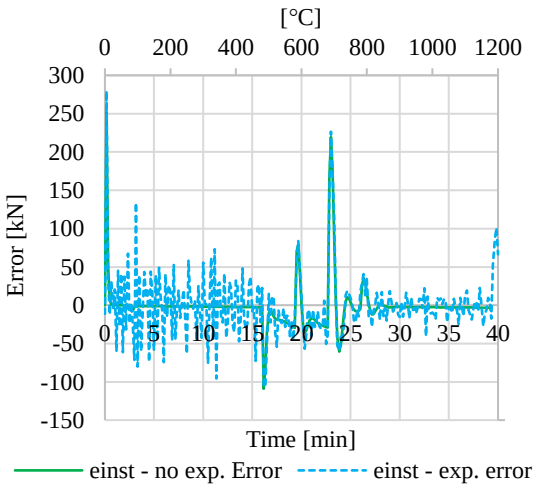

(c) Instantaneous error

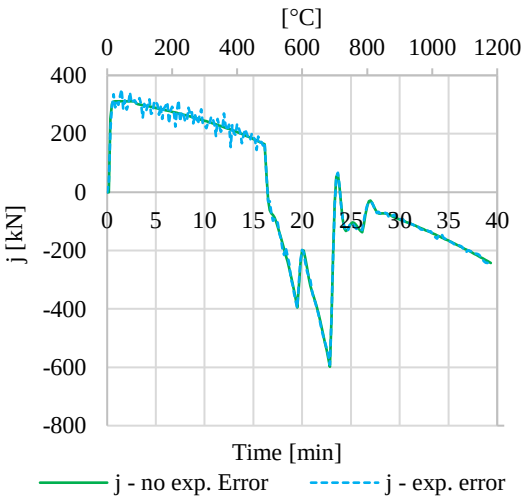

(d) Integral term

Fig. II-53 One-DOF example with and without experimental error $\pm 0.1\%, \pm 0.005\ mm$

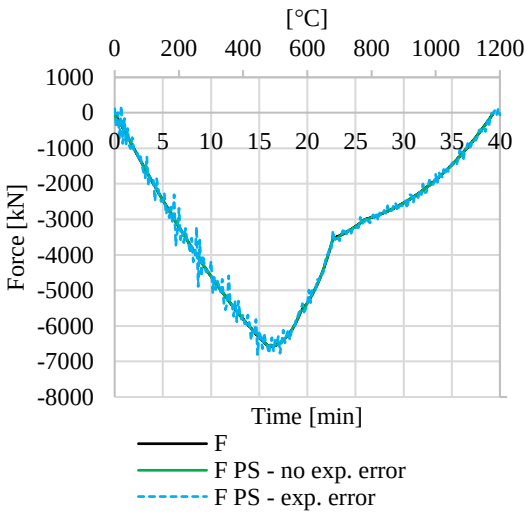

(a) Normal Force

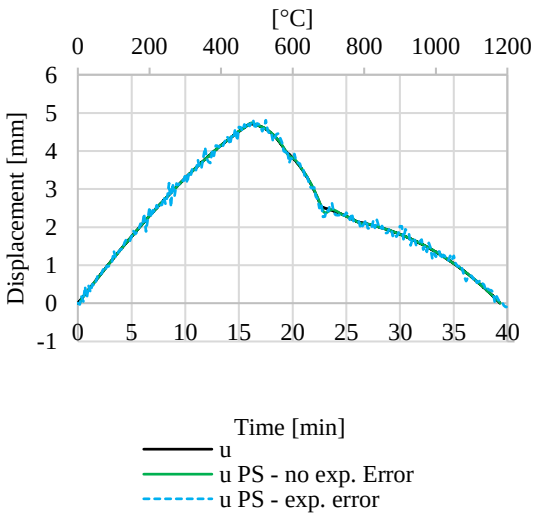

(b) Displacement

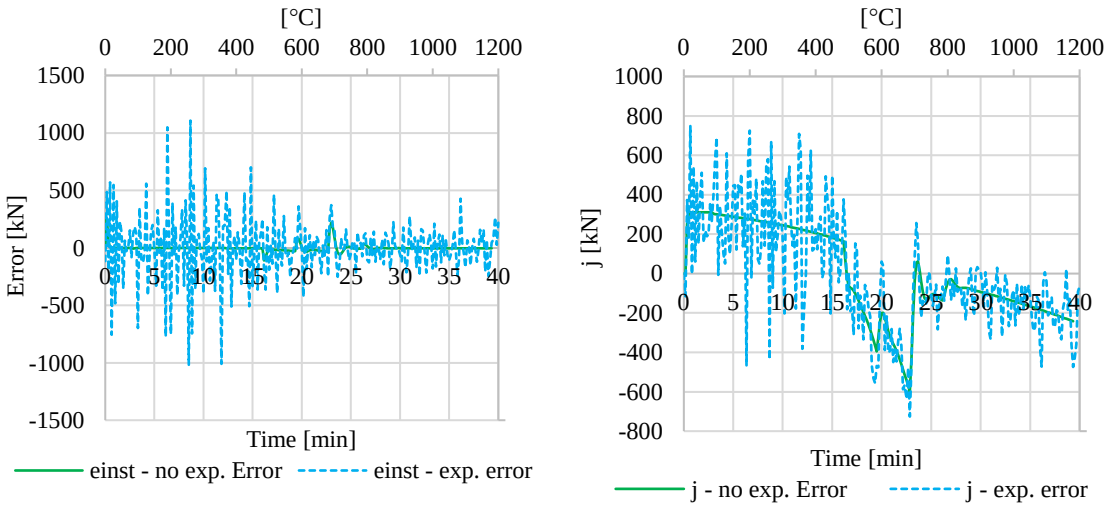

(c) Instantaneous error *(d) Integral term*

Fig. II-54 One-DOF example with and without experimental error $\pm 1\%, \pm 0.05$ mm

II.5.5 Corotational transformations

It is not always possible to control all the DOFs obtained after extraction of the PS from the entire structure. For instance, in Fig. II-55, the PS is a beam of a multi-storey building. After substructuring, there are six DOFs. However, all of them cannot be controlled in the furnace.

A powerful tool that allows to deal with this issue is the corotational theory that was developed to deal with large displacement of structures. Large displacements can in fact lead to the development of complex models. However, very often, large transformations of slender structures are associated only with small deformations of their constituent elements. The movements are therefore mainly made up of a rigid body motion. In the corotational description, the motion of the body is decomposed into rigid body motion and relative deformation. The usual approaches provide a non-linear framework in which linear measures of stress and strain can be applied locally without significant loss in accuracy. For this reason, the corotational theory is gaining popularity among the engineering community for the non-linear analysis of both planar and spatial beam structures.

Corotational theory has been widely developed for several types of beams (Bernoulli, Timoshenko, etc.). For these slender structures, one generally prefers to choose a corotational coordinate system linked to the geometry of the elements and rotating with them (see Fig. II-56). One then makes carry the non-linearities of the great movements on the changes of reference marks, the elementary strains remaining linear in the corotational reference.

A complete synthesis of Corotational Finite Elements is proposed in (Felippa et Haugen 2005). It follows on from previous work presented, among others, in (Wempner 1969), (Belytschko et Hsieh 1973), (Bergan et Horrigmoe 1976), (Nour-Omid et Rankin 1991) and (Crisfield et Moita 1996). This approach assumes small perturbations in the corotational frame. It has the advantage of allowing the use of the operators of already existing conventional linear elements.

Corotational theory has not only been applied to beams. Formulation for plates, shell and solid element has been also developed. Polar decomposition is often chosen to deal with shell and deformable solids. Such approaches and the associated mathematical tools, in particular for the computation of rotation operators and for derivations, are studied in (Truesdell et Toupin 1960), (Bathe, Ramm et Wilson 1973), (Belytschko et Hsieh 1979), (Hughes, Pister et Taylor 1979) and

(Argyris 1982). For plates, the usual corotational transformations are similar to the one developed for beams.

In earthquake engineering, the corotational transformations are widely used in hybrid testing and some of them are provided in (Schellenberg , Mahin et Fenves 2009). In Section II.6 and in Chapter III, the PS consists of a beam and a column. Consequently, the corotational transformation that will be used is based on the previous work in this field. The reference used in this dissertation is (Urthale et Reddy 2005) that provides formulations for analysis of planar beams. They will be given explicitly in the relevant sections.

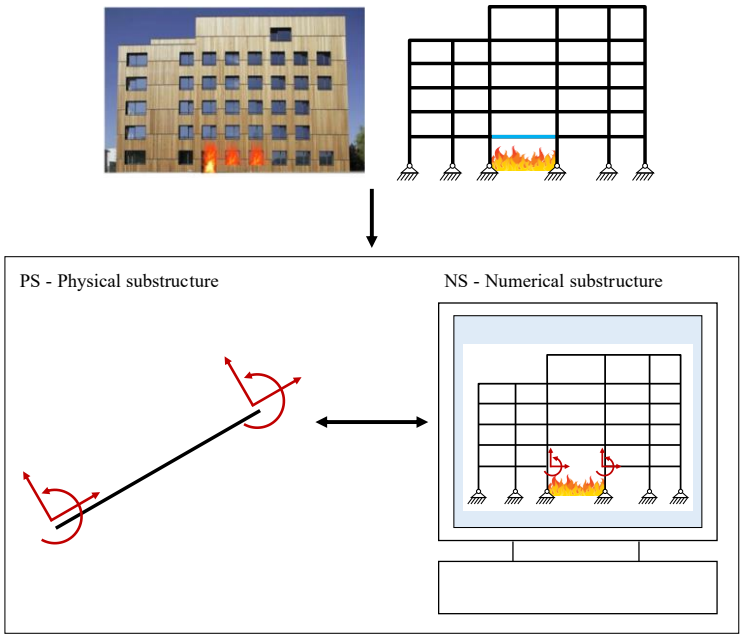

Fig. II-55 Extraction of the PS from the complete structure

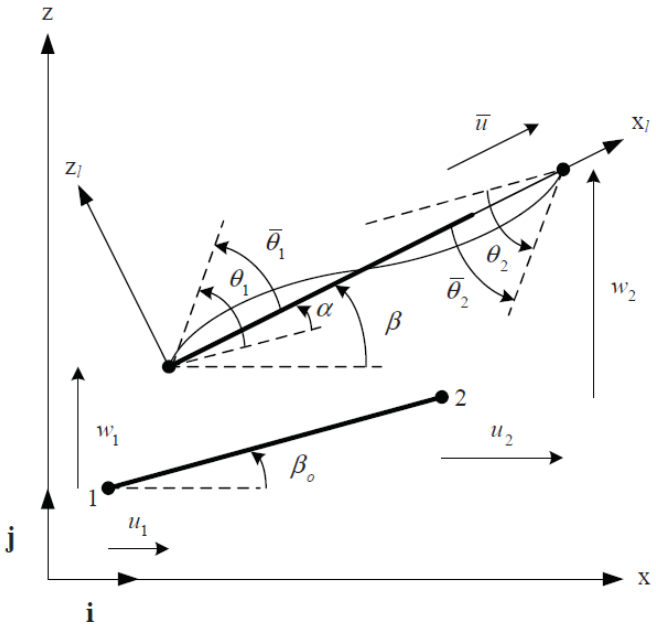

Fig. II-56 Beam kinematics (Urthale et Reddy 2005)

II.6 Numerical application of the proportional integral controller

This Section approaches an application of the proportional integral controller through a "virtual" HFT (VHFT): the PS is modelled in SAFIR® (Franssen et Gernay 2017) instead of being tested physically. The temperatures in the section are precalculated, depending on the nominal fire curve. The NS is also modelled, separately, in SAFIR® which allows accounting for its nonlinear response and the fact that it is partly heated.

In this VHFT, the proportional integral controller is first designed with the exact stiffness of the PS. Then, a parametric study is performed, and the controller is designed with different estimations of this stiffness. Realistic experimental errors and delay are considered for both cases.

II.6.1 Case of study

Multi-storey Frame

The multi-storey frame is a moment resistant frame proposed by (Sadek, et al. 2010). The building is a 10-storey 5-bay frame. It is designed according to the ASCE 7-02 and is representative of a generic office building. ASTM A992 structural steel with yield strength 344.8 MPa is considered for each structural element. The layout, elevation, section and loads are shown in Fig. II-57.

The analysis is performed on a 2D internal frame with beam span of 9.1 m. The load combination is equation A-4-1, presented in the ANSI/AISC 360-16 in Appendix 4. Notional loads are used to represent the effects of initial system imperfections in the position of points of intersection of members (ANSI/AISC 360-16, Section C2.2b). The composite action between beams and concrete slab is neglected. Thus, the moment resisting frame is loaded with distributed loads, vertical concentrated forces (reactions from the transversal frame), and horizontal forces (imperfections).

The fire initiates on the eighth floor and spreads horizontally. The compartments that are affected are highlighted in Fig. II-57 and labelled as Ci, where "i" refers to the bay number.

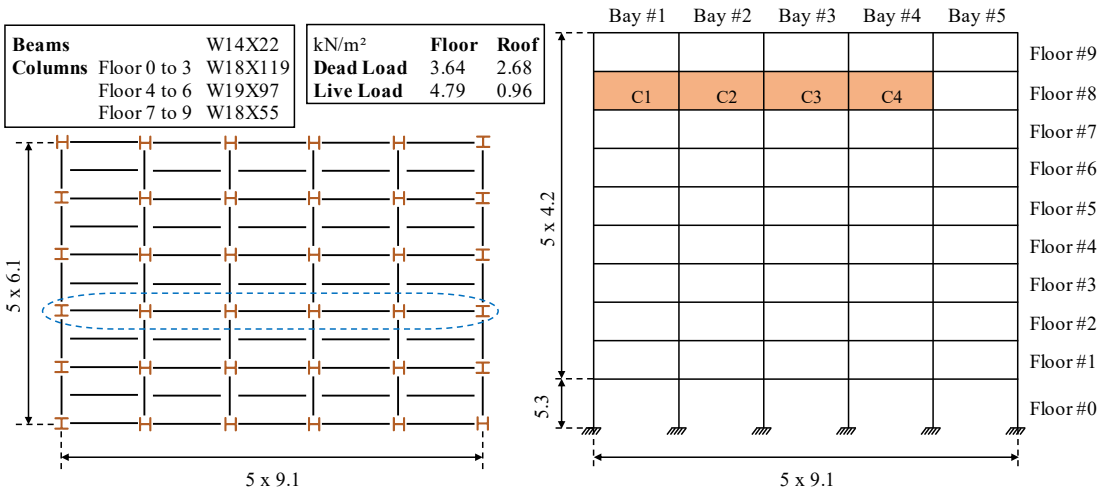

Fig. II-57 Plan layout, elevation, sections and loads. Dimension units are in meters

Temperature

The evolution of the temperature is given by equations A.1 and A11C in EN1991-1-2, Appendix A (the parameter Γ is set to 1) and can be seen in Fig. II-58 (a). The duration of the heating

phase is 180 min. The fire starts in a new compartment every 50 min. $\theta_h(t)$ is the temperature during the heating phase:

$$\theta_h(t) = 20 + 1325 - 429{,}3\exp\left(-\frac{0.2t}{3600}\right) - 270{,}3\exp\left(-\frac{1.7t}{3600}\right) - 625{,}4\exp\left(-\frac{19t}{3600}\right) \quad \text{(II-123)}$$

$\theta_c(t)$ is the temperature of the cooling phase:

$$\theta_c(t) = \theta_h(5400) - 250\left(\frac{t}{3600} - 3\right) \quad \text{(II-124)}$$

The temperature of the beams and columns in several compartments (precalculated in SAFIR®) is presented in Fig. II-58 (b) and (c).

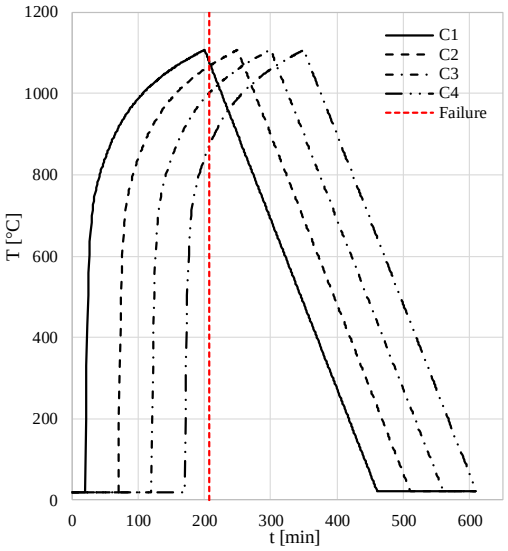

(a) Time-Temperature curve given by equations A.1 and A11C, in EN1991-1-2, Appendix A

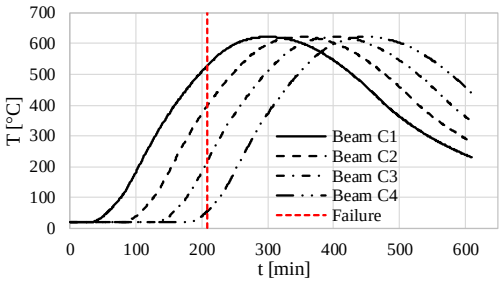

(b) Temperature in Beams (performed in SAFIR®)

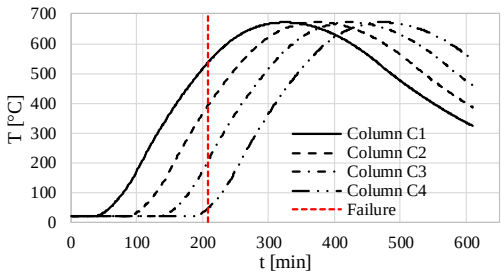

(c) Temperature in Columns (performed in SAFIR®)

Fig. II-58 Temperature curves

SAFIR model

Thermal and structural analysis of the whole building was performed in SAFIR®. The following assumptions were made for the structural model: beams and columns are beam elements rigidly connected to each other and the supports of ground floor columns are fixed. Eurocode dependent material properties (CEN. EN 1993-1-2:2005) are used for all structural elements. Before being heated, the structure is loaded linearly for 20 minutes.

The beam located in compartment C1 collapses at 208 minutes after the formation of plastic hinges at its ends. The mean temperature of the section is equal to 532°C, with approximately 630 °C in the upper flange and 830°C in the lower flange. The beam is under compression and bending during the analysis and the behaviour changes to tensile action at the end of the test. The bending moments and normal force diagram of this beam are illustrated in Fig. II-59. The curves of the displacements and the internal forces in function of time are shown in Fig. II-60. For clarity, the loading phase of the structure is not shown. The time axis starts at t = 20 min.

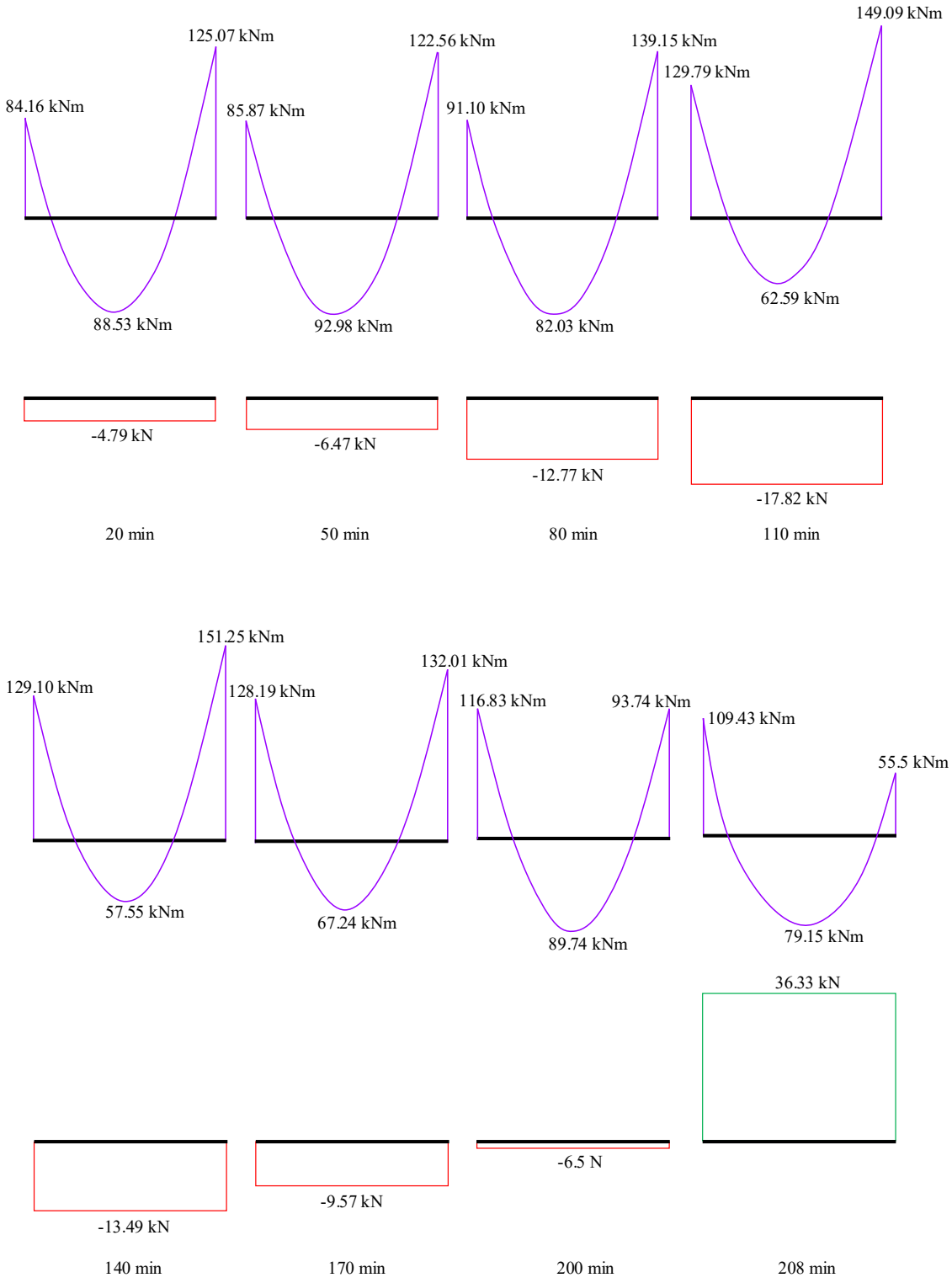

Fig. II-59 Bending moment and normal diagram of the beam in compartment C1

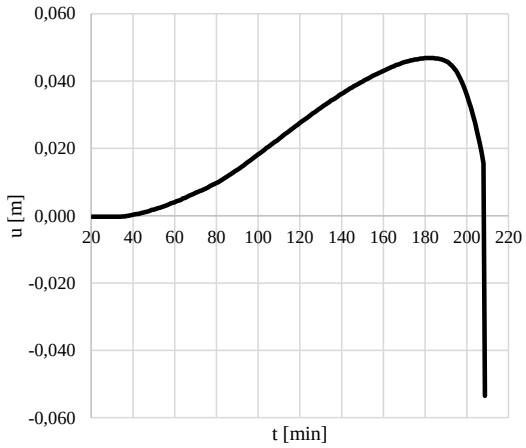

(a) Axial displacement

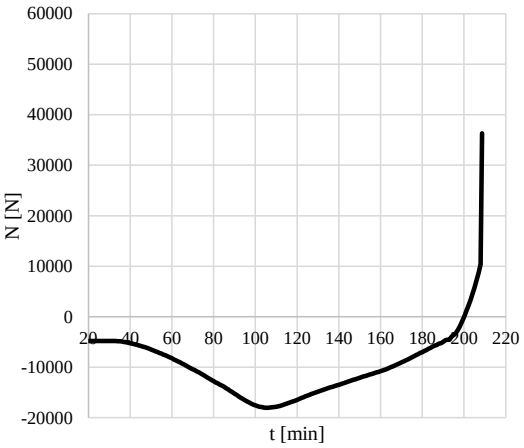

(b) Axial force

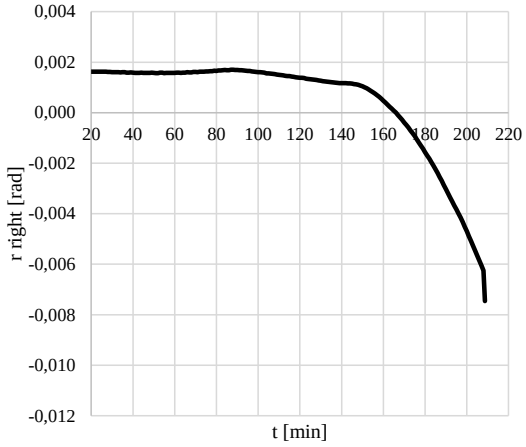

(c) Rotation (right)

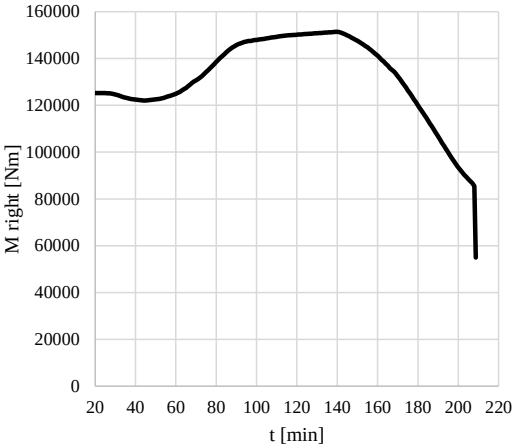

(d) Bending moment (right)

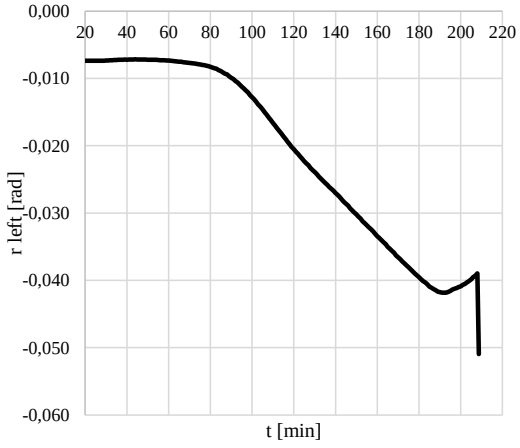

(e) Rotation (left)

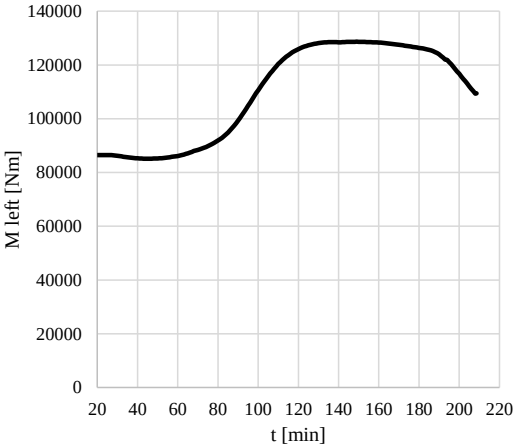

(f) Bending moment (left)

Fig. II-60 Displacements and internal forces of the beam in compartment C1

II.6.2 Parameter of the VHFT

Physical and numerical substructure

The PS is a steel beam W14x22 (located in compartment C1) and is exposed to fire on three sides. The NS is the remaining substructure. To perform a VHFT with PS and NS modelled in SAFIR®, the HFT methodology is implemented as an automatic procedure. An intermediate software was developed to ensure the connections between PS and NS. The framework is illustrated in Fig. II-61.

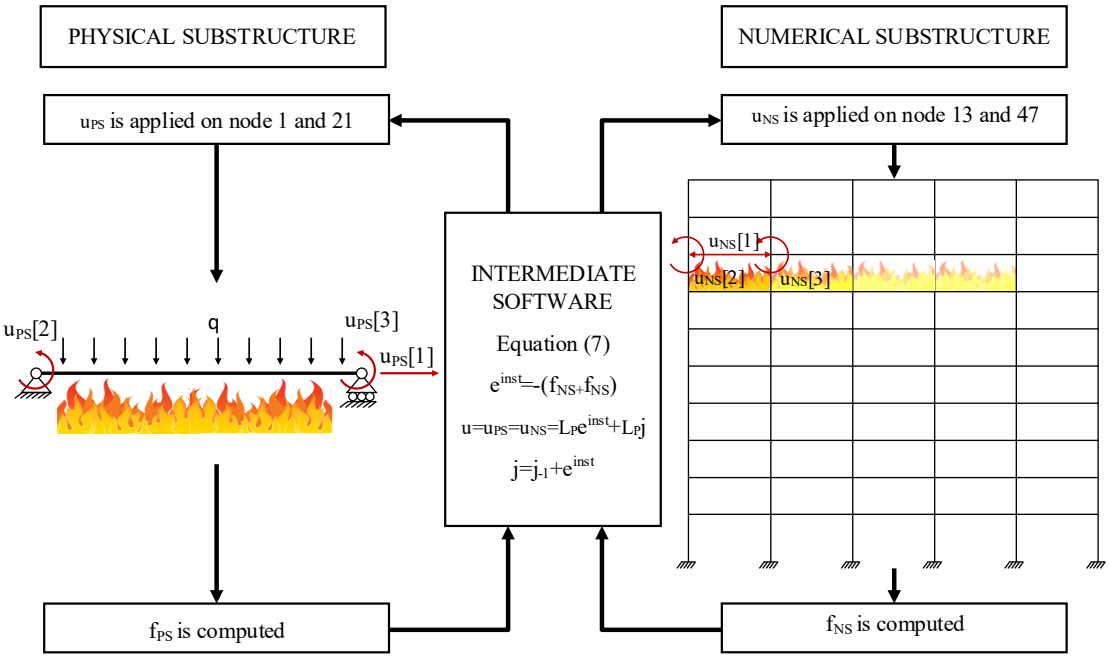

Fig. II-61 Framework of the VHFT

After substructuring, there are six DOFs at the interface of the PS as the NS. However, in a furnace, rigid body motion must be avoided, and it is thus necessary to suppress DOFs and block both vertical and one horizontal displacements. The model of the PS in SAFIR® considers this limitation and is a beam with two supports. The axial displacement and the rotations at both extremities of the beam are controlled and noted $\mathbf{u}_{\mathrm{PS}}$ in Fig. II-61. This condensation of the controlled DOFs keeps the modes of deformation that generates internal forces. An experimental setup for this configuration was proposed by (Sauca 2017, pp 175-185). The link between the six "global" DOFs and the three "local" DOFs is given by the corotational theory, is shown in Fig. II-62 and can be found in (Urthale et Reddy 2005):

$$\begin{aligned} \mathbf{u}_{\mathrm{PS,r}}[1] &= \mathrm{L_n} - \mathrm{L} \\ \mathbf{u}_{\mathrm{PS,r}}[2] &= \mathbf{u}_{\mathrm{PS}}[3] - \alpha \\ \mathbf{u}_{\mathrm{PS,r}}[3] &= \mathbf{u}_{\mathrm{PS}}[6] - \alpha \end{aligned} \tag{II-125}$$

$$\mathrm{L_n} = \sqrt{(\mathrm{L} + \mathbf{u}_{\mathrm{PS}}[4] - \mathbf{u}_{\mathrm{PS}}[1])^2 + (\mathbf{u}_{\mathrm{PS}}[5] - \mathbf{u}_{\mathrm{PS}}[2])^2}$$

$$\alpha = \mathrm{atan}\left(\frac{\mathbf{u}_{\mathrm{PS}}[5] - \mathbf{u}_{\mathrm{PS}}[2]}{\mathrm{L} + \mathbf{u}_{\mathrm{PS}}[4] - \mathbf{u}_{\mathrm{PS}}[1]}\right)$$

Every time step, the three reduced displacements are computed with the control law:

$$\begin{bmatrix} \mathbf{u}_{\mathrm{PS_r}}[1] \\ \mathbf{u}_{\mathrm{PS_r}}[2] \\ \mathbf{u}_{\mathrm{PS_r}}[3] \end{bmatrix}_{\mathrm{i+1}} = \begin{bmatrix} \mathbf{u}_{\mathrm{PS_r}}[1] \\ \mathbf{u}_{\mathrm{PS_r}}[2] \\ \mathbf{u}_{\mathrm{PS_r}}[3] \end{bmatrix}_{\mathrm{i}} - \mathbf{L_P}\left(\begin{bmatrix} \mathbf{f}_{\mathrm{PS}}[1] \\ \mathbf{f}_{\mathrm{PS}}[2] \\ \mathbf{f}_{\mathrm{PS}}[3] \end{bmatrix}_{\mathrm{i}} + \begin{bmatrix} \mathbf{f}_{\mathrm{NS}}[1] \\ \mathbf{f}_{\mathrm{NS}}[2] \\ \mathbf{f}_{\mathrm{NS}}[3] \end{bmatrix}_{\mathrm{i}}\right) + \mathbf{L_J}\mathbf{j}_{\mathrm{i}} \tag{II-126}$$

$\mathbf{f}_{PS}[1]$, $\mathbf{f}_{PS}[2]$ and $\mathbf{f}_{PS}[3]$ are respectively the normal force, the right bending moment, and the left bending moment of the PS. $\mathbf{f}_{NS}[1]$, $\mathbf{f}_{NS}[2]$ and $\mathbf{f}_{NS}[3]$ are the normal force, the right bending moment, and the left bending moment of the NS. The vector $\mathbf{u}_{PS_r}$ can be directly applied to the beam with two supports. As the NS has six DOFs to be controlled, $\mathbf{u}_{PS_r}$ must be adapted. The displacement $\mathbf{u}_{NS} \in \mathbb{R}^{6\times1}$ must be reduced to $\mathbf{u}_{NS,r} \in \mathbb{R}^{3\times1}$. The four translation components are summed up to the relative distance between the node 13 and node 14 of the NS (see Fig. II-61). The elongation in the NS is imposed using the method of Lagrange multipliers, that allows to find the local maxima and minima of a function subject to equality constraints. Details about the method is given in Appendix B. The two rotations are equal to $\mathbf{u}_{PS_r}[2] + \alpha$ and $\mathbf{u}_{PS_r}[3] + \alpha$, α, being the rigid body rotation. This rigid body rotation results from the vertical and horizontal displacements and is thus not directly available. It was chosen to use the rotation of rigid body of the previous time step:

$$\begin{aligned}
\mathbf{u}_{NS,r}[1] &= L + \mathbf{u}_{PS_r}[1] \\
\mathbf{u}_{NS,r}[2] &= \mathbf{u}_{PS_r}[2] + \alpha_{i-1} \\
\mathbf{u}_{PS,r}[3] &= \mathbf{u}_{PS_r}[3] + \alpha_{i-1} \\
\alpha_{i-1} &= \operatorname{atan}\left(\frac{\mathbf{u}_{NS_{i-1}}[5] - \mathbf{u}_{NS_{i-1}}[2]}{L + \mathbf{u}_{NS_{i-1}}[4] - \mathbf{u}_{NS_{i-1}}[1]}\right)
\end{aligned} \tag{II-127}$$

The components are shown in Fig. II-63.

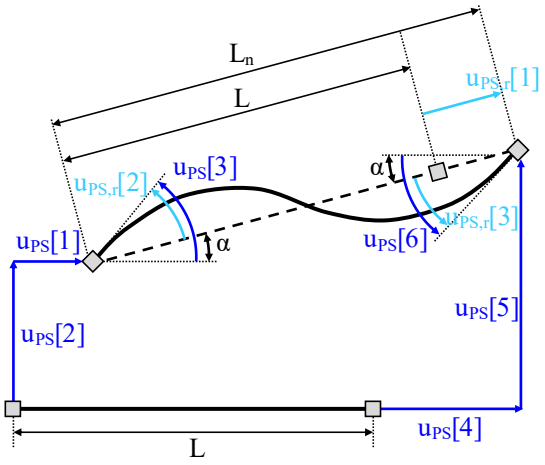

Fig. II-62 Corotational transformations

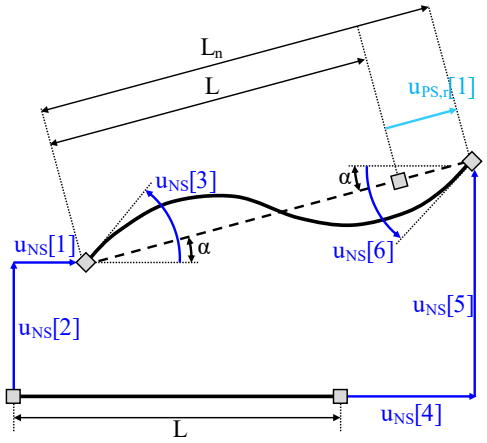

Fig. II-63 Displacement components of the NS

Experimental error and Delays

Experimental errors in displacements and forces of the PS are introduced following the type B evaluation of standard uncertainty of the "Guide to the expression of uncertainty in measurement" (BIPM 2008).

One considers the case presented in the Section 4.3.5 of (BIPM 2008). Based on the available information, one states that the probability that the value of the input quantity lies within an interval $[a^-, a^+]$ is equal to 0.5. In this case, one can assume a normal distribution of possible values of displacements or forces with standard deviation σ equal to $1.48s$, "s" standing for the half-width of the interval, $\frac{a^+ - a^-}{2}$. The following intervals are assumed for the instruments:

- $\pm 0.1\%$ of the full scale for the load cells
- $\pm 0.02\%$ of the full scale for the inclinometers
- ± 0.001 mm for the displacement transducers.

One considers that the highest capacity of the load cell is equal to 100 kN and that the range of the inclinometer is $+/- 10°$.

τ_C and τ_P are neglected and τ_N is set to 20 s. Because of this large delay, large thermal forces (especially in the axial direction) will develop during this interval because of the restrained displacement. This problem was observed by (Wang, et al. 2018) and was eliminated by the implementation of a continuous movement of the actuator, based on the compensation delay technique that was developed in seismic field in (Horiuchi et Konno 1996). Delay compensation and continuous movement of the actuator is used in the simulation based on the development made in (Wang, et al. 2018).

II.6.3 VHFT $\mathbf{K_{PS_0}^{EST} = K_{PS_0}}$

Design of the proportional integral controller

To design the controller, the stiffness of the PS and NS are calculated before the virtual hybrid test using the method proposed by (Sauca 2017, pp. 146-148). The matrices are given hereunder. All the values presented next are expressed in [N], [m] and [rad].

$$\mathbf{K}_{\mathrm{PS}_0} = 10^4 \begin{bmatrix} 9662.1 & 0 & 0 \\ 0 & 762.3 & 381.1 \\ 0 & 381.1 & 762.3 \end{bmatrix} \quad \mathbf{K}_{\mathrm{NS}_0} = 10^4 \begin{bmatrix} 80.8 & 4.1 & 6.1 \\ 4.1 & 623.3 & -333.3 \\ 6.1 & -333.3 & 7667.7 \end{bmatrix} \quad \text{(II-128)}$$

The system contains six eigenvalues that must be chosen. As mentioned in Section II.2.5, to get around this problem, the controller is designed to obtain non-null dominant eigenvalues. It allows to approximate a 6th order system to a first order (one dominant eigenvalue) or second order system (a pair of dominant eigenvalues) that can be linked to the parameter of the step response given in Section II.2.4. One approximates the system to a second order system with double eigenvalues (the others are set to 0).

The multi-storey frame used in this paper is highly protected (Sadek, et al. 2010), meaning that the temperature will evolve slowly. The hypothesis is made that the displacement and the forces of the system can be discretized with an interval of 80 s. The rise time is thus fixed to 80 s. Overshoot is set to 0, meaning that no deviation of system output from its final value is accepted. The value of the double eigenvalue is thus determined using the equation (II-35):

$$\lambda^* = \exp\left(-2.72\frac{\tau}{80}\right) = \exp\left(-2.72\frac{20}{80}\right) = 0{,}51 \quad \text{(II-129)}$$

Equation (II-115) is written with two eigenvalues equal to 0.51 and the others are set to 0. One obtains a system of six equations and six unknowns. An automatic procedure was implemented in MATLAB® and the following gain matrices are obtained for $\mathbf{K}_{\mathrm{PS}_0}^{\mathrm{EST}} = \mathbf{K}_{\mathrm{PS}_0}$:

$$\mathbf{L}_{\mathrm{P}} = 10^{-7}\begin{bmatrix} 0{,}1499 & 0 & 0 \\ 0 & 1{,}0136 & 0 \\ 0 & 0 & 0{,}2413 \end{bmatrix} \quad \mathbf{L}_{\mathrm{J}} = 10^{-7}\begin{bmatrix} 0{,}0489 & 0 & 0 \\ 0 & 0{,}3232 & 0 \\ 0 & 0 & 0{,}1232 \end{bmatrix} \tag{II-130}$$

As the controller is linear, the design consists in finding the gain matrices to obtain stability and appropriate step response properties in the cold phase. When the structure is heated, as the properties are not known, the gain matrices cannot be adapted and consequently the step response properties are degraded. The evolution of the dynamics matrix is simplified and the stability is checked using this simplification in what follows.

Poles Locations

Fig. II-64 (a) shows the location of the poles at the initial phase. These poles are the eigenvalue of the dynamics matrix:

$$\begin{bmatrix} \mathbf{I} - \mathbf{L}_{\mathrm{P}}\left(\mathbf{K}_{\mathrm{PS}_0} + \mathbf{K}_{\mathrm{NS}_0}\right) & \mathbf{L}_{\mathrm{J}} \\ -\left(\mathbf{K}_{\mathrm{PS}_0} + \mathbf{K}_{\mathrm{NS}_0}\right) & \mathbf{I} \end{bmatrix}$$

$$= \begin{bmatrix} -0{,}448 & -0{,}001 & -0{,}001 & 4{,}813\mathrm{E}(-9) & 0 & 0 \\ -0{,}004 & -0{,}372 & -0{,}047 & 0 & 3{,}119\mathrm{E}(-8) & 0 \\ -0{,}001 & -0{,}011 & -0{,}961 & 0 & 0 & 1{,}145\mathrm{E}(-8) \\ -9{,}744\mathrm{E}7 & -4{,}073\mathrm{E}4 & -6.080\mathrm{E}4 & 1 & 0 & 0 \\ -4{,}073\mathrm{E}4 & -1.386\mathrm{E}7 & -4.781\mathrm{E}5 & 0 & 1 & 0 \\ -6.080\mathrm{E}4 & -4.781\mathrm{E}5 & -8.430\mathrm{E}7 & 0 & 0 & 1 \end{bmatrix} \tag{II-131}$$

Where $\mathbf{K}_{\mathrm{PS}_0}$ and $\mathbf{K}_{\mathrm{NS}_0}$ are given in equation (II-128). As mentioned in Section II.5.2 (multi-DOF system), the Gershgorin circles of the matrix are not helpful to determine the spectrum of this matrix and cannot guarantee that the poles do not go outside the unit circle. Consequently, the eigenvalues are explicitly computed using the simplified dynamics matrix:

$$\begin{bmatrix} \mathbf{I} - \mathbf{L}_{\mathrm{P}}\left(\alpha\mathbf{K}_{\mathrm{PS}_0} + \mathbf{K}_{\mathrm{NS}_0}\right) & \mathbf{L}_{\mathrm{J}} \\ -\left(\alpha\mathbf{K}_{\mathrm{PS}_0} + \mathbf{K}_{\mathrm{NS}_0}\right) & \mathbf{I} \end{bmatrix} \tag{II-132}$$

Fig. II-64 (b) shows the location of the poles for $\alpha = [0\colon 0.2\colon 1.0]$ and $\beta = 1$. As observed in a one-DOF system in Section II.5.1, the eigenvalues are located on the perimeter of circles and do not go outside the unit circle. The following observations can be made:

- The module of these poles increases. One expects that the system will be gradually less reactive because of the degradation of the physical stiffness.
- There is a pair of complex conjugate poles (Pair 1, in Fig. II-64 (b)) with a high complex part and high module. The pair seems to be scattered on the perimeter of a circle of radius ~0.5 and centred in abscissa ~0.5. These poles can involve overshoots.
- There is a pair of complex conjugate poles (Pair 2, in Fig. II-64 (b)) that seem to be scattered on the perimeter of a circle of radius ~0.25 and centred in abscissa ~0.75. These poles have great module and great real part, compared to its complex part. These poles tend to dampen the system and could reduce overshoots.
- The third pair of complex conjugates (Pair 3, in Fig. II-64 (b)) has small module and has less influence than the other two pairs.
- One does not obtain a system with dominant eigenvalues and thus cannot precisely evaluate parameters of the step response for $\alpha \neq 1$.

Axial displacement, rotations, normal force and bending moment

The VHFT is performed and the results of the axial displacement and the rotations of the PS over time are shown in Fig. II-69 (a), (c) and (e) ("Reference" is the correct behaviour of the frame modelled as a whole). The normal forces and bending moments of the specimen can be seen in Fig. II-69 (b), (d) and (f). The interface forces of the NS are also shown in these figures. For clarity, the loading phase of the structure is not displayed as in Fig. II-60. The time axis starts at t = 20 min.

As expected by Fig. II-64 (b), the system is stable, which indicates that the simplified state representation used is reliable for this case. Despite the degradation of the time properties, the controller remains sufficiently reactive during the simulation, except at the end. Overshoots are not significant, as foreseen by the poles in Fig. II-64 (b). In fact, when the beam collapses, Fig. II-69 (a), (c) and (e) show that the displacements are applied with some delay because of the high non-linearities. In addition to this, the equilibrium is lost for the normal force, as can be seen in Fig. II-69 (b). At the moment of failure, the controller is not reactive enough to follow this fast phenomenon. Moreover, the design was based on static equations, which is no longer the case when the beam collapses.

Fig. II-69 (b), (d) and (f) shows that the equilibrium of the interface forces is globally ensured. However, one can observe spikes on the three curves of NS. These spikes are particularly significant in Fig. II-69 (d) that shows the bending moment $\mathrm{M(right)}$. These spikes are due to the small overcorrections that appear in the error and integral term of the control law because of experimental errors as explained in Section II.5.4. These spikes are more visible in Fig. II-69 (d) because the highest diagonal term of the stiffness matrix of NS, $\mathbf{K}_{\mathrm{NS}_0}$, corresponds to the DOF associated with this bending moment.

The instantaneous error quantifies and assesses the quality of the algorithm. Fig. II-73 (a)-(c) shows the relative instantaneous error between $\mathbf{f}_{\mathrm{PS}}$ and $\mathbf{f}_{\mathrm{NS}}$ in function of time for each DOF. This error is computed as:

$$\mathrm{Err\ N} = \frac{\mathrm{N_{NS}} + \mathrm{N_{PS}}}{\mathrm{N_{PS}}}\ [\%] \tag{II-133}$$

$$\mathrm{Err\ M_{right}} = \frac{\mathrm{M_{PS}(right)} + \mathrm{M_{NS}(right)}}{\mathrm{M_{PS}(right)}}\ [\%] \tag{II-134}$$

$$\mathrm{Err\ M_{left}} = \frac{\mathrm{M_{PS}(left)} + \mathrm{M_{NS}(left)}}{\mathrm{M_{PS}(left)}}\ [\%] \tag{II-135}$$

In Fig. II-73 (a), the relative error Err N is high at the beginning of the test and then decreases gradually during the virtual test until it is included in the interval $[-5\%, +5\%]$. It increases at the end of the test to follow the collapse of the beam. The errors $\mathrm{Err\ M_{right}}$ and $\mathrm{Err\ M_{left}}$ are low, in particular $\mathrm{Err\ M_{right}}$ that remains under 5% and varies not much. One can however notice that $\mathrm{Err\ M_{left}}$ is greater that $\mathrm{Err\ M_{right}}$. This difference is due to the high spikes of the NS for the right bending moment (Fig. II-69 (d)).

One can also observe that the relative errors of normal force are clearly higher than $\mathrm{Err\ M_{right}}$ and $\mathrm{Err\ M_{left}}$. It is explained by the fact that the stiffness of the PS associated with this axial DOF is much higher than the ones of the rotations. The corrections in displacement and experimental errors have thus more effect on the value of the normal component of the unbalanced force vector.

A VHFT without experimental error was performed to confirm the influence of these errors. The results can be seen Fig. II-70 and the interface errors are shown in Fig. II-73 (d)-(e). If the experimental errors are removed from the test, the spikes of the NS disappear, and the interface errors are lower.

Despite experimental errors and delay, Fig. II-69 shows that the "Reference" is globally well capture by the algorithm. Moreover, although it is based on static equations, one can see that the results follow quite well the curve before failure, even when the beam is close to collapse.

II.6.4 VHFT $\mathbf{K}_{\mathbf{PS_0}}^{\mathbf{EST}} = \boldsymbol{\nu}\mathbf{K}_{\mathbf{PS_0}}$

A parametric study of the steel frame is led for different estimation of the stiffness $\mathbf{K}_{\mathrm{PS}_0}$. This Section aims to test the reliability of the simplified state representation and observe the effect of overestimating and underestimating $\mathbf{K}_{\mathrm{PS}_0}$ on the proportional integral controller.

Design of the proportional integral controller

The gain matrices are computed using the following dynamics matrix:

$$\begin{bmatrix} \mathbf{I} - \mathbf{L}_\mathrm{P}(\nu\mathbf{K}_{\mathrm{PS}_0} + \mathbf{K}_{\mathrm{NS}_0}) & \mathbf{L}_\mathrm{J} \\ -(\nu\mathbf{K}_{\mathrm{PS}_0} + \mathbf{K}_{\mathrm{NS}_0}) & \mathbf{I} \end{bmatrix} \tag{II-136}$$

With $\nu = 1 + \mathrm{n}$. Overestimated (n>0, from +10% to +50%) and underestimated (n<0, from -10% to -50%) of $\mathbf{K}_{\mathrm{PS}_0}$ are considered. Several $\mathbf{L}_\mathrm{P}$ and $\mathbf{L}_\mathrm{J}$ are computed:

$$\mathbf{L}_\mathrm{P} = \begin{bmatrix} \mathrm{L_P(u)} & 0 & 0 \\ 0 & \mathrm{L_P(r\ left)} & 0 \\ 0 & 0 & \mathrm{L_P(r\ righ)} \end{bmatrix} \quad \mathbf{L}_\mathrm{J} = \begin{bmatrix} \mathrm{L_J(u)} & 0 & 0 \\ 0 & \mathrm{L_J(r\ left)} & 0 \\ 0 & 0 & \mathrm{L_J(r\ righ)} \end{bmatrix} \tag{II-137}$$

The gain values for each DOF are shown in Fig. II-68 (a)-(c) for each estimation (from -50% to +50%). One can observe that the values of $\mathbf{L}_\mathrm{P}$ and $\mathbf{L}_\mathrm{J}$ are globally decreasing functions:

- In case of underestimation, higher values of gain are obtained, meaning high reactive controller and possible oscillations and instabilities.
- In case of overestimation, the element of $\mathbf{L}_\mathrm{P}$ and $\mathbf{L}_\mathrm{J}$ are lower. A low reactive controller is thus excepted.

These observations fully align on the findings of Sections II.4.5 and II.5.1.

Poles Locations

As in Section II.5.3, two poles are drawn on 0.51 (real axis) and the others are set to 0 (origin). However, this is not the true position of the poles in the complex plane. Fig. II-65 and Fig. II-66 show the poles of the matrix (II-132) with $\mathbf{L}_\mathrm{P}$ and $\mathbf{L}_\mathrm{J}$ that are computed with matrix (II-136).

Fig. II-65 (a) shows the effect of underestimation on the position of the poles at the initial phase when the PS is not heated. One can see that some eigenvalues are outside the unit circle: the system is thus unstable if the underestimation n is higher than 40%, at the beginning of the test. This limit is valid for this case of study and would be different for another structure. Fig. II-66 (a) shows the effect of overestimation. The poles are scattered on the right side of the unit circle, but their module is not higher than one. As these poles are complex, overshoot is excepted.

For the other cases, Fig. II-65 (b) and Fig. II-66 (b) give the location of the poles during the heating phase. The parameters $\alpha \in [0\colon 0.2\colon 1]$ and $\beta = 1$ are used.

According to Fig. II-66 (b), overestimation is not problematic because there are no poles outside the unit circle. Fig. II-67 (b) compares the case $\nu = 1$ and $\nu = 1.5$. One can see that the real part of the poles increases, which suggests more damping.

Fig. II-65 (b) shows that underestimations from -30% to -10% lead to stable systems but contain poles with negative real part that involves significant oscillations at the beginning of the test. Fig. II-67 (a) compares the case $\nu = 1$ and $\nu = 0.7$ (-30%).

Axial displacement, rotations, normal force and bending moment

To avoid overloading the graphs, the results in case of overestimation and underestimation are split into two figures: Fig. II-71 and Fig. II-72. (a), (c) and (e) are the displacements and (b), (d) and (f) are the forces.

One can see that the simplified model that gives the location of the poles in Fig. II-65 (b) and (d) and the numerical simulation of the HFT corresponds to each other:

- An underestimation higher that 40% is critical because the system becomes unstable, as it was predicted.
- The underestimation from 10 to 30 % does not cause instabilities. However, one can observe in Fig. II-72 (b) oscillations at the beginning of the HFT that are quite high. This is due to the high negative real part of some eigenvalues, as shown in Fig. II-65 (a) and (c).
- The stability of the solution for this scenario is not sensitive to overestimated stiffness and as foreseen by the poles in Fig. II-65 (d), the behaviour is close to the one without estimation.

Relative interface errors are computed for the extreme cases +50% and -30% and are given in Fig. II-74. Err N, Err M_{right} and Err M_{left} are also compared with the interface errors of the controller that was designed with $\mathbf{K}_{\mathrm{PS}_0}^{\mathrm{EST}} = \mathbf{K}_{\mathrm{PS}_0}$. Fig. II-74 (a), (b) and (c) show that the interface error in the case of +50%, is similar to what was shown in Fig. II-73. In the case -30%, the errors at the beginning of the test are higher than the one generated by the controller that was designed exact stiffness because of the oscillations of the negative poles.

The curves that lead to stable system (from -30% to +50%) fit the curve of the reference in an acceptable way. Proportional integral control is also robust to the tested experimental errors and to delays.

II.6.5 Figures

Poles Locations

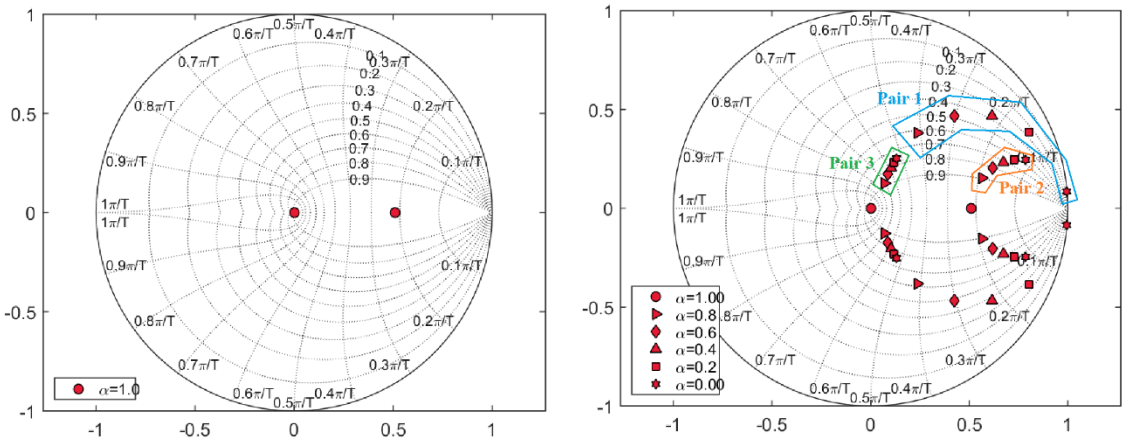

(a) Initial phase *(b) Hot Phase*

Fig. II-64 Poles location $\boldsymbol{K}_{PS_0}^{EST} = \boldsymbol{K}_{PS_0}$

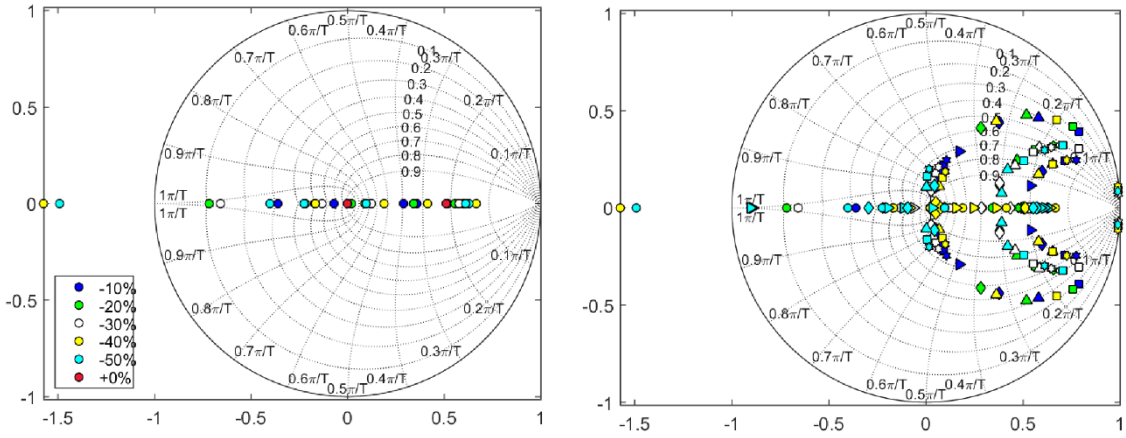

(a) Initial phase *(b) Hot phase*

Fig. II-65 Poles location in case of underestimation

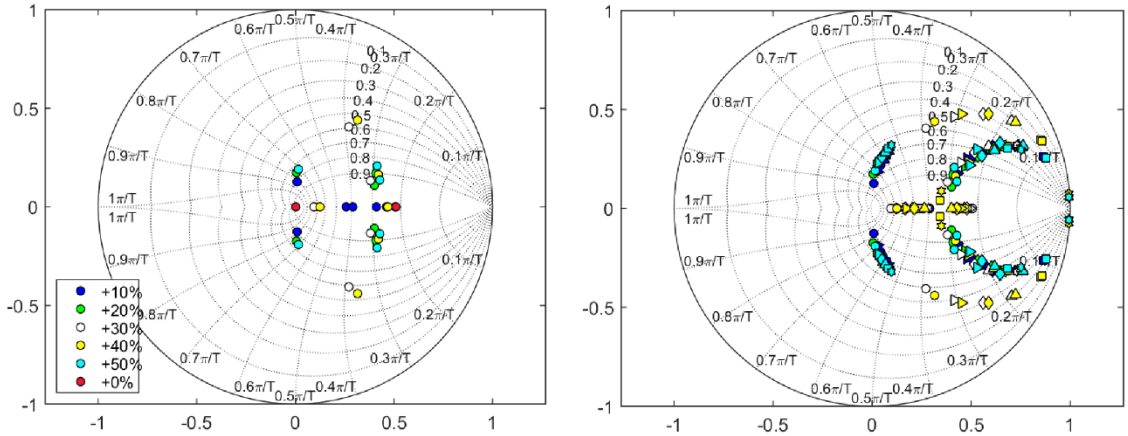

(c) Initial phase *(d) Hot phase*

Fig. II-66 Poles location in case of overestimation

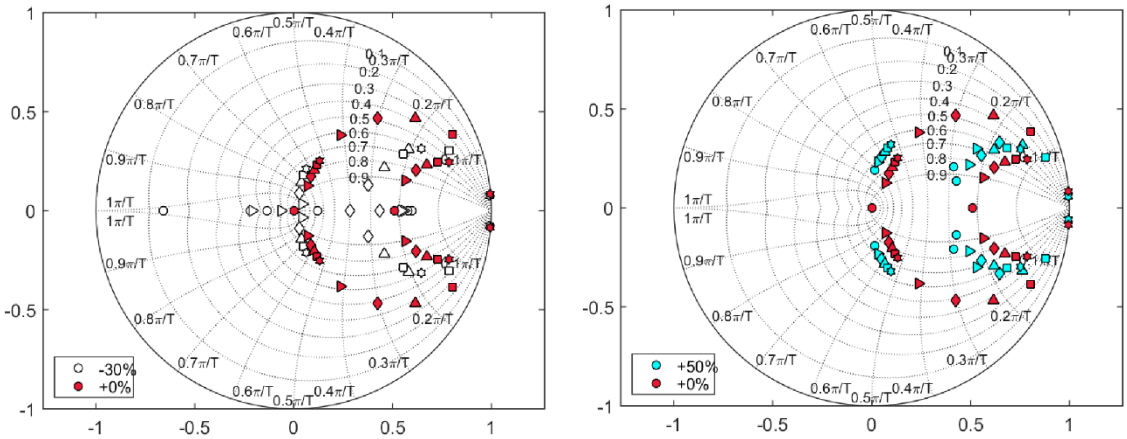

(a) -30% and 0% *(b) +50% and 0%*

Fig. II-67 Comparison of -30% and +50% with 0%

Design of the PI controller

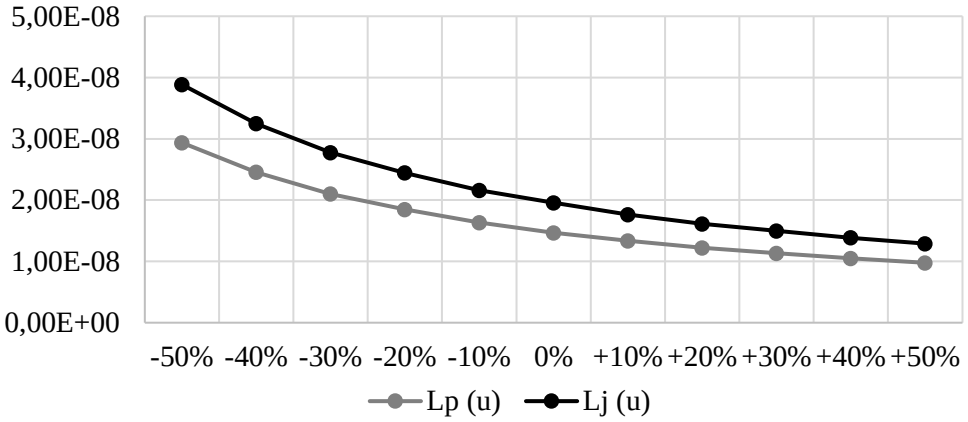

(a) Proportional and integral gain of axial DOF

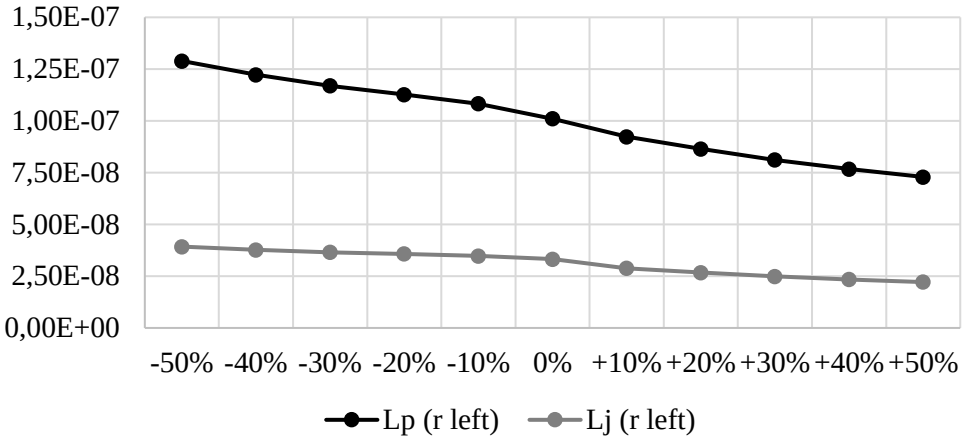

(b) Proportional and integral gain of the left rotation DOF

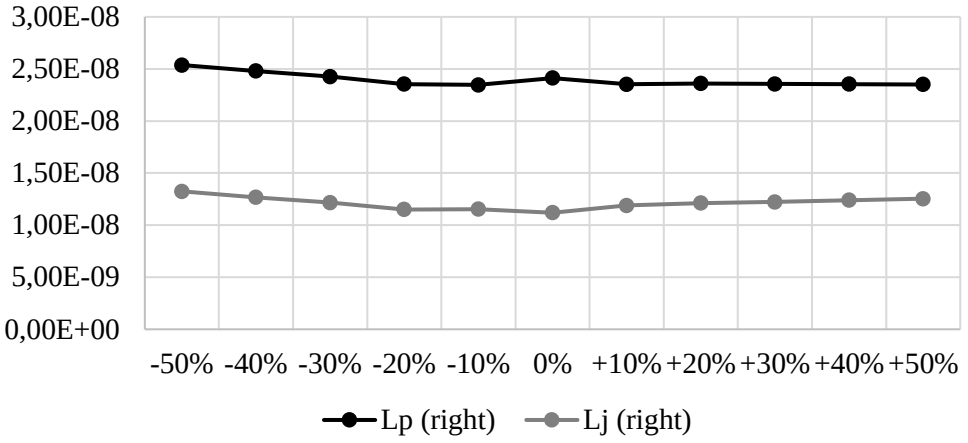

(c) Proportional and integral gain of the right rotation DOF

Fig. II-68 Gains for $\nu = [0.5 ; 0.6 ; 0.7 ; 0.8 ; 0.9 ; 1.0 ; 1.1 ; 1.2 ; 1.3 ; 1.4 ; 1.5]$

Axial displacement, rotations, normal force and bending moments $\boldsymbol{K}_{PS_0}^{EST} = \boldsymbol{K}_{PS_0}$

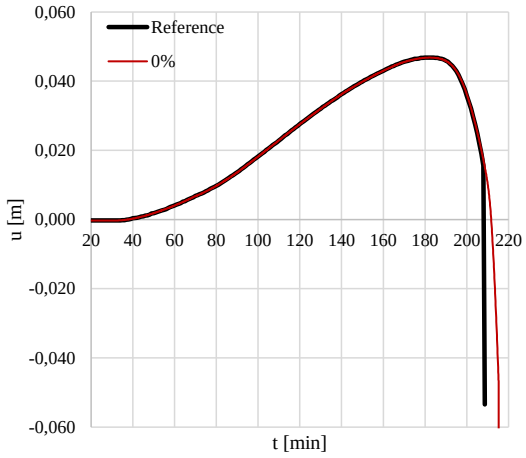

(a) Axial displacement

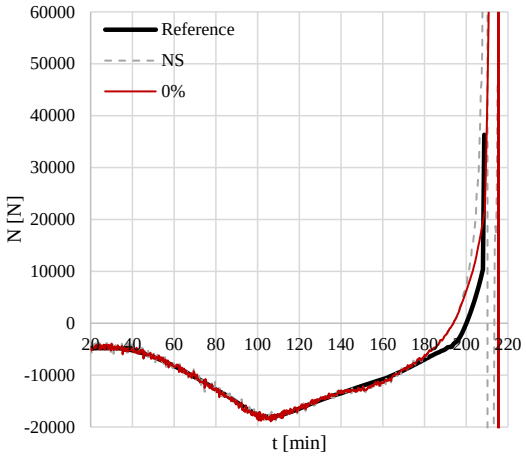

(b) Axial force

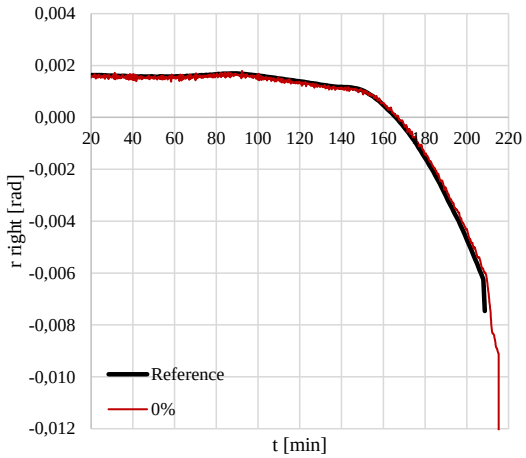

(c) Rotation (right)

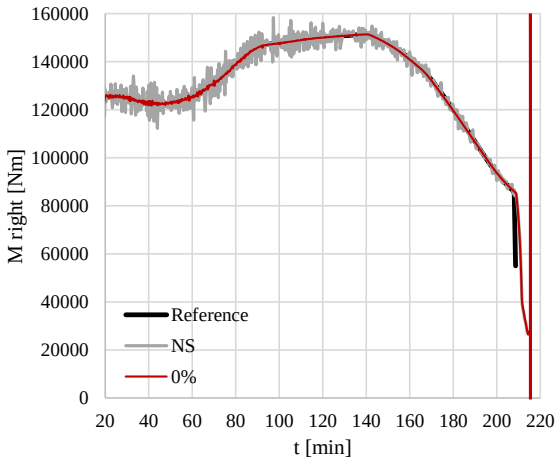

(d) Bending moment (right)

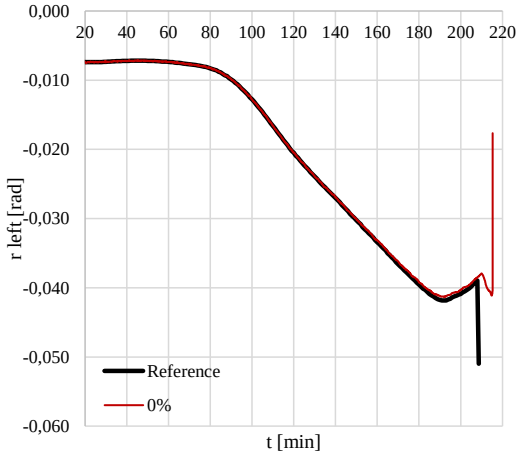

(e) Rotation (left)

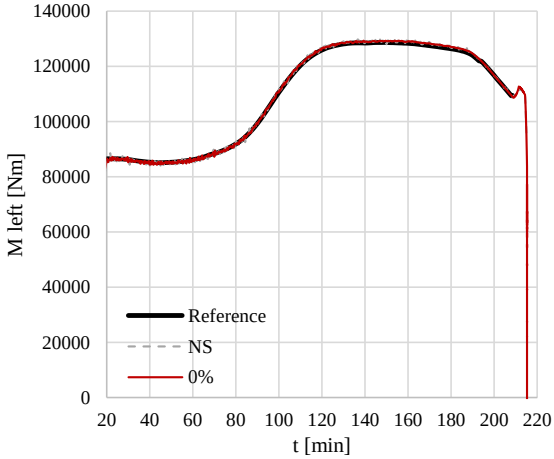

(f) Bending moment (left)

Fig. II-69 VHFT, Proportional integral controller designed with $K_{PS_0}^{EST} = K_{PS_0}$

Axial displacement, rotations, normal force and bending moments $\boldsymbol{K}_{PS_0}^{EST} = \boldsymbol{K}_{PS_0}$ (without experimental errors)

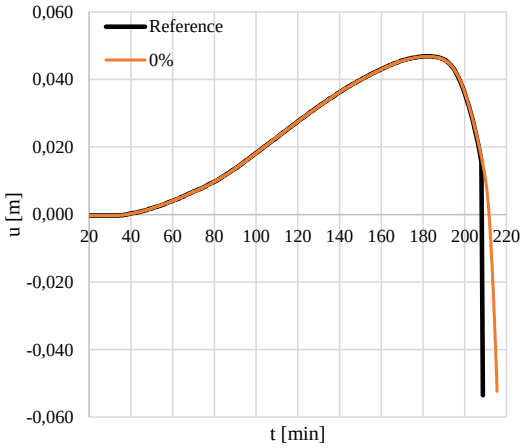

(a) Axial displacement

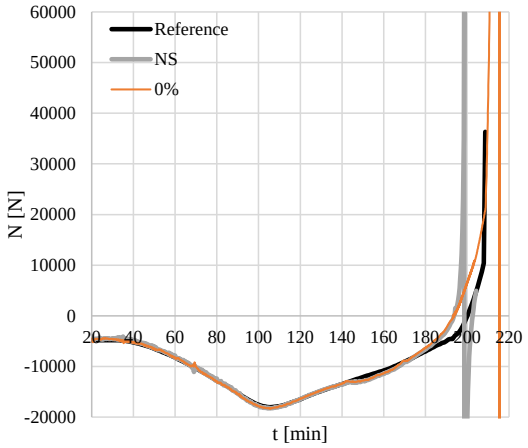

(b) Axial force

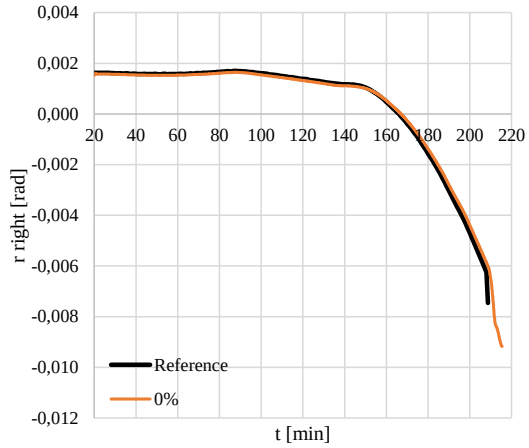

(c) Rotation (right)

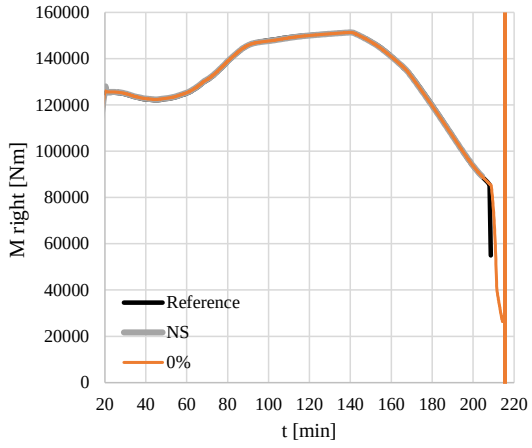

(d) Bending moment (right)

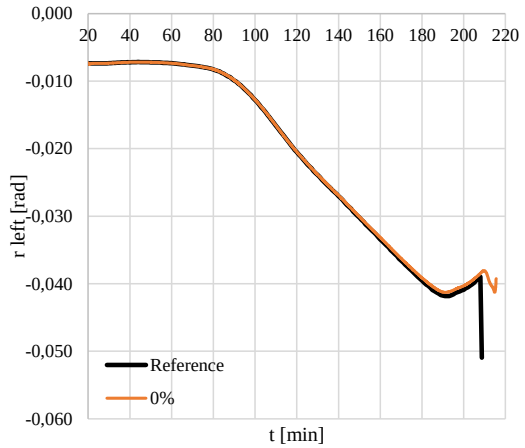

(e) Rotation (left)

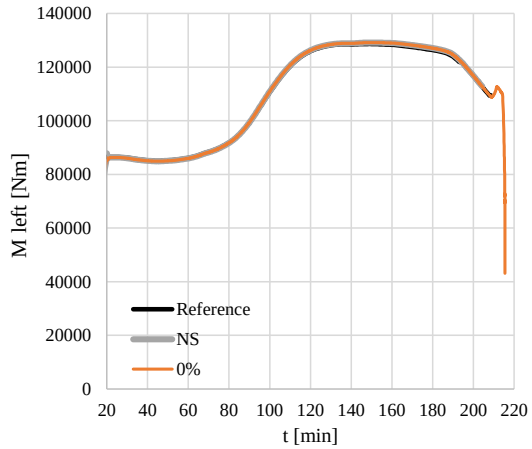

(f) Bending moment (left)

Fig. II-70 VHFT, Proportional integral controller designed with $K_{PS_0}^{EST} = K_{PS_0}$ (no experimental errors)

Axial displacement, rotations, normal force and bending moments $\boldsymbol{K}_{PS_0}^{EST} = \nu \boldsymbol{K}_{PS_0}$ $(\nu > 1)$

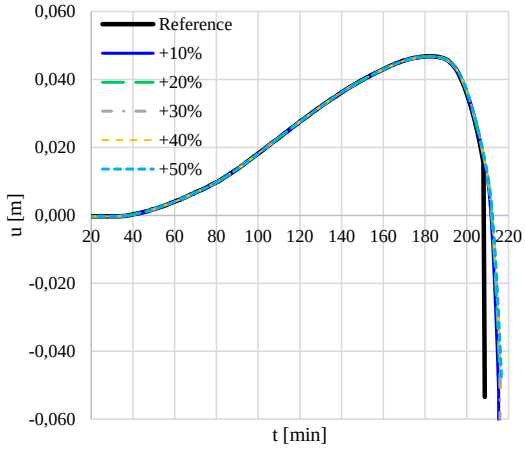

(a) Axial displacement

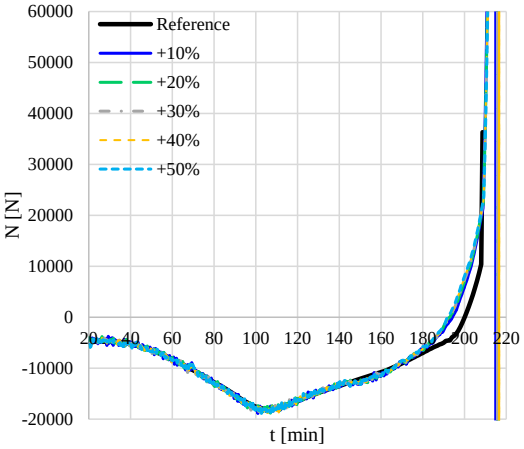

(b) Axial force

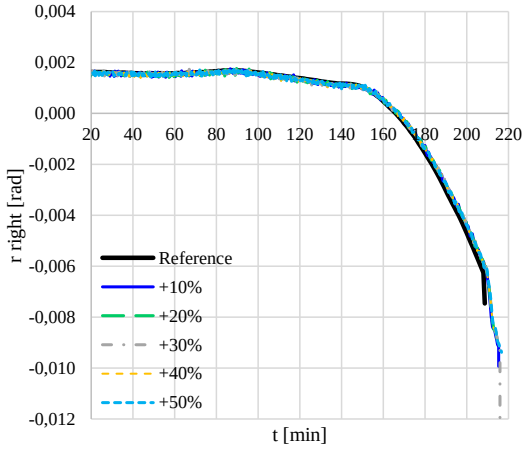

(c) Rotation (right)

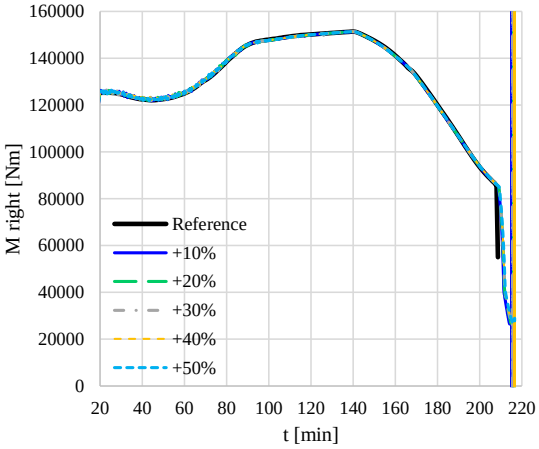

(d) Bending moment (right)

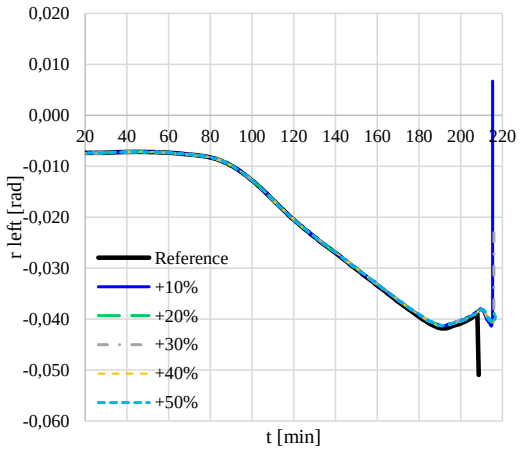

(e) Rotation (left)

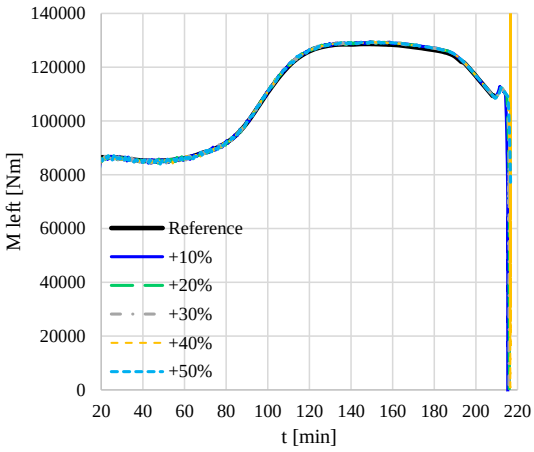

(f) Bending moment (left)

Fig. II-71 VHFT, Proportional integral controller designed with $\boldsymbol{K}_{PS_0}^{EST} = \nu \boldsymbol{K}_{PS_0}$

$\nu = [1.1 ; 1.2 ; 1.3 ; 1.4 ; 1.5]$

Axial displacement, rotations, normal force and bending moments $\boldsymbol{K}_{PS_0}^{EST} = \nu \boldsymbol{K}_{PS_0}$ $(\nu < 1)$

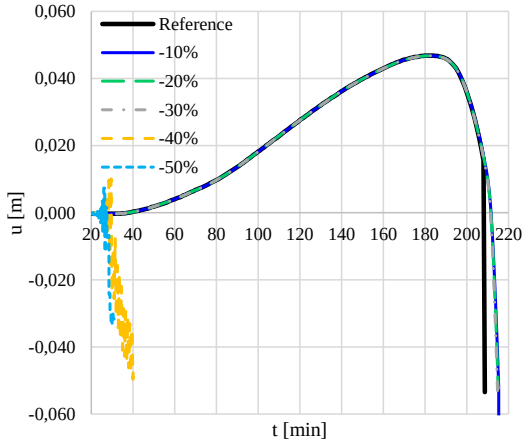

(a) Axial displacement

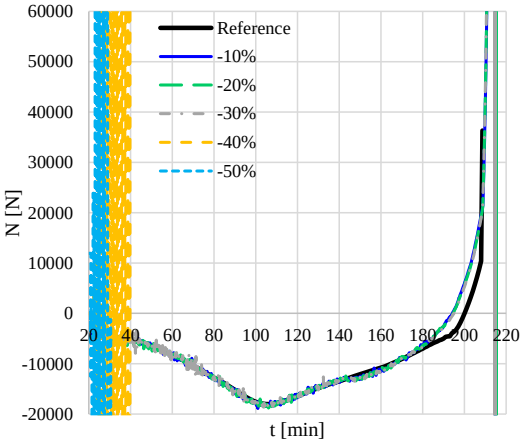

(b) Axial force

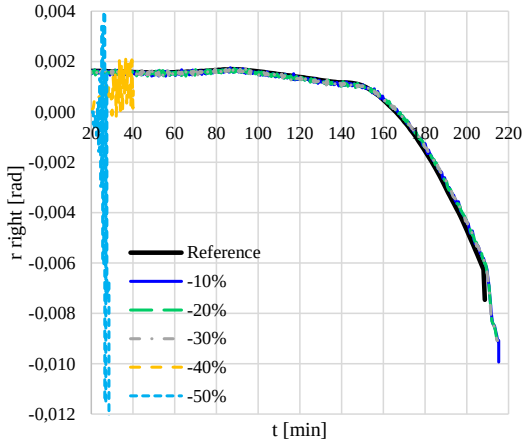

(c) Rotation (right)

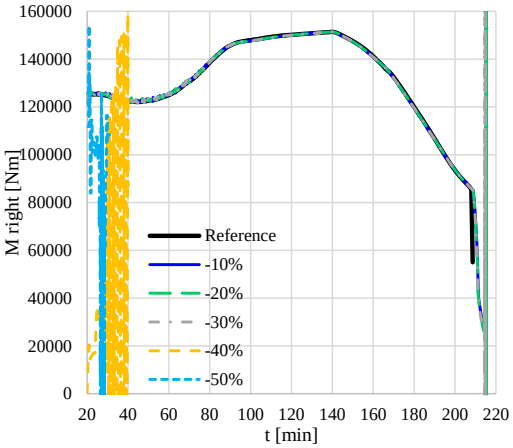

(d) Bending moment (right)

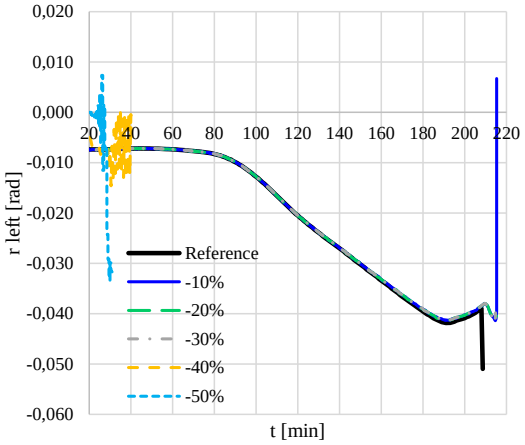

(e) Rotation (left)

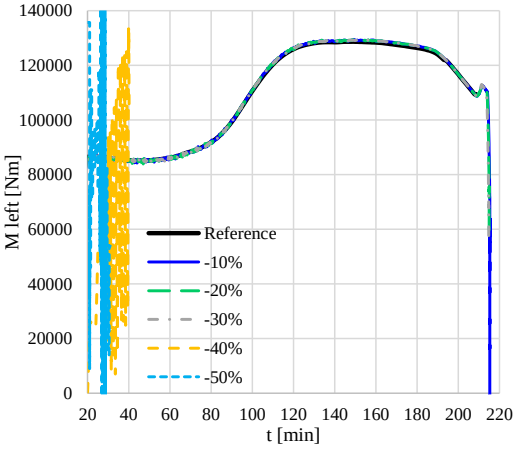

(f) Bending moment (left)

Fig. II-72 VHFT, Proportional integral controller designed with $\boldsymbol{K}_{PS_0}^{EST} = \nu \boldsymbol{K}_{PS_0}$

$\nu = [0.9\ ;\ 0.8\ ;\ 0.7\ ;\ 0.6\ ;\ 0.5]$

Interface errors $\boldsymbol{K_{PS_0}^{EST} = K_{PS_0}}$

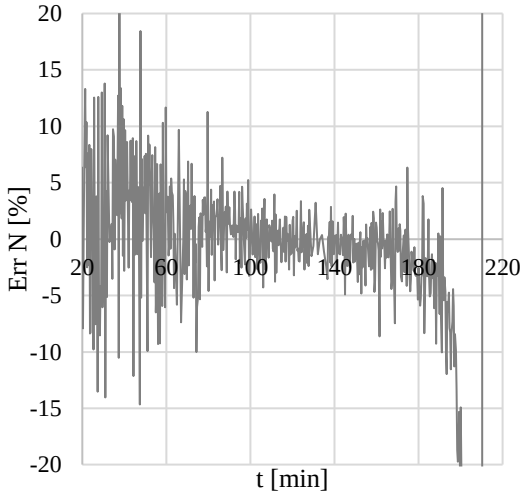

(a) Normal force error

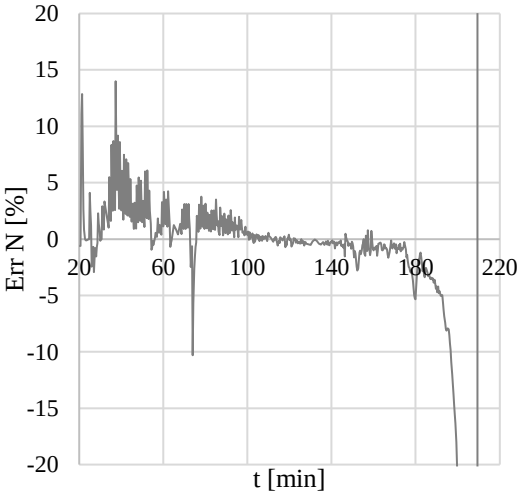

(d) Normal force error, no experimental errors

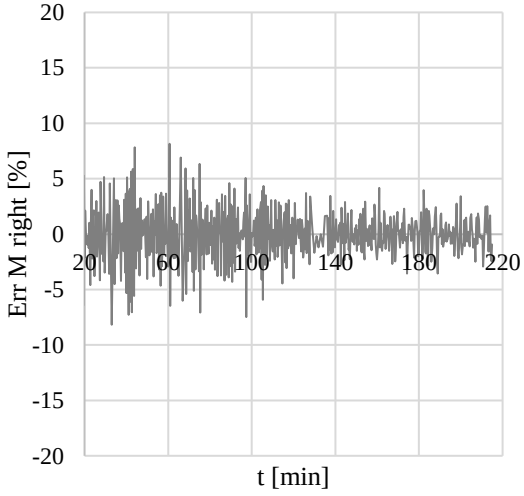

(b) Bending moment (right) error

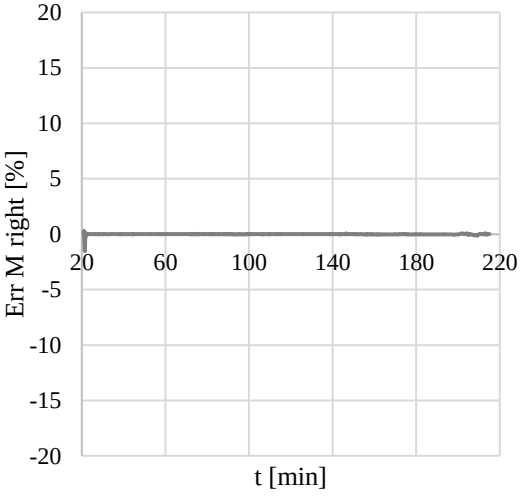

(e) Bending moment (right) error, no experimental errors

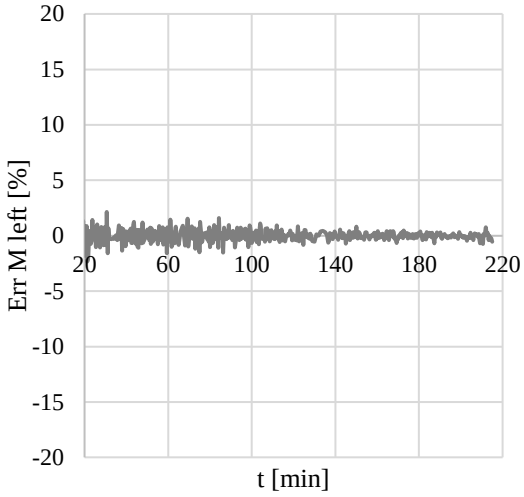

(c) Bending moment (left) error

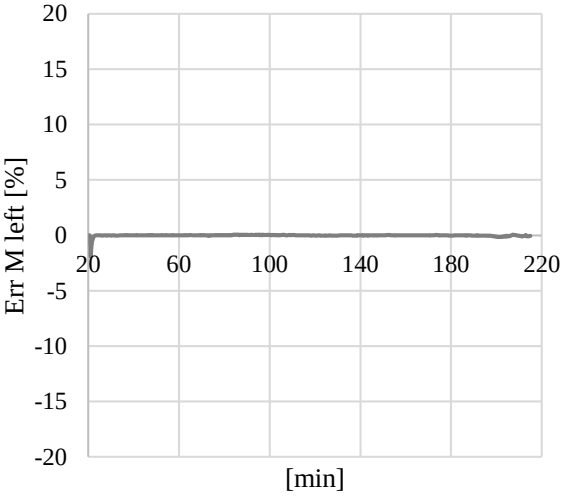

(f) Bending moment (left) error, no experimental errors

Fig. II-73 Error of the interface forces between NS and PS ($\boldsymbol{K_{PS_0}^{EST} = K_{PS_0}}$)

Interface errors $\boldsymbol{K_{PS_0}^{EST} = \nu K_{PS_0}}$

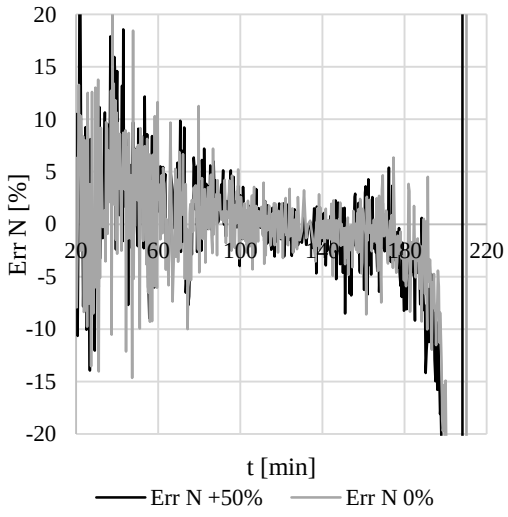

(a) Normal force error (+50 %, 0%)

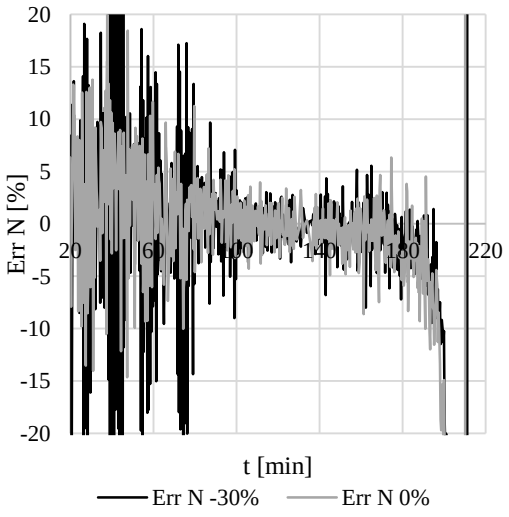

(d) Normal force error (-30 %, 0%)

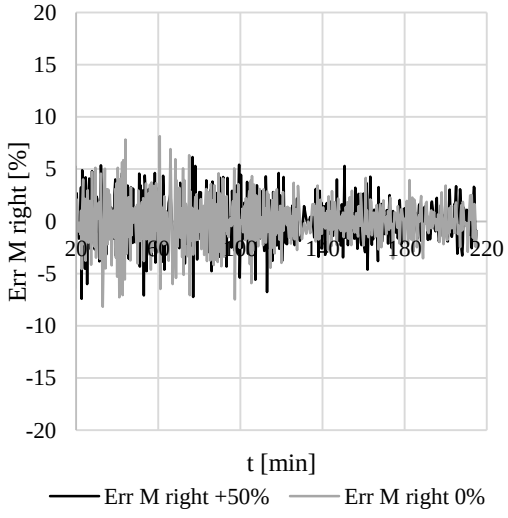

(b) Bending moment (right) error (+50 %, 0%)

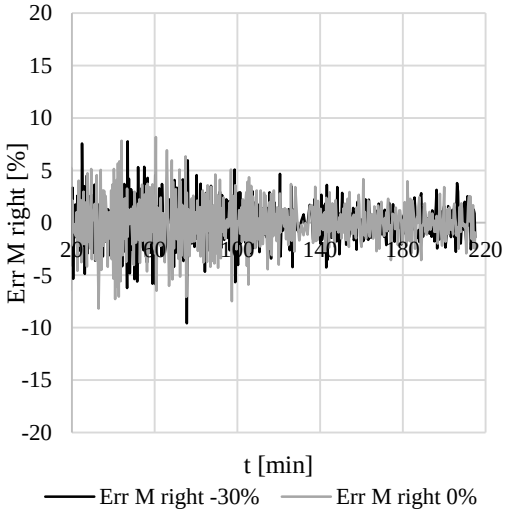

(e) Bending moment (right) error (-30 %, 0%)

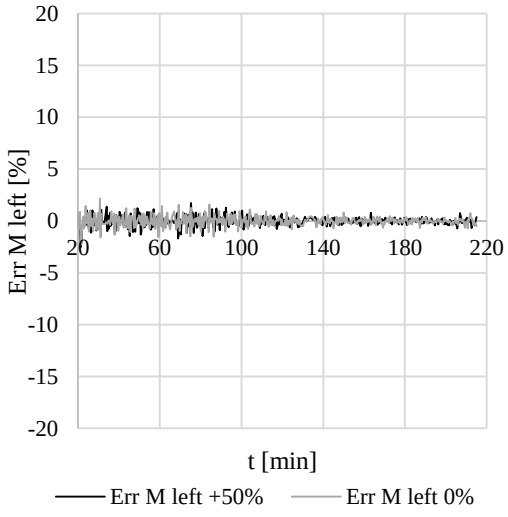

(c) Bending moment (left) error (+50 %, 0%)

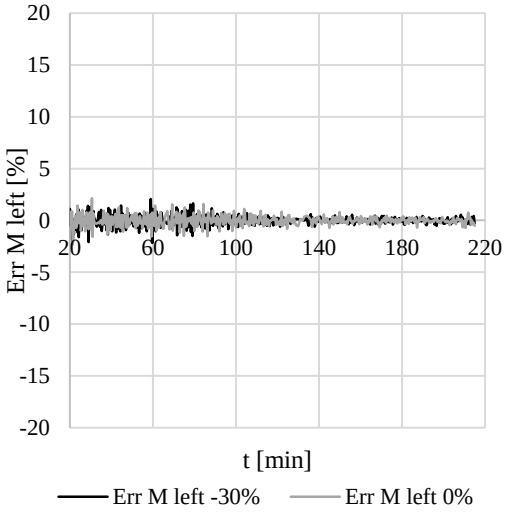

(f) Bending moment (left) error (-30 %, 0%)

Fig. II-74 Error of the interface forces between NS and PS ($\boldsymbol{K_{PS_0}^{EST} = \nu K_{PS\,0}}$)

II.7 Summary and outlook

State-space representation is a valuable tool to analyse the dynamics of the system and shows that there are inherent problems of stability in HFT. Numerous procedures can be used to stabilise the system, controlling displacements or force, with substructure in series or in parallel. A displacement control procedure with subsystems in parallel has been preferred as it is convenient for linear control and not limited to non-floating substructures.

A proportional controller can be used to perform a hybrid test. The stability conditions of this controller have been formulated in the chapter for a system with one controlled DOF. Tendencies could be identified for the case of a system with several DOFs. This controller could be compared to an existing method (Sauca, Gernay, et al. 2018). Nevertheless, as the corrections allowed by controller is only based on the instantaneous error between interface forces, the controller is therefore ill-suited when the stiffness of the PS deteriorates, in particular if the sampling time is high. A proportional integral controller is thus proposed to make corrections more efficient. The conditions of stability are given for a one-DOF system. No tendencies could be extracted for multi-DOF system, but a simplified method is proposed. Through, the framework of control theory and state equations, the chapter has investigated the effect of the estimation of the stiffness, experimental errors, and delays of HFT using proportional integral control.

A first important issue for a HFT using this controller is the estimation of the stiffness that may lead to an inappropriate design of the controller. As it has been demonstrated through a single-DOF system, the underestimation of the stiffness is specifically harmful because the system becomes unstable immediately at the beginning of the test. Simplified equations were developed for multi-DOF system, but no specific rules can be extracted. One performed a parametric study of the estimation of the stiffness and compared the results given by the virtual HFT of a steel frame and the corresponding simplified model. This model predicted similar results to the virtual HFT. Moreover, this virtual test shows that observations similar to single-DOF system can be made for a multi-DOF system. Although it could be a serious concern, one can notice that the underestimation must be high to cause instability.

The experimental errors can also disturb the HFT. Nevertheless, their impact on the stability of the system can be neglected compared to the effect of the estimation of the stiffness. Delays are finally a crucial issue in real-time tests and can be analysed in the light of control theory: if the delay increases, the controller is less efficient but not unstable. Large delay and experimental errors were introduced on the virtual HFT. As expected, the proportional integral control is marginally affected.

A PID-controller is not envisaged because it increases the order of the system. It leads to a level of complexity for the design of the controller that is not offset by a significant increase of the accuracy. For that matter, the proportional integral controller provides a balance of complexity and capability that makes this controller widely used in process control applications.

In the next Chapter, the proportional integral controller is used to perform multi-DOF experimental tests.

Chapter III
Experimental Tests

This Section approaches real-time fully automated HFT performed on half-scale steel specimen in the Fire Test Laboratory of Liege University and using proportional integral control procedure. Three tests were performed: a one DOF-test, a two-DOF test and a three-DOF test.

III.1 Procedure and experimental setup

III.1.1 Modification of the proportional integral control

The test procedure is based on the algorithm developed in the previous Chapter with the basic equation:

$$\begin{aligned} \mathbf{u}_{\mathrm{PS}_{i+1}} &= \mathbf{u}_{\mathrm{PS}_i} + \mathbf{L}_P \mathbf{e}_i^{\mathrm{inst}} + \mathbf{L}_J \mathbf{j}_i \\ \mathbf{j}_{i+1} &= \mathbf{j}_i + \mathbf{e}_i^{\mathrm{inst}} \end{aligned} \tag{III-1}$$

With $\mathbf{e}_i^{\mathrm{inst}} = -\left(\mathbf{f}_{\mathrm{NS}_i} + \mathbf{f}_{\mathrm{PS}_i}\right)$. The state -space representation is:

$$\begin{aligned} \begin{bmatrix} \mathbf{u}_{\mathrm{PS}_{i+1}} \\ \mathbf{j}_{i+1} \end{bmatrix} &= \begin{bmatrix} \mathbf{I} - \mathbf{L}_P(\mathbf{K}_{\mathrm{PS}_i} + \mathbf{K}_{\mathrm{NS}_i}) & \mathbf{L}_J \\ -(\mathbf{K}_{\mathrm{PS}_i} + \mathbf{K}_{\mathrm{NS}_i}) & \mathbf{I} \end{bmatrix} \begin{bmatrix} \mathbf{u}_{\mathrm{PS}_i} \\ \mathbf{j}_i \end{bmatrix} + \begin{bmatrix} -\mathbf{L}_P\left(\mathbf{f}_{\mathrm{NS}_i}^{\mathrm{TH}} + \mathbf{f}_{\mathrm{PS}_i}^{\mathrm{TH}}\right) \\ -\left(\mathbf{f}_{\mathrm{NS}_i}^{\mathrm{TH}} + \mathbf{f}_{\mathrm{PS}_i}^{\mathrm{TH}}\right) \end{bmatrix} \\ \mathbf{y}_i &= \mathbf{u}_{\mathrm{PS}_i} \end{aligned} \tag{III-2}$$

This procedure is illustrated in Fig. III-1 and has been validated numerically in Section II.6 but can face three difficulties when used in a experimental test.

First, as it is a displacement control procedure, the actuators must move continuously in order to avoid large thermal forces (especially in the axial direction of a member). This problem was observed by (Wang, et al. 2018) and was eliminated by the implementation of a continuous movement of the jack, based on the compensation delay technique that was developed in seismic field.

Then, the procedure requires that the displacements of the two substructures are compatible. The actuators must therefore accurately apply the corrected displacement to PS. If this is not the case, the evaluation of the instantaneous error $\mathbf{e}_i^{\mathrm{inst}}$ will be inaccurate. This problem is seen especially in the axial direction: small errors in displacement can lead to large errors in force when the test specimen is very stiff. Section II.6 has shown that the method is robust in terms of stability but can show variations in the forces due to measurement and control errors.

Finally, in case of multi-DOF tests, a displacement (elongation, rotation) in a specimen is not necessarily related to the movement of a single actuator. For instance, a rotation can correspond to the difference in position between two jacks. This can make displacement control quite complex and is particularly the case in the setup which is presented in Section III.1.2.

This latter difficulty required that equation (III-9) be reformulated for testing. Instead of the displacement of the PS $\mathbf{u}_{\mathrm{PS_i}}$, the commanded displacement $\mathbf{u}_{\mathrm{C_i}}$ (or measured actuator's stroke) is used in the basic equation:

$$\begin{aligned} \mathbf{u}_{\mathrm{C_{i+1}}} &= \mathbf{u}_{\mathrm{C_i}} + \mathbf{L}_{\mathrm{P}}\mathbf{e}_{\mathrm{i}}^{\mathrm{inst}} + \mathbf{L}_{\mathrm{J}}\mathbf{j}_{\mathrm{i}} \\ \mathbf{j}_{\mathrm{i+1}} &= \mathbf{j}_{\mathrm{i}} + \mathbf{e}_{\mathrm{i}}^{\mathrm{inst}} \end{aligned} \tag{III-3}$$

Where $\mathbf{u}_{\mathrm{C_i}} \in \mathbb{R}^{\mathrm{d'\times 1}}$. d′ is the number of actuators that are used to control the displacements of the PS. Each actuator is associated to a load cell that measures $\mathbf{F}_{\mathrm{cell_i}} \in \mathbb{R}^{\mathrm{d'\times 1}}$. The instantaneous error $\mathbf{e}_{\mathrm{i}}^{\mathrm{inst}}$ is defined as $-\mathbf{T}'\left(\mathbf{f}_{\mathrm{NS_i}} + \mathbf{f}_{\mathrm{PS_i}}\right)$, where $\mathbf{T}'$ is the transformation matrix between the internal forces and the forces measured by the load cells. In the same way as Section II.5, the interface forces can be substituted with equation (II-11) and (II-12) and the displacement vector $\mathbf{u}_{\mathrm{NS}}$ with $\mathbf{u}_{\mathrm{PS}}$ according to the compatibility of displacement. If one assumes that the displacement vector of the specimen $\mathbf{u}_{\mathrm{PS}}$ is linked to the one of the actuators $\mathbf{u}_{\mathrm{C}}$ by a transformation matrix $\mathbf{T}''$, the state-space representation can be rewritten as follows:

$$\begin{bmatrix} \mathbf{u}_{\mathrm{C_{i+1}}} \\ \mathbf{j}_{\mathrm{i+1}} \end{bmatrix} = \begin{bmatrix} \mathbf{I} - \mathbf{L}_{\mathrm{P}}\mathbf{T}'(\mathbf{K}_{\mathrm{PS_i}} + \mathbf{K}_{\mathrm{NS_i}})\mathbf{T}'' & \mathbf{L}_{\mathrm{J}} \\ -\mathbf{T}'(\mathbf{K}_{\mathrm{PS_i}} + \mathbf{K}_{\mathrm{NS_i}})\mathbf{T}'' & \mathbf{I} \end{bmatrix} \begin{bmatrix} \mathbf{u}_{\mathrm{C_i}} \\ \mathbf{j}_{\mathrm{i}} \end{bmatrix} + \begin{bmatrix} -\mathbf{L}_{\mathrm{P}}\mathbf{T}\left(\mathbf{f}_{\mathrm{NS_i}}^{\mathrm{TH}} + \mathbf{f}_{\mathrm{PS_i}}^{\mathrm{TH}}\right) \\ -\mathbf{T}\left(\mathbf{f}_{\mathrm{NS_i}}^{\mathrm{TH}} + \mathbf{f}_{\mathrm{PS_i}}^{\mathrm{TH}}\right) \end{bmatrix} \tag{III-4}$$

$$\mathbf{y}_{\mathrm{i}} = \mathbf{u}_{\mathrm{c_i}}$$

The gain matrices $\mathbf{L}_{\mathrm{P}}$ and $\mathbf{L}_{\mathrm{J}}$ must be designed with the new dynamics matrix with initial stiffness $\mathbf{K}_{\mathrm{PS_0}}$ and $\mathbf{K}_{\mathrm{NS_0}}$. The condition of stability developed in Chapter II do not change. In fact, one can define the equivalent stiffness $\mathbf{K}_{\mathrm{PS_i}}^{*} = \mathbf{T}'\mathbf{K}_{\mathrm{PS_i}}\mathbf{T}''$ and $\mathbf{K}_{\mathrm{NS_i}}^{*} = \mathbf{T}'\mathbf{K}_{\mathrm{NS_i}}\mathbf{T}''$. The state equation (III-4) is thus as:

$$\begin{bmatrix} \mathbf{u}_{\mathrm{c_{i+1}}} \\ \mathbf{j}_{\mathrm{i+1}} \end{bmatrix} = \begin{bmatrix} \mathbf{I} - \mathbf{L}_{\mathrm{P}}(\mathbf{K}_{\mathrm{PS_i}}^{*} + \mathbf{K}_{\mathrm{NS_i}}^{*}) & \mathbf{L}_{\mathrm{J}} \\ -(\mathbf{K}_{\mathrm{PS_i}}^{*} + \mathbf{K}_{\mathrm{NS_i}}^{*}) & \mathbf{I} \end{bmatrix} \begin{bmatrix} \mathbf{u}_{\mathrm{c_i}} \\ \mathbf{j}_{\mathrm{i}} \end{bmatrix} + \begin{bmatrix} -\mathbf{L}_{\mathrm{P}}\mathbf{T}\left(\mathbf{f}_{\mathrm{NS_i}}^{\mathrm{TH}} + \mathbf{f}_{\mathrm{PS_i}}^{\mathrm{TH}}\right) \\ -\mathbf{T}\left(\mathbf{f}_{\mathrm{NS_i}}^{\mathrm{TH}} + \mathbf{f}_{\mathrm{PS_i}}^{\mathrm{TH}}\right) \end{bmatrix} \tag{III-5}$$

$$\mathbf{y}_{\mathrm{i}} = \mathbf{u}_{\mathrm{c_i}}$$

The procedure is modified and is shown in Fig. III-2 (b). To ensure the compatibility of the displacement, the displacement $\mathbf{u}_{\mathrm{PS}}$ is measured and directly applied to the NS. Depending on the studied structure, it will be necessary to add rigid body motion or to perform corotational transformations on $\mathbf{u}_{\mathrm{PS}}$ to obtain $\mathbf{u}_{\mathrm{NS}}$. The matrices $\mathbf{T}'$ and $\mathbf{T}''$ depend on the testing configuration and the stiffness of the setup. These changes are not necessary if one displacement can be assigned to one actuator.

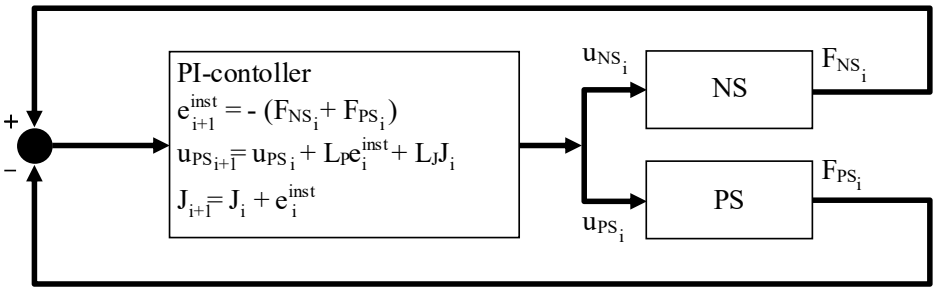

Fig. III-1 Proportional integral control developed in Section II.5

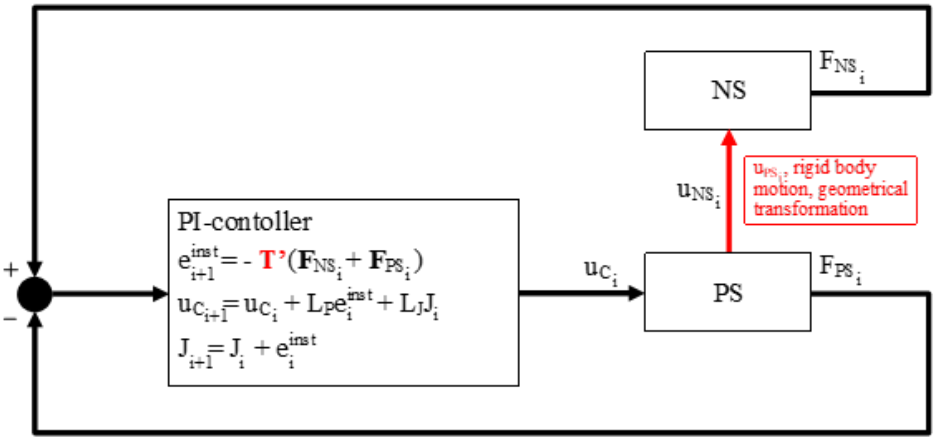

Fig. III-2 Proportional integral control of the HFT performed in Section III.3-5

III.1.2 Experimental setup

An experimental setup was built in the Fire Test Laboratory of Liege University to perform hybrid fire tests. The setup is made of two steel frames (frame 1 and frame 2) bolted on two horizontal beams and braced by diagonal elements (Fig. III-3).

Three electric jacks are mounted on supports and apply displacements through cross struts. These actuators are 100 kN-capacity trapezoidal screw jacks. In these jacks, the rotation of the worm is transformed into axial translation of the screw using the rotation of the motor. The position of this threaded rod ($\mathbf{u_c}$) can be controlled accurately. Pictures of the experimental setup and actuators can be found in Appendix C (Fig. C-1 and Fig C-3).

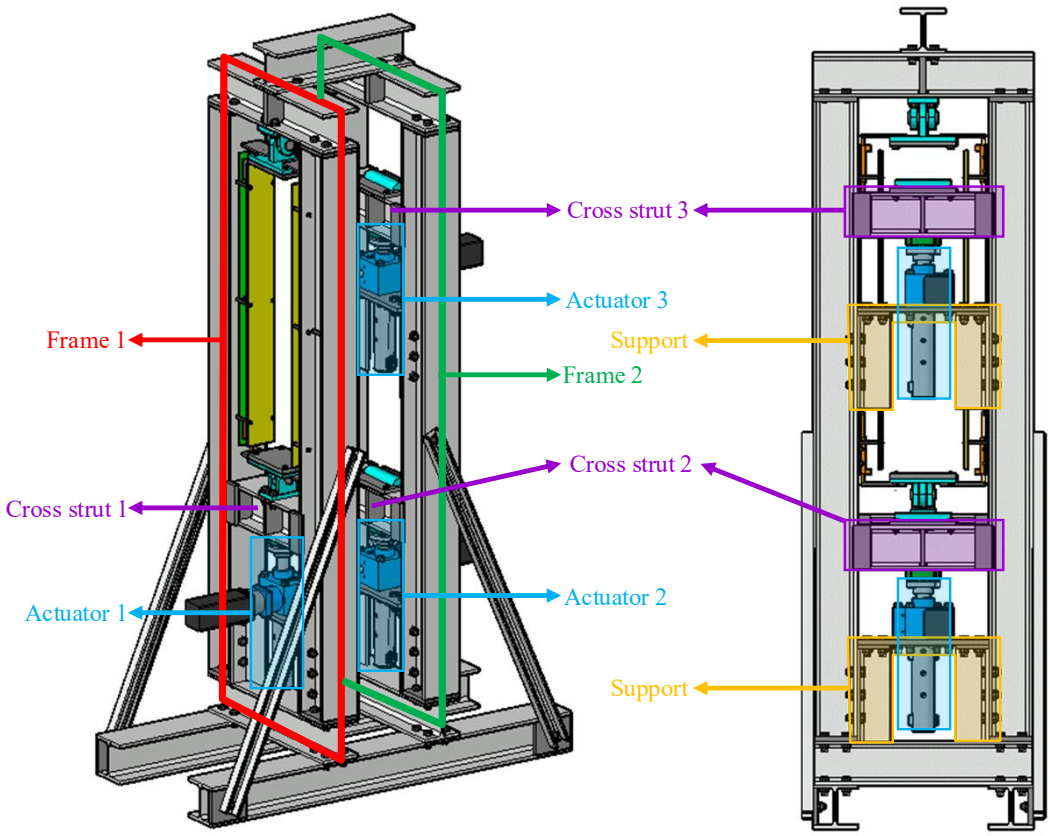

Fig. III-3 Experimental setup

The axial displacements are measured using potentiometric linear position sensors. Longitudinal movement is converted into a proportional electrical quantity. These sensors have return spring and

integrated signal conditioner. The rotations are measured with single axis inclinometers. The forces are measured by cell forces located between the rod of the actuator and the cross strut. Pictures of the displacement transducers, inclinometers and load cells can be found in Appendix C.

Flexible ceramic pad heaters are used to heat the specimen (Appendix C, Fig. C-5 (a)). They are manufactured from high grade nickel-chrome (NiCr) 80/20 wire which run through aluminium oxide ceramics beads. The alumina ceramic beads are made of sintered alumina ceramics that allow high temperature resistance, excellent insulating property, and efficient thermal conductivity. They heat the specimen with radiation. They are fastened to the specimen with nails welded as shown in Fig. C-5 (b) and (c) in Appendix C. They are powered by a 65kVA transformer unit with 6 temperature controllers (Appendix C, Fig. C-6 (a)). The output channels are controlled by means of energy regulators and temperature controllers (Appendix C, Fig. C-6 (b)). In the tests, the feedback variable of each electrical pad is the temperature of a thermocouple welded on the specimen.

III.1.3 Test procedure

Based on Chapter II and Section II.1.1, the process shown in Fig. III-4 follows the hereunder steps:

1. At the beginning of the time step, forces and displacements of the PS are measured by the datalogger of the laboratory and sent to the computer.
2. The measured displacements are imposed to the NS (considering geometrical transformations and rigid body motion if necessary). The NS is a FE model in SAFIR®. The interface forces are computed.
3. The forces of PS and NS are sent to an intermediate software mentioned in Section II.6.2 that ensures the connections between PS and NS. The instantaneous error $\mathbf{e}_i^{inst}$ is calculated. The new commanded displacement $\mathbf{u}_C$ and the integral term **j** are then computed with equation (III-3).
4. The new command $\mathbf{u}_{C_{i+1}}$ is sent to the actuator and applied to the PS at the end of the time step.

During the time step, the actuators do not stop moving. If $\mathbf{u}_{C_{i+1}}$ is computed before the end of the time step, the displacement is interpolated between $\mathbf{u}_{C_i}$ and $\mathbf{u}_{C_{i+1}}$, otherwise it is extrapolated:

Interpolation	$\mathbf{u}_{C_{i+1}}$ is computed	$\mathbf{u}_{C_{t_i+\Delta t}} = \frac{\mathbf{u}_{C_{i+1}} - \mathbf{u}_{C_i}}{T}\Delta t$	(III-6)
Extrapolation	$\mathbf{u}_{C_{i+1}}$ has not yet been computed	$\mathbf{u}_{C_{t_i+\Delta t}} = a(t_i + \Delta t) + b$ a, b linear regression with 4 points	(III-7)

T is the sample time as defined in Section II.2.4. The elements of the process are shown in Fig. C-2 in Appendix C.

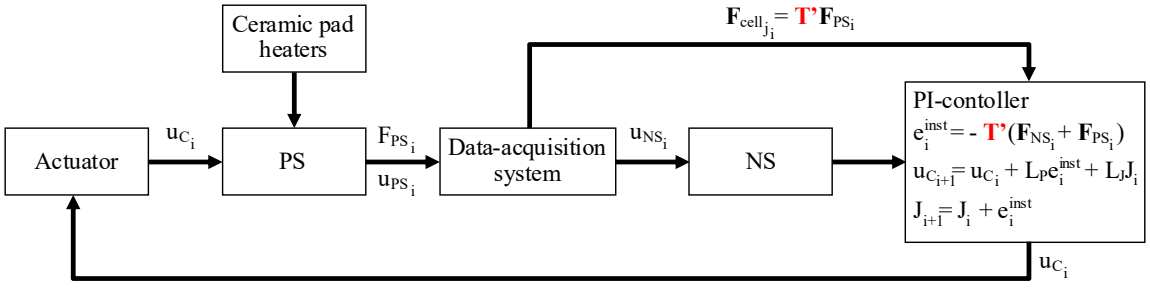

Fig. III-4 Test architecture

III.2 One-DOF test

III.2.1 Test configuration

The reference structure for the one-DOF test is shematized in Fig. III-5. It consists of two structural elements, a 1.5 m column and a 2 m loaded beam that are respectively the PS and the NS. The column is hinged at the top with a roller support and at the bottom with a pinned support. The NS has two roller supports. The setup is shown in Fig. III-6 (a).

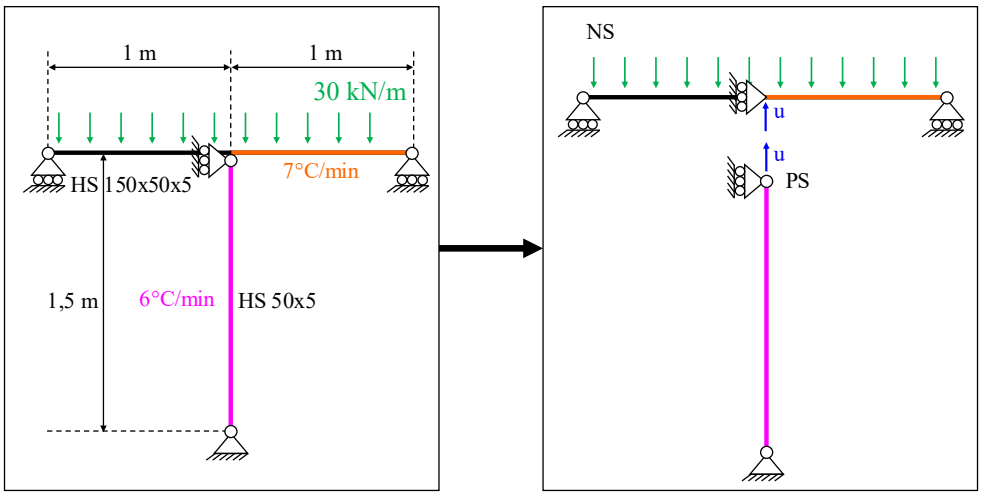

Fig. III-5 One-DOF test: PS and NS

The beam (NS) is made of a rectangular hollow section HS 150x50x5. Eurocode dependent material properties (CEN. EN 1993-1-2:2005) are used in the analysis of the NS that is performed in SAFIR®. The considered steel grade is S355. In the test presented here, one span of the beam NS is heated at a rate of 7°C/ minute on three faces.

The column (PS) is a squared hollow section HS 50x5. As shown in Fig. III-6 (a) and (b), the extremities of the specimen are welded to steel plates and these are bolted to hinges. The top hinge is bolted to the steel frame of the test set-up and the bottom one is bolted to a cross strut. An electrical jack (actuator 1 in Fig. III-6) applies the displacement through this cross strut which can move up and down while the horizontal position is maintained. The yield strength of steel in this column has been measured at 382 N/mm² with standardized tests.

The displacements at the interface between NS and PS are the axial elongation of the PS ($\mathbf{u}_{PS}$) and the vertical displacement at the middle of the NS ($\mathbf{u}_{NS}$). For this first test, the horizontal displacement at the top of the column is blocked in the reference structure to delete the rigid body motion and simplify the relationship between $\mathbf{u}_{NS}$ and $\mathbf{u}_{PS}$. This simplification will not be applied in Sections III.3 and III.4 where rigid body rotation is considered.

A load cell lies between the cross truss and the actuator (Load cell 1 in Fig. III-6 (a)) to measure the normal force in the column. The elongation is measured using potentiometric linear position sensors. Indeed, since the frame has some flexibility, the elongation of the column cannot be determined by simply measuring the displacement of the moving cross strut. Thus, the elongation of the column $\mathbf{u}_{PS}$ that will feed the NS at step 2 of the test procedure is obtained by the difference of the displacement of the cross strut and the displacement of the top beam of the set-up due to the force applied by the actuator. These displacements are obtained from four displacements sensors shown in Fig. III-6 (a). These sensors are not bolted directly on the frame profiles. Otherwise, they would follow the deflection of the setup. They are therefore screwed on an OSB plate which is fastened in its middle to the profile frame, making that it does not deform with the latter. One also

added gypsum plates to prevent the heating and thus thermal expansion of the OSB plates. The assembly is shown in Fig. C-8 and Fig. C-9 in Appendix C.
The PS is heated at a rate of 6°C/min, with four electrical pads. The pads are controlled with a thermocouple located in the middle of each zone. The column is wrapped with polyurethane fibre to keep the heating efficient (see Fig. C-7 (b) in Appendix C). The heating of the two substructures does not start immediately. The load of the NS is first applied linearly at 20°C in 20 min. Then the load is maintained for 5 minutes at room temperature. Even if the substructures are not heated, the procedure described in Section III.1.2 is followed. Eventually, both substructures are heated after 25 min and HFT begins. This procedure is shown in Fig. III-7 and is followed for the two-DOF test and three-DOF test.

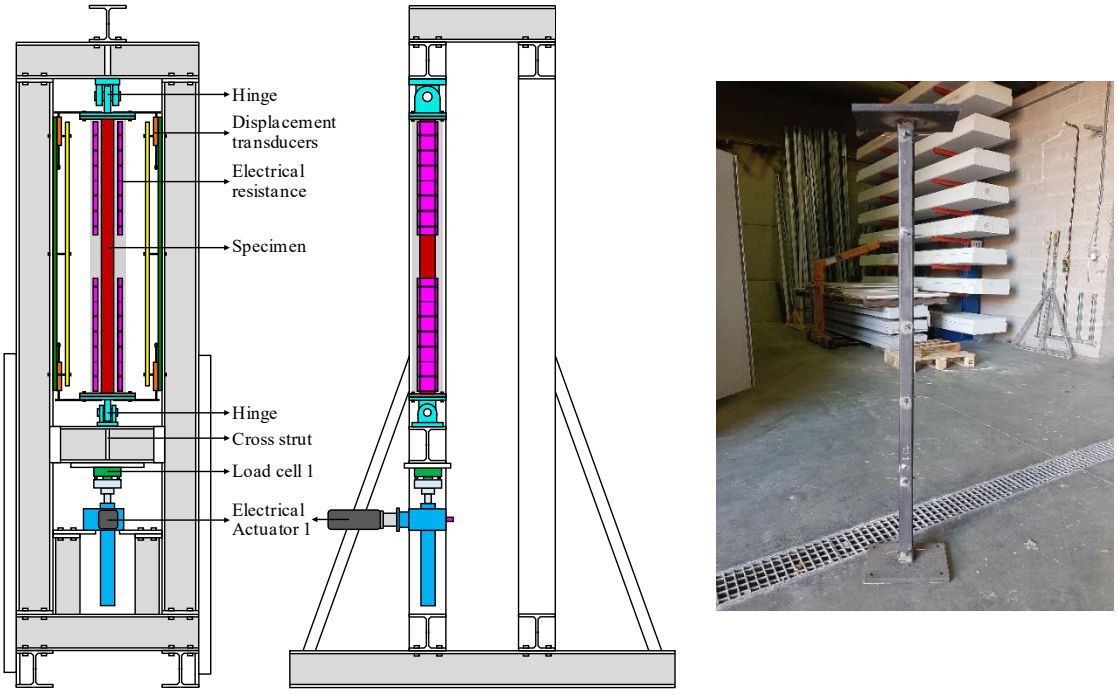

(a) Setup *(b) Specimen*

Fig. III-6 Material and setup of the one-DOF test

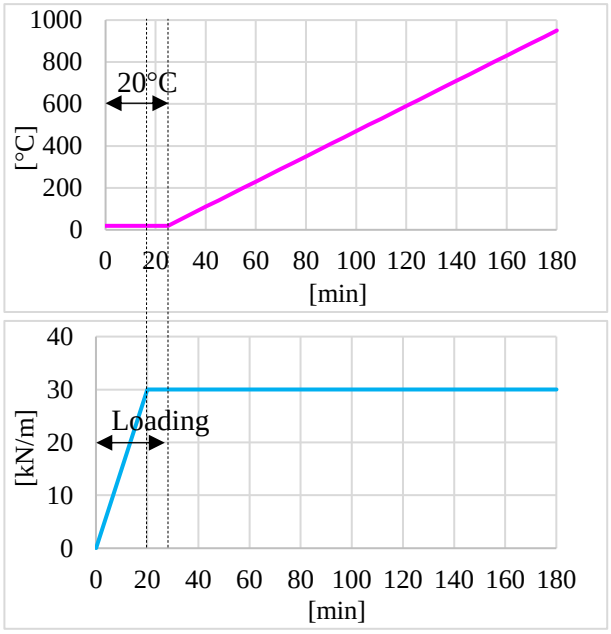

Fig. III-7 Loading and heating

The gain matrices $\mathbf{L_P}$ and $\mathbf{L_J}$ must be designed using the dynamics matrix of equation (III-4). The 1x1 transformation matrix $\mathbf{T'}$ and $\mathbf{T''}$ are necessary. As the load cell directly measures the normal force in the column, $\mathbf{T'}$ is equal to 1. The matrix $\mathbf{T''}$ would be also equal to 1 if the stiffness of the frame was infinite. Otherwise, the link between $\mathbf{u_{PS}}$ and $\mathbf{u_c}$ is as follows (Appendix D):

$$\mathbf{u_c} = \mathbf{u_{PS}} + \frac{\mathbf{F_{PS}}}{\mathbf{K_f}} = \left(1 + \frac{\mathbf{K_{PS_0}}}{\mathbf{K_f}}\right)\mathbf{u_{PS}} \tag{III-8}$$

And $\mathbf{T''}$ is thus equal to:

$$\mathbf{T''} = \left(1 + \frac{\mathbf{K_{PS_0}}}{\mathbf{K_f}}\right)^{-1} \tag{III-9}$$

$\mathbf{K_f}$ is the stiffness of the frame and is evaluated as being equal to 300 kN/mm. The initial stiffness matrices that are necessary for calculating the gain matrices are given hereunder:

$$\mathbf{K}_{\mathrm{PS_0}}^{\mathrm{EST}} = \left[\frac{\mathrm{EA}}{\mathrm{L}}\right] = 126\,000\,000\ \mathrm{N/m} \qquad \mathbf{K_{NS_0}} = 9\,500\,000\ \mathrm{N/m} \tag{III-10}$$

As equation (III-5) is 2x2 system, this HFT is a second order system. The relationship between the eigenvalues and the parameters of the step response of the system are well known as developed in Section II.5.1. The hypothesis is made that the displacement and the forces of the system can be discretized with an interval of 12 s. The rise time is thus fixed to 12 s. Overshoot is set to 0, meaning that no deviation of system output from its final value is accepted when $\mathbf{K_{PS}} = \mathbf{K_{PS_0}}$ and $\mathbf{K_{NS}} = \mathbf{K_{NS_0}}$. One assumes that the command $\mathbf{u_c}$ is updated every 3 s. The value of the double eigenvalue λ is thus determined using equation (II-35):

$$\lambda = \exp\left(-2.72\frac{3}{12}\right) = 0{,}51 \tag{III-11}$$

The gain matrices can be directly determined with the equations developed in Chapter II for a single DOF system:

$$\mathrm{L_P} = \frac{2(1-\lambda^*)}{\mathrm{K}_{\mathrm{PS_0}}^{\mathrm{EST}^*} + \mathrm{K}_{\mathrm{NS_0}}^*} = 10.27 \times 10^{-9} \qquad \mathrm{L_J} = \frac{(1-\lambda^*)^2}{\mathrm{K}_{\mathrm{PS_0}}^{\mathrm{EST}^*} + \mathrm{K}_{\mathrm{NS_0}}^*} = 2.52 \times 10^{-9} \tag{III-12}$$

The poles of the simplified matrix $\begin{bmatrix} \mathrm{I} - \mathrm{L_P}(\alpha \mathrm{K}_{\mathrm{PS_0}}^* + \mathrm{K}_{\mathrm{NS_0}}^*) & \mathrm{L_J} \\ -(\alpha \mathrm{K}_{\mathrm{PS_0}}^* + \mathrm{K}_{\mathrm{NS_0}}^*) & \mathrm{I} \end{bmatrix}$ are explicitly determined to verify the stability and are shown in the hereunder figure for $\alpha \in [0,1]$. They lie in the unit circle.

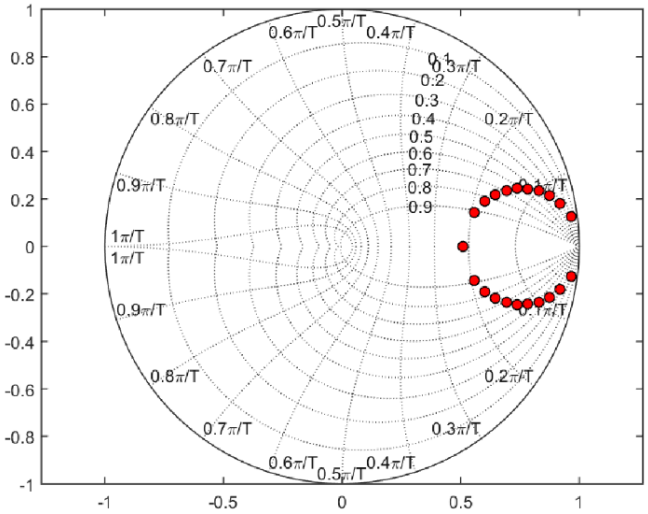

Fig. III-8 One-DOF test: Predicted location of the poles for $\alpha \in [0,1]$

III.2.2 Results and discussion

The test was performed on June 18, 2020. Fig. III-9 shows the column during the test (a) and after buckling (b). The specimen collapses around 110 minutes after the beginning of the test.

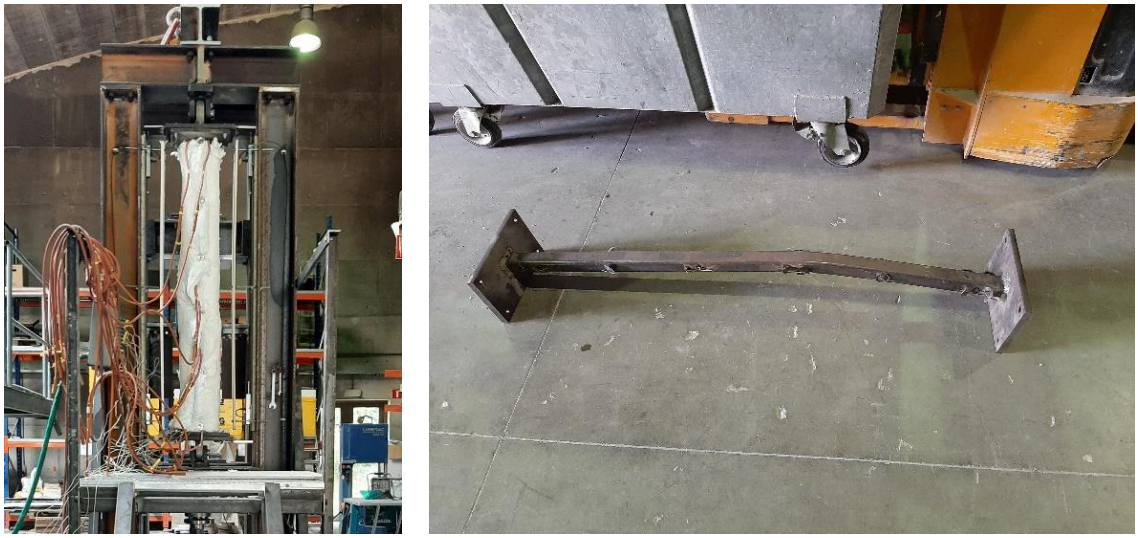

(a) PS during the test *(b) PS after buckling*

Fig. III-9 One-DOF test

In Fig. III-10, the force–displacement relationship of the column is given, as well as the commanded temperature. Displacements/forces are shown as a function of time in Fig. III-11 (a) and (b). The expected temperature of the column (6°C/min after t=25 min) is mentioned at the top of the graphs. The blue curve corresponds to the loading phase ("cold phase") and the red curve to the "hot phase".

In Fig. III-10 and Fig. III-11, one can see that for 20 min, forces and displacements increase linearly because of loading. Then, the load is maintained. The column is shortened by 0.475 mm and the normal force stabilises around -32.9 kN.

The heating starts 25 min after the beginning of the test. Thermal expansion of the column makes that the axial displacement increases. This thermal expansion is not free and the connected beam (NS) acts as an axial elastic end-restraint. Thus, the normal force increases linearly. When the temperature is higher than 200 °C (a little before 60 min), the Young modulus degradation begins, and it can be seen in Fig. III-10 that the curve gradually flattens out. The force-displacement relationship is almost constant around 400°C and at a temperature of 422 °C, the displacement and force started to decrease due to plastic deformation of the specimen. Buckling occurs at 534°C.

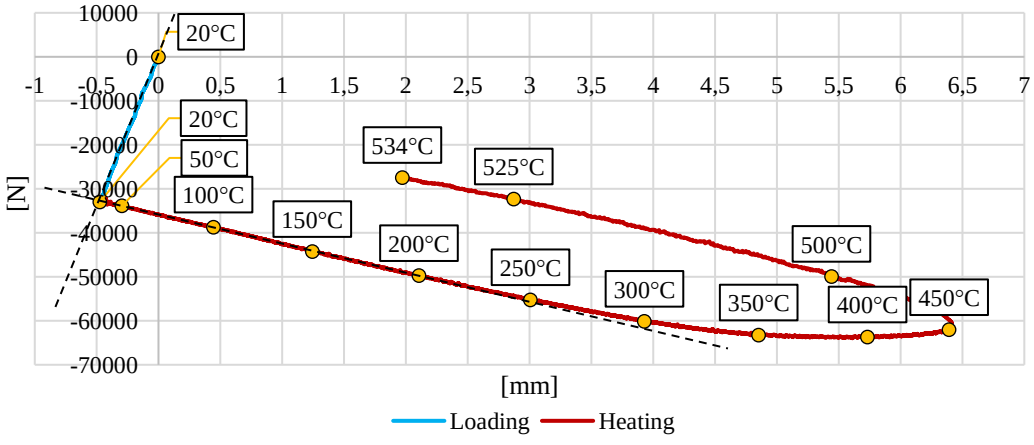

Fig. III-10 One-DOF test: Force–displacement relationship

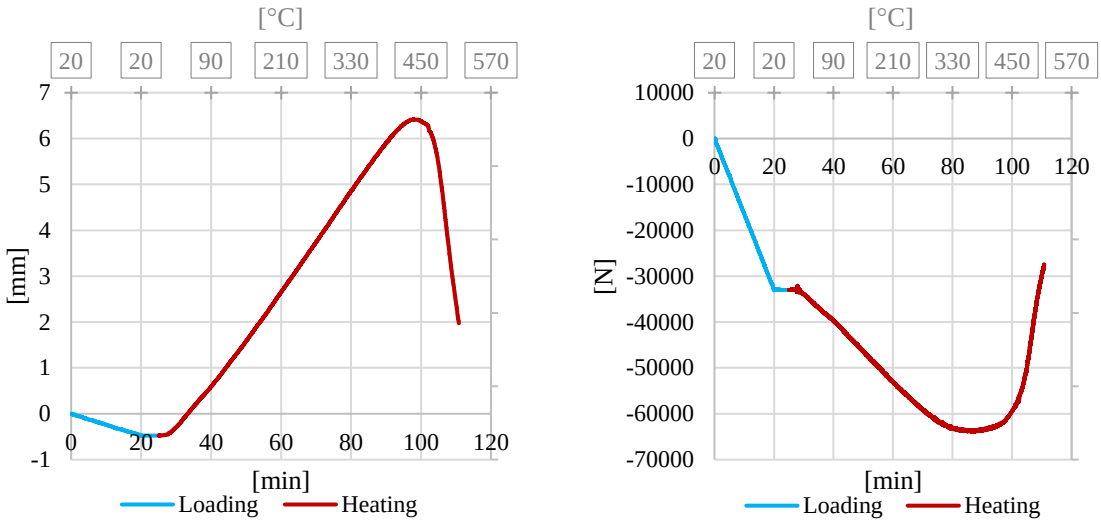

(a) displacement u *(b) Normal force F*

Fig. III-11 One-DOF test: Displacement u and normal force F of the PS

The bending moment of the NS is shown in Fig. III-12 and Fig. III-13. During the heating phase, the moment at the middle of the beam increases until it reaches a maximum at 86 minutes. As half of the beam is heated, the Young modulus of the heated part of the beam decreases (Fig. III-14).

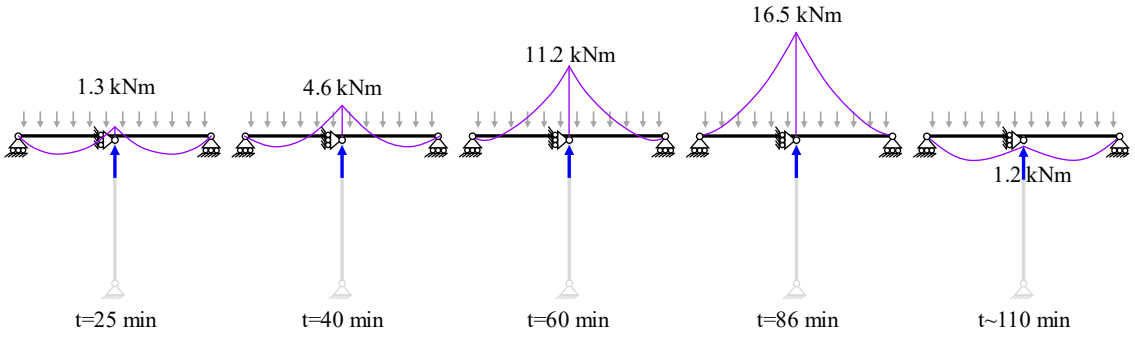

Fig. III-12 Bending moment diagram of the NS during the test

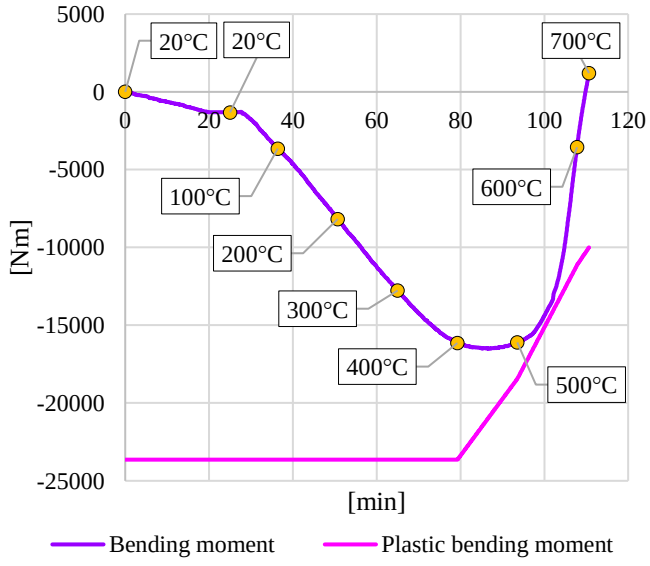

Fig. III-13 Bending moment of the NS during the test

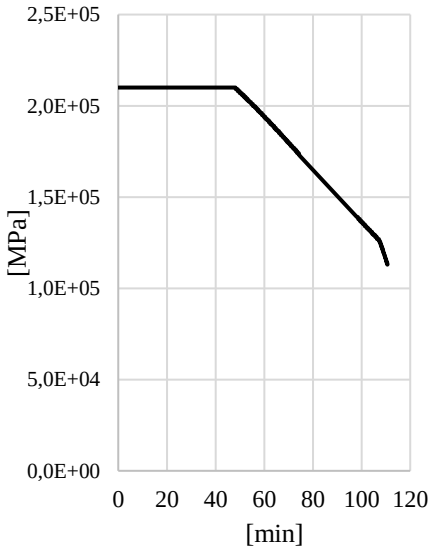

Fig. III-14 Young modulus of the heated part of the NS

Interface error

The approach of substructuring can only yield accurate results if both displacement compatibility and force equilibrium are satisfied at the interface between the NS and the PS. In Fig. III-15, "u PS" and "N PS" stand for the axial displacement and the normal force measured during the HFT. "u NS" and "N NS" are the displacement and force of the NS.

Fig. III-15 (a) shows that the interface displacements are compatible, which is excepted as the displacement of the specimen is directedly applied to the NS. The compatibility of the displacement is thus ensured by the testing process. Fig. III-15 (b) shows that the interface forces are in equilibrium.

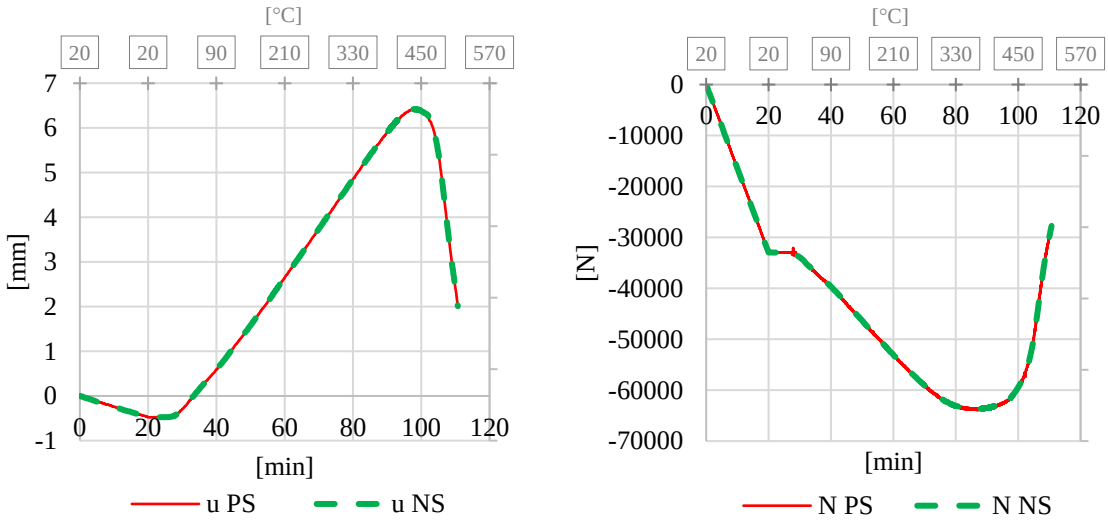

(a) Displacement of PS and NS *(b) Normal force of PS and NS*

Fig. III-15 One-DOF test: Interface displacements and forces

The interface error between forces is important as it quantifies and assesses the quality of the algorithm. It can be summarized in Fig. III-16 that shows the relative instantaneous error between $\mathbf{f}_{PS}$ and $\mathbf{f}_{NS}$ in function of time. This error Err N is computed as:

$$\text{Err N} = \frac{f_{NS}[1] + f_{PS}[1]}{f_{PS}[1]} \text{ [\%]} \tag{III-13}$$

The relative error is high (more than 100%[4] because $f_{PS}[1] \approx 0$ and $f_{NS}[1] \neq 0$ at the first step) at the very start of the test but decreases extremely fast to reach equilibrium. The value is then under 2% during the loading.

The error increases again when the heating starts. This increasing can be explained by the fact that while maintaining the load on the column ($t \in [20\text{ min}, 25\text{ min}]$), the instantaneous error and the integral term are around zero as can be seen in Fig. III-17 that shows the computed error e^{inst} and the integral term J in N. When the heating start, the instantaneous error increases, and the displacement is corrected. However, the correction is not sufficient at the beginning as the integral term needs some time steps to increase and allows a reactive behaviour of the proportional integral controller. Consequently, the normal force increases too fast at the nearly beginning of the heating. The situation is however quickly stabilised by the algorithm. During the test, the value of the error remains low (less than 2%) until failure where a slight increasing is observed. The integral term increases during the test to handle changes in the forces due to loading and heating and is close to

[4] The limits of the vertical axes of the graph in Fig. III-16 have been reduced for better understanding.

0 when the load is constant. The increasing of J is particularly high at the end of the test as large corrections are necessary because of buckling.

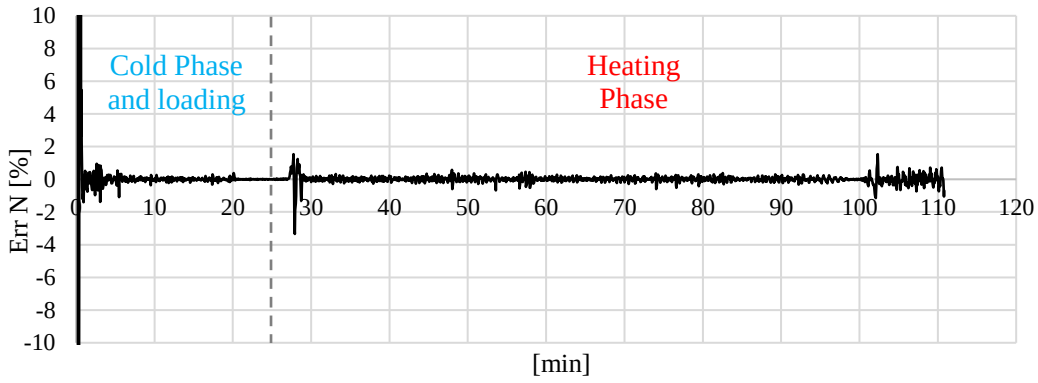

Fig. III-16 One-DOF test: Relative instantaneous error

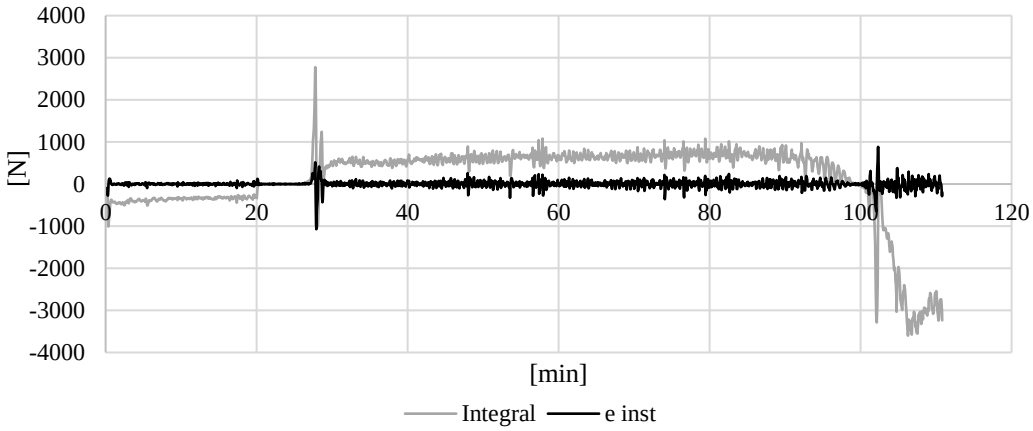

Fig. III-17 One-DOF test: Instantaneous error and integral term computed during the test

Comparison with numerical simulation

The results of the specimen were also compared with a numerical simulation of the complete structure performed in SAFIR®. The curves "u REF (predicted)" and "N REF (predicted)" were computed from the behaviour of the complete structure, assuming that steel in the PS behaves as foreseen by the Eurocode (CEN. EN 1993-1-2:2005) and that the temperature is uniform in the column. An initial geometrical imperfection of 1.5 mm was considered. According this simulation, the buckling of the specimen should occur around 130 minutes when the temperature would be around 550 °C. During the loading phase at ambient temperature (from 0 to 25 min), the behaviour of the PS corresponds to the one that was predicted. When the column is heated, one notices that the curves are shifted, and that PS seems to lag its predicted behaviour. Also, the failure occurs sooner, around 100 minutes.

The observed differences with the reference curves must be put into perspective. The reference curves, even corrected, are calculated by making numerous assumptions about the behaviour of the steel and the geometric imperfections of the specimen. Only the trend and the orders of magnitude must be taken into account. Moreover, the curve of the reference structure is calculated considering that the temperature is uniform in the PS, which is not the case during the test. Indeed, each electrical resistance that heats the columns is controlled with a single thermocouple. If the desired temperature is reached at this point, it is not necessarily reached in the other parts of the column. As shown in

Fig. E-2 in Appendix E, some parts such as the bottom of the column are cooler and others may be warmer, especially the upper parts.

The measurements of the thermocouples made it possible to calculate a second curve after the test which considers the real temperatures of the column. These new curves are called "u REF (corrected)" and "N REF (corrected)" in Fig. III-18. The axial displacement and normal force are closer to this corrected curve although failure occurred earlier in the test than in the numerical simulation. The force-displacement relationship of the PS and the numerical simulation (corrected) is shown in Fig. III-19.

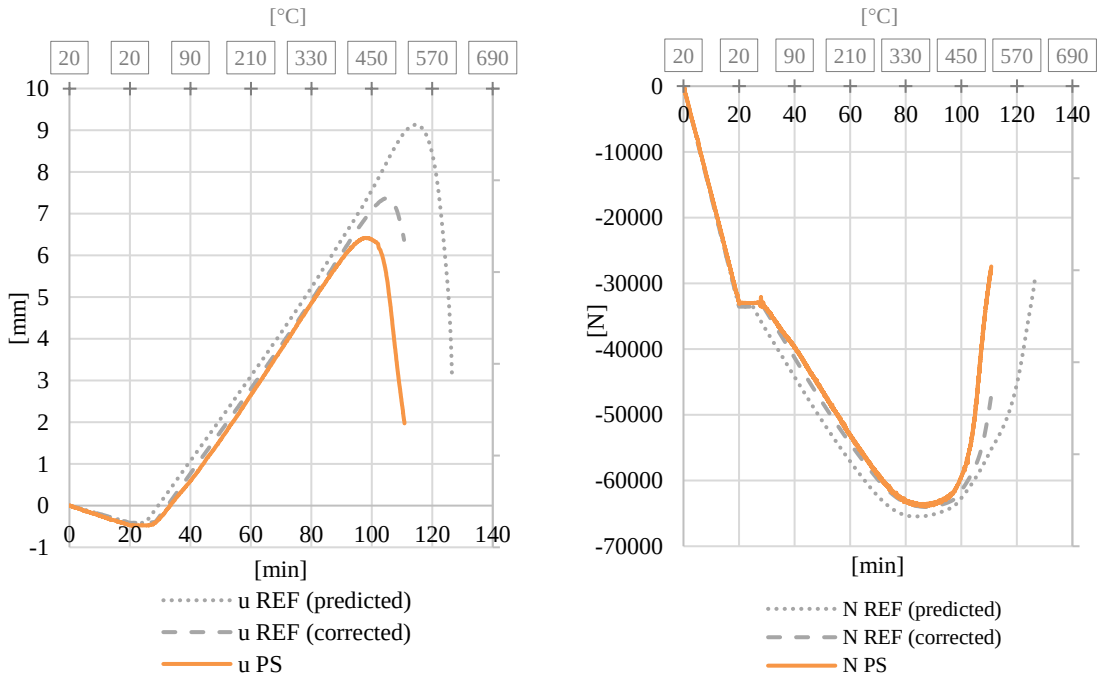

(a) Elongation u *(b) Normal force N*

Fig. III-18 One-DOF test: Comparison with numerical simulations

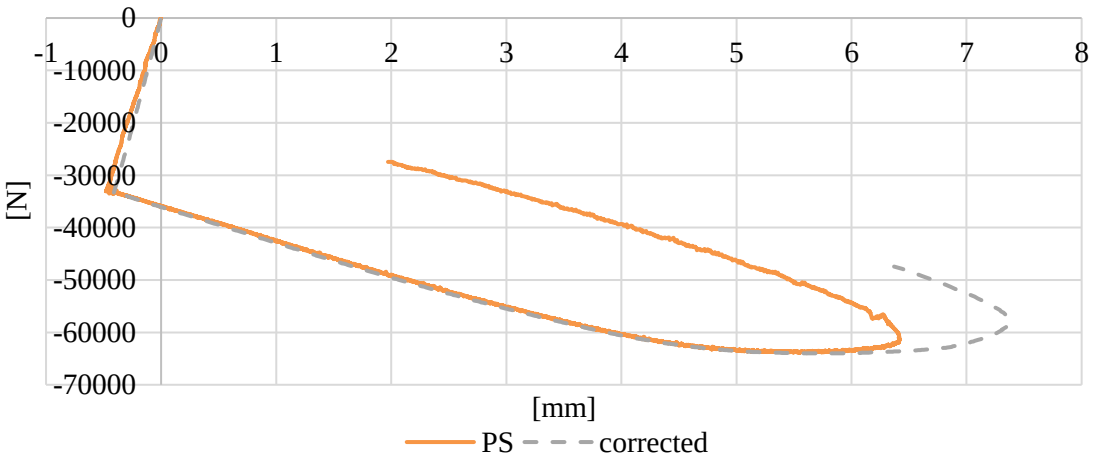

Fig. III-19 One-DOF test: Force–displacement relationship of the PS and numerical simulation

III.3 Two-DOF test

III.3.1 Test configuration

The reference structure of the two-DOF test (shown in Fig. III-9) also consists of two structural elements: a 1.4m column (PS) and a uniformly loaded 1.2m beam (NS). The column which is a squared hollow section HS 80x5 has a hinged support and is rigidly connected to the beam, made of a rectangular hollow section HS 160x80x5. The support of the NS is completely fixed. The PS and the NS are heated but at different rate as shown in Fig. III-9. The beam is heated on three faces. The yield strength of the PS has been measured at 460 N/mm² and thus steel grade S460 is considered for the elements of the NS.

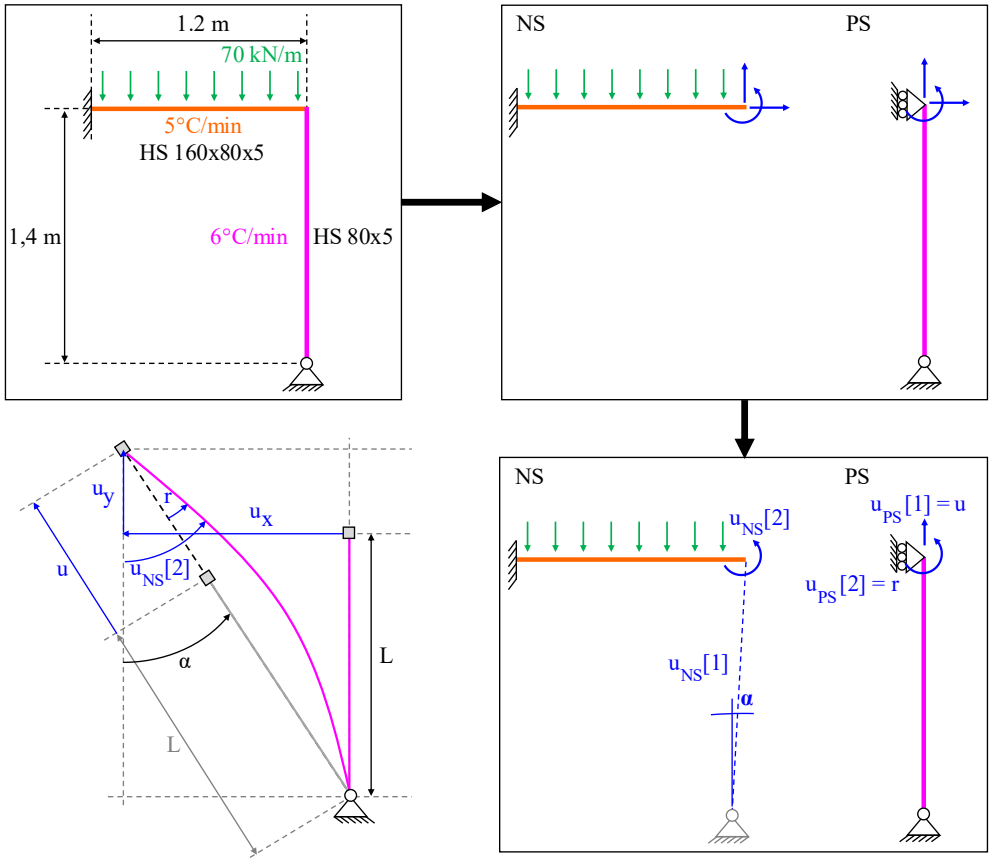

Fig. III-20 Two-DOF test: PS and NS

After substructuring, as the horizontal displacement at the top of the column is not blocked, there are three DOFs at the interface of the PS as the NS (two translations and one rotation). However, in the setup, rigid body motion must be avoided. It is thus necessary to block both horizontal DOFs and one vertical DOF of the PS. The column is thus tested with two supports, a roller support and a pinned support. Consequently, the interface displacements of the PS are:

- the axial elongation of the column
- the rotation at one end

For the NS, they consist of:

- the relative distance between the free extremity of the beam and the virtual position of the support of the column, $u_{NS}[1]$
- the rotation of the joint with the PS, $u_{NS}[2]$. This rotation is not equal to the one of the PS as the rigid body rotation must be taken into account.

The transformations that are considered is as follows (see Fig. III-9):

$$u_{NS}[1] = 1.4 + u \qquad u_{NS}[2] = r + \alpha = r + \operatorname{atan}\left(\frac{u_x}{1.4 + u_y}\right) \qquad \text{(III-14)}$$

The relative distance $u_{NS}[1]$ is imposed in SAFIR® using the Lagrange multipliers method. The way this method is applied is described in Appendix B.

The column is tested upside down as shown in Fig. III-21: the extremity with the support is at the top and the other one where the displacements are controlled is at the bottom. As in the single DOF test, the top of the specimen is welded to a steel plate bolted to a hinge. The bottom of the steel column that corresponds to the extremity that is rigidly connected to the beam is welded to a HEB100-lever arm that allows applying a bending moment in addition to the normal force. The axial elongation of the column is measured as in Section II.2. An inclinometer lies on the lever arm to measure the rotation (inclinometer 1 in Fig. III-21(a)). The load cells (load cell 1 and load cell 2) are between the cross struts and the actuators (actuator 1 and actuator 2).

Unlike the normal force which should remain in compression, the moment is expected to change sign towards the end of the test. As the setup does not allow the actuators to pull on the load cell, the cross strut has been preloaded to be able to apply a bending moment of -1700 kNm. The cross member is attached to the lever arm with four threaded rods that are bolted to a steel plate. A cylinder is placed between the plate and the lever arm. Drawings and picture of the setup are shown in Appendix C (Fig. C-10 and Fig. C-11).

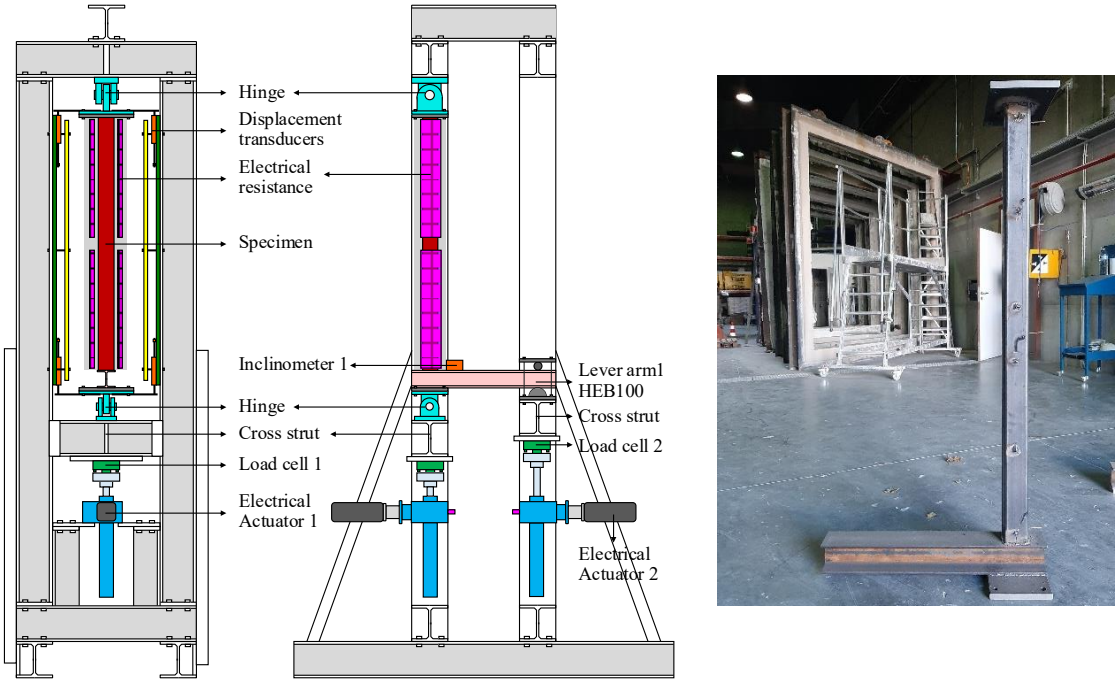

(a) Setup *(b) Specimen*

Fig. III-21 Material and setup of the two-DOF test

The 2x2 transformation matrices $\mathbf{T}'$ and $\mathbf{T}''$ must be determined to design of the gain matrices. The normal force is the sum of the two forces measured with load cell 1 and load cell 2. The bending moment also consists of two terms. First, the force of the load cell 2 multiplied by the lever arm. Then, due to assembly inaccuracies in the set-up, the first actuator is slightly offset by 2.5 mm towards the inside. As a result, a contribution from the force of the load cell 1 must thus also be considered. The matrix $\mathbf{T}'$ is thus as follows:

$$\mathbf{T}' = \begin{bmatrix} 1 & 1 \\ a_1 & a_2 \end{bmatrix}^{-1} \tag{III-15}$$

With a_1 and a_2, respectively, the eccentricity of actuator 1 and the length of the lever arm, equal to 0.0025 m and 0.61 m. The matrix $\mathbf{T}''$ is also determined. The relationship between measured displacements and the actuator's strokes is more complex than in the single DOF system and consists of large expressions that are presented in Appendix D, Section D.2.

To design the controller, the stiffness of the PS and NS are required and are then calculated/estimated. They are given hereunder. All the values presented are expressed in [N], [m] and [rad]:

$$\mathbf{K}_{PS_0}^{EST} = 10^3 \begin{bmatrix} 225000 & 0 \\ 0 & 846 \end{bmatrix} \qquad \mathbf{K}_{NS_0} = 10^3 \begin{bmatrix} 229400 & 10400 \\ 10400 & 6040 \end{bmatrix} \tag{III-16}$$

The system contains four eigenvalues that must be chosen. Nowadays, the behaviour of 4th order systems is not well-known in literature, as first- or second-order system. The controllers of such systems are thus hard to design. As in Chapter II, to get around this problem, the controller is designed to have a pair of non-null dominant eigenvalues. The following step parameters and eigenvalues are chosen:

$$\begin{gathered} T = 3\ s \\ T_r = 12\ s \\ \lambda = \exp\left(-2.72\frac{3}{12}\right) = 0{,}51 \end{gathered} \tag{III-17}$$

The 4th order system is approximated to second order system, by setting a double eigenvalue equal to 0.51 with the others set to 0. Using the MATLAB® automatic procedure of Chapter II, the following gain matrices are obtained:

$$\mathbf{L}_P = 10^{-9} \begin{bmatrix} 4.520 & 0 \\ 0 & 52.99 \end{bmatrix} \qquad \mathbf{L}_J = 10^{-9} \begin{bmatrix} 0.227 & 0 \\ 0 & 1.322 \end{bmatrix} \tag{III-18}$$

The poles of the simplified matrix $\begin{bmatrix} \mathbf{I} - \mathbf{L}_P(\mathbf{K}_{PS_i}^* + \mathbf{K}_{NS_i}^*) & \mathbf{L}_J \\ -(\mathbf{K}_{PS_i}^* + \mathbf{K}_{NS_i}^*) & \mathbf{I} \end{bmatrix}$ are shown in the hereunder figure for $\alpha \in [0,1]$ and lie in the unit circle. Stability is thus ensured. A pair of poles have a high complex part, which involves overshoots. Nevertheless, some damping will be ensured by the eigenvalues that have a large real part.

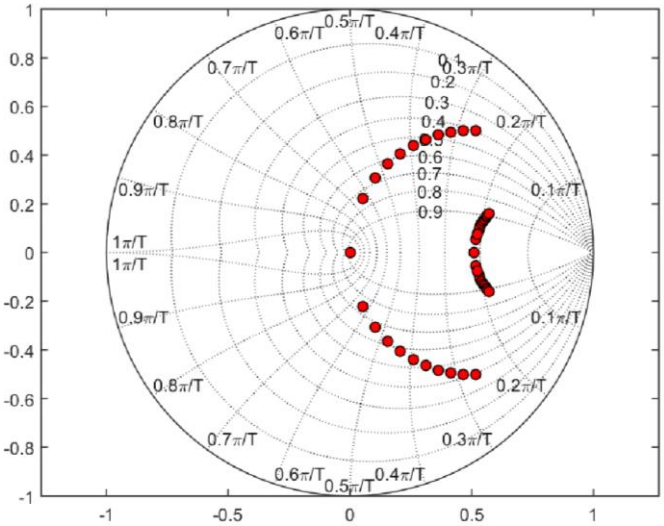

Fig. III-22 Two-DOF test: Predicted location of the poles for α ∈ [0,1]

III.3.2 Results and discussion

The test was performed on September 18, 2020. Fig. III-23 (a), (b) and (c) show the column during the test and after buckling.

(a) PS during the test (front)

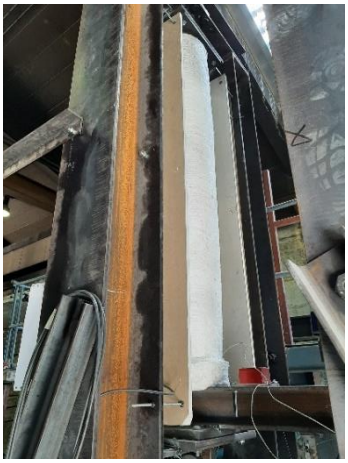

(b) PS during the test (behind)

(c) PS after buckling

Fig. III-23 Two-DOF test

Fig. III-24 (a) and (b) give the force-displacement relationship of the PS and the Fig. III-29 (a)-(d) show the displacement and internal forces of the same specimen in function of time. After loading, the shortening of the column is 0.249 mm and the rotation is equal to 0.0763 rad. The normal force is -36.26 kN and bending moment is 758,48 Nm. When the heating starts, the column expands. As this expansion is not free because of the beam, the normal force and the bending moment increases linearly. When 200°C is exceeded, the linearity is lost as the Young modulus decreases. After 90 minutes, bending moment and normal force decrease until buckling. The collapse of the specimen occurs after approximatively 140 min. It can be seen in Fig. III-23 (c) that the column buckled out of plane.

During the test, the NS is heated on three faces. The bending moments of the NS and the PS are shown in Fig. III-25. After t=55min, the Young modulus of the NS degrades as can be seen in Fig. III-26.

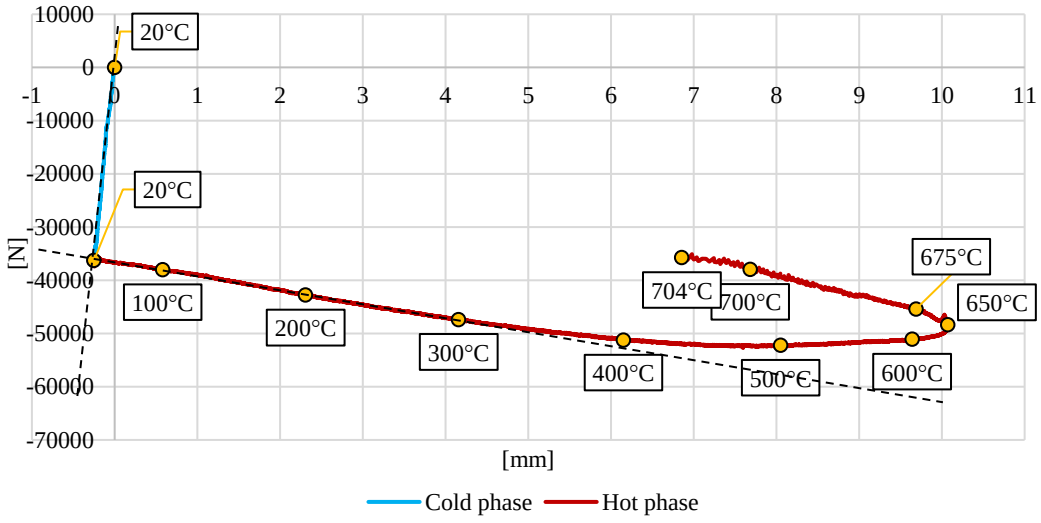

(a) Elongation-Normal force

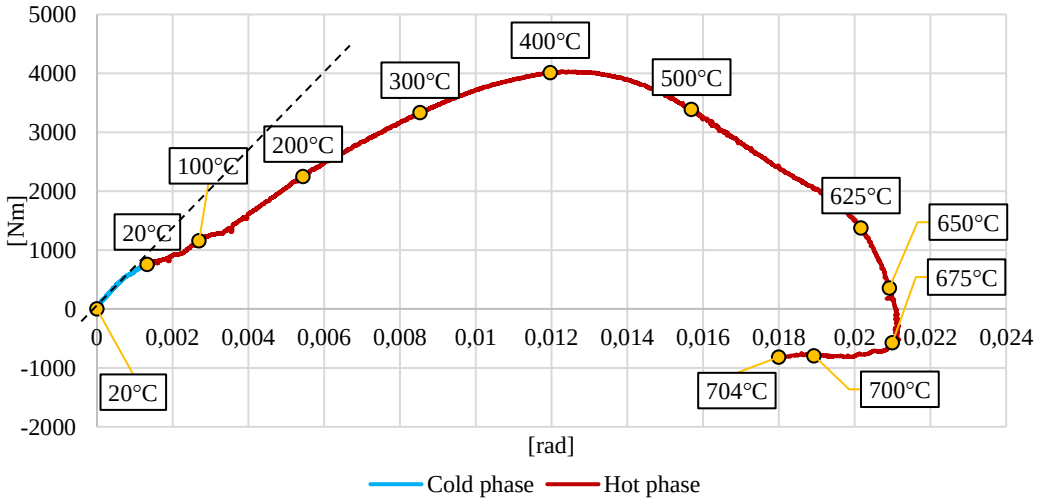

(b) Rotation-Bending moment

Fig. III-24 Two-DOF test: Force–displacement relationship

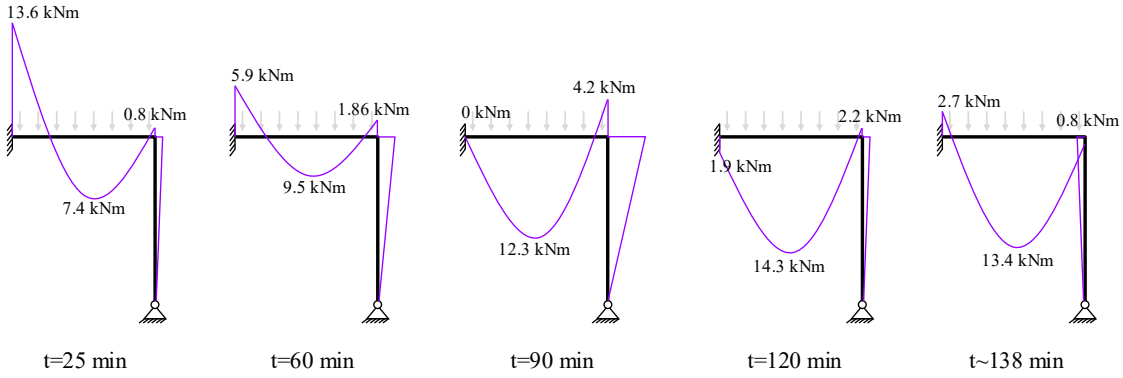

Fig. III-25 Bending moment diagram of NS and PS during the test

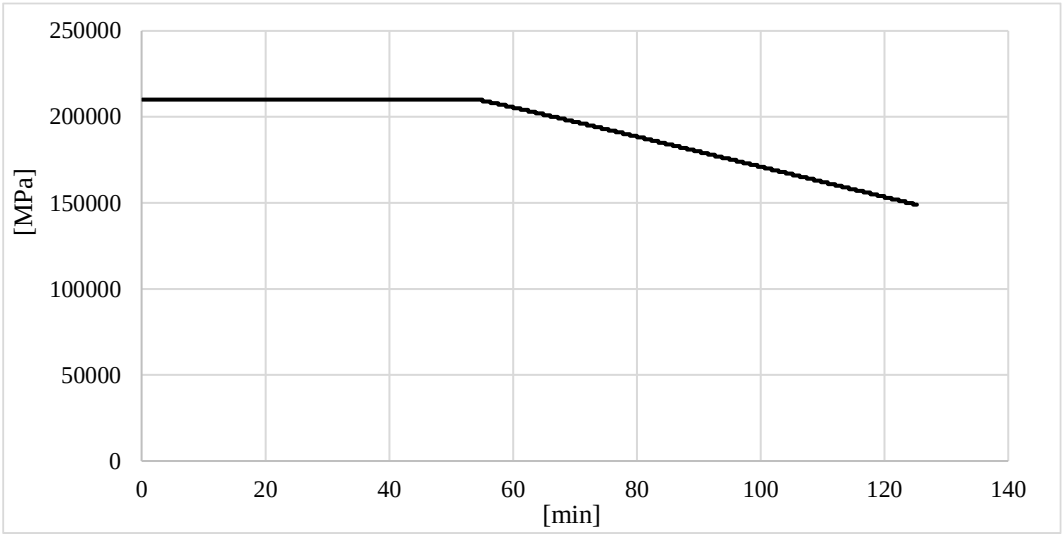

Fig. III-26 Young modulus of the NS

Interface error

To evaluate the efficiency of the algorithm, the equilibrium of the forces is verified. Fig. III-27 (a) shows the normal forces of the NS and the PS and Fig. III-27 (b) shows the relative error as expressed in equation (III-19) :

$$\text{Err N} = \frac{f_{NS}[1] + f_{PS}[1]}{f_{PS}[1]}\ [\%] = \frac{f_{NS}[1] + f_{cell}[1] + f_{cell}[2]}{f_{cell}[1] + f_{cell}[2]}\ [\%] \qquad \text{(III-19)}$$

$f_{cell}[1]$ and $f_{cell}[2]$ stand for the force measured by "load cell 1" and "load cell 2" (see Fig. III-21(a)).

The results are similar to the one DOF-test. The relative error of the normal force is low and rarely exceeds 2% during the test. It increases at the beginning of the test when the heating starts and when the specimen collapses.

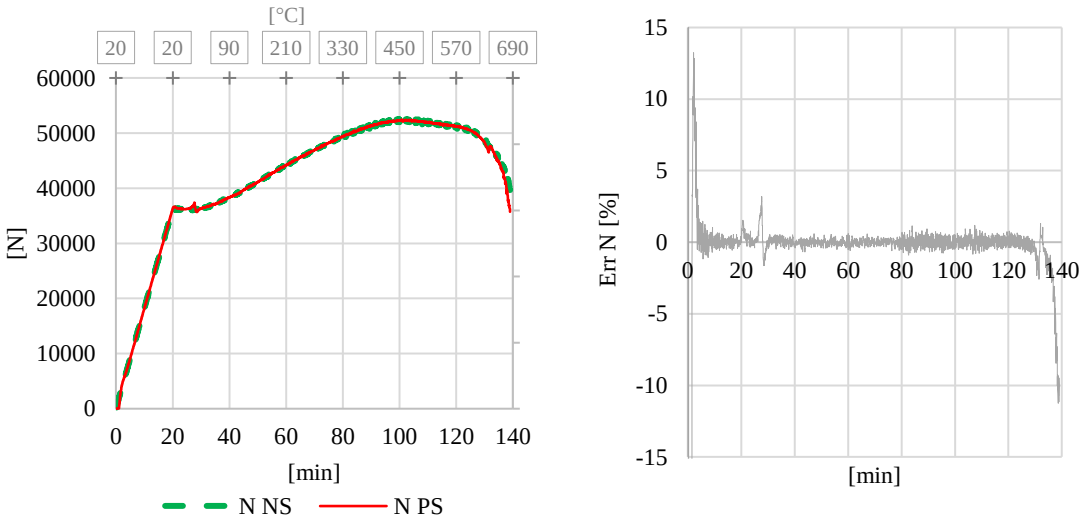

(a) Normal force at the interface of NS and PS *(b) Relative instantaneous error Err N*

Fig. III-27 Two-DOF test: Equilibrium of normal forces

Fig. III-28 (a) shows the bending moment at the interface between the PS and the NS and Fig. III-28 (b) shows the relative error between these interface forces. This error "Err M" is computed as follows:

$$\text{Err M} = \frac{f_{NS}[2] + f_{PS}[2]}{f_{PS}[2]}\ [\%] = \frac{f_{NS}[1] + a_1 f_{cell}[1] + a_2 f_{cell}[2]}{a_1 f_{cell}[1] + a_2 f_{cell}[2]}\ [\%] \qquad \text{(III-20)}$$

In Fig. III-28 (a), one can notice that the curve of the NS is not smooth and present numerous spikes. These variations can be explained by the fact that the inclinometer measurement is directly used to calculate the rotation to be applied to the NS. This rotation therefore presents small variations. These are due to the noise of the sensor, which is of the order of $1\text{-}2 \times 10^{-5}$ radiant. Equation (III-16) shows that the order of magnitude the diagonal term of $\mathbf{K}_{NS_0}$ is 6×10^6. Therefore, variations of 10-20 Nm are expected in the bending moment of the NS, which corresponds to the peaks that can be seen on the graph. These fluctuations would be less marked for a case where the rotations and bending moment would be higher. The relative error of the bending moment is thus higher (Fig. III-28 (b)), especially at the beginning and at the end of the test when the column collapses but remains around 5% during the majority of the HFT, showing the reliable performances of the algorithm.

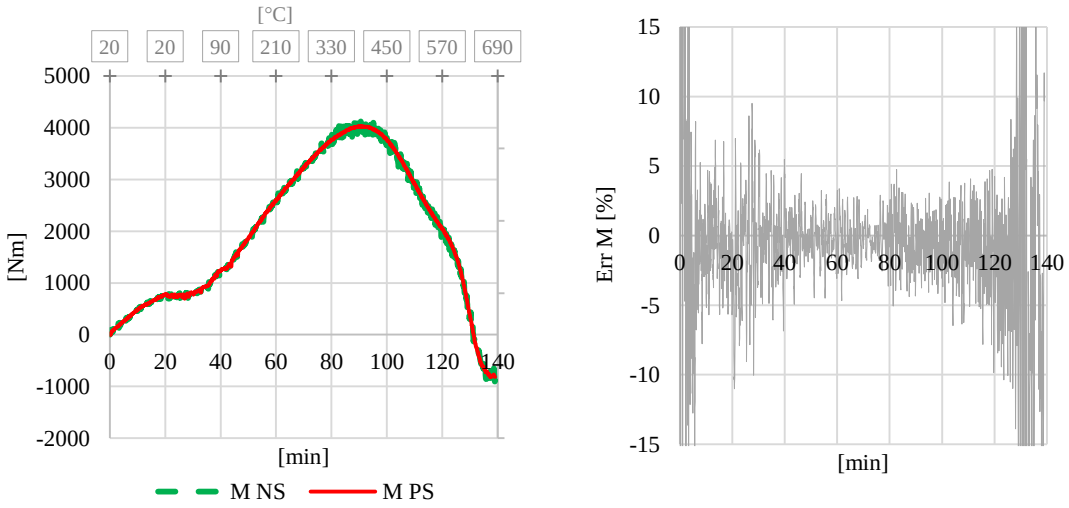

(a) Bending moment at the interface of NS and PS *(b) Relative instantaneous error Err M*

Fig. III-28 Two-DOF test: Equilibrium of bending moment

Comparison with numerical simulation

The elongation and rotation of the column are shown in Fig. III-29 (a) and (c). The axial force and bending moment can be seen in Fig. III-29 (b) and (d).

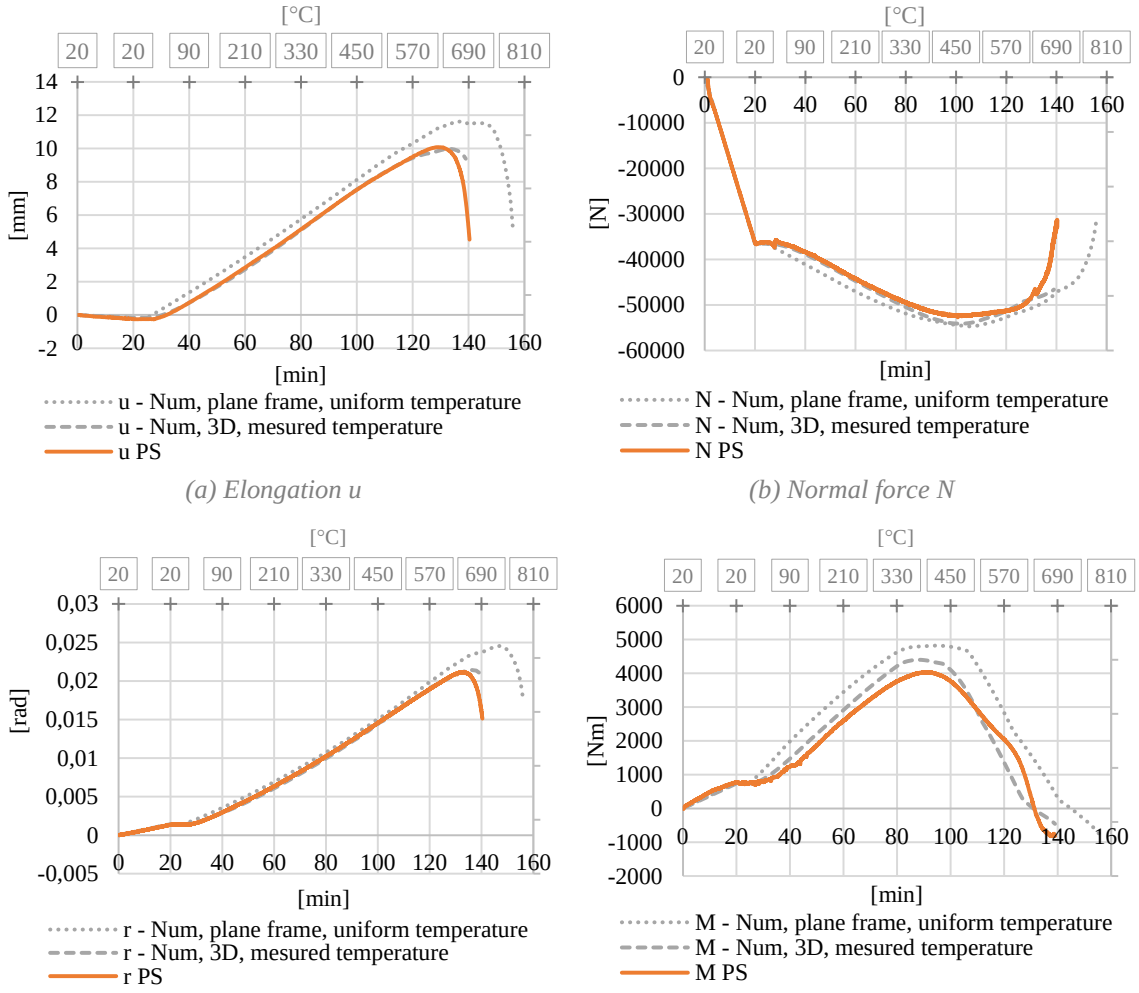

(a) Elongation u *(b) Normal force N*

(c) Rotation r *(d) Bending moment M*

Fig. III-29 Two-DOF test: Comparison with numerical simulations

The results were compared to numerical simulation of the complete frame. The curves “Num, plane frame, uniform temperature” were computed using a "plane frame" structure and considering uniform temperature. This simulation predicts the buckling at a temperature of 792°C after approximatively 157 min. One can make similar observations as in the one-DOF test when one compares HFT curves (“U PS”, “r PS”, “N PS” and “M PS”) with these results: there is a lag, and the failure occurs earlier. Moreover, the column buckled out of plane.

However, it is important to specify that the curves were computed using a "plane frame" structure, whereas the column is tested in an imperfect environment that proved to display a three-dimensional character: the hinges are not completely rigid in the out-of-plane direction and allow a slight rotation that could cause this early failure (Appendix C, Fig. C-12 and Fig. C-13).

The "corrected" numerical simulation was therefore performed, considering a three-dimensional column that is pinned in the direction perpendicular to the plane of the reference structure. An initial geometrical imperfection of 2.8 mm was added. The temperatures were also corrected with the curves that can be found in Appendix E, Section E.2. Under these conditions, a buckling in this direction was in fact observed. One can see in Fig. III-29 that the internal forces and displacements obtained during the test are closer to the corrected simulations. Similar observations can be made for the force-displacement relationship of the PS and the corrected numerical simulation, shown in Fig. III-30.

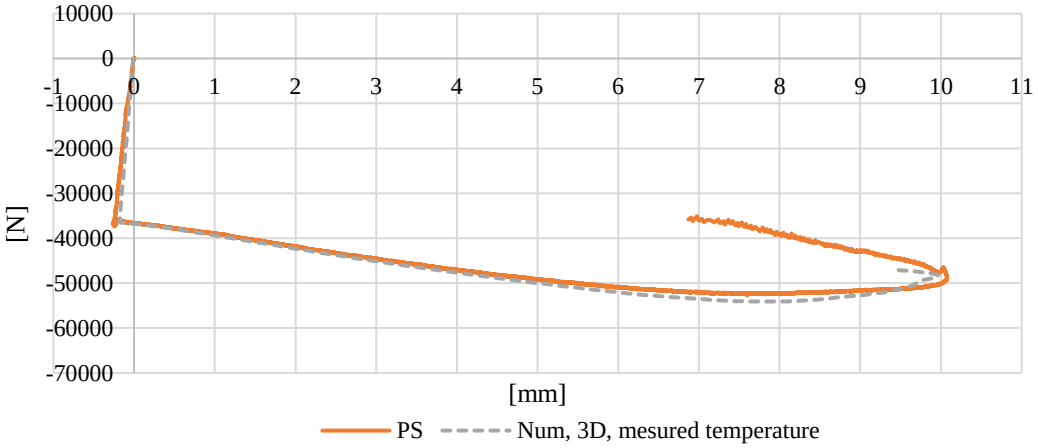

(a) Elongation-Normal force

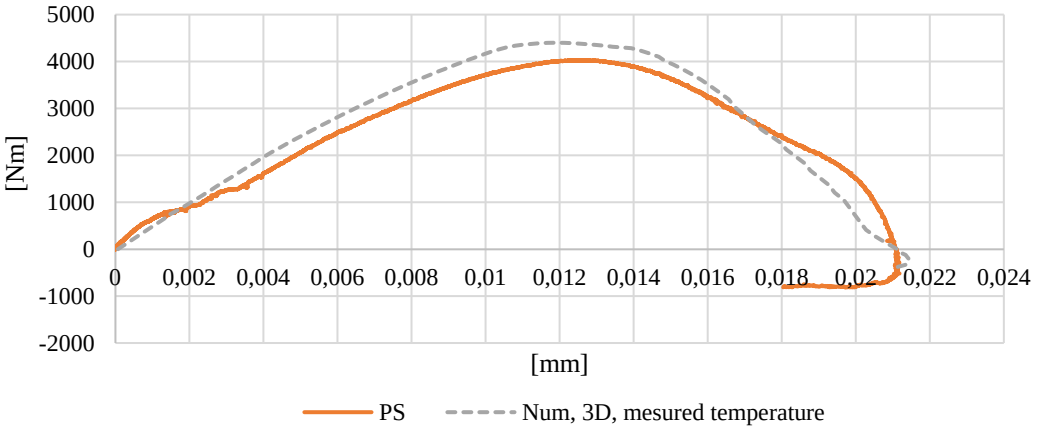

(b) Rotation-bending moment

Fig. III-30 Two-DOF test: Force–displacement relationship of the PS and numerical simulation

III.4 Three-DOF test

III.4.1 Test configuration

The reference structure is a two-storey half scaled building with four longitudinal bays, as shown in Fig. III-31. It is composed of 1.3 m steel beams (HS160x80x5, S460) and 1.3 m columns (HS80x5, S460). The PS is a HS80x5 steel column located at the edge of the building in a heated compartment. NS is the remaining structure.

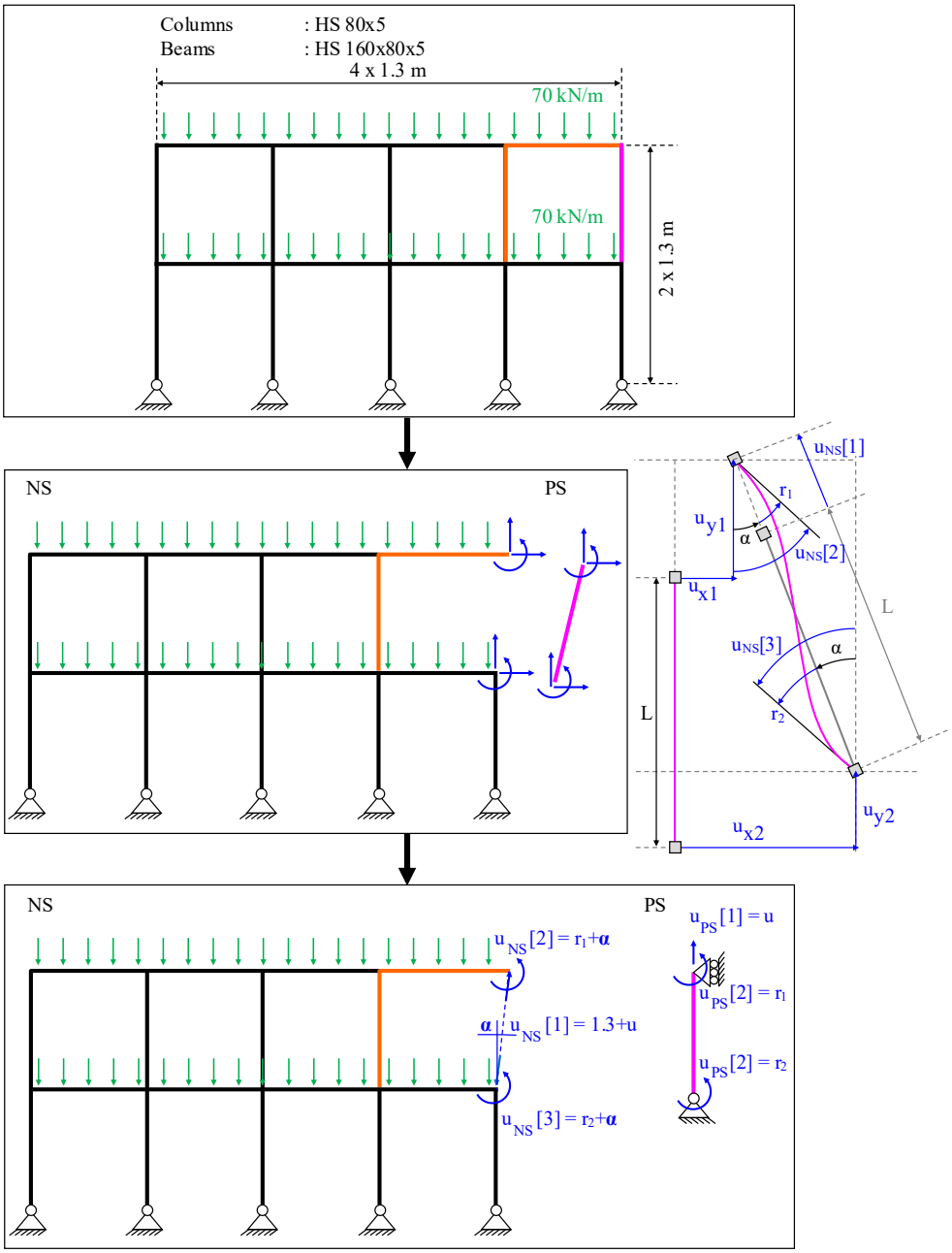

Fig. III-31 Three-DOF test: NS and PS

As in Section III-3, the specimen is tested with a roller support and a pinned support. The interface displacements of the PS are the elongation of the column and two rotations, at the top and at the end of the element. In the NS, these displacements consist of:

- the relative distance between the two extremities of the column, $u_{NS}[1]$

- two rotations to which rigid body rotations are added, $u_{NS}[2]$ and $u_{NS}[3]$

The transformations are as follows (see Fig. III-31):

$$u_{NS}[1] = 1.3 + u$$

$$u_{NS}[2] = r_1 + \alpha = r_1 + \operatorname{atan}\left(\frac{u_{x2} - u_{x1}}{1.3 + u_{y1} - u_{y2}}\right) \qquad u_{NS}[3] = r_2 + \alpha = r_2 + \operatorname{atan}\left(\frac{u_{x2} - u_{x1}}{1.3 + u_{y1} - u_{y2}}\right) \tag{III-21}$$

The column is tested upside down as shown in Fig. III-32 (a). The two extremities of the PS are welded to HEB100-lever arms. These beams are welded to plates, bolted to hinges (see Fig. III-32 (b)).

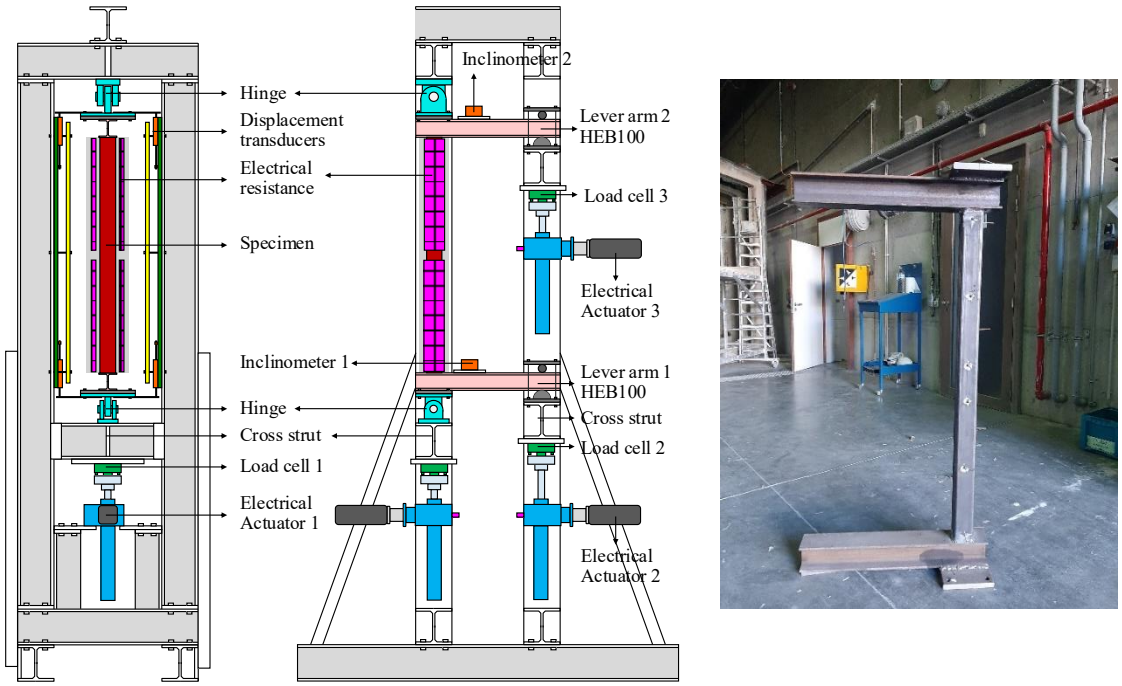

(a) Setup *(b) Specimen*

Fig. III-32 Material and setup of the three-DOF test

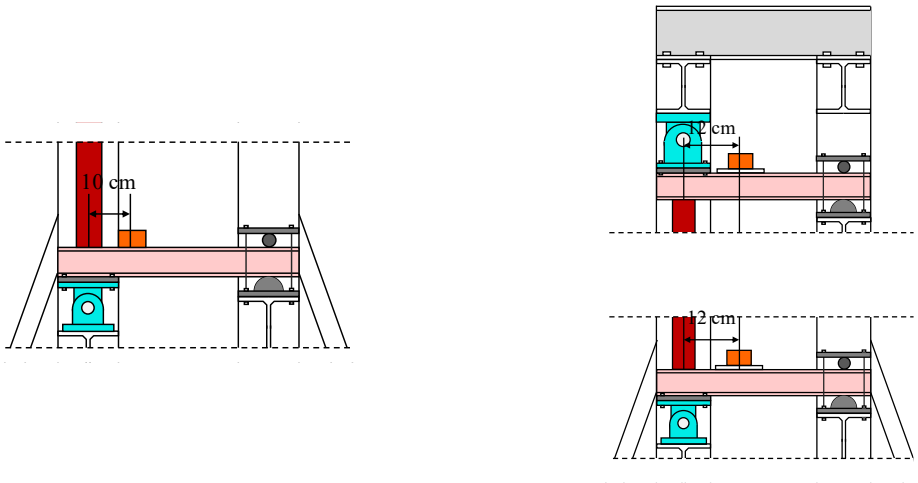

(a) Inclinometer of the two-DOF test *(b) Inclinometer of the three-DOF test*

Fig. III-33 Mounting of the inclinometers

During the two-DOF test, high temperatures were measured at the inclinometer and therefore it was decided to protect them further from temperature rises by increasing the distance between the inclinometer and the bottom of the column and placing a plasterboard under the sensor. The difference between the two setups is shown in Fig. III-33 (a) and (b).

The 3x3 transformation matrix $\mathbf{T}'$ and $\mathbf{T}''$ and the initial stiffness matrices, $\mathbf{K}_{\mathrm{PS}_0}^{\mathrm{EST}}$ and $\mathbf{K}_{\mathrm{NS}_0}$ are also determined, as in the previous cases. The matrix $\mathbf{T}'$ gives the following relationship between the interface forces and the forces measured by the load cells:

$$\mathbf{T}' = \begin{bmatrix} 1 & 1 & 0 \\ a_1 & a_2 & 0 \\ 0 & 0 & b \end{bmatrix}^{-1} \tag{III-22}$$

With b equal to 0.61 m. The matrix $\mathbf{T}'$ is given in Appendix D, Section D.3. The stiffness matrices are as follows (in [N], [m] and [rad]):

$$\mathbf{K}_{\mathrm{PS}_0}^{\mathrm{EST}} = 10^3 \begin{bmatrix} 237461 & 0 & 0 \\ 0 & 885 & 442.5 \\ 0 & 442.5 & 885 \end{bmatrix} \quad \mathbf{K}_{\mathrm{NS}_0} = 10^3 \begin{bmatrix} 4944 & 170 & -3895 \\ 170 & 4040 & -130 \\ -3895 & -130 & 4827 \end{bmatrix} \tag{III-23}$$

One obtains a 6th order system. As in Section II-6, it is approximated to a second order system with two dominant eigenvalues. The following time parameters are considered:

$$\begin{gathered} \mathrm{T} = 3\ \mathrm{s} \\ \mathrm{T_r} = 12\ \mathrm{s} \\ \lambda = \exp\left(-2.72\frac{3}{12}\right) = 0{,}51 \end{gathered} \tag{III-24}$$

The gain matrices are computed:

$$\mathbf{L}_{\mathrm{P}} = 10^{-9} \begin{bmatrix} 4.502 & 0 & 0 \\ 0 & 65.366 & 0 \\ 0 & 0 & 123.58 \end{bmatrix} \quad \mathbf{L}_{\mathrm{J}} = 10^{-9} \begin{bmatrix} 0.186 & 0 & 0 \\ 0 & 15.352 & 0 \\ 0 & 0 & 57.778 \end{bmatrix} \tag{III-25}$$

To verify the stability, the eigenvalues of the simplified matrix $\begin{bmatrix} \mathbf{I} - \mathbf{L}_{\mathrm{P}}(\mathbf{K}_{\mathrm{PS_i}}^{*} + \mathbf{K}_{\mathrm{NS_i}}^{*}) & \mathbf{L}_{\mathrm{J}} \\ -(\mathbf{K}_{\mathrm{PS_i}}^{*} + \mathbf{K}_{\mathrm{NS_i}}^{*}) & \mathbf{I} \end{bmatrix}$ are explicitly computed for $\alpha \in [0,1]$. The resulting poles are shown in the hereunder figure. On can notice that there is a high complex part for some eigenvalues, indicating overshoots. These overshoots would be partially damped by the other poles, but not completely. This design could not be improved.

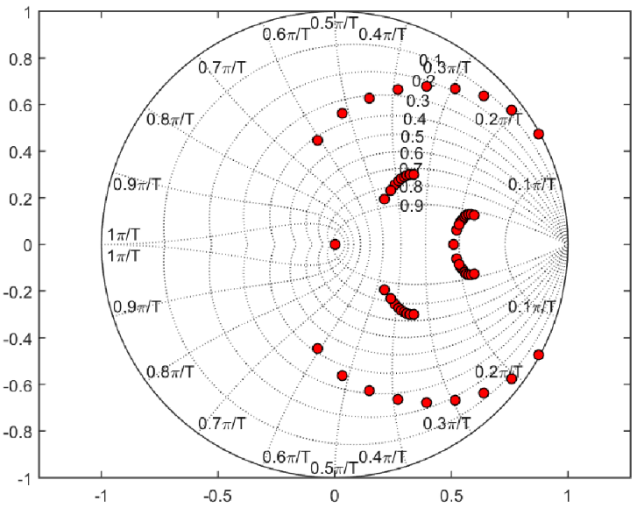

Fig. III-34 Three-DOF test: Predicted location of the poles

III.4.2 Results and discussion

The test was performed on October 8, 2020. Fig. III-35 (a), (b) and (c) show the column during the test and after buckling.

(a) During the test (front) *(b) During the test (behind)* *(c) After buckling*

Fig. III-35 Three-DOF test

In this Section M_1 and M_2 stand for the bending moment, respectively, at the top of the column and the bottom in Fig. III-31.

The behaviour of the column is similar to the one of the two-DOF test. The specimen buckled out-of-plane. Fig. III-36 shows the force–displacement relationship. Forces and displacements in function of time are given in Fig. III-41 (a)-(f). Rotations, axial displacement and forces increases linearly during the loading phase. After 25 min, the heating starts, and NS restrains the thermal expansion of the PS. Thus, normal force and bending moments increase until the temperature reach around 400°C. Afterwards, the interface forces decrease and buckling occurs around 600 °C.

During the test, the NS is heated. The bending moment diagram of the column and the upper beam of the compartment can be seen in Fig. III-37. Fig. III-38 shows the degradation if the Young modulus in this upper beam.

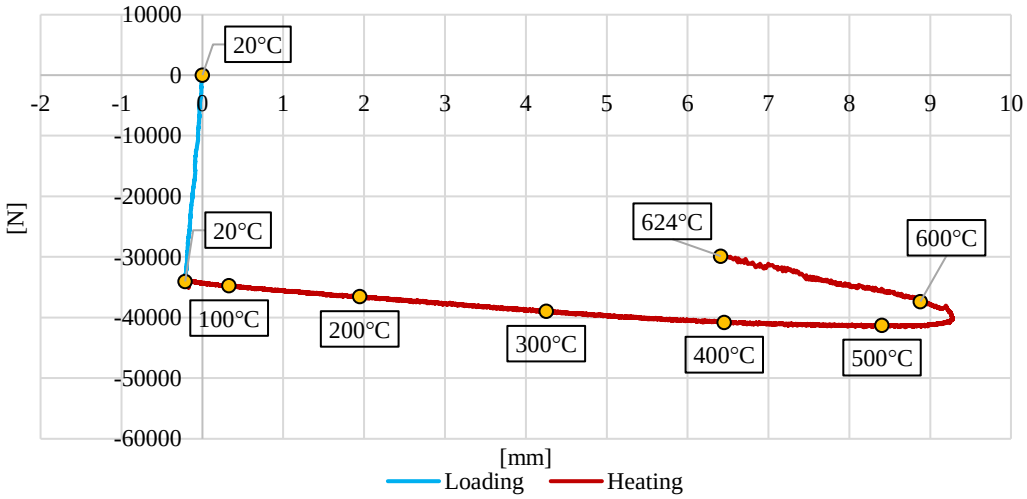

(a) Elongation-Normal force

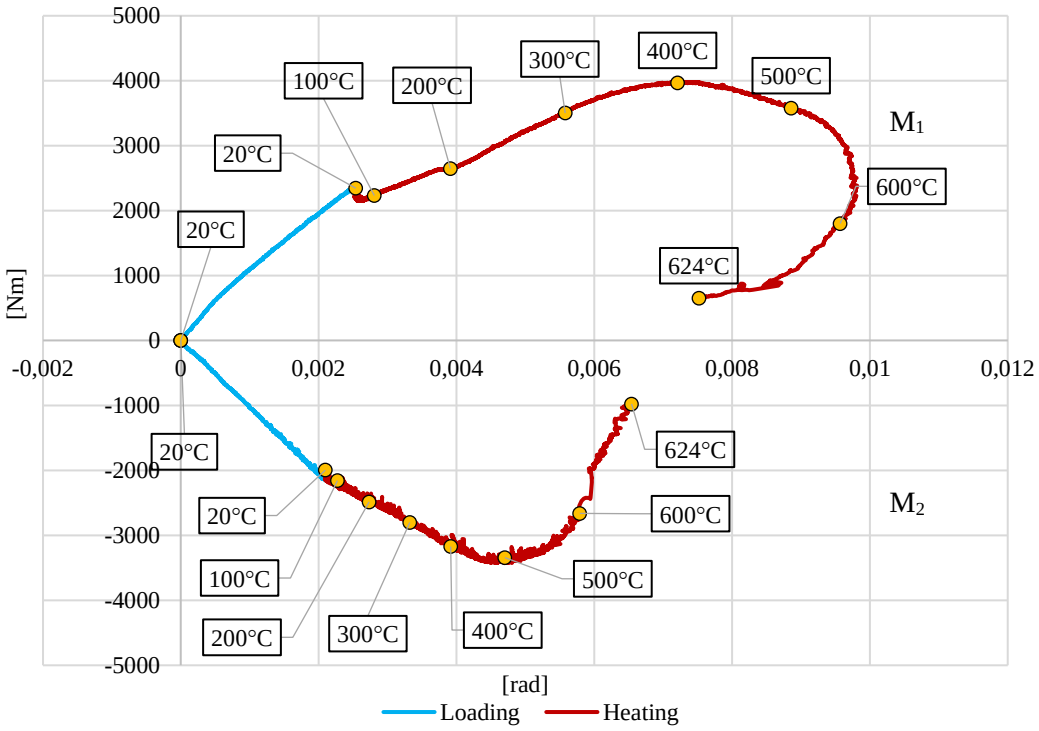

(b) Rotation-Bending moment

Fig. III-36 Three-DOF test: Force–displacement relationship

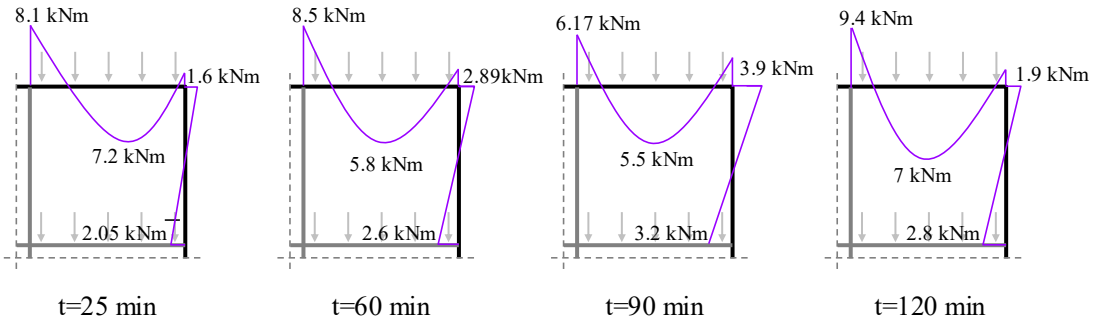

Fig. III-37 Bending moment diagram of NS and PS during the test

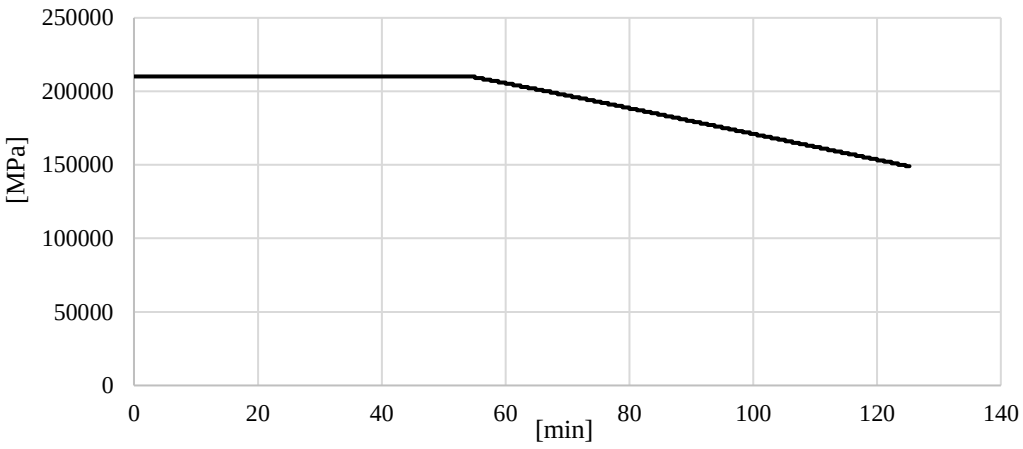

Fig. III-38 Young modulus of the NS (upper beam)

Interface error

As can be seen in Fig. III-39 (a), the normal forces at the interface between NS and PS are in equilibrium, with a slight gap at the end. The relative error Err N is computed as follows:

$$\text{Err N} = \frac{f_{NS}[1] + f_{PS}[1]}{f_{PS}[1]}\ [\%] = \frac{f_{NS}[1] + f_{cell}[1] + f_{cell}[2]}{f_{cell}[1] + f_{cell}[2]}\ [\%] \qquad \text{(III-26)}$$

$f_{cell}[1]$ et $f_{cell}[2]$ are the forces measured by "load cell 1" and "load cell 2" (see Fig. III-32 (a)). Err N mainly remains below 2%, except, at the beginning of the loading, when the heating starts and at the end of the test. The error increases at these three times for the same reasons mentioned in Section III.2.2.

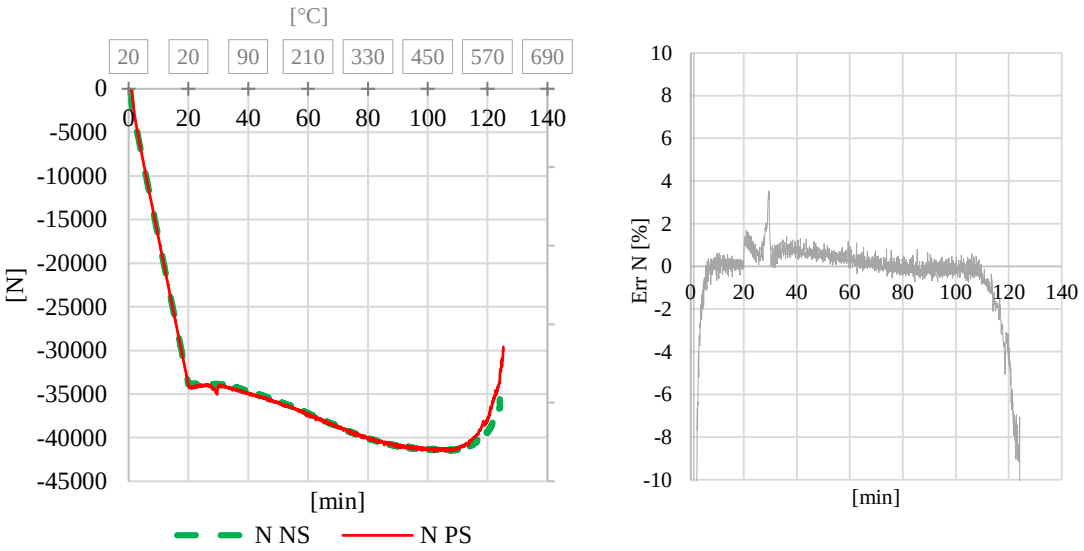

(a) Normal force at the interface of NS and PS *(b) Relative instantaneous error Err N*

Fig. III-39 Three-DOF test: Equilibrium of the normal force

The relative errors Err M_1 and Err M_2 are given by the hereunder equations.

$$\text{Err } M_1 = \frac{f_{NS}[2] + f_{PS}[2]}{f_{PS}[2]}\ [\%] = \frac{f_{NS}[1] + a_1 f_{cell}[1] + a_2 f_{cell}[2]}{a_1 f_{cell}[1] + a_2 f_{cell}[2]}\ [\%] \qquad \text{(III-27)}$$

$$\text{Err } M_2 = \frac{f_{NS}[2] + f_{PS}[2]}{f_{PS}[2]}\ [\%] = \frac{f_{NS}[1] + b f_{cell}[3]}{b f_{cell}[3]}\ [\%] \qquad \text{(III-28)}$$

$f_{cell}[3]$ is the force measured by "load cell 3". The interface errors vary during the test but remains most of time in the interval $[-5\%, +5\%]$. Similar to the two-DOF test, M_1 and M_2 of the NS displays spikes throughout the test because of experimental errors. These spikes are higher in the graph M_2 and one can observe that both NS and PS presents these variations. This difference can be explained:

- The rotational stiffness of the NS is higher at the bottom (see stiffness matrix in (III-23)), making that the experimental errors increase the spikes. This was already observed in the numerical HFT (see Section II.6.3)
- The gains $\mathbf{L_P}$ and $\mathbf{L_J}$ related to this DOF are higher, especially the $\mathbf{L_J}$ term. In this three DOF test, the hypothesis of decoupled DOFs is widely questionable, resulting in gains that entail less

satisfying behaviour. Moreover, poles with high complex parts were obtained in Fig. III-34, which involves overshoots.

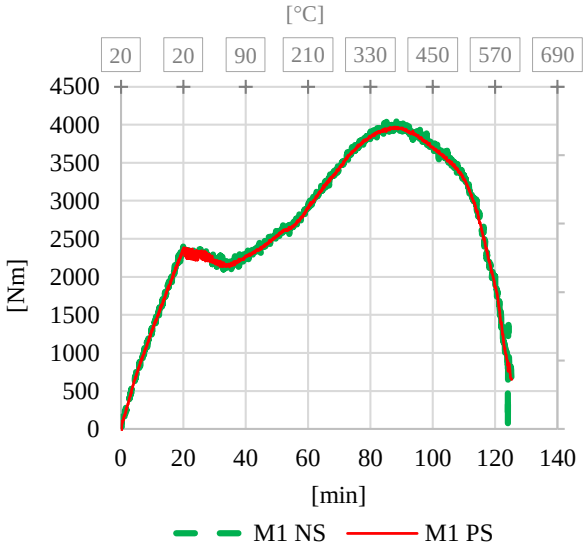

(a) Bending moment at the interface of NS and PS M_1

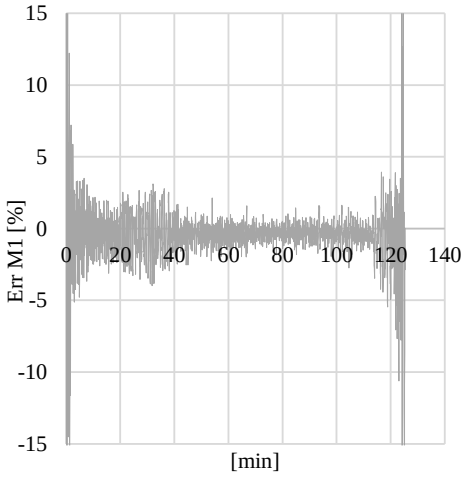

(b) Relative instantaneous error Err M_1

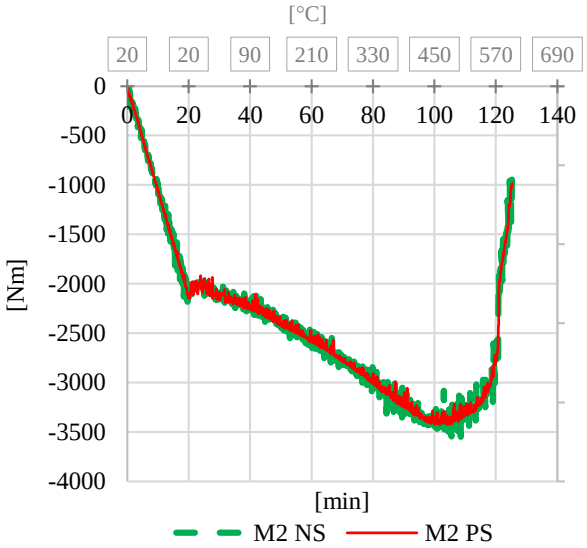

(a) Bending moment at the interface of NS and PS M_2

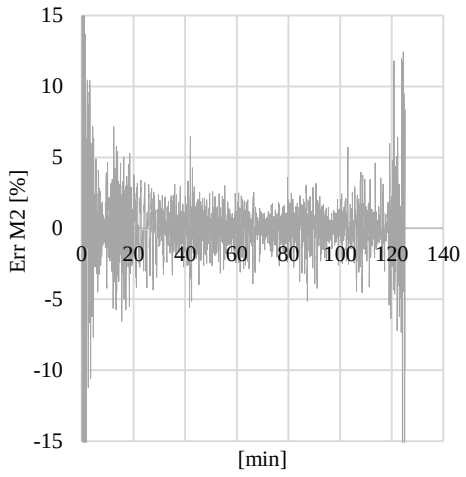

(b) Relative instantaneous error Err M_2

Fig. III-40 Three-DOF test: Equilibrium of the bending moments

Comparison with numerical simulation

Results of the axial displacement and the rotations of the PS as a function of time are shown in Fig. III-41 (a), (c) and (e). The normal forces and bending moments of the specimen can be seen in Fig. III-41 (b), (d) and (f). Fig. III-42 shows the force-displacement relationship of the PS and the numerical simulation (corrected, with 3D frame and real temperature).

The results of the test are compared to numerical simulations of the complete structure. The first simulation is a 2D plane structure with PS uniformly heated with an eccentricity of 2.6 mm. A second model was then performed, considering the temperature measured during the test (see Appendix E, Fig E-8 and Fig. E-9) and a 3D model that allows out-of-plane buckling. With the second numerical simulation, the differences between the experimental results and the numerical behaviour are reduced and the correct failure mode is obtained. An eccentricity of 2.6 mm was considered out-of-plane.

One can observe that the normal force and the axial displacements are close the second numerical simulation. The rotations and the bending moment follow similar trends but there are differences, in the rotations. Such deviations do not appear in the rotation and bending moment of the two-DOF test, which suggests that the difference between the two inclinometer mountings, as shown in Fig. III-33, might have influenced the results.

However, the trends are well reproduced for the forces and displacements and the limited errors in the interface forces suggests that the hybrid test allowed the equilibrium of the forces and the compatibility of displacements between the two substructures.

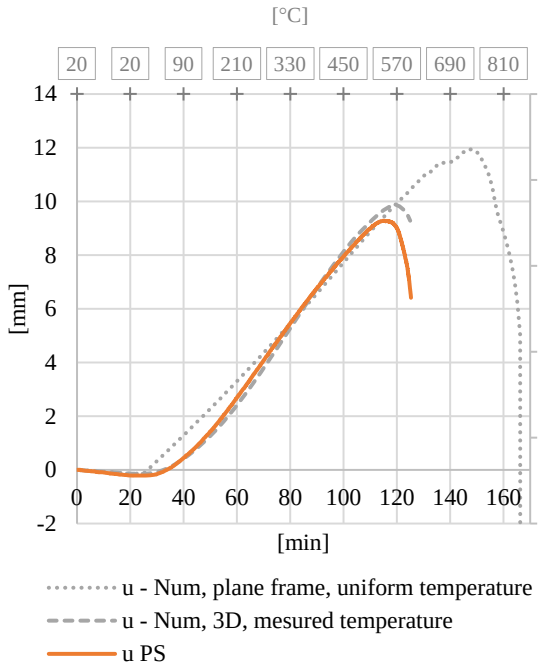

(a) Elongation u

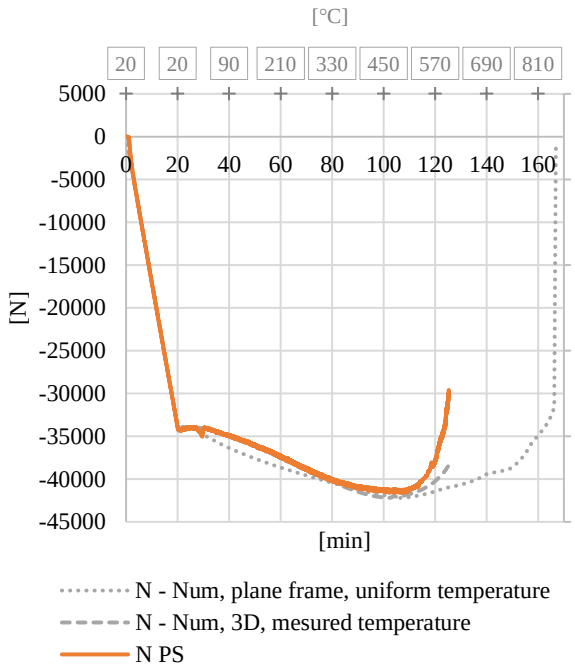

(b) Normal force N

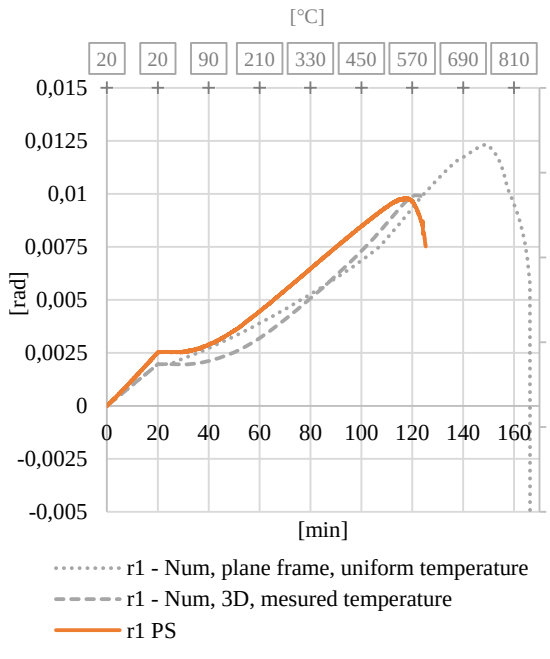

(c) Rotation r

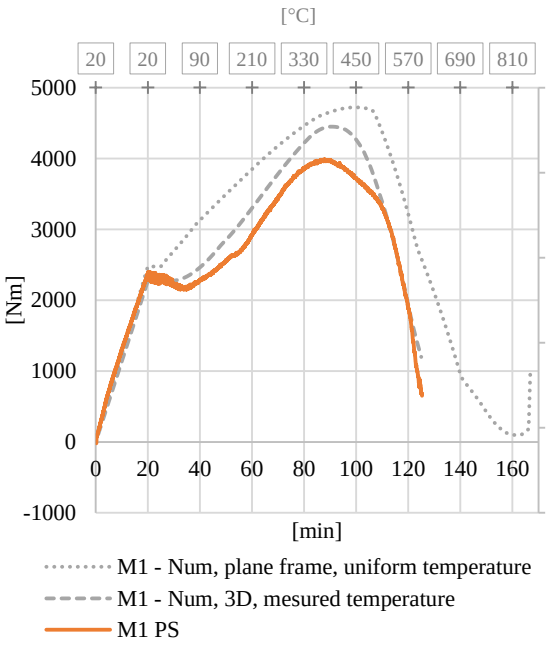

(d) Bending moment M

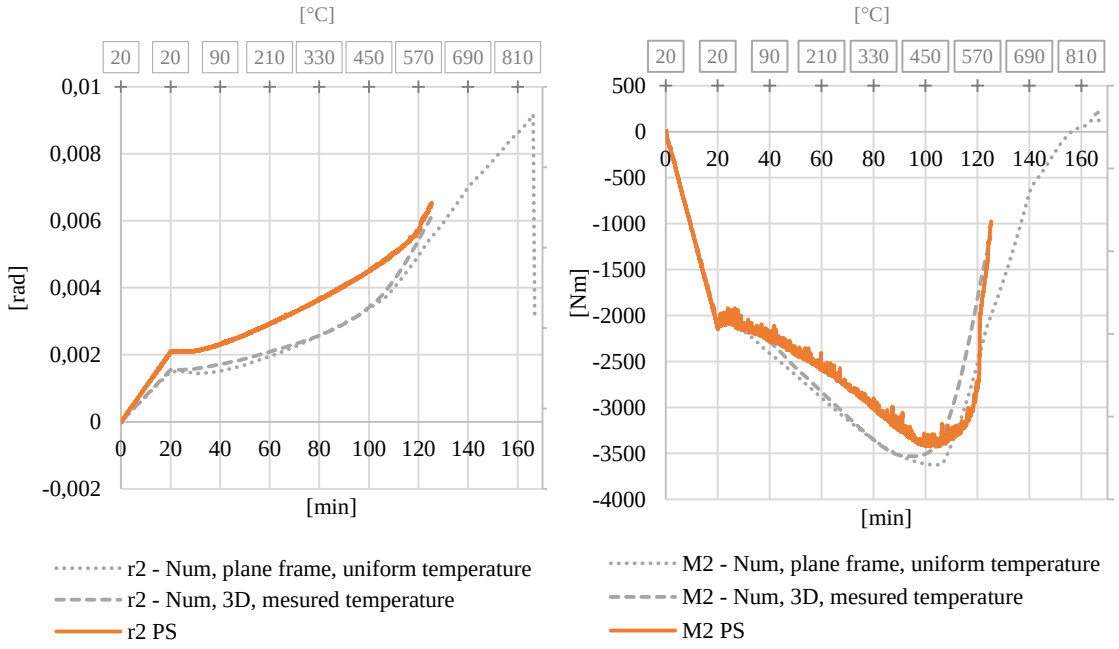

(e) Rotation r *(f) Bending moment M*

Fig. III-41 Three-DOF test: Comparison with numerical simulations

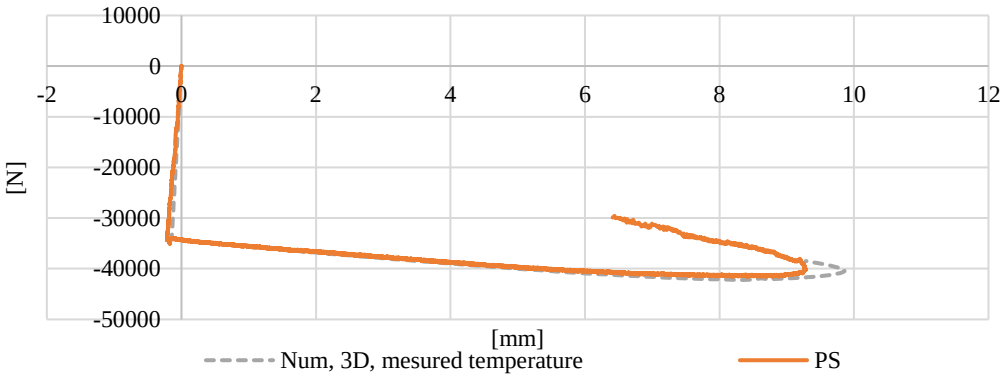

(a) Elongation-Normal force

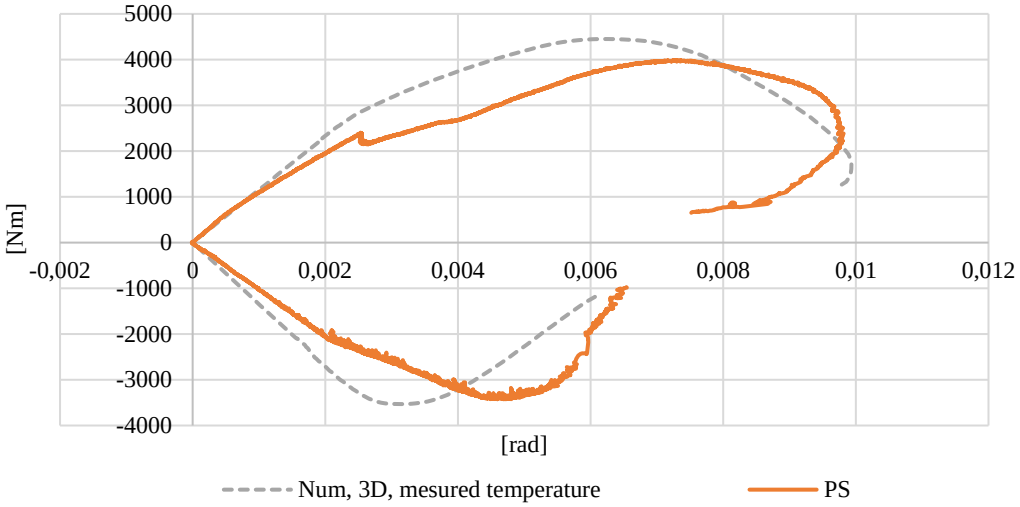

(b) Rotation-Bending moment

Fig. III-42 Three-DOF test: Force–displacement relationship

Conclusion

Hybrid testing is a very appealing method in structural engineering as it combines the benefits of both numerical simulations and experimental testing. The testing technique has a history of more than 30 years in earthquake engineering and many applications have demonstrated its effectiveness. However, despite this long-standing experience in the seismic field, a straightforward use of hybrid testing in fire engineering is not feasible because of several physical phenomena. In fact, the heated specimen is subjected to thermal expansion and thermal induced degradation of stiffness and strength and exhibits a time-dependent material behaviour when exposed to high temperature. Considerable complexity is thus added to the tested structural element. Hybrid fire testing is thus a separate field of research. The technique has been investigated in fire engineering since 1990's. Many algorithms have been developed but most have only been validated numerically. Some experimental hybrid tests have been published. However, they were limited to one-DOF system. The review of the state of the art also shows that the algorithms that were developed so far used the instantaneous responses of the substructures to correct the displacement without considering the history of the test.

Contribution

The algorithm that is proposed in this thesis is based on the design of a proportional integral controller. The displacements of the substructures are updated considering the instantaneous errors between the interface forces and the history of this error. This algorithm is relatively simple to apply in comparison with methods based on decomposition of domains and performs better than some methods like (Sauca, Gernay, et al. 2018) by adding an integral term.

In addition to the development of this algorithm, the thesis made use of the state-space representation developed by modern control theory to formulate the process of HFT. This framework is valuable tool that allows to formulate the stability conditions of the system and determine the parameter of the step response of the system, which allows to compare the design of several controllers and predict the behaviour of the system. It also gave keys to understanding the effect of experimental errors and delays in the process.The tool of VHFT that was developed for the thesis is a powerful tool to evaluate the efficiency, stability and the effect of delays and experimental errors.

The numerical validation and experimental tests performed in this research significantly advance the state of the art of hybrid fire testing. For the first time, fully automated multi-DOF test has been performed. Moreover, the numerical substructure was also subjected to fire. Stability, compatibility of displacement and equilibrium of forces were ensured during the tests and the results follow the trends of numerical simulations of the predicted behaviour.

Limitations

However, it is important to be aware of the limitations of the presented algorithms and provide an outlook for future research:

- The method is based on the hypothesis of decoupled DOFs, which is widely questionable in the case of a beam with three DOFs. This hypothesis considerably simplifies the design of the controller as the gain matrices are diagonal. However, the less valid this assumption is, the less efficient the controller will be during the test. It is to be expected that the controller cannot process some systems where the DOFs are strongly coupled. A research perspective is to explore the use of non-diagonal gain matrix.
- Another important limitation is the use of linear control. Constant gain matrices do not consider the degrading physical stiffness of the PS and result to less efficient controllers and overshoots. Adaptive control and learning gains are both options that should be investigated in further research.
- The use of initial mechanical properties is also a significant limitation because their availability cannot be guaranteed when it comes to testing new materials. The estimation of the stiffness is possible by preliminary tests. However, as demonstrated in the thesis, this estimate harms the efficiency of the controller and can affect stability.
- One can also mention that the increase in the number of DOFs doubles the order of the state representation and therefore the size of the gain matrices to be determined. A possibility would consist in improving the proportional controller with adaptive gains instead of complexify the proportional integral controller.
- The dynamics matrix that is used to design the controller is based on static equations. Although this assumption is valid during most of the test, it would be wise to refine the design of the controller with dynamic equations with the velocity in addition to displacement as a state variable. The use of a dynamics model that mimic the behaviour of a static model can be considered.
- The tests were performed using in-house interface software to make the link between numerical simulation, the specimen, the control system, and the sensors. Further research should now turn systematically to more general interfaces such as the generic object-oriented framework, called OpenFresco, in order to promote inter-institutional collaborations.

References

1993-1-2, BS EN. “Eurocode 3: Design of steel structures Part 1-2: General rules — Structural fire design.” 2005.

Abbiati, G., P. Covi, N. Tondini, O. S. Bursi, and B. Stojadinović. “A Real-Time Hybrid Fire Simulation Method Based on Dynamic Relaxation and Partitioned Time Integration.” *Journal of Engineering Mechanics*, September 2020.

Argyris, J. H. “An excursion into large rotations. Computer Methods.” *Applied Mechanics and Engineering*, 1982: 85-155.

Åström, K. J., and R. M. Murray. *Feedback Systems: An Introduction for Scientists and Engineers.* Princeton University Press, 2008.

Bas, E. E., and M. A. Moustafa. “Real-Time Hybrid Simulation with Deep Learning Computational Substructures: System Validation Using Linear Specimens.” *Machine Learning*, 2020: 469–489.

Bathe, K.-J., E. Ramm, and E. L. Wilson. “Finite element formulations for large deformation dynamic analysis.” *Computer Methods in Applied Mechanics and Engineering*, 1973: 255–271.

Belytschko, T., and B. J. Hsieh. “Application of higher order corotational stretch theories to nonlinear finite element analysis.” *Computers & Structures*, 1979: 175–182.

—. “Nonlinear transient finite element analysis with convected coordinates.” *International Journal for Numerical Methods in Engineering*, 1973: 255–271.

Bergan, P. G., and G. Horrigmoe. “Incremental variational principles and finite element models for nonlinear problems.” *Computer Methods in Applied Mechanics and Engineering*, 1976: 201–217.

BIPM, IEC, IFCC, ILAC, ISO, IUPAC, IUPAP and OIML. *Guide to the Expression of Uncertainty in Measurement.* JCGM 100 (GUM 1995 with minor corrections), 2008.

Campbell, S., and B. Stojadinovic. “A system for simultaneous pseudodynamic testing of multiple substructures.” *Sixth U.S. National Conference on Earthquake Engineering*, Seattle (United States), 1998.

Carrion, J. E., and B. F. Spencer. “Real-time hybrid testing using model-based delay compensation.” *4th International Conference on Earthquake Engineering*, Taipei (Taiwan), 2006.

Carrion, J., and B. F. Spencer. *Model-based Strategies for Real-time Hybrid Testing.* Technical Report, University of Illinois at Urbana-Champaign, Champaign: Newmark Structural Engineering Laboratory, 2007.

Chae, Y., K. Kazemibidokhti, and J. M. Ricles. “Adaptive time series compensator for delay compensation of servo-hydraulic actuator systems for real-time hybrid simulation.” *Earthquake Engineering & Structural Dynamics*, 2013: 1697–1715.

Chang , S. Y. “Improved explicit method for structural dynamics.” *Journal of Engineering Mechanics*, 2007: 748-760.

Chen, C. “Development and numerical simulation of hybrid effective force testing method (PhD Dissertation).” *Dept. of Civil and Environmental Engineering*, Lehigh University, Bethlehem (PA, United States), 2007.

Chen, C., and J. M. Ricles. “Stability analysis of SDOF real-time hybrid testing systems with explicit integration algorithms and actuator delay.” *Earthquake Engineering & Structural Dynamics*, 2008: 597-613.

—. “Tracking error-based servo-hydraulic actuator adaptive compensation for real-time hybrid simulation.” *Journal of Structural Division (ASCE)*, 2010: 432-440.

Chen, P.-C., and K. C. Tsai. “Dual compensation strategy for real-time hybrid testing.” *Earthquake Engineering & Structural Dynamics*, 2013: 1-23.

Christenson, R., Y. Z. Lin, A. Emmons, and B. Bass. “Large-scale experimental verification of semiactive control through real-time hybrid simulation.” *Journal of Structural Engineering*, 2008: 522-534.

Combescure, D., and P. Pegon. “α-Operator splitting time integration technique for pseudodynamic testing error propagation analysis.” *Soil Dynamics and Earthquake Engineering*, 1997: 427-443.

Construction, American Institute of Steel. *ANSI/AISC 360-16 Specification for structural steel buildings.* AISC, 2016.

Correia, A. M., J. P. C. Rodrigues, and M. Korzen. “Experimental research on the loadbearing capacity of partially encased steel columns under fire conditions.” *Journal of Structural Fire Engineering,*, 2012: 81–93.

Crisfield, M. A., and G. F. Moita. “A unified co-rotational for solids shells and beams.” *International Journal of Solids and Structures*, 1996: 2969–2992.

Darby, A. P., M. S. Williams, and A. Blakeborough. “Stability and delay compensation for real-time substructure testing.” *Journal of Engineering Mechanics*, 2002: 1276-1284.

Dermitzakis, S. N., and S. A. Mahin. *Development of substructuring techniques for on-line computer controlled seismic performance testing.* Technical report (UCB/EERC - 85/04), University of California, Berkeley: Earthquake Engineering Research Center, 1985.

Dimig, J., C. Shield, C. French, F. Bailey, and A. Clark. “Effective force testing: A method of seismic simulation for structural testing.” *Journal of Structural Engineering*, 1999, ASCE ed.: 1028-1037.

Evmorfbpoulos, N. *Some results on diagonally dominant matrices with positive diagonal elements.* UTH Technical Report, University of Thessaly, n.d.

Farhat, C., and F. X. Roux. “A method of finite element tearing and interconnecting and its parallel solution algorithm.” *International Journal for Numerical Methods in Engineering*, 1991, John Wiley & Sons ed.: 1205–1227.

Felippa, C. A., and B. Haugen. “A unified formulation of small-strain corotational finite elements : I. Theory.” *Computer Methods in Applied Mechanics and Engineering*, 2005: 2285–2335.

Fontana, M., M. Knobloch, and A. Frangi. “Global structural behavior in fire and consolidated consolidated testing of steel structures.” *Research and Applications in Structural Engineering, Mechanics and Computation,* 2013: 687–688.

Franssen, J.-M., and T. Gernay. “Modeling structures in fire with SAFIR®: Theoretical background and capabilities.” *Journal of Structural Fire Engineering,* 2017: 300–323.

Guo, Y., Y. Xiao, and Q. Hu. “NetSLab-based remote hybrid testing in current hierarchical network environment.” *4th International Conference on Earthquake Engineering,* Taipei (Taiwan), 2006.

Hakuno, M., M. Shidawara, and T. Hara. “Dynamic destructive test of a cantilever beam controlled by an analog-computer.” *Proceedings of the Japan Society of Civil Engineers,* 1969, Japan Society of Civil Engineers ed.: 1-9.

Hilber, H. M., T. J. R. Hughes, and R. L. Taylor. “Improved numerical dissipation for time integration algorithms in structural dynamics.” *Earthquake Engineering & Structural Dynamics,* 1977: 283-292.

Horiuchi , T., and T. Konno. “Development of a real-time hybrid experimental system with actuator delay compensation.” *11th World Conference on Earthquake Engineering,* Acapulco (Mexico) 1996.

Horiuchi, T., and T. Konno. “A new method for compensating actuator delay in real-time hybrid experiments.” *Philosophical Transaction: Mathematics, Physics and Engineering Science,* 2001: 1893-1909.

Horiuchi, T., M. Inoue, T. Konno, and Y. Namita. “Real-time hybrid experimental system with actuator delay compensation and its application to a piping system with energy absorber.” *Earthquake Engineering & Structural Dynamics,* 1999: 1121-1141.

Hosser, D., J. Ameler, T. Dorn, B. Gensel, and H. Schlülter. *Entwicklung einer ”lntelligenten Prüfmaschine”zur Untersuchung von Gesamttragwerken unter lokaler Brandbeanspruchung (Abschlussbericht zur 2. Phase des Forschungsvorhabens).* Technical report, Technical University Brunswick, 1993.

Hosser, D., J. Ameler, T. Dorn, B. Gensel, and H. Schülter. *Entwicklung einer ”lntelligenten Prüfmaschine” zur Untersuchung von Gesamttragwerken unter lokaler Brandbeanspruchung (Abschlussbericht zur 3. Phase des Forschungsvorhabens).* Technical report, Technical University Brunswick, 1995.

Hughes, T. J. R., K. S. Pister, and R. L. Taylor. “Implicit-explicit finite elements in nonlinear transient analysis.” *Computer Methods in Applied Mechanics and Engineering,* 1979: 159-182.

Hung, C.-C., and S. El-Tawil. “Full operator algorithm for hybrid simulation.” *Earthquake Engineering & Structural Dynamics,* 2009: 1545-1561.

Hung, C-C, W-M Yen, and W-T Lu. “An unconditionally stable algorithm with the capability of restraining the influence of actuator control errors in hybrid simulation.” *Engineering Structures,* 2010: 168-178.

Iemura, H., A. Igarashai, and Y. Takahashi. “Substructured hybrid techniques for actuator loading and shake table tests.” *First Inetrnational Conference on Advances in Structural Engineering and Mechanics,* Seoul (South Korea), 1999.

Igarashi, A., H. Iemura, and T. Suwa. “Development of substructured shaking table test method.” *Proceedings of the 12th World Conference on Earthquake Engineering,* 2000.

Jung, R.-Y., and B. P. Shing. “Performance evaluation of a real-time pseudodynamic test system.” *Earthquake Engineering & Structural Dynamics*, 2006: 789-810.

Kalman, R. E. “An approach to linear filtering and prediction problems.” *Transactions of the ASME, Journal of Basic Engineering*, 1960: 35-45.

Kiel, M. *Entwicklung einer Intelligenten Prüfmaschine für Brandbeansprüchte gesamttragwerke.* Technical report, Technical University Brunswick, 1989.

Kim, S. J., R. Christenson, and B. Phillips. “Geographically distributed real-time hybrid simulation of MR dampers for seismic hazard mitigation.” *20th Analysis & Computation Specialty Conference ASCE*, Chicago (United States), 2012.

Korzen, M., G. Magonette, and P. Buchet. “Mechanical loading of columns in fire tests by means of the substructuring method.” *Proceedings of the Eighth Interflam Conference*, Edinburgh (United Kingdom), 1998: 911–914.

Korzen, M., I. C. Neves, J. P. C. Rodrigues, and J. C. Valente. “Behaviour in fire of thermally restrained compressed steel members experimental and numerical approach.” *Proceedings of the 4th international workshop, Structures in fire*, Aveiro (Portugal), 2006.

Korzen, M., J. C. P. Rodrigues, and L. M. S. Laím. “columns, Fire circular tests on circular concrete.” *13th International Conference and Exhibition on Fire Science and Engineering (Interflam 2013)*, Royal Holloway College (United Kingdom), 24-26 June 2013.

Korzen, M., J. P. C. Rodrigues, and A. M. Correia. “Thermal restraint effects on the fire resistance of steel and composite steel ans concrete columns.” *Application of Structural Fire Engineering*, Prague (Czech Republic), 19-20 February 2009.

Korzen, M., K.-U. Ziener, S. Riemer, G. Magonette, and P. Butchet. “Some remarks on the substructuring method applied to fire resistance tests of columns.” *World Congress on Housing*, Coimbra (Portugal), 2002.

Kwon, O.-S., and V. Kammula. “Model updating method for substructure pseudo-dynamic hybrid simulation.” *Earthquake Engineering & Structural Dynamics*, 2013.

Lee, S. K., E. C. Park, and K. W. Min. “Real-time substructuring technique for the shaking table test of upper substructures.” *Engineering Structures*, 2007: 2219–2232.

Lim, C. N., S. A. Neild, D. P. Stoten, C. A. Taylor, and D. Drury. “Using adaptive control for dynamic substructuring tests.” *13th World Conference on Earthquake Engineering*, Vancouver (Canada), 2004.

Ma, Q. T., P. Omenzetter, J. M. Ingham, J. W. Butterworth, and M. J. Pender. “Overview of NZNEES@Auckland.” *Proceedings of 2007 New Zealand Society for Earthquake Engineers Conference*, Palmerston North (New Zealand), 2007.

Magonette, G. “Development and application of large-scale continuous pseudodynamic.” *Philosophical Transaction of the Royal Society A*, September 2001, Royal Society ed.: 1771–1799.

Mahin, S. A., P. B. Shing, C. R. Thewalt , and R. D. Hanson. “Pseudodynamic test method. Current status and future directions.” *Journal of Structural Engineering*, 1989: 2113-2128.

Mandel, J. “Balancing domain decomposition.” *Communications in Numerical Methods in Engineering*, March 1993, John Wiley & Sons ed.: 233–241.

McCrum, D. P., and M. S. Williams. “An overview of seismic hybrid testing of engineering structures.” *Engineering Structures*, 2016.

Menari, M., X. Wang, H. Mahmoud, and O. Kwon. “Response of a structure subjected to fire following an earthquake event.” *ASCE Journal of Structural Engineering*, 2020.

Mercan, O., and J. Ricles. “Stability analysis for real-time pseudodynamic and hybrid psedodynamic testing with multiple sources of delay.” *Earthquake Engineering & Structural Dynamics*, 2008: 1269 - 1293.

—. “Stability and accuracy analysis of outer loop dynamics in real-time pseudodynamic testingof SDOF systems.” *Earthquake Engineering & Structural Dynamics*, 2007: 1523-1543.

Mergny, E, G. Drion, T. Gernay, and J.-M. Franssen. “Hybrid fire testing in a non-linear environment using a proportional integral controller.” *Journal of Structural Fire Engineering*, 2019.

Mosqueda, G., B. Stojadinovic , and S. A. Mahin . *Implementation and accuracy of continuous hybrid simulation with geographically distributed substructures.* UCB/EERC 2005–02, BerkeleyReturn : Earthquake Engineering Research Center, University of California, 2005.

Mosqueda, G., B. Stojadinovic, and S. Mahin. “Geographically distributed continuous hybrid simulation.” *Proceedings of the 13th World Conference on Earthquake Engineering*, Vancouver (Canada), 2004: 0595.

Mostafaei, H. “Hybrid fire testing for assessing performance of structures in fire –Application,.” *Fire Safety Journal*, 2013a: 30–38.

—. “Hybrid fire testing for assessing performance of structures in fire –Methodology.” *Fire Safety Journal*, 2013b: 170–179.

Nakashima, M., and N. Masaoka. “Real-time on-line test for MDOF systems.” *Earthquake Engineering & Structural Dynamics*, 1999, John Wiley & Sons ed.: 393-420.

Nakashima, M., H. Kato, and E. Takaoka. “Development of real-time pseudo dynamic testing. Earthquake Engineering & Structural Dynamics.” *Earthquake Engineering and Structural Dynamics*, 1992, John Wiley & Sons ed.: 79-92.

Nakashima, M., T. Kaminoso, M. Ishida, and K. Ando. “Integration techniques for substructuring pseudodynamic test.” *Proceedings 4th US National Conference On Earthquake Engineering*, Palm Springs (United States), 1990: 515-524.

Nakata, N., B. Spencer, and A. S. Elnashai. “Mixed load/displacement control strategy or hybrid simulation.” *Proceedings, 4th International Conference on Earthquake Engineering*, 2006.

Neild, S. A., D. P. Stoten, D. Drury, and D. J. Wagg. “Control issues relating to real-time substructuring experiments using a shaking table.” *Earthquake Engineering & Structural Dynamics*, 2005: 1171-1192.

Nour-Omid, B., and C. C. Rankin. “Finite rotation analysis and consistent linearization using projectors.” *Computer Methods in Applied Mechanics and Engineering*, 1991: 353–384.

Ogata, K. *Modern Control Engineering.* Pearson, 2009.

Palacio-Betancur, A., and M. Gutierrez Soto. “ Adaptive tracking control for real-time hybrid simulation of structures subjected to seismic loading.” *Mechanical Systems and Signal Processing*, 2019.

Park, D.-U., C.-B. Yun, J.-W. Lee, K. Nagata, E. Watanabe, and K. Sugiura. “On-line pseudodynamic network testing on base-isolated bridges using Internet and wireless Internet.” *Experimental Mechanics*, 2005: 331-343.

Qureshi, R., N. E. Khorasani, and M. Sivaselvan. “Developing real-time hybrid simulation to capture column buckling in a steel frame under fire.” *The 11th International Conference on Structures in Fire*, Brisbane (Australia), December, 2020.

Qureshi, R., N. E. Khorasani, and T. Gernay. “Adaption of active boundary conditions in structural fire testing.” *Journal of Structural Fire Engineering*, July 2019.

Renard, S., J.-C. Mindeguia, F. Robert, S. Morel, and J.-M. Franssen. “An adaptive controller for hybrid testing.” *Experimental Techniques*, Juin 2020: 701–714.

Robert, F., S. Rimlinger, and C. Collignon. “Structure fire resistance: a joint approach between modelling and full scale testing (substructuring system).” *3rd fib International Congress*, 2010.

Sadek, F., J. A. Main, H. S. Lew, S. D. Robert, V. P. Chiarito, and S. El-Tawil. “Experimental and Computational Study of Steel Moment Connection under a Column Removal Scenario.” NIST Technical Note 1669, 2010.

Saleem, K., J. Parra-Fuente, M. Ojaghi, M. Williams, and A. Blakeborough. “UK-NEES: grid services architecture for earthquake.” *Proceedings of the WSEAS (World Scientific and Engineering Academy and Society) International*, Istanbul (Turkey), 2008: 174-181.

Sauca, A. “ Development and implementation of a methodology for hybrid fire testing applied to concrete structures with elastic boundary conditions (Dissertation).” *Liege University*, 2017.

Sauca, A., T. Gernay, F. Robert, N. Tondini, and J.-M. Franssen. “Hybrid fire testing: Discussion on stability and implementation of a new method in a virtual environment.” *Journal of Structural Fire Engineering*, December 2018.

Schellenberg , A. H., S. A. Mahin, and G. L. Fenves. *Advanced implementation of Hybrid Simulation.* PEER Report 2009/104, Berkeley: University of California, 2009.

Schellenberg, A., H. K. Kim, Y. Takahashi, G. L. Fenves, and S. A. Mahin. *OpenFresco.* Berkeley: University of California, 2009.

Schulthess, P. “Consolidated Fire Analysis - Coupled Numerical Simulation and Physical Testing for Global Structural Fire Analysis (Dissertation).” *Eidgenössische Technische Hochschule, Zürich*, 2019.

Schulthess, P., M. Neuenschwander, K. M. Mosalam, and M. Knobloch. “A computationally rigorous approach to hybrid fire testing.” *Computers and Structures*, May 2020.

Schulthess, P., M. Neuenschwander, M. Knobloch, and M. Fontana. “Consolidated fire analysis - Coupled thermo-mechanical modelling for global structural fire analysis.” *Proceedings of the Ninth International Conference, Structures in fire*, Lancaster (PA, United States) 2016: 819–826.

—. “Consolidated fire testing - Coupled thermo-mechanical modelling for analysis of the global structural fire behaviour.” *Proceedings of the Sixth International Conference on Structural Engineering, Mechanics and Computation*, Cape Town (South Africa) 2016: 633–634.

—. “Consolidated fire testing - A framework for thermomechanical modelling.” *Sixth International Conference on Computational Methods for Coupled Problems in Science and Engineering*, Spain (Barcelona), 2015: 222–229.

Schwarz, H. A. *Gesammelte Mathematische Abhandlungen.* Vol. 2. Berlin: Springer, 1890.

Shao, X., A. M. Reinhorn, and M. Sivaselvan. “Real-time dynamic hybrid testing using force-based substructuring.” *ASCE Structures Congress*, Reston (United States), 2006.

Shing, P. B., and S. A. Mahin. “Cumulative experimental errors in pseudodynamic tests.” *Earthquake Engineering & Structural Dynamics* (Earthquake Engineering & Structural Dynamics), 1987: 409-424.

—. “Computational aspects of a seismic performance test method using on-line computer control.” *Earthquake Engineering & Structural Dynamics*, 1985: 507-526.

Shing, P. B., and S. A. Mahin. *Experimental error propagation in pseudodynamictesting.* Report UCB/EERC-83/12, Berkeley: Earthquake Engineering Research Center, University of California, 1983.

Shing, P. B., and T. Manivannan. “On the accuracy of implicit algorithm for pseudodynamic tests.” *Earthquake Engineering & Structural Dynamics*, 1990: 631-651.

Shioya, R., M. Ogino, H. Kanayama, and D. Tagami. “Large Scale Finite Element Analysis with a Balancing Domain Decomposition Method.” *Key Engineering Materials*, July 2003: 21-26.

Spencer, B. F., and al. “NEESGRID: A distributed collaboratory for advanced earthquake engineering experiment and simulation, in 13th World Conference on Earthquake.” *13th World Conference on Earthquake Engineering*, Vancouver (Canada), 2004.

Takanashi, K., and K. Ohi. *Earthquake response analysis of steel structures by rapid computer-actuator on-line system, (1) a progress report, trial system and dynamic response of steel beams.* Technical report, University of Tokyo, Tokyo: Earthquake Resistant Structrure Research Center (ERS), Institute of Industrial Science, 1983.

Takanashi, K., K. Udagawa, M. Seki, T. Okada, and H. Tanaka. “Non-linear earthquake response analysis of structures by a computer-actuator on-line system (part 1 detail of the system).” *Transactions of the Architectural Institute of Japan*, March 1975: 77-83.

Tao, J., and O. Mercan. “A study on a benchmark control problem for real-time hybrid simulation with a tracking error-based adaptive compensator combined with a supplementary proportional-integral-derivative controller.” *Mechanical Systems and Signal Processing*, 2019.

Thewalt, C. R., and S. A. Mahin. *Hybrid solution techniques for generalized pseudodynamic testing.* UCB/EERC-87/09, Berekeley: Earthquake Engineering Research Center, University of California, 1987.

Tondini, N., G. Abbiati, L. Posidente, and B. Stojadinovici. “A Static Partitioned Solver for Hybrid Fire Testing.” *9th International conference on Structures in Fire*, 8-10 June 2016: 827-835.

Truesdell, C., and R. A. Toupin. “The classical field theories.” *Handbuch Der Physik*, 1960: 226–790.

Urthale, Y., and J. N. Reddy. *Communications in Numerical Methods in Engineering*, 2005: 553–570.

Wagg, D. J., and D. P. Stoten. “Substructuring of dynamic systems via the adaptive minimal control synthesis algorithm.” *Earthquake Engineering & Structural Dynamics*, 2001: 865–877.

Wallace, M. I., D. J. Wagg, and S. A. Neild. “An adaptive polynomial based forward prediction algorithm for multi-actuator real-time dynamic substructuring.” *Proceedings of the Royal Society A: Mathematical, Physical and Engineering Science*, 2005: 3807–3826.

Wallace, M. I., J. Sieber, A. Neild, D. J. Wagg, and B. Krauskopf. “Stability analysis of real-time dynamic substructuring using delay differential equation models.” *Earthquake Engineering & Structural Dynamics*, 2005.

Wang, J. T., Y. Gui, and F. Zhu. “Real-time hybrid simulation of multi-story structures installed with tuned liquid damper.” *Structural Control and Health Monitoring*, 2016: 1015–1031.

Wang, K. J., K. C. Tsai, S. J. Wang, W. C. Cheng, and Y. S. Yang. “ISEE: Internet-based simulations for earthquake engineering Part II: The application protocol appraoch.” *Earthquake Engineering & Structural Dynamics*, 2007: 2307-2323.

Wang, K. J., S. J. Wang, Y S. Yang, W. C. Cheng, and K. C. Tsai. “Internet-based simulations for earthquake engineering part I: The application protocol approach.” *International Workshop on Steel and Concrete Composite Construction*, Taipei (Taiwain), 2003.

Wang, X., R. E. Kim, O.-S. Kwon, and I. Yeo. “Hybrid Simulation Method for a Structure Subjected to Fire and Its Application to a Steel Frame.” *Journal of Structural Engineering*, August 2018: 04018118-1-04018118-11.

Wang, Y-P, C-L Lee, and T-H Yo. “Modified state-space procedures for pseudodynamic testing.” *Earthquake Engineering & Structural Dynamics*, 2001: 59-80.

Wang, Z., X. Ning, G. Xu, H. Zhou, and B. Wu. “High performance compensation using an adaptive strategy for real-time hybrid simulation.” *Mechanical Systems and Signal Processing*, 2019.

Watanabe, E., C. Yun, K. Sugiura, D. Park, and K. Nagata. “On-line interactive testing between KAIST and Kyoto University.” *Proceedings of the 14th KKNN Symposium on Civil Engineering*, Kyoto (Japan), 2001.

Watanabe, E., K. Sugiura, K. Nagata, and Y. Suzuka. “Development of parallel pseudodynamic pseudodynamic.” *Proceedings of 10th Japan Earthquake Engineering Symposium*, Yokohama (Japan), 1998.

Watanabe, E., T. Kitada, K. Sugiura, and K. Nagata. “Parallel Pseudo-Dynamic Seismic Loading Test on Elevated Bridge System Through the Internet.” *Proceedings of the Eighth East Asia-Pacific Conference on Structural Engineering and Construction*, 2001.

Wempner, G. A. “Finite elements, finite rotations and small strains of flexible shells.” *International Journal of Solids and Structures*, 1969: 117–153.

Whyte, C. A., K. R. Mackie, and B. Stojadinovic. “Hybrid Simulation of Thermomechanical Structural Response.” *Journal of Structural Engineering*, 2016: 04015107-1 – 04015107-11.

Winget, J., and T. J. R. Hughes . “Finite rotation effects in numerical integration of rate constitutive equations arising in large deformation analysis.” *International Journal for Numerical Methods in Engineering*, 1980: 1862–1867.

Wu, B., G. Xu, Q. Wang, and M. S. Williams. “Operator-splitting method for real-time substructure testing.” *Earthquake Engineering & Structural Dynamics*, 2006: 293-314.

Wu, B., Z. Wang, and O. S. Bursi. “Actuator dynamics compensation based on upper bound delay for real-time hybrid simulation.” *Earthquake Engineering & Structural Dynamics*, 2013: online.

Xu, D., H. Zhou, X. Shao, and T. Wang. “Performance study of sliding mode controller with improved adaptive polynomial-based forward prediction.” *Mechanical Systems and Signal Processing*, 2019.

Xu, W., C. Chen, T. Guo, and M. Chen. “Evaluation of frequency evaluation index based compensation for benchmark study in real-time hybrid simulation.” *Mechanical Systems and Signal Processing*, 2019: 649–663.

Yang, Y. S., K. C. Tsai, A. S. T. Elnashai, and T.-J. Hsieh. “An online optimization method for bridge dynamic hybrid simulations.” *Simulation Modelling Practice and Theory,* 2012.

Yang, Y. S., S. J. Wang, K. J. Wang, K. C. Tsai, and S. H. Hsieh. “ISEE: Internet-based Simulation for Earthquake Engineering - Part I: Database approach.” *Earthquake Engineering & Structural Dynamics,* December 2007, John Wiley & Sons ed.: 2291 - 2306.

Zhao, J., C. French, C. Shield, and T. Posbergh. “Considerations for the development of real-time dynamic testing using servo-hydraulic actuation.” *Earthquake Engineering & Structural Dynamics,,* 2003: 1773-1794.

Appendix A
Equations of DD methods

This appendix contains additional explanations about the domain decomposition methods.

A.1 Balancing domain decomposition

The interface problem that is solved by (Shioya, et al. 2003) is the following:

$$\mathbf{Ku} = \mathbf{f} \tag{A-1}$$

The interface problem arises from a finite element discretization of a linear, elliptic, self-adjoint boundary value problem in domain Ω. The following sets and variables are considered:

- Ω is the domain where the problem of equation () is defined.
- Ω_i are the non-overlapping subdomains of Ω, with $i = 1, \dots, k$
- $\delta\Omega_i$ are the subdomains boundaries.
- Γ is the union of all subdomains boundaries $\delta\Omega_i$.
- $\mathbf{u}_i$ is the vector of degrees of freedom (DOFs) corresponding to all elements in subdomain (in this case, displacement vector).
- V_i is the space of the DOFs on $\delta\Omega_i$ of dimension n^i.
- V is the space DOFs of freedom on Γ.
- $\mathbf{K}$ is the stiffness matrix.
- $\mathbf{f}$ is the force vector.
- $\mathbf{N}_i$ is a 0-1 matrix that maps $\mathbf{u}_i$.

$\mathbf{u}_i$ can split into $\mathbf{u}_{B_i}$ (DOFs that correspond to the interface) of the subdomains Ω_i and $\mathbf{u}_{I_i}$ (remaining DOFs). The subdomain stiffness matrices are also split. The new system is:

$$\begin{bmatrix} \mathbf{K}_{II_i} & \mathbf{K}_{IB_i} \\ \mathbf{K}_{IB_i}^T & \mathbf{K}_{BB_i} \end{bmatrix} \begin{bmatrix} \mathbf{u}_{I_i} \\ \mathbf{u}_{B_i} \end{bmatrix} = \begin{bmatrix} \mathbf{f}_{I_i} \\ \mathbf{f}_{B_i} \end{bmatrix} \tag{A-2}$$

The unknowns in the interiors of the subdomain $\mathbf{u}_I^i$ is eliminated by reducing the problem to the Schur complement on the subdomain interface. The system (A-2) is rewritten as follow:

$$\mathbf{S}\mathbf{u}_B = \mathbf{g} \tag{A-3}$$

S is the Schur complement and is the assembly of the local ones complements $\mathbf{S_i}$ (positive semidefinite):

$$\mathbf{S} = \sum_{i=1}^{k} \mathbf{N}_{B_i} \mathbf{S}_i \mathbf{N}_{B_i}^T$$
$$\mathbf{S}_i = \mathbf{K}_{BB_i} - \mathbf{K}_{IB_i}^T \mathbf{K}_{II_i}^T \mathbf{K}_{IB_i} \quad \text{(A-4)}$$

The problem of equation (A-3) is thus defined in space V. To solve this problem, the preconditioned conjugate gradient method is chosen. This method requires at each step the solution of an auxiliary problem:

$$\mathbf{Mz} = \mathbf{r} \quad \text{(A-5)}$$

With a symmetric positive definite matrix **M**, called a preconditioner. The algorithm of BDD returns $\mathbf{z} = \mathbf{M}^{-1}\mathbf{r}$, where:

$$\mathbf{M}^{-1} = \left[\mathbf{P} + (\mathbf{I} - \mathbf{P}) \left(\sum_{i=1}^{k} \mathbf{N}_{B_i} \mathbf{D}_i \mathbf{S}_i^{+} \mathbf{D}_i^T \mathbf{N}_{B_i}^T \right) \mathbf{S} (\mathbf{I} - \mathbf{P}) \right] \mathbf{S}^{-1} \quad \text{(A-6)}$$

The following variable are used:

- $\mathbf{S}_i^{+}$ is the Moore-Penrose pseudoinverse
- $\mathbf{D}_i$ is a collection of matrices that form a decomposition of unity:

$$\sum_{i=1}^{k} \mathbf{N}_{B_i} \mathbf{D}_i \mathbf{N}_{B_i}^T = \mathbf{I} \quad \text{(A-7)}$$

  The simplest choice for $\mathbf{D}_i$ is the diagonal matrix with diagonal elements equal to the reciprocal of the number of subdornains with which the degree of freedom is associated.
- **P** be the S-orthogonal projection onto W, the coarse space (subspace) of V defined by:

$$\mathbf{W} = \left\{ \mathbf{v} \in \mathbf{V} \mid \mathbf{v} = \sum_{i=1}^{k} \mathbf{N}_{B_i} \mathbf{D}_i \mathbf{u}_i \, , \mathbf{u}_i \in \text{Range } \mathbf{Z}_i \right\} \quad \text{(A-8)}$$

- $\mathbf{Z}_i$ are the $n_i \times m_i$ matrices of full column rank ($0 \leq m_i \leq n_i$) such as Range $\mathbf{Z}_i \supset$ Null $\mathbf{S}_i$. For an elastic stress problem Null $\mathbf{S}_i$ can be considered to correspond to the degrees of freedom of rigid displacement. $\mathbf{Z}_i$ is defined by assembling $\mathbf{Z}_{P_i}$:

$$\mathbf{Z}_i = \sum_{P} \mathbf{B}_{P_i} \mathbf{Z}_{P_i} \quad \text{(A-9)}$$

  $\mathbf{Z}_{P_i}$ is defined at the point $X(x_1, x_2, x_3)$ on the interface of the subdomain Ω_i:

$$\mathbf{Z}_{P_i} = \begin{bmatrix} 1 & 0 & 0 & 0 & x_3 & -x_2 \\ 0 & 1 & 0 & x_3 & 0 & x_1 \\ 0 & 0 & 1 & x_2 & -x_2 & 0 \end{bmatrix} \quad \text{(A-10)}$$

  $\mathbf{B}_P^i$ is the 0-1 matrix that maps the DOFs **P** into global DOFs defined at the point $X(x_1, x_2, x_3)$ on the interface of the subdomain Ω^i :

(Mandel 1993) shows that for given $\mathbf{r} \in \mathbf{V}$, the computation of $\mathbf{z} = \mathbf{M}^{-1}\mathbf{r}$ is equivalent to the following algorithm:

The auxiliary problem is solved for unknown vectors $\boldsymbol{\lambda}_i \in \Re^{m^i}$:

Step 1
$$\mathbf{Z}_i \mathbf{N}_{B_i}^T \left(\mathbf{r} - \mathbf{S} \sum_{j=1}^{k} \mathbf{N}_{B_j} \mathbf{D}_j \mathbf{Z}_j \boldsymbol{\lambda}_j \right) = 0 \tag{A-11}$$

Then, $\mathbf{s}$ and $\mathbf{s}_i$ are computed:

Step 2
$$\mathbf{s} = \mathbf{r} - \mathbf{S} \sum_{i=1}^{k} \mathbf{N}_{B_i} \mathbf{D}_i \mathbf{Z}_i \boldsymbol{\lambda}^i \tag{A-12}$$
$$\mathbf{s}^i = \mathbf{Z}_i \mathbf{D}_i^T \mathbf{N}_B^{iT} \mathbf{s}$$

Step 3 For each of the local problems, any solutions $\mathbf{u}_i$ can be found:
$$\mathbf{u}_i = \mathbf{S}_i \mathbf{s}_i \tag{A-13}$$

The auxiliary problem is solved for unknown vectors $\boldsymbol{\mu}_i \in \Re^{m^i}$:

Step 4
$$\mathbf{Z}_i \mathbf{D}_i^T \mathbf{N}_{B_i}^T \left(\mathbf{r} - \mathbf{S} \sum_{i=1}^{k} \mathbf{N}_{B_i} \mathbf{D}_i (\mathbf{u}_i + \mathbf{Z}_i \boldsymbol{\mu}_i) \right) = 0 \tag{A-14}$$

$\mathbf{z}$ is computed by averaging the result on the interfaces according to:

Step 5
$$\mathbf{z} = \sum_{i=1}^{k} \mathbf{N}_{B_i} \mathbf{D}_i (\mathbf{u}_i + \mathbf{Z}_i \boldsymbol{\mu}_i) = 0 \tag{A-15}$$

A.2 FETI

FETI method enforces the equality of the solution between the subdomain by Lagrange multipliers. Lagrange multipliers is a general method to find the local maxima and minima of a multivariate function $f(x_1, \dots, x_n)$ subject to constraints $g(x_1, \dots, x_n) = 0$. It consists to solve the equation:

$$\begin{aligned} &\nabla_{x_1,\dots,x_n,\lambda} \mathcal{L}(x_1, \dots, x_n, \lambda) = 0 \\ &\frac{\delta f}{\delta x_i} + \lambda \frac{\delta g}{\delta x_i} = 0 \qquad i = 1 \dots k \end{aligned} \tag{A-16}$$

The variable λ is called a Lagrange multiplier. $\mathcal{L}(x_1, \dots, x_n, \lambda)$ is the Lagrangian function and is written as follows:

$$\mathcal{L}(x_1, \dots, x_n, \lambda) = f(x_1, \dots, x_n) - \lambda g(x_1, \dots, x_n) \tag{A-17}$$

The system (A-16) can be summarized by the following system:

$$\begin{aligned} &\frac{\delta f}{\delta x_i} + \lambda \frac{\delta g}{\delta x_i} = 0 \qquad i = 1 \dots k \\ &g(x_1, \dots, x_n) = 0 \end{aligned} \tag{A-18}$$

Let consider the finite element domain Ω divided an arbitrary number N_s of non-overlapping subdomains Ω_i. The finite element mesh is also divided into a set of disconnected meshes. Within

the subdomain Ω_i, n_i^s is the number of interior nodal unknowns and n_i^I is the number of interface nodal unknowns. n_I is the number of interface nodal unknowns in Ω.

If small displacements are considered, the general problem that must be solved on Ω is the following:

$$f(\mathbf{u}) = \frac{1}{2}\mathbf{u^T K u} - \mathbf{f} \tag{A-19}$$

K, **u** and **f** denotes the stiffness matrix, the displacement vector and the force vector. Each subset Ω_i is characterized by a stiffness matrix $\mathbf{K}_i$, displacement vector $\mathbf{u}_i$, force vector $\mathbf{f}_i$ and a set Boolean symbolic matrix $\mathbf{B}_i^j$ that is set up to interconnect the mesh of Ω_i with those of its neighbours Ω_j. In general, $\mathbf{B}_i^j$ is $n_I \times (n_j^s + n_j^I)$ can be written as follow:

$$\mathbf{B}_i^j = \begin{bmatrix} \mathbf{O}_1(i,j) \\ \mathbf{C}_i^j \\ \mathbf{O}_2(i,j) \end{bmatrix} \tag{A-18}$$

The component of this matrix are:

- $\mathbf{O}_1(i,j)$ that is a $m_1(i,j) \times (n_i^s + n_j^s)$ zero matrix
- $\mathbf{O}_2(i,j)$ that is a $m_2(i,j) \times (n_i^s + n_j^s)$ zero matrix
- $\mathbf{C}_i^j$ that is the $m_c(i,j) \times (n_i^s + n_j^s)$ connectivity matrix

$m_c(i,j)$ is the number of Lagrange multipliers that interconnect Ω_i and Ω_j. The positive integers $m_1(i,j)$, $m_2(i,j)$ are as $m_1(i,j) + m_2(i,j) + m_c(i,j) = n_I$. The connectivity matrix has the following pattern:

$$\mathbf{C}_i^j = \begin{bmatrix} \mathbf{O}_3(i,j) & \mathbf{I}_i^j & \mathbf{O}_4(i,j) \end{bmatrix} \tag{A-19}$$

This matrix consists of:

- $\mathbf{O}_3(i,j)$ that is a $m_c(i,j) \times m_3(i,j)$ zero matrix
- $\mathbf{O}_4(i,j)$ that is a $m_c(i,j) \times m_4(i,j)$ zero matrix
- $\mathbf{C}_i^j$ that is the $m_c(i,j) \times m_c(i,j)$ identity matrix

The positive integers $m_3(i,j)$, $m_4(i,j)$ are as $m_3(i,j) + m_4(i,j) + m_c(i,j) = n_i^s + n_i^I$. The interfaces between the subdomains must satisfy the continuity constraint $g(\mathbf{u})$. It can be written as follow between Ω_i and Ω_j:

$$\mathbf{B}_i^j \mathbf{u}_i = \mathbf{B}_j^i \mathbf{u}_j \tag{A-20}$$

For $i = 1, N_s$ and Ω_j connected to Ω_i. If a_i denotes, the number of subdomains Ω_j that are adjacent to Ω_i. The algebraic system that must be treated in the FETI method is the following:

$$\mathbf{K}_j \mathbf{u}_j = \mathbf{f}_j + \sum_{k=1}^{k=a_j} \mathbf{B}_i^{jT} \lambda \qquad j = 1, N_s \tag{A-21}$$

$$\mathbf{B}_i^j \mathbf{u}_i = \mathbf{B}_j^i \mathbf{u}_j \qquad \begin{matrix} j = 1, N_s, \text{ and } \Omega_j \\ \text{connected to } \Omega_i \end{matrix} \tag{A-22}$$

Appendix B
Lagrange multipliers

The method of Lagrange multipliers is a strategy for finding the local maxima and minima of a function subject to equality constraints. The maximum or minimum of a function $f(\mathbf{x})$ subjected to the equality constraint $g(\mathbf{x}) = 0$, is determined by equalling the gradient of the Lagrangian function $\mathbf{\Lambda}$ to the null vector:

$$\nabla\mathbf{\Lambda} = \nabla\big(f(\mathbf{x}) - \lambda g(\mathbf{x})\big) = 0 \tag{B-1}$$

The function f that must be minimized/maximized is the following:

$$f(\Delta\mathbf{u}) = \frac{1}{2}\Delta\mathbf{u}^{T}\mathbf{K}\Delta\mathbf{u} - \Delta\mathbf{u}^{T}\Delta\mathbf{f} \tag{B-2}$$

The constraint consists in imposing a relative distance $L + \Delta$ between node 1 and node 2 (See Fig. B-1):

$$d(\text{node } 1, \text{node } 2) = L + \Delta \tag{B-3}$$

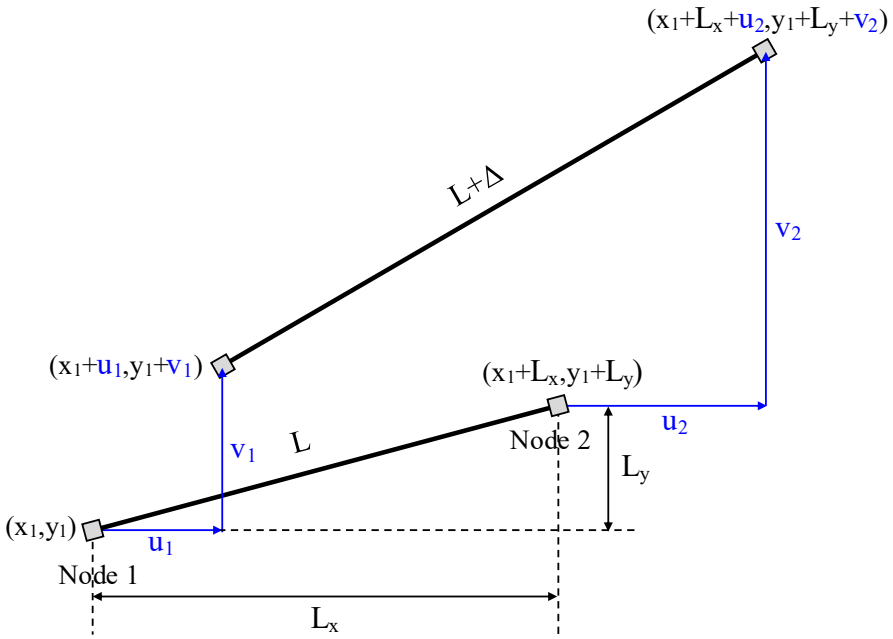

Fig. B-1

The constraint can be written as follows:

$$\sqrt{\left(L_x + u_{2_{i-1}} + \Delta u_2 - u_{1_{i-1}} - \Delta u_1\right)^2 + \left(L_y + v_{2_{i-1}} + \Delta v_2 - v_{1_{i-1}} - \Delta v_1\right)^2} = L + \Delta \tag{B-4}$$

$\Leftrightarrow$

$$\left(L_x + u_{2_{i-1}} + \Delta u_2 - u_{1_{i-1}} - \Delta u_1\right)^2 + \left(L_y + v_{2_{i-1}} + \Delta v_2 - v_{1_{i-1}} - \Delta v_1\right)^2 - L^2 - 2\Delta L - \Delta^2 = 0 \tag{B-5}$$

Finally, the constraint $g(\Delta\mathbf{u})$ is expressed:

$$g(\Delta\mathbf{u}) = \left(L_x + u_{2_{i-1}} + \Delta u_2 - u_{1_{i-1}} - \Delta u_1\right)^2 + \left(L_y + v_{2_{i-1}} + \Delta v_2 - v_{1_{i-1}} - \Delta v_1\right)^2 - L^2 - 2\Delta L - \Delta^2 \tag{B-6}$$

The functions $f(\Delta\mathbf{u})$ and $g(\Delta\mathbf{u})$ form the Lagrangian function:

$$\mathbf{\Lambda} = f(\Delta\mathbf{u}) - \lambda g(\Delta\mathbf{u}) \tag{B-7}$$

The Lagragian method consists in applying equation (B-1) to the previous equation (B-7):

$$\nabla_{\Delta\mathbf{u},\lambda}\mathbf{\Lambda} = \begin{bmatrix} \frac{\partial\Lambda}{\partial\Delta\mathbf{u}} \\ \frac{\partial\Lambda}{\partial\lambda} \end{bmatrix} = \begin{bmatrix} 0 \\ 0 \end{bmatrix} \tag{B-8}$$

One can develop the derivative:

$$\frac{\partial\Lambda}{\partial\Delta\mathbf{u}} = \frac{\partial f(\Delta\mathbf{u})}{\partial\Delta\mathbf{u}} - \lambda\frac{\partial g(\Delta\mathbf{u})}{\partial\Delta\mathbf{u}} = \mathbf{K}\Delta\mathbf{u} - \Delta\mathbf{f} - \lambda\phi\Delta\mathbf{u} - \lambda\mathbf{S} \tag{B-9}$$

$$\frac{\partial\Lambda}{\partial\lambda} = \frac{\partial f(\Delta\mathbf{u})}{\partial\lambda} - \frac{\partial\lambda g(\Delta\mathbf{u})}{\partial\lambda} = 0 - g(\Delta\mathbf{u}) \tag{B-10}$$

The following system must thus be solved:

$$\begin{bmatrix} K\Delta\mathbf{u} - \Delta\mathbf{f} - \lambda\boldsymbol{\phi}\Delta\mathbf{u} - \lambda\mathbf{S} \\ -g(\Delta\mathbf{u}) \end{bmatrix} = \begin{bmatrix} 0 \\ 0 \end{bmatrix} \tag{B-11}$$

System (B-11) is solved using the Newton-Raphson method:

$$\begin{bmatrix} \Delta\mathbf{u}^{k+1} \\ \lambda^{k+1} \end{bmatrix} = \begin{bmatrix} \Delta\mathbf{u}^{k} \\ \lambda^{k} \end{bmatrix} - J^{-1}_{\Delta\mathbf{u}^k,\lambda^k} \begin{bmatrix} \mathbf{K}\Delta\mathbf{u}^k - \Delta\mathbf{f} - \lambda^k\phi\Delta\mathbf{u}^k - \lambda^k\mathbf{S} \\ -g\left(\Delta\mathbf{u}^k\right) \end{bmatrix} \tag{B-12}$$

$J_{\Delta\mathbf{u}^k,\lambda^k}$ is the Jacobian matrix of $\nabla_{\Delta\mathbf{u},\lambda}\mathbf{\Lambda}$:

$$J_{\Delta\mathbf{u}^k,\lambda^k} = \begin{bmatrix} \frac{\partial}{\partial\Delta\mathbf{u}}\left(\frac{\partial\Lambda}{\partial\Delta\mathbf{u}}\right) & \frac{\partial}{\partial\lambda}\left(\frac{\partial\Lambda}{\partial\Delta\mathbf{u}}\right) \\ \frac{\partial}{\partial\Delta\mathbf{u}}\left(\frac{\partial\Lambda}{\partial\lambda}\right) & \frac{\partial}{\partial\lambda}\left(\frac{\partial\Lambda}{\partial\lambda}\right) \end{bmatrix} = \begin{bmatrix} \mathbf{K} - \lambda^k\boldsymbol{\phi} & -\boldsymbol{\phi}\Delta\mathbf{u}^k - \lambda\mathbf{S} \\ -\boldsymbol{\phi}\Delta\mathbf{u}^k - \mathbf{S} & 0 \end{bmatrix} \tag{B-13}$$

This resolution was implemented in SAFIR®.

Appendix C
Experimental setup, sensors and electrical heating

This appendix gathers pictures of the experimental setup presented in Chapter III.

C.1 Experimental setup

(a) *(b)*

Fig. C-1 Setup

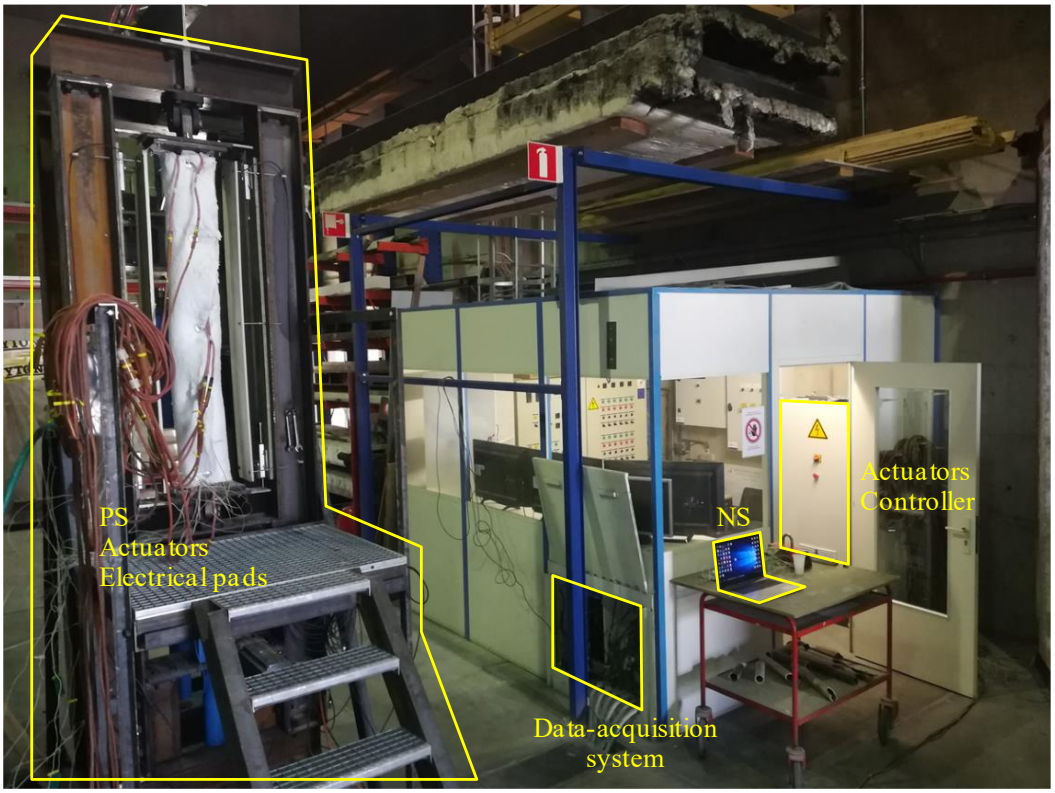

Fig. C-2 Elements of the test

C.2 Actuators

(a) Actuator 1 *(b) Actuator 2* *(c) Actuator 3*

Fig. C-3 Actuators

C.3 Displacement transducers and load cell

(a) Inclinometer

(b) Displacement transducer

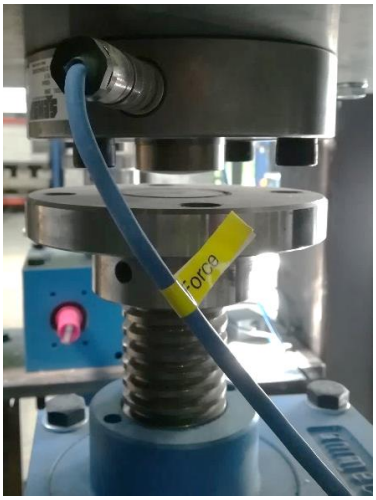

(c) Load cell

Fig. C-4 Sensors

C.4 Heating system

(a) Electrical pads

(b) Fixation

(c) Fixation 2

Fig. C-5 Heating system

(a) 65kVA transformer unit

(b) 6-channel controller

Fig. C-6

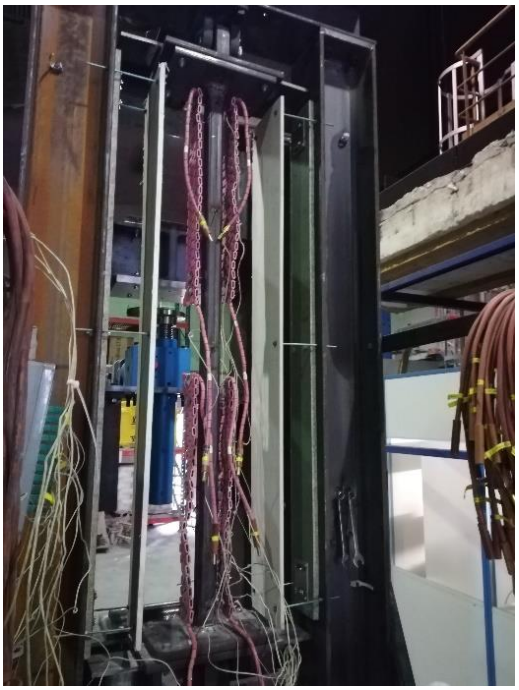

(a) Specimen with electrical pads

(b) Specimen wrapped in fibre

Fig. C-7

C.5 Measure of the elongation

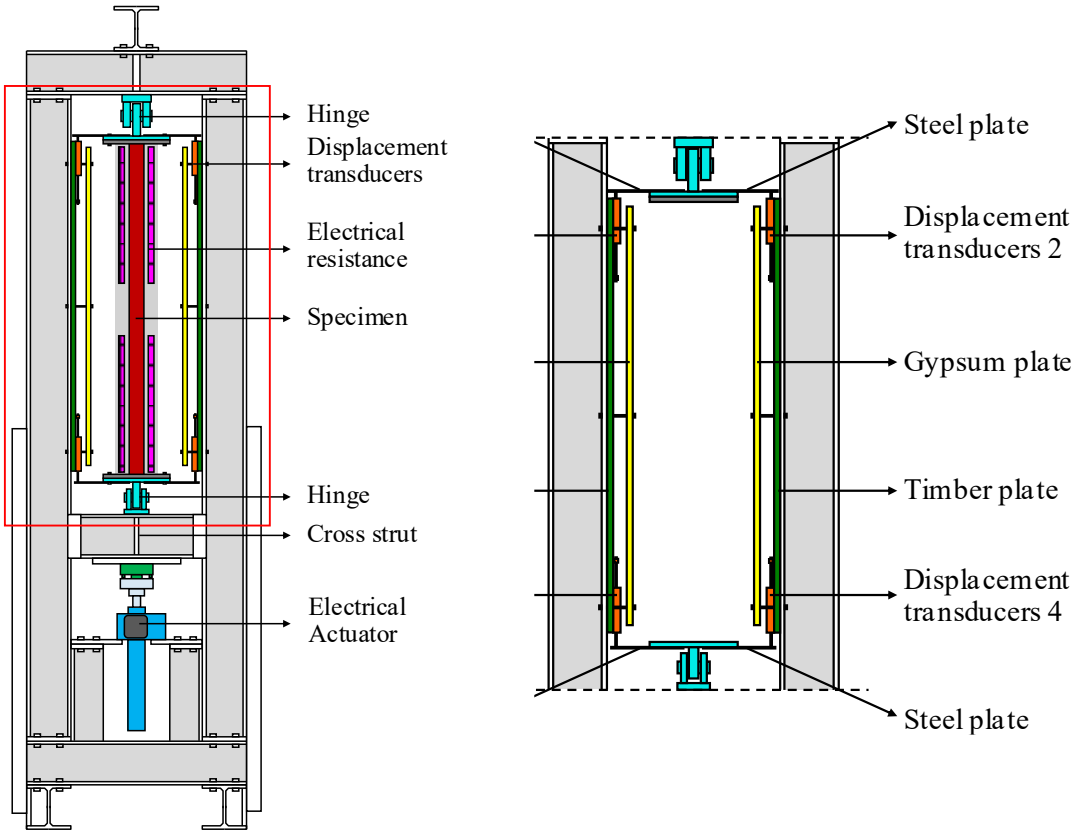

(a) *(b)*

Fig. C-8 Measurement of the elongation of the column

(a) Top *(b) Bottom*

Fig. C-9 Transducers

C.6 Application of the negative moment

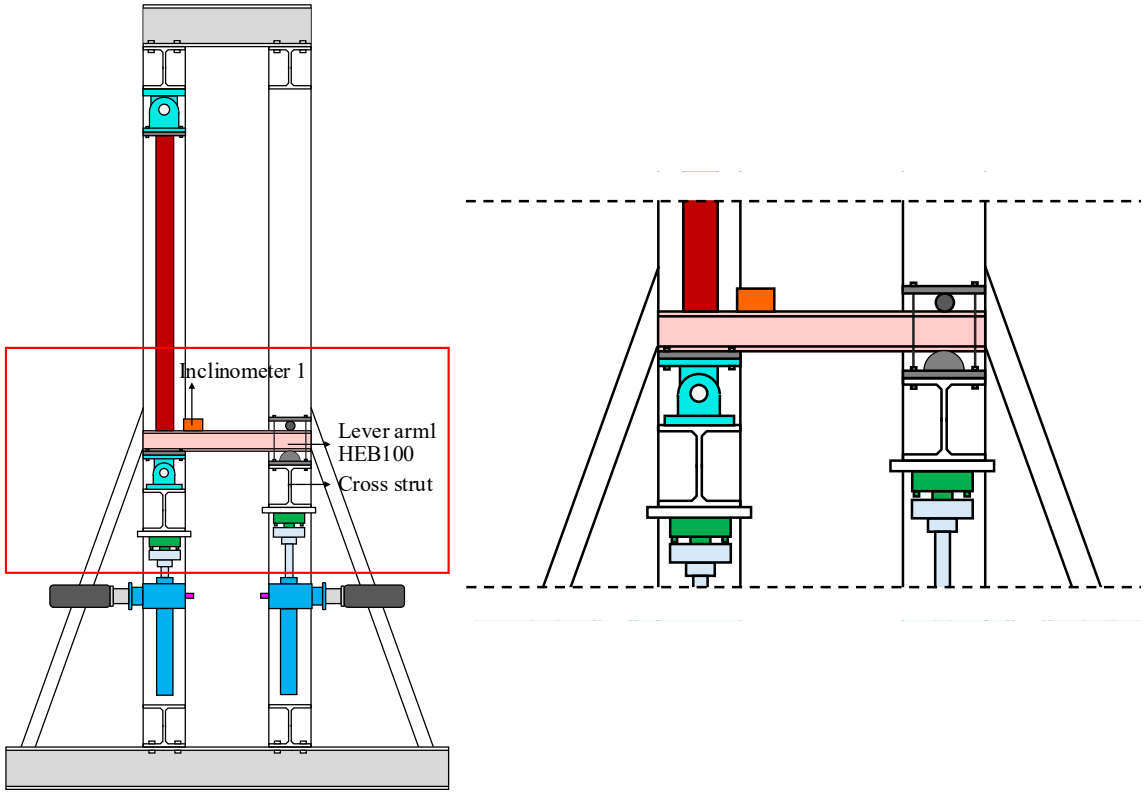

(a) *(b)*

Fig. C-10 Setup to apply negative bending moment: drawings

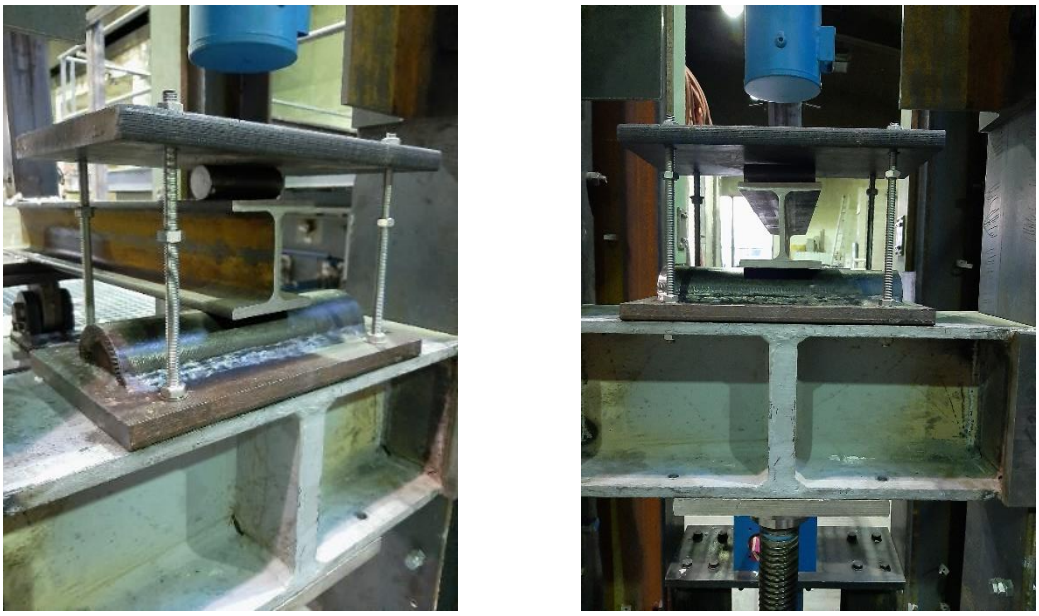

(a) *(b)*

Fig. C-11 Setup to apply negative bending moment: pictures

C.7 Hinges

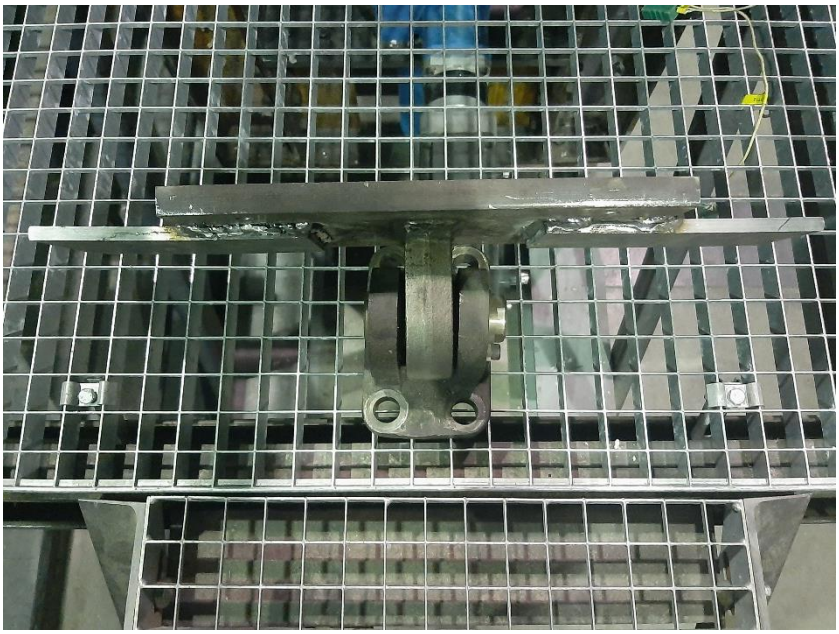

Fig. C-12 Hinge

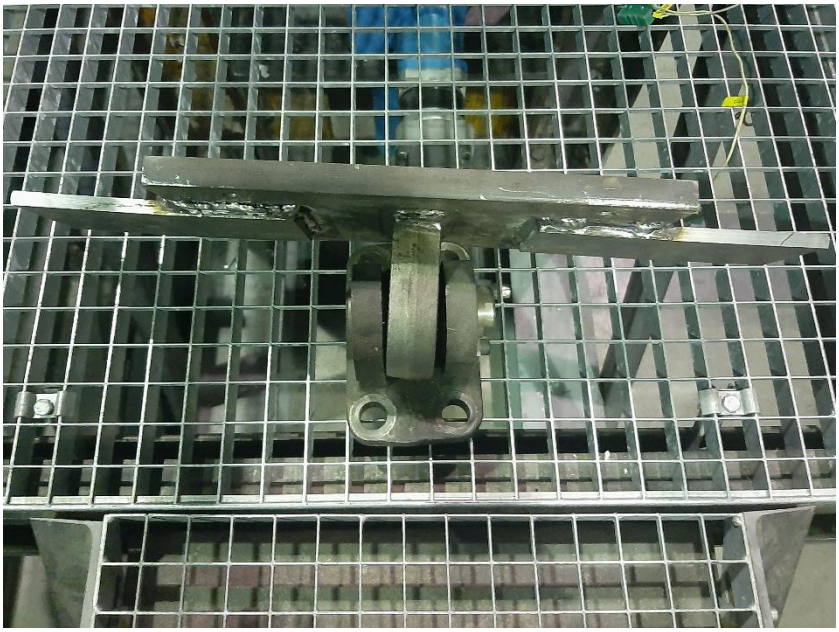

Fig. C-13 Movement of the hinge

Appendix D
Transformation Matrix T''

This appendix presents the transformation matrices T'' used in Chapter III to design the proportional integral controller.

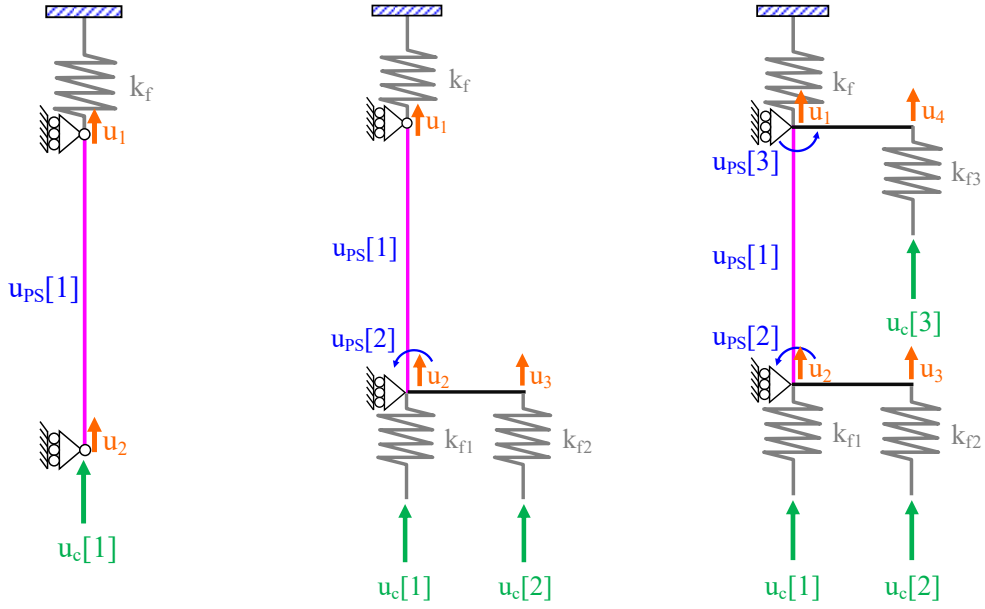

(a) One-DOF test *(b) Two-DOF test* *(c) Three-DOF test*

Fig. D-1 Plamne frame model of the setup

D.1 One-DOF test

$$u_{PS}[1] = u_1 - u_2 \tag{D-1}$$

$$[u_{PS}[1]] = [1 \quad -1]\begin{bmatrix} u_1 \\ u_2 \end{bmatrix} = A\begin{bmatrix} u_1 \\ u_2 \end{bmatrix} \tag{D-2}$$

$$\begin{bmatrix} u_1 \\ u_2 \end{bmatrix} = \begin{bmatrix} \frac{k_f}{k_{PS} + k_f} \\ 1 \end{bmatrix}[u_C[1]] = B[u_C[1]] \tag{D-3}$$

$$[u_{PS}[1]] = A \times B \times [u_C[1]] = T'' \times [u_C[1]] \tag{D-4}$$

D.2 Two-DOF test

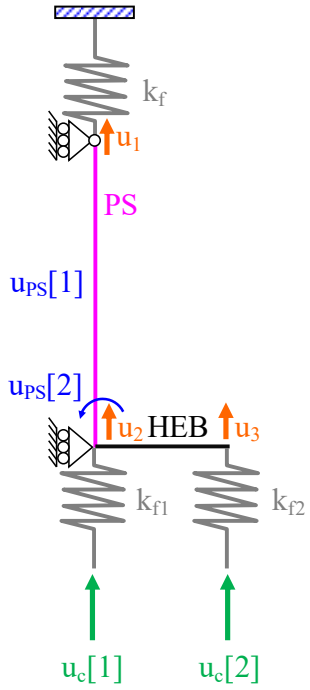

$$u_{PS}[1] = u_1 - u_2$$
$$u_{PS}[2] \approx \frac{u_3 - u_2}{a} \tag{D-5}$$

$$\begin{bmatrix} u_{PS}[1] \\ u_{PS}[2] \end{bmatrix} = \begin{bmatrix} 1 & -1 & 0 \\ 0 & -1/a & 1/a \end{bmatrix} \times \begin{bmatrix} u_1 \\ u_2 \\ u_3 \end{bmatrix} = A \times \begin{bmatrix} u_1 \\ u_2 \\ u_3 \end{bmatrix} \tag{D-6}$$

$$\begin{bmatrix} u_1 \\ u_2 \\ u_3 \end{bmatrix} = B \times \begin{bmatrix} u_C[1] \\ u_C[2] \end{bmatrix} = (B')^{-1} \times B'' \times D \times \begin{bmatrix} u_C[1] \\ u_C[2] \end{bmatrix} \tag{D-7}$$

$$\begin{bmatrix} u_{PS}[1] \\ u_{PS}[2] \end{bmatrix} = A \times B \times \begin{bmatrix} u_C[1] \\ u_C[2] \end{bmatrix} = T'' \times \begin{bmatrix} u_C[1] \\ u_C[2] \end{bmatrix} \tag{D-8}$$

$$B' = \begin{bmatrix} k_{PS} - k_f & 0 & -k_{PS} & 0 & 0 & 0 \\ 0 & \frac{4EI_{PS}}{L} & 0 & \frac{2EI_{PS}}{L} & 0 & 0 \\ -k_{PS} & 0 & \frac{12EI_{HEB}}{L^3} + k_{f1} + k_{PS} & \frac{6EI_{HEB}}{L^2} & -\frac{12EI_{HEB}}{L^3} & \frac{6EI_{HEB}}{L^2} \\ 0 & \frac{2EI_{PS}}{L} & \frac{6EI_{HEB}}{L^2} & \frac{4EI_{HEB}}{L} & -\frac{6EI_{HEB}}{L^2} & \frac{2EI_{HEB}}{L} \\ 0 & 0 & -\frac{12EI_{HEB}}{L^3} & -\frac{6EI_{HEB}}{L^2} & \frac{12EI_{HEB}}{L^3} + k_{f2} & -\frac{6EI_{HEB}}{L^2} \\ 0 & 0 & \frac{6EI_{HEB}}{L^2} & \frac{2EI_{PS}}{L} & -\frac{6EI_{HEB}}{L^2} & \frac{4EI_{HEB}}{L} \end{bmatrix} \tag{D-9}$$

$$B'' = \begin{bmatrix} 0 & 0 \\ 0 & 0 \\ -k_{f1} & 0 \\ 0 & 0 \\ 0 & -k_{f2} \\ 0 & 0 \end{bmatrix} \tag{D-10}$$

$$D = \begin{bmatrix} 1 & 0 & 0 & 0 & 0 & 0 \\ 0 & 0 & 1 & 0 & 0 & 0 \\ 0 & 0 & 0 & 0 & 1 & 0 \\ 0 & 0 & 0 & 0 & 0 & 0 \end{bmatrix} \tag{D-11}$$

D.3 Three-DOF test

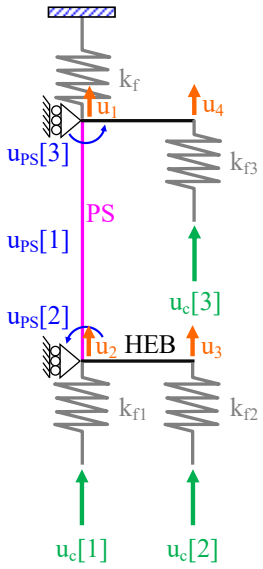

$$\begin{aligned} u_{PS}[1] &= u_1 - u_2 \\ u_{PS}[2] &\approx \frac{u_3 - u_2}{a} \\ u_{PS}[3] &\approx \frac{u_4 - u_1}{a} \end{aligned} \tag{D-12}$$

$$\begin{bmatrix} u_{PS}[1] \\ u_{PS}[2] \\ u_{PS}[3] \end{bmatrix} = \begin{bmatrix} 1 & -1 & 0 & 0 \\ 0 & -1/a & 1/a & 0 \\ -1/a & 0 & 0 & 1/a \end{bmatrix} \times \begin{bmatrix} u_1 \\ u_2 \\ u_3 \\ u_4 \end{bmatrix} = A \times \begin{bmatrix} u_1 \\ u_2 \\ u_3 \\ u_4 \end{bmatrix} \tag{D-13}$$

$$\begin{bmatrix} u_1 \\ u_2 \\ u_3 \\ u_4 \end{bmatrix} = D \times B \begin{bmatrix} u_C[1] \\ u_C[2] \\ u_C[3] \end{bmatrix} = D \times (B')^{-1} \times B'' \times \begin{bmatrix} u_C[1] \\ u_C[2] \\ u_C[3] \end{bmatrix} \tag{D-14}$$

$$\begin{bmatrix} u_{PS}[1] \\ u_{PS}[2] \\ u_{PS}[3] \end{bmatrix} = A \times D \times (B')^{-1} \times B'' \begin{bmatrix} u_C[1] \\ u_C[2] \\ u_C[3] \end{bmatrix} = T'' \times \begin{bmatrix} u_C[1] \\ u_C[2] \\ u_C[3] \end{bmatrix} \tag{D-15}$$

$$B' = \begin{bmatrix} B'_{11} & B'_{12} \\ B'_{21} & B'_{22} \end{bmatrix} \tag{D-16}$$

$$B'_{11} = \begin{bmatrix} k_{f3} + \frac{12EI_{HEB}}{a^3} & \frac{6EI_{HEB}}{a^2} & -\frac{12EI_{HEB}}{a^3} & \frac{6EI_{HEB}}{a^2} \\ \frac{6EI_{HEB}}{a^2} & \frac{4EI_{PS}}{L} & -\frac{6EI_{HEB}}{a^2} & \frac{2EI_{HEB}}{a} \\ -\frac{12EI_{HEB}}{a^3} & -\frac{6EI_{HEB}}{a^2} & k_{PS} - k_f + \frac{12EI_{HEB}}{a^3} & -\frac{6EI_{HEB}}{a^2} \\ \frac{6EI_{HEB}}{a^2} & \frac{2EI_{HEB}}{a} & -\frac{6EI_{HEB}}{a^2} & \frac{4EI_{PS}}{L} + \frac{4EI_{HEB}}{a} \end{bmatrix} \tag{D-17}$$

$$B'_{22} = \begin{bmatrix} 0 & 0 & 0 & 0 \\ 0 & 0 & 0 & 0 \\ -k_{PS} & 0 & 0 & 0 \\ 0 & \frac{2EI_{PS}}{L} & 0 & 0 \end{bmatrix} \qquad B'_{12} = \begin{bmatrix} 0 & 0 & -k_{PS} & 0 \\ 0 & 0 & 0 & \frac{2EI_{PS}}{L} \\ 0 & 0 & 0 & 0 \\ 0 & 0 & 0 & 0 \end{bmatrix} \tag{D-18}$$

$$B'_{22} = \begin{bmatrix} k_{PS} + \frac{12EI_{PS}}{a^3} & \frac{6EI_{HEB}}{a^2} & -\frac{12EI_{PS}}{a^3} & \frac{6EI_{HEB}}{a^2} \\ \frac{6EI_{HEB}}{a^2} & \frac{4EI_{PS}}{L} + \frac{4EI_{HEB}}{a} & -\frac{6EI_{HEB}}{a^2} & \frac{2EI_{HEB}}{a} \\ -\frac{12EI_{HEB}}{a^3} & -\frac{6EI_{HEB}}{a^2} & k_{f2} + \frac{12EI_{PS}}{a^3} & -\frac{6EI_{HEB}}{a^2} \\ \frac{6EI_{HEB}}{a^2} & \frac{2EI_{HEB}}{a} & -\frac{6EI_{HEB}}{a^2} & \frac{4EI_{HEB}}{a} \end{bmatrix} \tag{D-19}$$

$$B'' = \begin{bmatrix} 0 & 0 & -k_{f3} \\ 0 & 0 & 0 \\ 0 & 0 & 0 \\ 0 & 0 & 0 \\ -k_{f3} & 0 & 0 \\ 0 & 0 & 0 \\ 0 & 0 & 0 \\ 0 & -k_{f2} & 0 \\ 0 & 0 & 0 \end{bmatrix} \tag{D-20}$$

$$D = \begin{bmatrix} 1 & 0 & 0 & 0 & 0 & 0 & 0 & 0 \\ 0 & 0 & 1 & 0 & 0 & 0 & 0 & 0 \\ 0 & 0 & 0 & 0 & 1 & 0 & 0 & 0 \\ 0 & 0 & 0 & 0 & 0 & 0 & 1 & 0 \end{bmatrix} \tag{D-21}$$

Appendix E

Temperature

This appendix includes the temperatures measured by the thermocouples during the three hybrid tests carried out in Chapter III.

E.1 One-DOF test

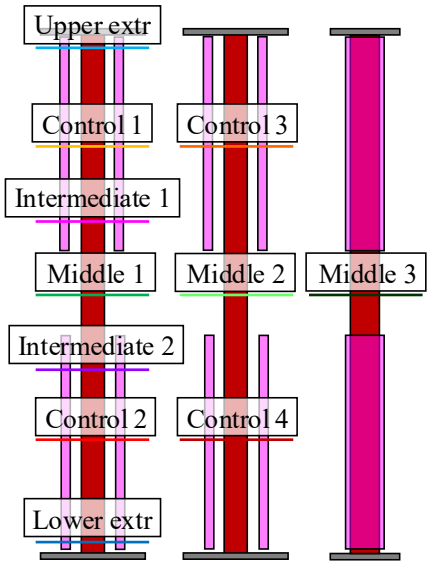

Fig. E-1 Location of the thermocouples

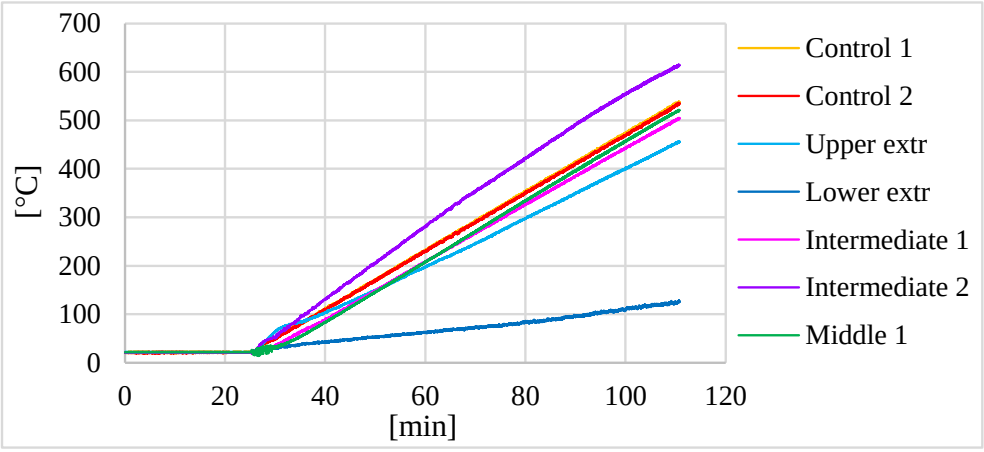

Fig. E-2 Temperatures

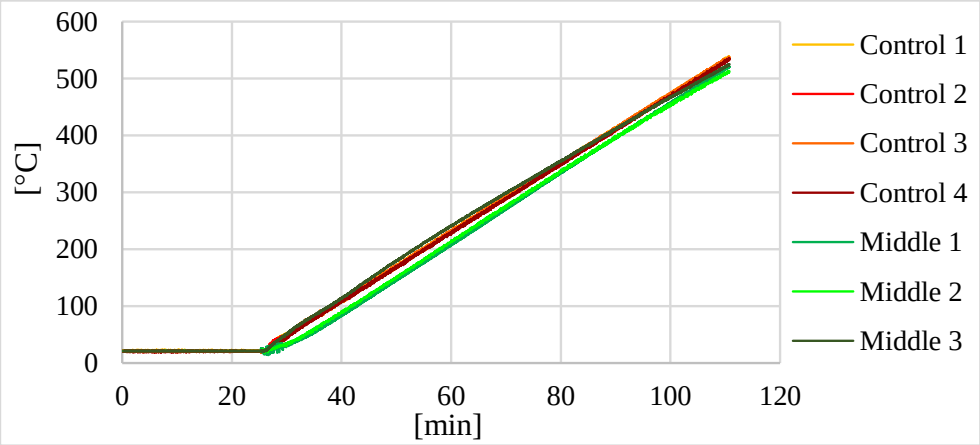

Fig. E-3 Temperatures

E.2 Two-DOF test

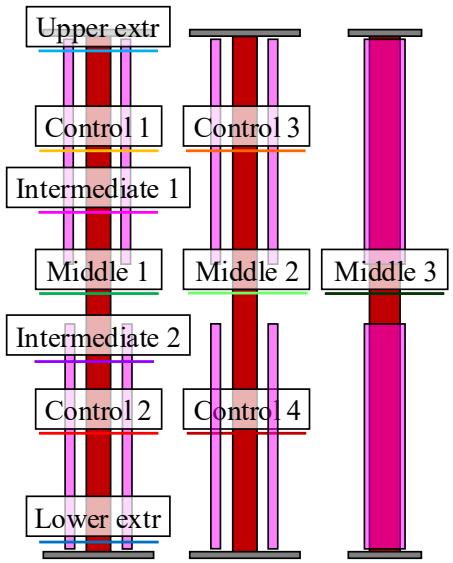

Fig. E-4 Location of the thermocouples

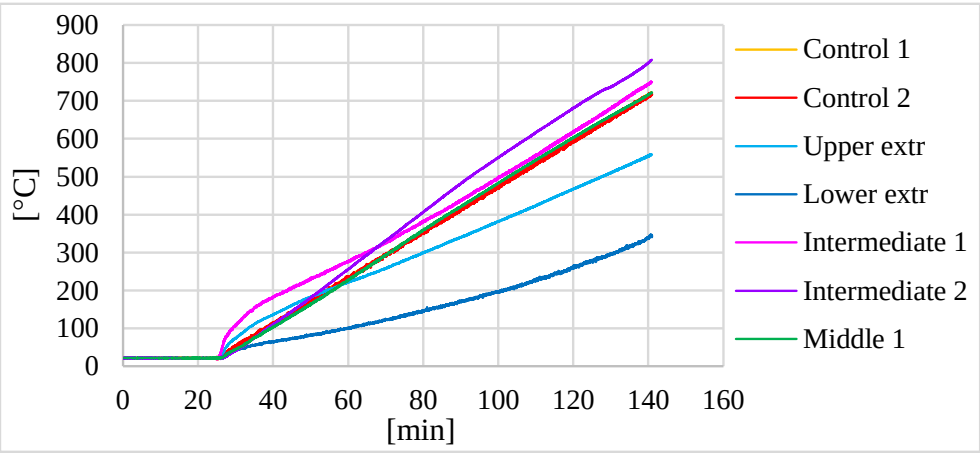

Fig. E-5 Temperatures

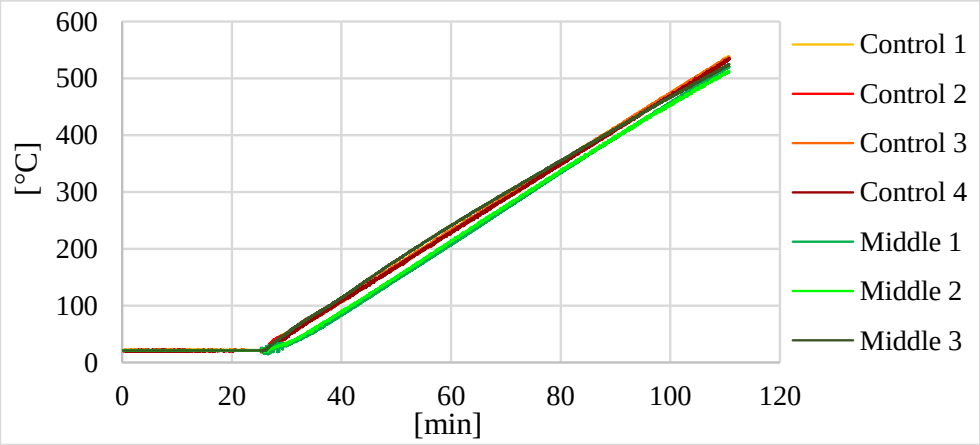

Fig. E-6 Temperatures

E.3 Three-DOF test

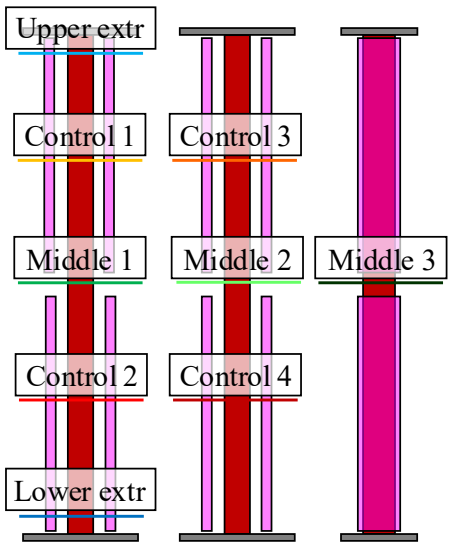

Fig. E-7 Location of the thermocouples

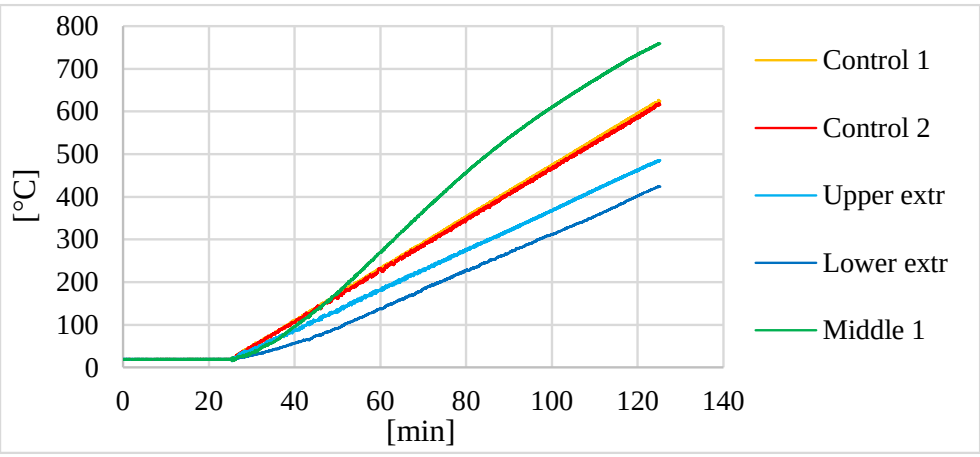

Fig. E-8 Temperatures

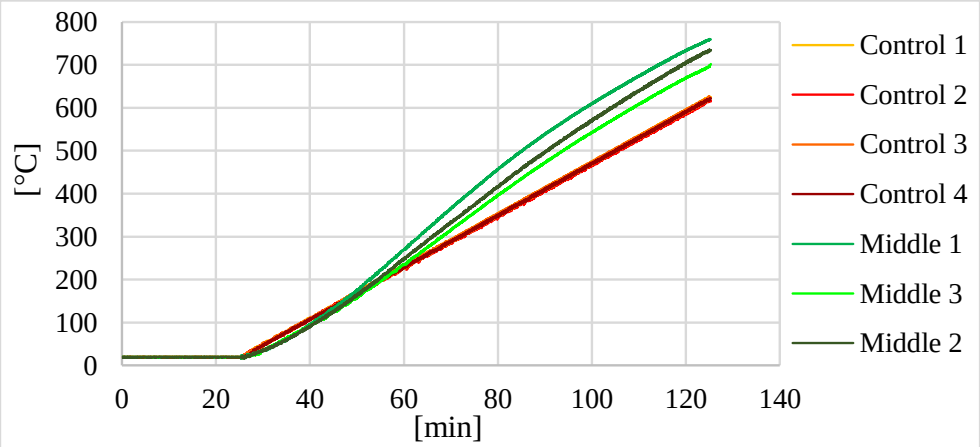

Fig. E-9 Temperatures


LIÈGE
université